OPTIMISATION OF COMPUTATIONAL, BIOLOGICAL AND PHYSICAL METHODS TO STUDY THE CELLULAR ENTRY OF NANOPARTICLES

by

PHILIP J SMITH

A thesis submitted to
The University of Birmingham
for the degree of
DOCTOR OF PHILOSOPHY

School of Chemistry
College of Engineering and Physical Sciences
The University of Birmingham
September 2015

Abstract

Recent advances in nanotechnology have generated great potential for use of nanomaterials in the manufacturing, cosmetic, pharmaceutical and bio-medical sectors. This has provoked great interest in utilisation of nanomaterials in disease diagnostics and treatment, as well as significant concern over the potential for unwanted exposure. Thus, understanding mechanisms by which nanoparticles, structures with at least one dimension <100 nm, interact with cells, gain entry to the intracellular space, and potentially affect cellular functions and viability is relevant and timely.

This thesis focuses on current methods for nanoparticle characterisation and analysis of cellular interactions. The specific interaction between HeLa cells and 20 nm carboxylate-modified polystyrene nanoparticles is examined in detail, and the effects of serum proteins in corona formation is analysed. Fluorescence microscopy image acquisition is studied, with particular attention given to colocalisation analysis. An automated program is presented, making use of a novel de-noising algorithm which makes analysis of low signal-to-noise images possible without additional input. This is validated using computer generated images, and data acquired and analysed by hand. This program was used to analyse confocal microscopy images to quantify nanoparticle colocalisation with intracellular protein markers and membrane stains. A protocol is developed to enable use of total internal reflection fluorescence (TIRF) microscopy for the study of nanoparticle internalisation. Finally, innovative TIRF methods that permit identification of areas of local plasma membrane curvature and super-resolution analysis of fluorophore motion in Z are examined, and significant steps are made to combine these into a single imaging system. Thus, this project will develop computational analysis methods, novel biological assays, and physical enhancements to existing hardware with the aim of accelerating the characterisation of nanoparticle-cell interactions.

ACKNOWLEDGEMENTS

A great number of people and organisations have seen me through this project; mentally, emotionally, financially and spiritually. Thank you all.

First and foremost to my supervisors Dr. Joshua Rappoport, Dr. Rosemary Dyson, Prof. Jon Preece and Prof. Ela Claridge. Thank you all for your guidance, knowledge- and most notably your patience!

Thank you to everyone in the Rappoport lab for persevering with the painful task of teaching Biology to a Physicist. Special mentions to Abdullah Khan and Dr. Julie Mazzolini for not only expanding my mind, but also my heart. And my muscles.

Thank you to Dr. Jochen Kronjaeger for the invaluable suggestions and guidance with the building of the laser unit, and for letting me borrow a lot of expensive equipment to test it with.

Thank you to all the staff and students in PSIBS, particularly Alan, Ali and James for their frequent yet welcome distractions from reality.

The ESPRC for funding via a studentship through the PSIBS Doctoral Training Centre (EP/F50053X/1), and the Wellcome Trust for their additional grant.

Thanks Mum and Dad for having me; I wouldn't be here without you. It's all your fault.

And finally thank you to my amazing wife for not only keeping me sane, but also making me go to Australia for a year to write this thesis.

CONTENTS

LIST OF FIGURES

CHAPTER 1

INTRODUCTION

1.1 Nanoparticles

Nanoparticles are defined as structures with at least one dimension smaller than 100 nm[1]. Their use spans as far back as the ninth century BC in Mesopotamia in the form of metallic lusters on pots, giving a glittering finish. However their characterisation and manufacture has increased exponentially in the last century, with the dawn of the electron microscope and their potential in the medical[2], engineering and research sectors. The reason for such scientific interest is, unsurprisingly, due to their size. They provide the bridge between macroscopic and molecular structures, where their high surface area to volume ratio can result in unexpected properties. These characteristics are often completely unpredictable based on the nature of the bulk material alone. These can include changes in electric conductivity, colour, melting point, strength and magnetic moment[3, 4, 5]. An example of differences that can occur between nanoparticles manufactured from identical material can be seen in Figure 1.1, which features silica nanoparticles of differing sizes.

Gold offers an example of how a nanoscale version of a material can vastly differ from its macroscopic counterpart. Gold nanoparticles display a melting temperature far lower than that of bulk gold, around 300°C for 2.5 nm particles compared to 1064°C for a slab of pure gold[3]. Unexpected optical properties also appear, for example with gold nanoparticles in solution exhibiting a deep red colour[4]. Quantum size effects have also

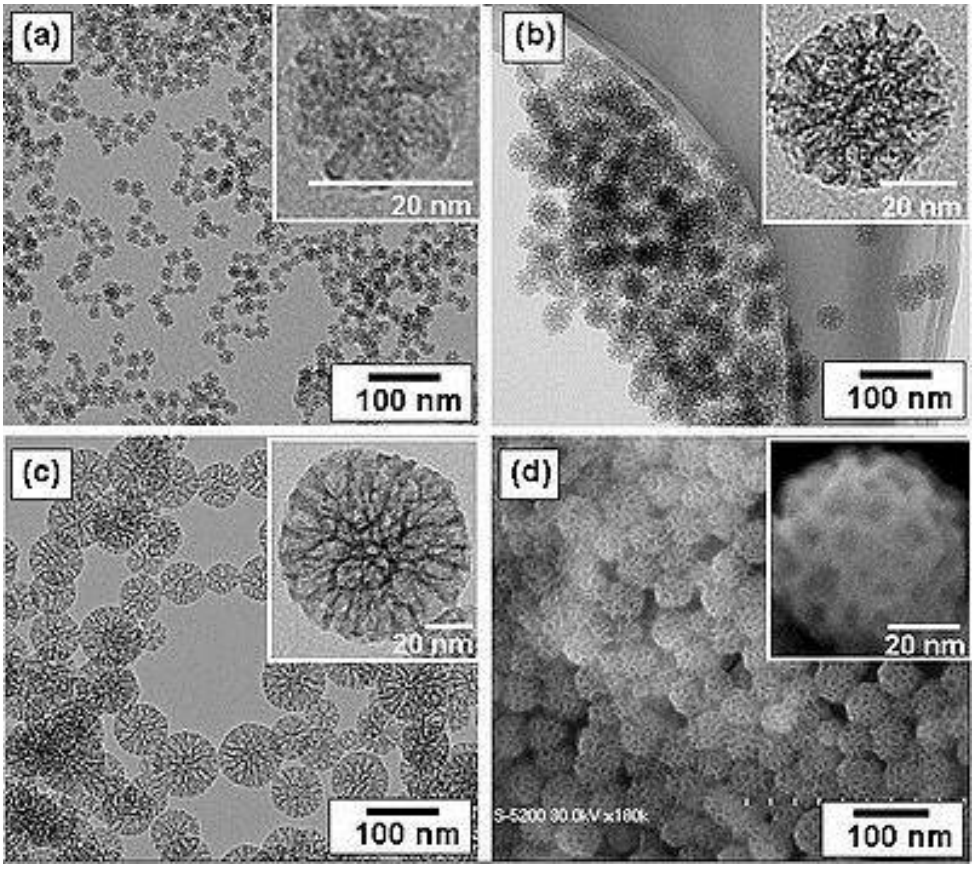

Figure 1.1: *Electron microscope images of mesoporous silica nanoparticles. A) Transmission electron microscope (TEM) image of a 20 nm particle. B) TEM image of a 45 nm particle. C) TEM image of an 80 nm particle. D) A scanning electron microscope image of the nanoparticles displayed in B). Image used with permission under CC BY-NC 3.0 US*

been observed in the difference in electric potential between nanoparticles of 5 and 20 nm. Standing electron waves with discrete energy levels can be formed in these particles due to the gap between atomic valance and conduction bands- something not possible with bulk metals[5].

1.1.1 Commercial and therapeutic uses for nanoparticles

Given the novel and exciting behaviours exhibited by nanoscopic materials, the wide range of applications for them is unsurprising. From industry to imaging, and therapeutics to textiles, the fields in which uses are being found for them are highly varied.

In computing, storage properties of hard drives are constantly being increased with the introduction of nanoparticles. Using nanomagnets- individual ferromagnetic dots- to represent a bit of information can increase the capacity (or decrease the size) of traditional hard disk drives by one or two orders of magnitude[6]. Traditionally made from silicon semiconductors, logic gates are the building blocks of digital circuits. However, the capability for further improvement of these is reaching its limit[7]. In an attempt to develop alternatives to these traditional systems, the use of gold nanoparticles has proved effective in the production of nucleic acid based logic gates. These have found uses in the detection of certain cancers[8]. While an organic computer is far from realisation, the screening for complex conditions on cell membranes using these organic/nanoparticle logic gates shows the potential of these constructs for programming complex functional systems[9].

Textiles are being engineered with incorporated nanoparticles in the emerging interdisciplinary field of 'nanofabrics'. The 'Lotus effect', which describes the superhydrophobicity found on lotus leaves due to the nanoscopic structures on their surface, has been recreated on fabrics with the addition of 40 nm wide silicon nanofibres[10], creating garments that completely repel water. Garments with odour eliminating properties have been achieved via the conversion of ethyl mercaptan to diethyl disulphide with the incorporation of copper coated silica nanoparticles[11]. Nanocomposite fibres, consisting of nanoparticles embedded in a polymeric matrix, have increased elasticity, strength, wrinkle resistant properties[12], and bacterial resistance[13].

It has long been known that silver ions and salts possess antibacterial and antimicrobial properties. However, studies have shown clearly that silver nanoparticles have effective antimicrobial effects against yeast, *Escherichia coli* and *Staphlyococcus aureus*[14]. This is significant considering the emergence of increased bacterial resistance to traditional antibiotics, and the difficulties faced in developing new ones[15]. Other nanoparticles that destroy or disrupt bacteria have been made from iron, silicon, zinc, silver, gold, copper,

aluminium, titanium, and their respective oxides[16]. These work in a variety of ways, including the generation of reactive oxygen species, electrostatic interactions disrupting plasma membranes, and permeabilisation of bacterial cell walls.

The application of nanotechnology to medicine, or nanomedicine, is arguably one of the most exciting fields in the area. New discoveries utilising nanoparticles are pushing forward the frontiers of drug delivery, anti-cancer agents, tissue engineering, and biomedical imaging[17]. Nanoparticles have shown promise in the treatment of tuberculosis, with the ability to control and sustain drug delivery from a polymeric matrix[18]. This was achieved over various routes of administration, including oral and inhalation. Methods for destroying tumours have also been developed. Non-toxic gold nanoparticles with tunable optical absorptivities were injected into mice and allowed to circulate. Tumours were then illuminated with a 808 nm diode laser for three minutes. 90 days later, mice were tumour free with no side effects[19].

The use of nanoparticles in drug delivery can improve bioavailability to specific markers[20]. Successfully implemented, they can allow minimal side effects and decreased toxicity to other organs[21]. Targeted, site-specific drug delivery is one of the most sought-after goals in cancer research. The ability to eliminate a tumorous growth without affecting healthy cells is becoming closer to realisation with the development of functionalised nanoparticles to target cancer-specific traits. Distribution profiles of anticancer drugs in tissues and cells can be controlled by their entrapment within polymeric nanocapsules[22]. Silica nanoparticles have also been tagged with antibodies, vitamins or peptides. Particles with these conjugations have been shown to preferentially associate with cancer cells[23]. Extended circulation of nanoparticles containing the anti-cancer drug doxorubicin was shown to be 300 times more effective at treating metastatic cancer and Kaposi's sarcoma than free doxorubicin[24, 25]. If it could be shown at the cellular level what makes certain properties of particles exhibit these behaviours, then research in this area could progress at a much faster rate[26, 27].

Nanoparticles exhibit many behaviours that make them a useful tool for studying cell biology. The size of nanoparticles for example lends perfectly to multifunctionalisation. This is where various different moieties can be conjugated to the outside of nanoparticles, or contained within an outer shell. This could allow multi-functional imaging, targeting of specific receptors, or the delivery of therapeutic agents[28] to target organs of interest and single cells. The potential for *in vivo* gene transfer has also been highlighted, using SiO_2 to transfect genes into mouse lung cells without cell toxicity[29].

Despite the vast number of ways nanoparticles are being used to improve and enhance our daily lives, there remain concerns about their effects on the human body[30]. This is due to their ability to enter cells[31, 32, 33] and potentially cause harm, as seen in the case of polyamidoamine dendrimer nanoparticles that have been shown to trigger autophagic cell death in lung cells[34].

1.1.2 Concerns regarding harmful effects of nanoparticles

At the time of writing, there were no official regulations on nanoparticle production or manufacture in the EU and US. This is also true for products that contain them. There are currently over 1600 nanoparticle-containing products on the market[35], and manufacturers are not legally required to label them as such. This means that the actual number of nanoproducts on the market is likely to be much higher. There is also no special legislation currently on consumables at regulatory bodies such as the Health and Consumer Protection Directorate of the European Commission, or the Food and Drug Administration in the US. This includes all aspects of production, handling and labelling.

In 1999 the Australian Therapeutic Goods Administration approved the use of nanoparticles in sunscreens[36], without the requirement for package labelling. Zinc oxide (ZnO) nanoparticles in particular provide effective protection against the sun's harmful ultraviolet radiation by both absorption and scattering, as well as providing preferred optical

properties to the sunscreen itself- turning it clear as opposed to white on the skin[37]. Extensive testing has shown that these particles, as well as the other commonly used nanoparticle titanium dioxide (TiO_2), are not genotoxic in common tests such as the Ames' Salmonella gene mutation test or the Comet assay[38]. They are also unable to penetrate healthy or previously sun burned skin[39].

As well as being used in sunscreens, TiO_2 nanoparticles are also a common additive to food products, mostly due to their desirable optical properties in sweets and toothpaste[40]. Other nanomaterials present include nanoclay composite in food and drink packaging, selenium nutrient delivery systems, soy isoflavones as a food supplement and polymerised nanocomposite in PET bottles as an oxygen scavenging barrier resin[41]. Some of these particles have shown to accumulate in the liver[42], induce *in vitro* toxicity in mesothelial cells[43], and cause oxidative stress in the brains of juvenile largemouth bass[44]. It is generally agreed upon that our knowledge of the effects that the widespread use of nanoparticles is having and will have in the future is far from certain, and much more study is required before any long-term effects can be agreed upon[45].

Although these particles are extensively tested in the conditions of their intended use, they will wash off and enter the environment. This introduces the potential for exposure in other, unexpected ways. It has been shown that ZnO nanoparticles induce toxicity in commonly used cell culture lines (RAW 264.7- murine macrophage, and BEAS-2B- human bronchial epithelial) via the generation of reactive oxygen species[46]. They have also been shown to be toxic to zebrafish embryos, a concern revealing the need for more investigation into ecotoxicity in water environments[47]. Animal experiments have shown that oral exposure to both 20 and 120 nm ZnO nanoparticles lead to accumulation in bone, heart, pancreas, spleen and liver[48].

The need to look at effects in the natural environment is highly necessary. TiO_2 nanoparticles alone do not have a detrimental effect on zebrafish larvae. However, when pentachlorophenol, an organochlorine compound used as a pesticide and disinfectant is

also present, reactive oxygen species are induced. These lead to lipid peroxidation and DNA damage in the larvae[49]. Clearly nanoparticles themselves need to be thoroughly tested, but they also need to be considered in all possible environments they may end up. This is considered in more detail in Section 1.1.4.

The potential for harm from nanoparticle exposure extends further than those manufactured for deliberate use. Nanoparticles have been generated for decades as undesirable waste products, chiefly from vehicular and industrial processes.

1.1.3 Environmental exposure to nanoparticles

Whilst deliberately manufactured nanoparticles can enter the environment unintentionally through washing off in the case of sunscreens, or landfill in the case of food and its packaging, they have also long been an unwanted side product from manufacturing processes and vehicle exhaust emissions. Studies into these have yielded findings of concern, with toxic consequences to both people and the environment[50, 51].

Both diesel and petrol engines in vehicles have been shown to release nanoparticles into the atmosphere. These fall into two broad categories, 'accumulation' mode particles which are carbonaceous in nature and are greater than 30 nm in size, and 'nucleation' mode particles which are comprised of condensed volatile material, generally heavy hydrocarbons and sulphate. These are typically smaller than 30 nm[52]. While a lot of research and legislation are going on to reduce the amount of these emissions, there is much work to still be done. This appears to be especially important in colder climates, where air pollution accumulates due to the weather[53, 54] and incomplete combustion of fuel on ignition due to the temperature releases significantly higher amounts of nanoparticles[55], resulting in a much greater level of human exposure. These have been shown to have an effect on the cardiovascular system, leading to morbidity and mortality[50, 56, 57]

Manufacturing processes also create nano-sized airborne particulate matter as an unwanted side product[58]. These include procedures such as welding, high speed machining and heat treatment[59], and can result in laryngeal or lung cancer, asthma, bronchial hyper responsiveness and lipoid pneumonia[60, 61, 62]. This is due to the nanoparticle's ability to enter the tracheobronchial and alveolar regions of the human respiratory tract when airborne[63]. Nanoparticlulate matter has caused harmful effects such as decreased lung function, increased respiratory infections and chronic obstructive pulmonary disease[64] in both the elderly[65] and children[66].

Much of the caution surrounding general nanoparticle use stems from the serious and fatal illnesses brought on from asbestos exposure. The desirable physical properties of asbestos, including resistance to heat and fire, lead to its widespread adoption in building and manufacture in the 1900s. Upon application of force, its brittle nature leads to fibres being formed which can be as thin as 10 nm, small enough to become readily airborne. Inhalation of these asbestos fibres can cause scarring, inflammation and cancer in the lungs and respiratory tract. Nowadays asbestos use is either completely banned or heavily regulated. However, parallels can be been drawn between asbestos fibres and carbon nanotubes. It has been shown that introducing carbon nanotubes (CNTs) into the abdominal cavity of mice showed asbestos-like pathogenicity[67], and that both asbestos and CNTs induce a pro-inflammatory response in human primary macrophages[68]. This has prompted the call for further research and greater caution before introducing nanoproducts into the market.

How a nanoparticle interacts on a cellular level depends on a myriad of variables. This partly relates to how the nanoparticle enters the body, be it inhalation as in the case of airborne particulate matter, ingestion in the form of food or drink, or via the bloodstream through deliberate medical introduction or unintentionally through a wound. However, nanoparticles have been shown to translocate from the point of entry and cause toxicity to other organs. For example, upon inhalation nanoparticles have been shown to evade

clearance from the lungs, and have been found in the liver, heart and brain of rats[69, 70] and humans[71] via the cardiovascular system[72]. The biological environment in which the nanoparticle finds itself determines formation of what is known as the 'protein corona', and it is this that cells ultimately react to.

1.1.4 Protein corona

When a nanoparticle is introduced into a biological fluid, it comes into contact with various proteins. These adsorb to the particles surface through a combination of Van der Waals and electrostatic forces. It is these proteins on the nanoparticle's surface, known as the protein corona, that play the greatest part in determining how the nanoparticle will behave in its environment. This can be visualised in Figure 1.2.

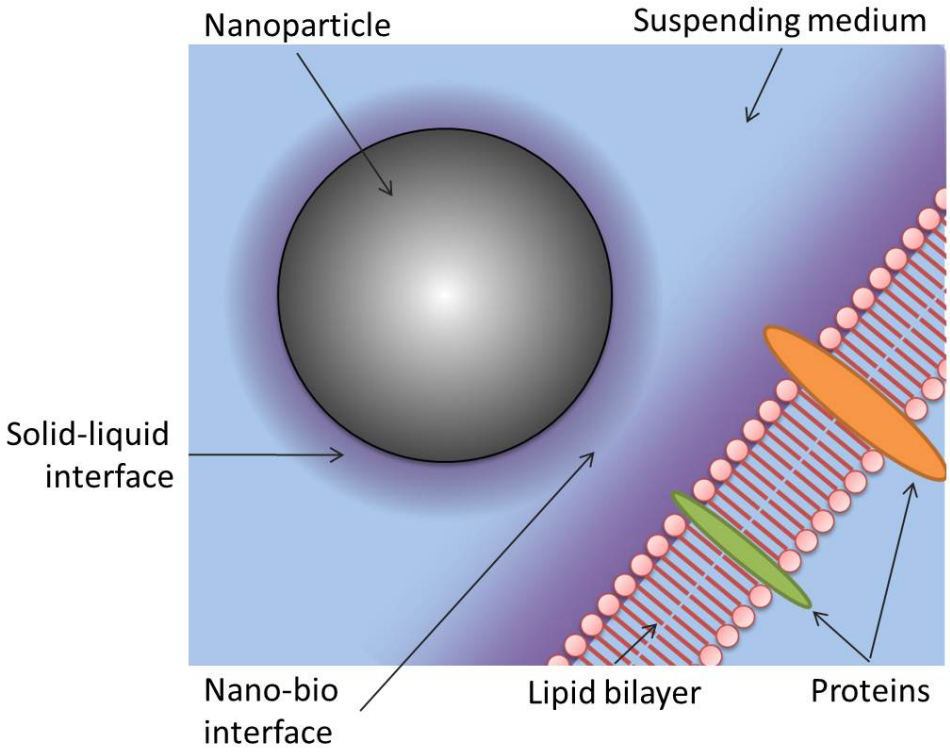

Figure 1.2: *The protein corona surrounding a nanoparticle. A change to any one of these highlighted factors can affect the corona composition, and hence dynamic interactions between nanoparticle and biological structure of interest. Adapted from [73].*

The interaction of a protein corona with its surroundings affects how a nanoparticle behaves when considering aggregation to other nanoparticles, binding to the plasma membrane, cellular uptake, and transport within a system[74]. This makes prior knowledge of the formation of a corona around a nanoparticle essential before valid studies can be undertaken. This will affect the toxicity of nanoparticles, as well as the effectiveness of any nanoparticle based drug delivery systems and the best way to administer them. This is due to the composition of the protein corona around a nanoparticle being able to induce conformational changes in biomolecules, membrane wrapping, and receptor-ligand binding[75].

Corona formation

The protein corona composition is affected by many variables, illustrated in Figure 1.2. Although the nature of the biological fluid (be it blood, mucus or cerebrospinal fluid) determines the types of proteins available for binding, the exact nature of the protein corona is also affected by the size and shape of the particles, as well as particle composition and surface functionalisation. A particle's zeta potential, a measure of the magnitude of the effective electric charge, also affects the affinity of different proteins for adsorbing onto the surface[76]. These factors determine the relevant binding energies of adsorption events, which can be thought of in thermodynamic terms. This is defined in Equation 1.1:

$$\Delta G_{ads} = \Delta H_{ads} - T\Delta S_{ads} < 0 \tag{1.1}$$

The binding energy associated with a adsorption event is known as the Gibbs Free Energy, a change in which is denoted as ΔG_{ads}. This is equal to the change in enthalpy during adsorption, ΔH_{ads}, minus the temperature, T, of the system multiplied by the change in entropy during adsorption, ΔS_{ads}.

In the early stages of introduction, the most abundant proteins play the largest part in the corona make-up. Known as the 'soft corona', this is a reversible coating with low binding energies between protein and particle[77]. Over time, conformational changes of abundant proteins and increased likelihood of contact with less abundant but more energetically favourable proteins causes the make-up of the corona to change. This results in covalent and non-covalent bonding, and as a result changes the nature of the nanoparticle[78]. Once this process becomes irreversible it is known as the 'hard corona'.

The time dependency of the protein corona can be seen in the nature of nanoparticles after differing incubation times in cell culture medium containing 10% serum[78]. After removal from the serum containing medium and rinsing, 10 nm gold nanoparticles incubated for 0-24 hours regained their previous characteristics (size as measured by DLS, and zeta potential), whereas the nature of the nanoparticles incubated for 48 hours never regained their initial properties. This suggests that those particles incubated for shorter times were affected by the soft corona, lightly bound proteins, which was reversible. However those incubated for longer periods of time were encased by proteins in a much more stable, irreversible configuration. This displacement of earlier adsorbed proteins by others with stronger binding affinities is known as the Vroman Effect. This can happen over the order of minutes or days, and critically affects nanoparticle pathophysiology, and hence, biological relevancy[79]. This change over time is illustrated in Figure 1.3.

Corona composition

As suggested earlier, the factors that determine the composition of the nanoparticle protein corona include the size, shape, and composition of the nanoparticle; the suspending medium's acidity, organic matter, and water content; the surface hydration, zeta potential, and aggregation at the solid-liquid interface; and the membrane/ biomolecule interactions at the nano-bio interface, which can include receptor-ligand binding, membrane wrapping or conformational change in biomolecules.

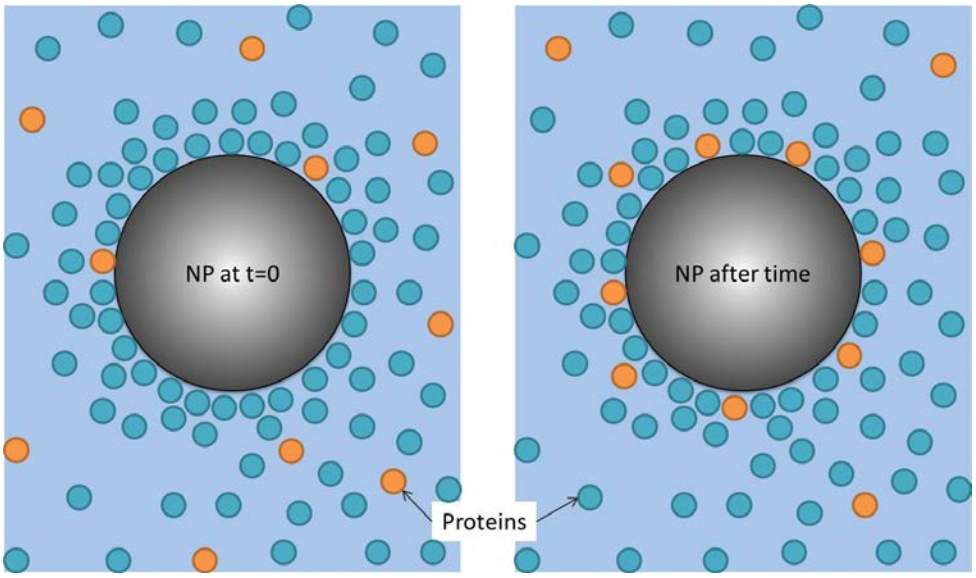

Figure 1.3: *An illustration of the time evolution of the protein corona, known as the Vroman effect. When the nanoparticle is introduced to the medium, the (soft) corona is chiefly comprised of the most abundant proteins present. As time passes, the corona evolves to include the less abundant, but more energetically favourable, proteins- making the hard corona.*

To see the complex nature of the corona composition, one study looked at polystyrene nanoparticles of two different sizes (50 and 100 nm), and three different surface functionalisations (plain polystyrene, carboxylate-modified, and amine-modified) in blood plasma[76]. It was shown that although many of the most abundant proteins were similar in each corona, a significant number differed from particle to particle, even with those differing only in size. With these less abundant proteins having significantly differing biological roles, the implications for nanomedicine are wide.

Another study looked at spherical nanoparticles of similar sizes (˜20 nm) and surface charges (˜-25 mV), namely TiO_2, ZnO and SiO_2[80]. It was seen that while the silicon and titanium dioxide nanoparticles adsorbed similar proteins over the time scale of the experiment, the composition of the zinc oxide protein corona was markedly different. The same study showed the difference particle shape has on the makeup of the protein corona. Whilst Apolipoprotein D and Clusterin bound readily to titanium dioxide nanospheres, they were not associated with nanotubes (average diameter 9 $\pm$ 1 nm) or nanorods (ellipsoids of average length 75 $\pm$ 23 nm and width 27 $\pm$ 7 nm).

Additional challenges faced when looking at the nature of protein corona formation were highlighted by a study performed using identically sized gold nanoparticles[81]. The only difference between them was the density of polyethyleneglycol (PEG) on their surfaces. Over 70 different blood serum proteins were adsorbed onto the surface of these particles, with both PEG size and density having a direct effect on the type and quantity of proteins adsorbed. This was shown to have significant outcomes affecting both the mechanism and efficiency of internalisation by a macrophage cell line.

Further complications arise when considering the nature of blood serum itself. It is a complex fluid containing approximately 3700 proteins at various concentrations, which vary between different members of the human population [82]. It is also worth noting that these relative concentrations also vary within each person at different times of the day. This could have an impact on the nature of protein corona formation and may determine what time of day any nanoparticle based drug delivery systems may be administered, and whether they are likely to have more of an effect in one individual over another.

It is interesting to note that when the formation of the protein corona is disrupted, for example when particles are modified to prevent the adsorption of blood serum proteins, they are removed within minutes from the blood stream by monocytes, cells that phagocytose foreign objects (see Section 1.2.1). Nanoparticles that lack this modification undergo immediate corona formation and are able to stay within the blood stream to fulfil their roles- *i.e.* stimulate or suppress immune responses[83]. It is clear that the nature of potential protein corona compositions must be considered when studying interactions at the cellular level.

1.2 Cells

In vitro studies are an essential tool, reducing much more complicated *in vivo* scenarios to their component parts. When looking at the impact of nanoparticles on a biological system, the ability to isolate different cell types is essential. This is because each cell type has unique properties that determine how they would interact with foreign objects. Examples of these can be seen in Figure 1.4. However it must be remembered that these cells are located in different parts of the body, so nanoparticles studied *in vivo* will have formed a unique protein corona based on the environment. This raises problems with *in vitro* studies where cells are generally treated identically, and will have to be accounted for.

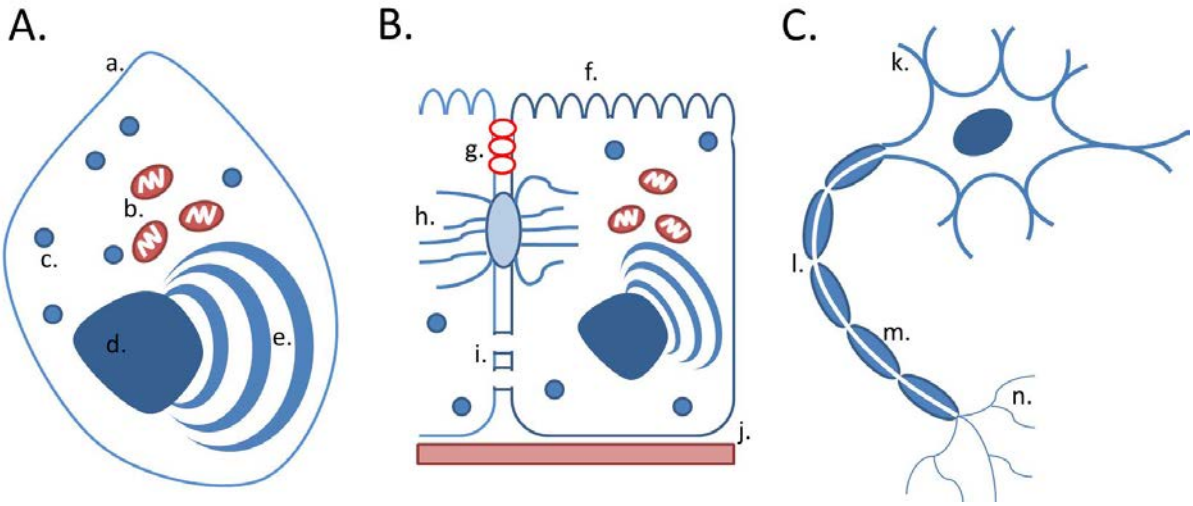

Figure 1.4: *Different cell types. A) An example of a neutrophil. a) Cell membrane. b) Mitochondria. c) Lysosome. d) Nucleus. e) Golgi apparatus. B) An example of an epithelial cell. f) Microvilli, on the free surface. g) Tight junction (impermeable). h) Anchoring junction with keratin filaments. i) Gap junction. j) Basal surface with underlying connective tissue. C) Nerve cell. k) Dendrite. l) Axon. m) Myelin sheath. n) Axon terminal*

These differences materialise in if and how nanoparticles are internalised. To understand better the ways this can happen, methods of active cell uptake, or endocytosis, have to be studied.

1.2.1 Endocytosis

Endocytosis is an energy dependent process by which molecules are engulfed and internalised by cells[84]. Due to the diversity of these molecules, *e.g.* membrane proteins; receptor ligands; drug delivery systems; and nanoparticles, it follows that there are a variety of mechanisms by which endocytosis can occur. Understanding what governs and regulates these pathways is essential to many areas of cell biology. For internalisation of a specific cargo, mechanisms for selection at the plasma membrane are first required. Next, the cell surface must invaginate and pinch off. Finally, vesicles must be tethered for trafficking to their intended destination[85].

The nature of the cargo for internalisation will determine how it is processed by the cell. There are two main categories of endocytosis. Phagocytosis translates from the Greek to mean 'cell eating', and is the uptake of large particles[86]. It is generally restricted to mammalian cells such as neutrophils, macrophages or dendritic cells. Pinocytosis translates to 'cell drinking', and is the uptake of fluid and solutes[87]. Pinocytosis occurs in all cells and in several different forms. These can be seen in Figure 1.5.

It has been shown that nanoparticle entry is possible via most, if not all, of these potential pathways. This will depend on the size, composition, shape and surface functionalisation of the particles. When designing new drugs or contrast agents, it is important to know how these nanoparticle properties affect cellular interactions, and hence uptake[88].

Dynamin Dynamin is a large guanosine triphosphatase (GTPase) that is essential for regulating many endocytosis pathways[89]. It is required at a late stage of vesicle formation, where in conditions of low ionic strength, it creates a collar on the neck of a budding pit through spontaneous spiral formation. GTP hydrolysis then leads to a conformational change which lengthens the dynamin spiral in a spring-like fashion and detaches the fully formed vesicle from the membrane[90], as illustrated in Figure 1.6.

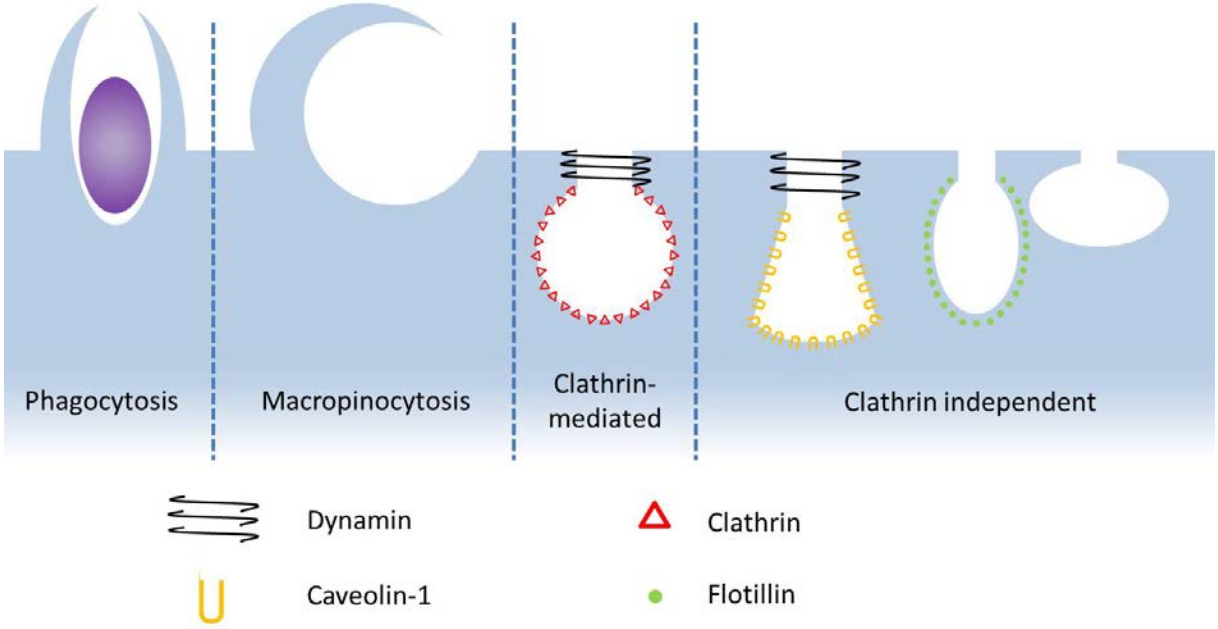

Figure 1.5: *Different forms of endocytosis. There are many different internalisation routes into cells, all of which can be used by nanoparticles. Phagocytosis is the 'eating' of larger particles, and pinocytosis is the uptake of fluid and solutes. This can be further characterised by looking at clathrin dependent and independent routes.*

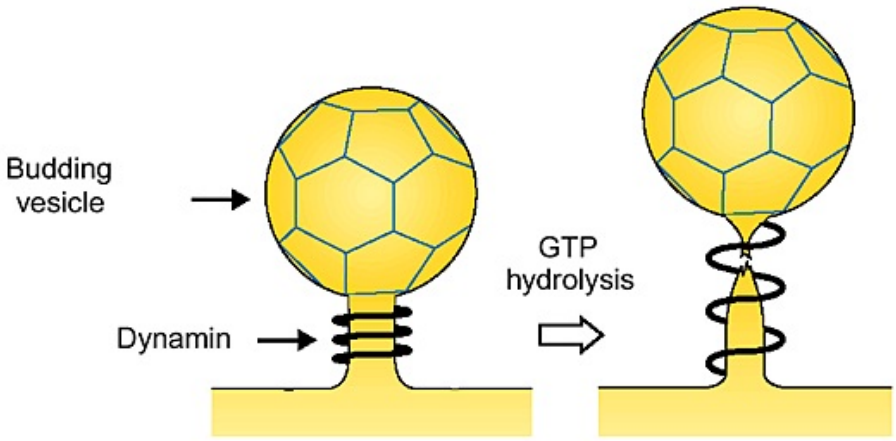

Figure 1.6: *How dynamin separates a vesicle from the cell membrane. Dynamin initially forms a tightly wound spiral around a forming vesicle. It then stretches, spring-like, after GTP hydrolysis, separating the vesicle from the cell membrane. Adapted from [90]*

Phagocytosis

Phagocytosis is the uptake of large particulate matter[86]. This includes pathogens and cell debris in the immune system by macrophages, or nutrients. Invaginations are progressively formed around the internalised cargo, and this both can or may not involve the

growth of membrane extensions. A phagosome is typically large enough that it can be seen under phase contrast microscopy.

It has been shown that nanoparticle uptake is possible through phagocytosis. Microglia (brain macrophages) have been shown to phagocytose superparamagnetic iron oxide nanoparticles for use as an MRI contrast, without resulting in cellular stress[91].

Macropinocytosis

Unlike phagocytosis and receptor-mediated endocytosis, macropinocytosis is not activated by the presence of a specific cargo. Rather, it is the increase of actin polymerisation at the cell surface caused by activation of receptor tyrosine kinases that leads to characteristic membrane ruffles being formed[92]. These result in a complete region of extracellular fluid being surrounded and absorbed by the cell.

Macropinocytosis is also a way in which nanoparticles have been shown to enter cells. It is suggested that this process is charge-dependent, with positively charged nanoparticles being preferentially endocytosed over negatively charged particles via this route of entry[93].

Clathrin-mediated endocytosis

The most researched and well known form of endocytosis is clathrin-mediated endocytosis (CME)[94]. Clathrin is a protein composed of three heavy and three light chains in a triskelion structure. When the triskelia polymerise they form a polyhedral lattice, creating an array of hexagons and pentagons. The relative ratio of these determines the resulting curvature of the membrane, and subsequently the size of the formed coated vesicles. These can range from 60 to 200 nm in diameter[94, 95], and the process can be seen in Figure 1.7. CME is receptor- mediated and dynamin- dependent. Examples of molecules that undergo CME include iron in the form of transferrin[96], growth factors[97], and cellular adhesion molecules[98].

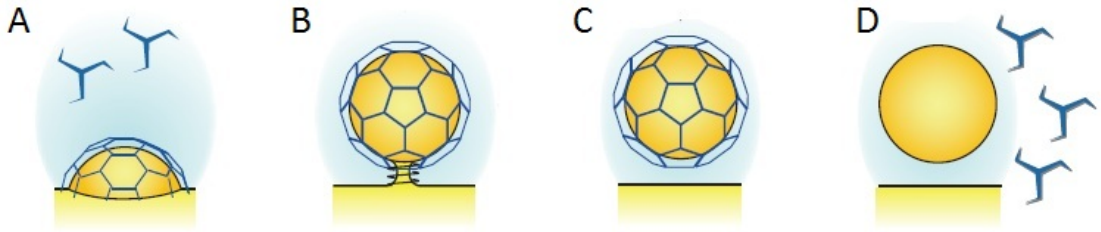

Figure 1.7: *An illustration of clathrin mediated endocytosis. (A) Clathrin triskelia interact to form a coated pit. (B) The pit buds into a vesicle, and the neck is pinched off by dynamin. (C) The clathrin coated vesicle detaches from the membrane. (D) The clathrin uncoats from the fully formed vesicle. Adapted from [99]*

Being such an important route of entry into cells, it is unsurprising that there is a vast amount of literature documenting nanoparticle uptake via CME. Amongst others, it has been shown that fullerenic[100], metal hydroxide[101], mesoporous silica[102], FITC-chitosan[103] and polystyrene[104] nanoparticles are all internalised, at least in part, via this route.

Caveolar endocytosis

Of the plasma membrane invaginations that are not clathrin-coated, the most common are known as caveolae ("little caves"). These tiny flask-shaped buds are around 60-80 nm in diameter, and are especially prevalent in endothelial, fibroblast, and smooth muscle cells[105]. Caveolae get their shape and structure from caveolin, of which there are three isoforms: caveolin-1 and -2, which are most prominently expressed in endothelial and fibrous cells, and caveolin-3, which is primarily located in smooth muscle cells[106]. All three types are integral membrane proteins with the COOH and NH_2 termini in the cytosol and a hydrophobic loop in the membrane[107]. Fluorescence microscopy studies using green fluoescent protein (GFP)-tagged caveolin-1 show localisation at the plasma membrane until a cargo-specific signalling cascade internalises the caveolae[108]. Caveolar endocytosis is regulated by the presence of dynamin.

Nanoparticles conjugated to bovine serum albumin (BSA) have been shown to induce caveolae-mediated endocytosis through the activation of membrane binding proteins[109]. This has been shown for not only 20 and 40 nm particles, but also for 100 nm particles, suggesting that caveolae may be able to accomodate larger cargo than previously assumed.

Caveolin and clathrin- independent endocytosis

Endocytic events that are independent of both clathrin and caveolin (CCI) can be split further into dynamin dependent and independent categories. However these have not been investigated as thoroughly and thus there exists considerably less literature on them. Dynamin- dependent CCI endocytosis is classified as either CDC42- dependent or RhoA-dependent, whereas dynamin independent CCI is classified as either Arf6- dependent or flotillin- dependent[110].

Very few nanomaterials are documented to utilise any of the CCI pathways. However, folate-modified nanoparticles have been shown to bind to glycosylphosphatidylinositol-anchored folate receptor, which is known to enter cells through CCI routes[111]. Another study displayed size- dependent entry of anionic polymeric particles, with 24 nm nanoparticles entering HeLa and HUVEC cells via a CCI route but 43 nm particles entering mainly via clathrin-mediated endocytosis[112].

Nanoparticles have been used to investigate these pathways also, with nano-gold structures bound to shiga toxin being used to show the role of the BAR domain protein endophilin-A2 in the dynamin independent CCI uptake of both shiga and cholera toxins[113].

The main challenge faced when trying to determine the nature of interaction of nanoparticles with cells is the sheer number of variables involved. From the size, shape and composition of the nanoparticle, to the nature of the surrounding biological milieu, to the type of cell that it comes into contact with, all have an effect on interactions and possible internalisation. One way to view these scenarios is via light microscopy, which allows the acquisition of real-time images and can offer insight into how changing these variables can alter the nature of nanoparticle-cell interactions.

1.3 Optics

1.3.1 Light

Visible light is a form of electromagnetic radiation. All forms of wave-like energy have characteristic electric and magnetic properties; manifested in the oscillating electric and magnetic fields as these waves propagate through space. The direction of propagation is perpendicular to the vibrations of both the electric and magnetic oscillating field vectors, which are also mutually perpendicular[114]. This is illustrated in Figure 1.8.

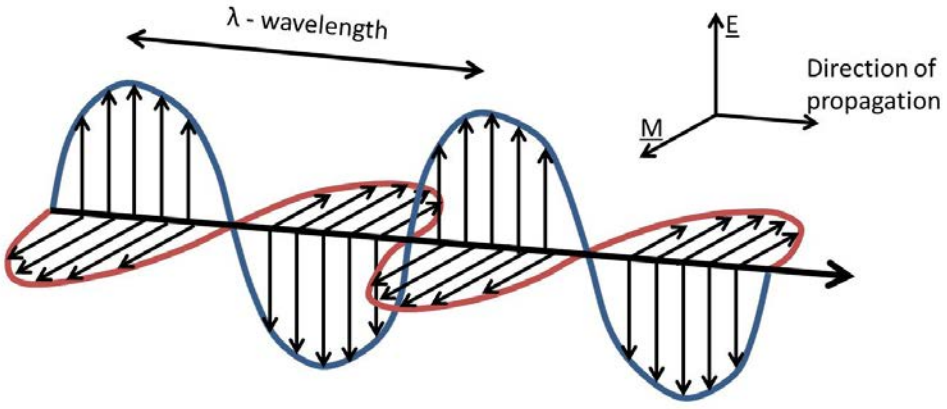

Figure 1.8: *The electric and magnetic components of light. These oscillate sinusoidally perpendicular to both each other and the direction of propagation of the photon. The wavelength of the light is defined by the distance between two of the peaks of the waves.*

A standard measure of all electromagnetic radiation is the magnitude of the wavelength. This varies from 10^{-15}m for high frequency gamma rays, to around 10^{9}m for low frequency radio waves[115]. The wavelength of visible light, to which our eyes are sensitive, ranges from 3.9×10^{-7}m to 7.5×10^{-7}m. Light in this range is used in fluorescence microscopy to excite specific fluorophores[116]. The wavelength of an electromagnetic wave is related to its frequency by the relation:

$$f = \frac{v}{\lambda} \tag{1.2}$$

where f and λ are the frequency and wavelength, and v is the velocity, defined in Equation 1.3.

1.3.2 Refraction

The refractive index, n, of a medium is a dimensionless number that describes how light propagates through that medium[117]. It is defined in Equation 1.3. Refraction is an optical phenomenon that occurs when light encounters a boundary between materials with different refractive indices. It results in a change in velocity, and hence wavelength of the light, which causes a change in direction. This can be visualised using wavelets via the Huygens-Fresnel principle[118], in Figure 1.9. Huygens proposed that the propagation of a wave can be determined by assuming that every point on a wave front is the source of a 'forward' travelling spherical wave. This assumption is used to describe reflection, refraction and diffraction effects of light. The frequency of the light must remain constant, as the electric and magnetic fields are continuous at the refractive index boundary. It is this property that is used in lenses to focus a beam of light onto a single point.

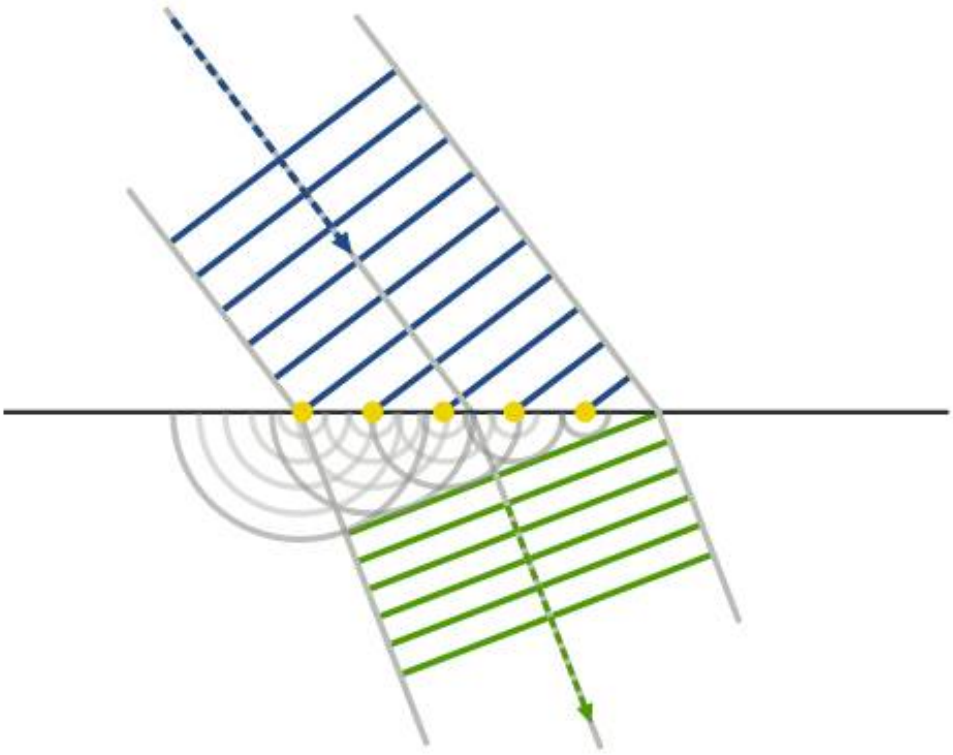

Figure 1.9: *Illustration of the Huygens-Fresnel principle. By assuming every point on the wavefront (blue) encountering the refractive index boundary is the source of a forward travelling spherical wave (yellow), refractive properties can be clearly illustrated, and a change in direction of the light can be seen (green). Image used with permission from [118].*

$$n = c/v \tag{1.3}$$

where c is the speed of light in a vacuum (3x10^8 m/s) and n is the refractive index of the medium, which is equal to 1 in a vacuum, and increases as the optical density gets greater. For instance, the respective refractive indices of water and crown glass are 1.333 and 1.520[119]. This means it takes light 1.333 times longer to propagate through water than in a vacuum. Materials with a higher refractive index slow light (and hence reduce wavelength) to a greater extent, and so exhibit a larger angle of refraction for incoming light rays passing through an air interface. Snell's Law, illustrated in Figure 1.10, defines the relationship between the angles of a light ray as it encounters a boundary between two materials of differing refractive indices:

$$n_1 sin(\theta_i) = n_2 \sin(\theta_r) \tag{1.4}$$

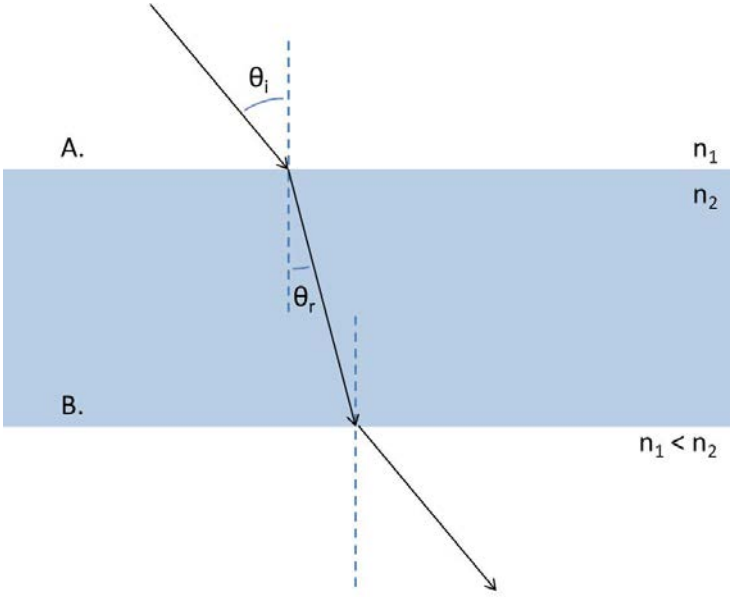

Figure 1.10: *Refraction of light rays upon experiencing a change in refractive index. A) the speed of light decreases upon experiencing a increase in refractive index, and so bends towards the normal. B) the speed of light increases upon experiencing an decrease in refractive index, and so bends away from the normal.*

1.3.3 Dispersion

Although mention has already been made to a fixed refractive index for a substance, in reality this is dependent on the wavelength of the incident light. This can be seen with a simple white light and prism set-up as illustrated in Figure 1.11. The glass refracts wavelengths present in white light by differing amounts, causing a characteristic rainbow to be formed. Light of a shorter wavelength experiences a higher degree of refraction[120]. This is known as the dispersion of light.

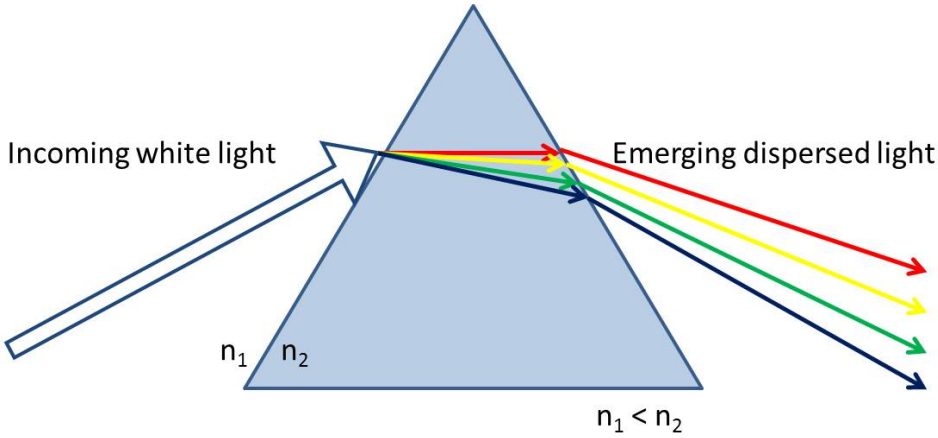

Figure 1.11: *The dispersion of light of different wavelengths. White light is made up of many wavelengths, which are split by a prism into a characteristic rainbow. Shorter wavelengths are bent more than longer wavelengths.*

1.3.4 Total Internal Reflection

Total internal reflection is an optical phenomenon that occurs when light encounters a boundary into a material with a lower refractive index. If incident light strikes the interface at an angle greater than the critical angle, by rearranging Equation 1.4:

$$\theta_c = \sin^{-1}(\frac{n_2}{n_1}) \tag{1.5}$$

where θ_c is the critical angle, n_2 is the refractive index of the material that the light is in, and n_1 is the refractive index of the material encountered by the light. Then as long as $n_1 < n_2$, instead of passing into the second medium, all of the light's energy is reflected back into the first medium[121] (Figure 1.12). Beyond the reflected beam into the second medium, the electromagnetic field extends into the Z-direction. This is physically necessary to satisfy the continuous boundary conditions described in Maxwell's equations[122], however it cannot be a sinusoidal, energy transmitting wave otherwise the incident and reflected waves would not have the same energy. Thus, the intensity of this field decays exponentially, and is known as an evanescent wave. The use of this evanescent wave is integral to Total Internal Reflection Fluorescence (TIRF) microscopy, which will be discussed in detail in Section 1.4.5.

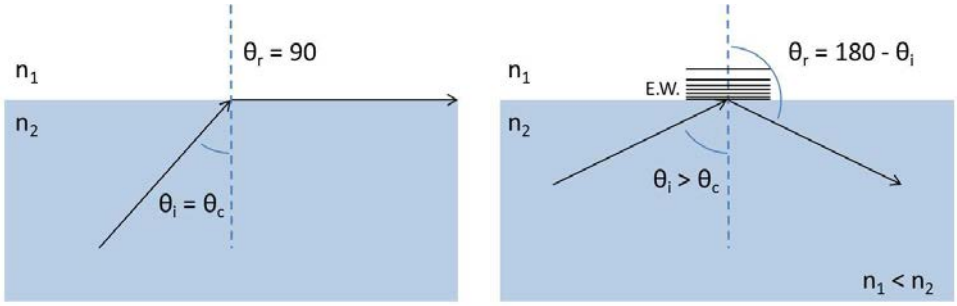

Figure 1.12: *A light ray encountering a boundary with a medium displaying a lower refractive index. A) If the light hits the boundary at the critical angle (Equation 1.5), then it travels along the boundary. B) If the light hits the boundary at greater than the critical angle, then it is totally internally reflected back into the original medium, and an evanescent wave (EW) is generated.*

The evanescent field intensity decays exponentially with increasing distance from the interface as described by the equation:

$$I_z = I_o e^{-\frac{z}{d}} \tag{1.6}$$

Where I_z is the intensity of the evanescent wave at a distance z from the boundary, I_o is the intensity of the evanescent wave at the boundary, and d is known as the penetration depth of the wave. The factors that affect d are the wavelength of the incident light, the refractive indices of the objective and sample, and the incident angle of the laser beam[123]:

$$d = \frac{\lambda}{4\pi(n_1^2 \sin^2\theta - n_2^2)^{\frac{1}{2}}} \tag{1.7}$$

For example, for a laser of 561 nm, coverslip and sample refractive indices of 1.52 and 1.33 respectively, and beam incident angle of 62°, the penetration depth of the evanescent wave is 248 nm. As a consequence of rearranging Equation 1.6, the intensity of the evanescent wave at the point $z = d$ is always $I_z = \frac{I_o}{e}$. Due to varying levels of refraction observed over different wavelengths, if the incident angle remains constant then a shorter wavelength of light will result in a shallower penetration depth of evanescent wave.

1.3.5 Fluorescence

If an electron is in a bound state, it has a discrete amount of energy[124]. It is possible for an orbital electron in a molecule or atom, for example, to transition from one energy level to another, increasing through the absorption of energy, and decreasing by spontaneous or stimulated emission, energy transfer to another molecule, or dissipation of the energy as heat. When an atom or molecule relaxes to its ground state through the emission of a photon of light, this is of a fixed wavelength. This is because the atomic or molecular energy levels, and hence the energy of the emitted photons, are fixed[125]. This is because of the Planck-Einstein relation:

$$E = hf \tag{1.8}$$

Where E is the energy of the photon, h is Planck's constant ($= 6.626 \times 10^{-34} m^2 kg s^{-1}$), and f is the frequency of the photon. The wavelength of the resultant photon can be calculated by substituting this into Equation 1.2. Knowing this allows the characterisation of an atom or molecule. The process can be visualised in a Jablonski diagram, seen in Figure 1.13.

A fluorophore is a chemical compound containing several combined aromatic (that is, cyclic and planar) groups, which can emit light upon excitation[126]. In cell biology the use of fluorophores as probes or molecular markers is commonplace. The application of fluorophores is discussed in greater detail in Section 3.2.1.

The efficiency of the fluorescence process is given by the quantum yield. This is defined as the ratio between the number of photons absorbed by a sample to the number of photons emitted. A quantum yield of a compound of 0.1 is considered relatively bright, or strongly fluorescent.

In general, an emitted photon has a longer wavelength and lower energy than the excitation photon. This is known as the Stokes shift[127]. This is most commonly, but not exclusively, due to the loss of some energy through non-radiative decay as heat.

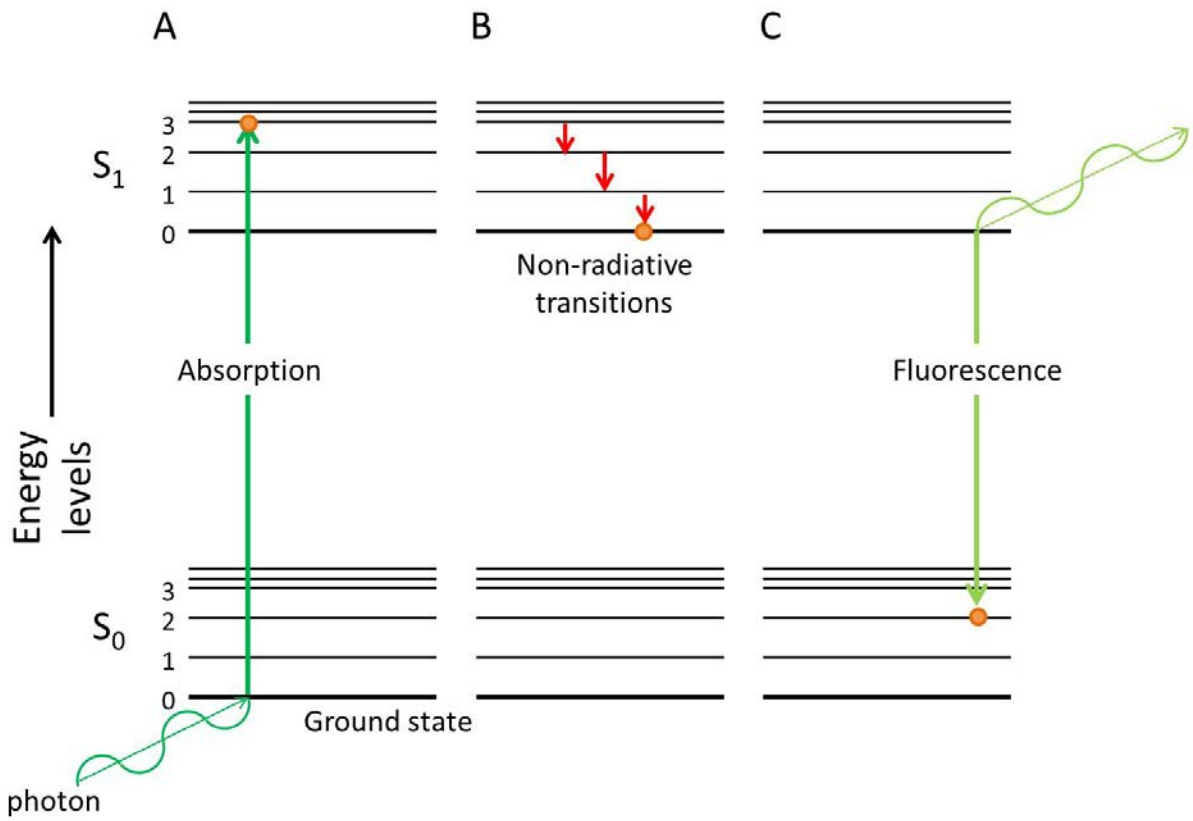

Figure 1.13: *An illustration of a Jablonski diagram. A) An orbital electron in a fluorophore in the ground energy state (S_0). When excited by a photon of the correct wavelength, the electron can absorb this light and increase in energy. B) An electron in a higher energy state (S_1). It usually undergoes non-radiative transitions of energy levels, where the energy is typically dissipated as heat or rotation of the fluorophore. C) The electron spontaneously drops to a lower energy level, and emits a photon of equal energy to the gap in levels.*

1.3.6 Lasers

The laser ('light amplification by stimulated emission of radiation') is a device commonly used in fluorescence microscopy, although light emitting diode (LED) light sources are becoming more popular. It has many qualities that make them superior to traditional mercury or xenon arc lamps, such as a higher intensity and the ability to focus to a narrower physical area[128]. This limits illumination to small parts of the sample, reducing unnecessary phototoxicity. They are also long lasting, and generate light of a specific wavelength, negating the need for filters between source and sample. Some lasers allow very short pulses of light to be created- as short as a femtosecond[129].

The way a laser works is based on similar principles to that of fluorescence, though instead of the excited-state electrons in the atoms decaying through spontaneous emission, they are stimulated by other photons. For a working laser, the majority of atoms in a population have to be in the excited state (generally achieved via a semiconductor diode or strong electric currents). When an excited atom is illuminated with an incoming photon of the same energy as the gap in transition states, the atom may be stimulated to return to its lower energy state and simultaneously emit a photon. This photon will be identical in wavelength, phase, direction and amplitude to the incident photon. If this happens on a large enough scale then a monochromatic, coherent beam will be created[130]. This can be seen in Figure 1.14.

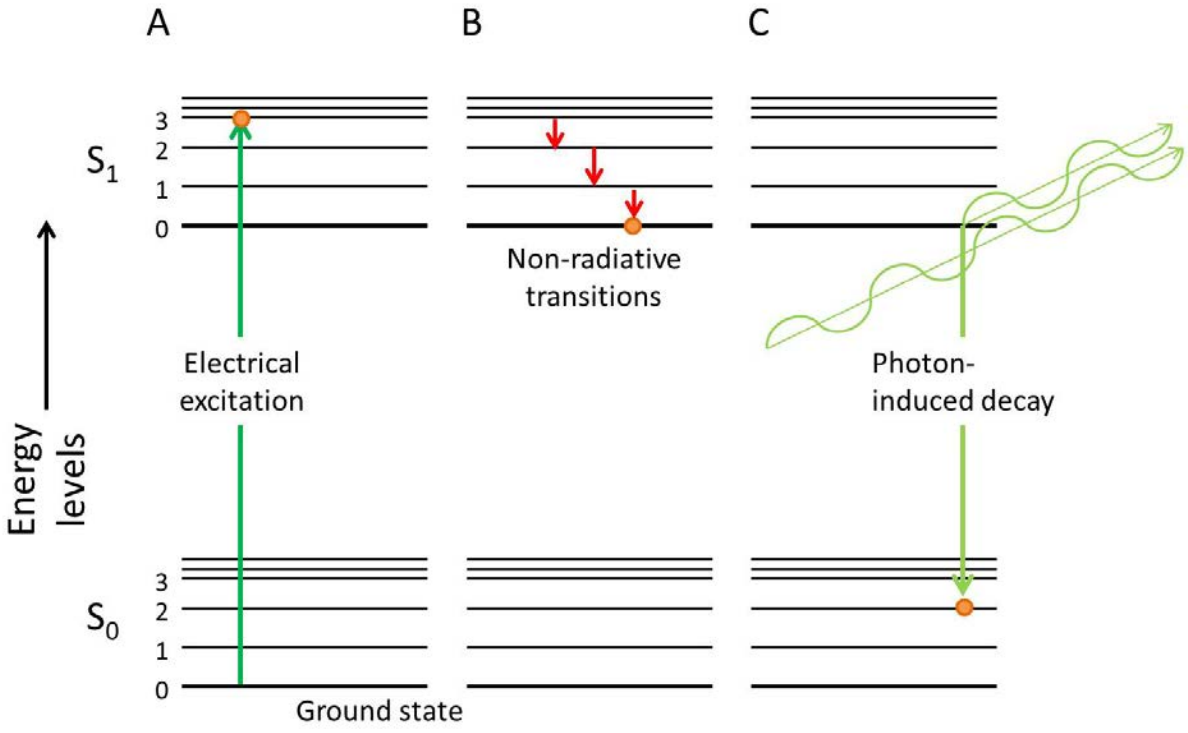

Figure 1.14: *An illustration of photon induced decay in the creation of a laser. A) An electron is excited to a higher energy level, typically by a laser diode or strong electric current. The majority of atoms in the sample have to be in this state. B) An electron in a higher energy state can undergo non-radiative transitions, where energy is lost as heat. C) When a photon of the correct energy (corresponding to the gap in energy levels) is incident on the excited electron, it can stimulate the production of an identical photon along with the decay of the electron to the lower energy level. When this happens on a mass scale, a working laser is created.*

The wavelength of the laser depends on what material the laser is made of[131]. Different compounds have differing gaps between energy levels, making many different wavelengths possible. For example, an argon laser creates a beam of 488 nm wavelength, whereas a zinc-selenium compound creates one of 560 nm.

1.3.7 Polarisation

When the electric field vectors of light all align, the light is said to be polarised, as illustrated in Figure 1.15[132]. This is typically achieved by passing the light through a absorptive filter, or by making use of the optical properties of certain prisms, as in Figure 1.16.

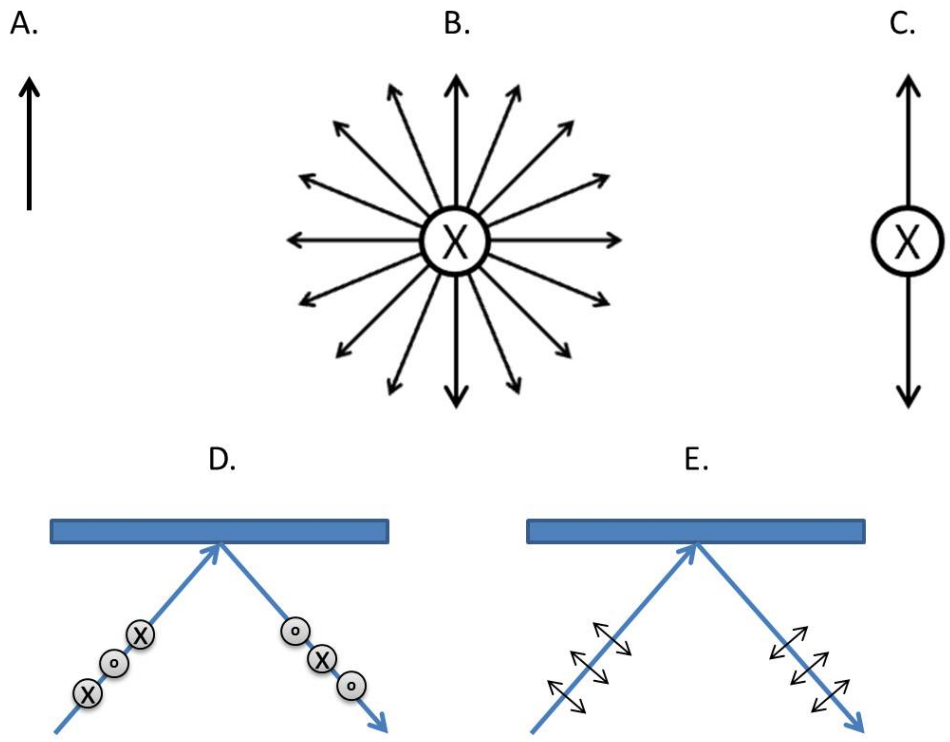

Figure 1.15: *An illustration of a polarised beam of light. A) An electric field vector as illustrated by a photon going into the page. B) A standard beam of light is unpolarised, as it has electric field vectors oscillating in all directions perpendicular to the direction of propagation. C) A polarised beam of light only has an electric component in one plane. D)* p*-polarised light. The electric field vectors of the light are parallel to the coverslip. E)* s*-polarised light. The electric field vectors of the light are perpendicular to the coverslip.*

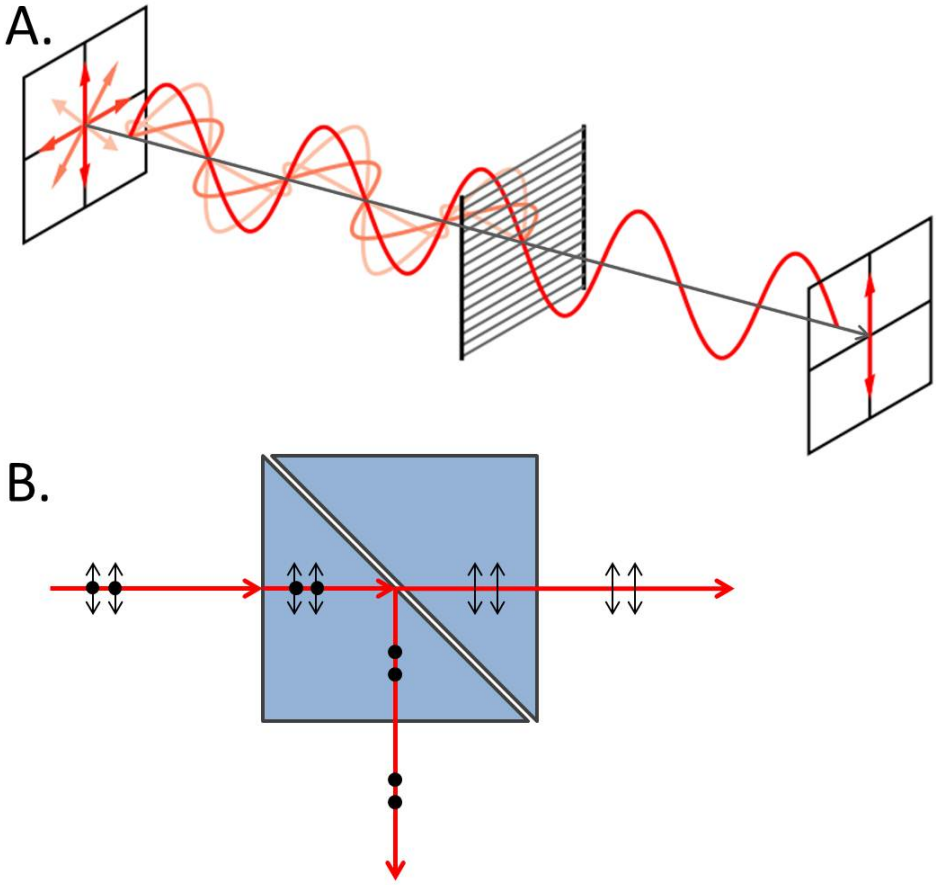

Figure 1.16: *This illustrates two methods of light polarisation. A) An absorptive polariser. Valence electrons in stretched polymer chains are free to move, absorbing the light polarised parallel to them, but transmitting the fraction polarised perpendicularly. B) A polarising prism,* e.g. *a Glan-Taylor prism. Two prisms of a birefringent material are joined with a small air gap separating them. This is done in such a way that* p*-polarised light is transmitted and* s*-polarised light is reflected out of the side.*

Throughout this thesis, reference will be made to what are known as *p*- and *s*- polarisations. This refers to the orientation of a polarised beam of light reflecting off of a surface (typically a coverslip in this case). When the electric field vectors are parallel to this plane the light is said to be *p*-polarised. When the electric field vectors are normal to the plane of incidence, the light is said to be *s*-polarised, from the German *senkrecht*, meaning perpendicular. This is illustrated in Figure 1.15 D and E, and expanded on in Chapter 5.

1.4 Microscopy

1.4.1 Fundamentals

The nature of light when applied to microscopy poses several limits on what can be accomplished. These form fundamental principles, which will be briefly touched on before discussing the techniques used in this research.

Airy disc

When light passes through a small circular aperture, such as those in a microscope, diffraction occurs. This is characterised by the Huygens-Fresnel principle[133]. The resulting constructive and destructive interference results in a pattern known as an Airy disc. This can be seen in Figure 1.17.

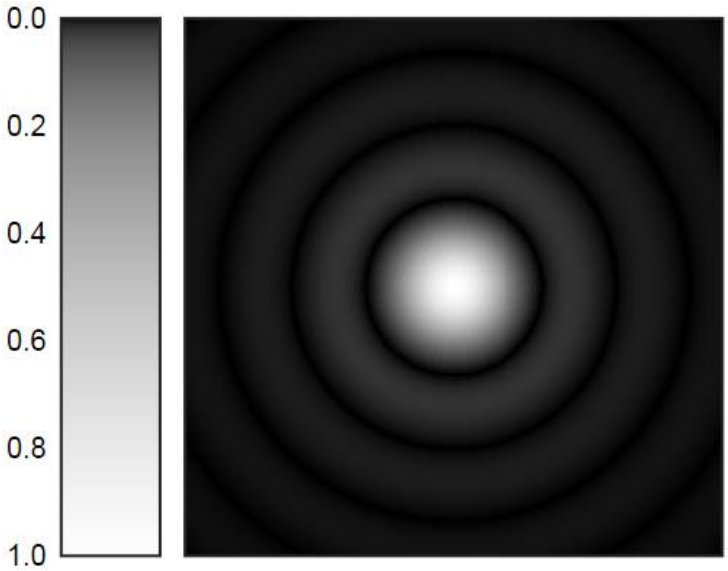

Figure 1.17: *A computer simulated image of an Airy disc. Image adapted with permission from [134].*

The central spot is surrounded by concentric rings that decrease in intensity with increasing distance from the centre. The radius of the Airy disc is defined as the distance from the centre of intensity to the first minimum. The size of the Airy disc depends on the wavelength of the light used and the size of the aperture[135], shown in Equation 1.9:

$$sin(\theta) = 1.22\frac{\lambda}{d_{ap}} \tag{1.9}$$

where θ is the angle in radians at which the first minimum in intensity occurs, measured from the direction of the incident light, and d_{ap} is the diameter of the aperture.

The Abbe resolution limit

The formation of Airy discs due to the wave-like nature of light gives rise to a fundamental limit on the theoretical maximum resolution of a light microscope. If a microscope's optics are as good as the theoretical limit, this instrument is then said to be *diffraction limited*. The resolution limit for a single point of light as defined by Ernst Abbe in 1873[136] is:

$$d = \frac{\lambda}{2nsin(\theta)} \tag{1.10}$$

Where λ is the wavelength of the light travelling in a medium of refractive index n, converging to a spot with angle θ, d is the radius of the spot that will be formed. This is normally simplified to state that the limit of the smallest measurable object is about half the wavelength of the light used.

Rayleigh resolution limit

Rayleigh later expanded on this definition by considering multiple sources of signal. The Rayleigh resolution limit defines two point-like structures being spatially resolved when the intensity maximum of one point is in line with the first intensity minimum of the other[137]. This is dependent on the wavelength of the light used and the numerical aperture (NA) of the objective lens of the microscope, which is defined in Equation 1.11.

$$NA = nsin(\theta) \tag{1.11}$$

where n is the refractive index of the medium in which the lens is working, and θ is the half angle of the maximum cone of light that can enter the lens. The NA of the objective lens relates to the Rayleigh criterion as shown in Equation 1.12.

$$d_{min} = 0.61\frac{\lambda}{NA} \tag{1.12}$$

Two identical diffraction limited spots can only be resolved if the distance between them is equal to or greater than d_{min}. Increasing the resolution of the system therefore depends on either using a smaller wavelength of light (which is only practical to an extent, as specific wavelengths have to be used in fluorescence microscopy), or increasing the NA of the objective lens[138]. A simplified illustration of this concept in one dimension can be seen in Figure 1.18. This concept is what determines the spatial resolution of a microscope.

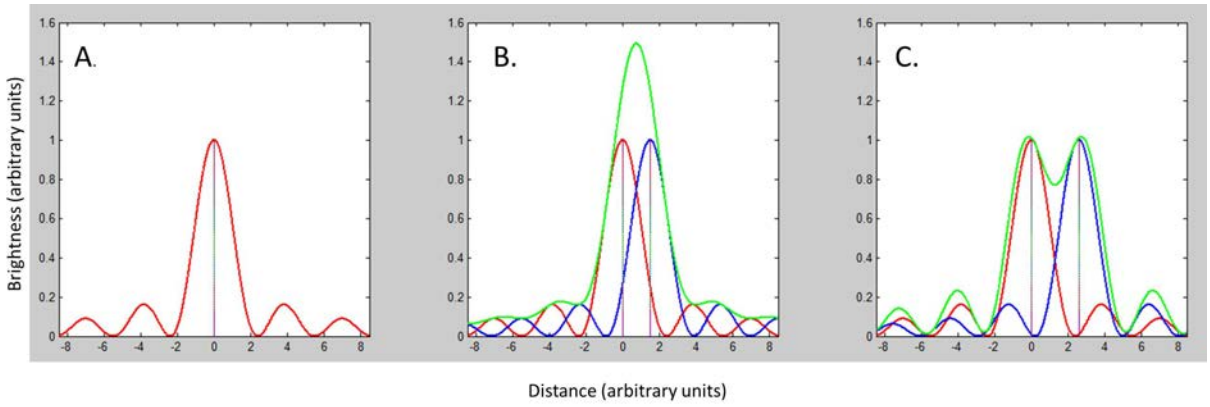

Figure 1.18: *Graphical representation of spatial resolution in one dimension. Point sources are shown in grey, with intensity profiles shown in red and blue, relating to the middle "focal place" of an Airy disc. The green line shows the combined light, and hence the level of intensity collected by the CCD. A) The intensity profile of a single point of light. B) The two points in the same system which are too close to be distinguished. In the image (not shown) it would appear as a single spot. C) The points are resolvable when the minima of one coincides with the maxima of the other.*

Point spread function

A perfect imaging system would image a point source of light as an Airy profile. However, no imaging system is perfect. Every microscope leaves a unique 'fingerprint' on an image, consistent artefacts which depend on the components and set-up of the system. The point spread function (PSF) of a microscope is what this looks like when imaging an infinitely small single point source. An optical imaging system follows the linearity property:

$$Image(Object_1 + Object_2) = Image(Object_1) + Image(Object_2) \tag{1.13}$$

i.e., the imaging of Object_1 is unaffected by the imaging of Object_2. This means that the entire image can be thought of as the perfect, exact image of the sample convoluted with the PSF of the system. If one knows the PSF of a system it is possible to obtain a much clearer image by undergoing a process known as 'deconvolution' of the original image with the PSF[139].

1.4.2 Nyquist criterion

For images to be formed in microscopy, analogue signal from light sources have to be recorded in digital form. The Nyquist theorem states that for an accurate representation of an analogue signal, it should be sampled at twice the highest frequency present[140]. What this means in terms of microscopy is that intensity levels have to be recorded at a distance of half the smallest structure size expected. In terms of 20 nm nanoparticles, there should be a maximum of 10 nm represented by every pixel in an image. Sampling at more that twice the highest frequency is known as 'oversampling', which will create a larger image file and may pick up useful nuances in information. Sampling at lower than the Nyquist rate will report false information about the data being recorded. Examples of these can be seen in Figure 1.19.

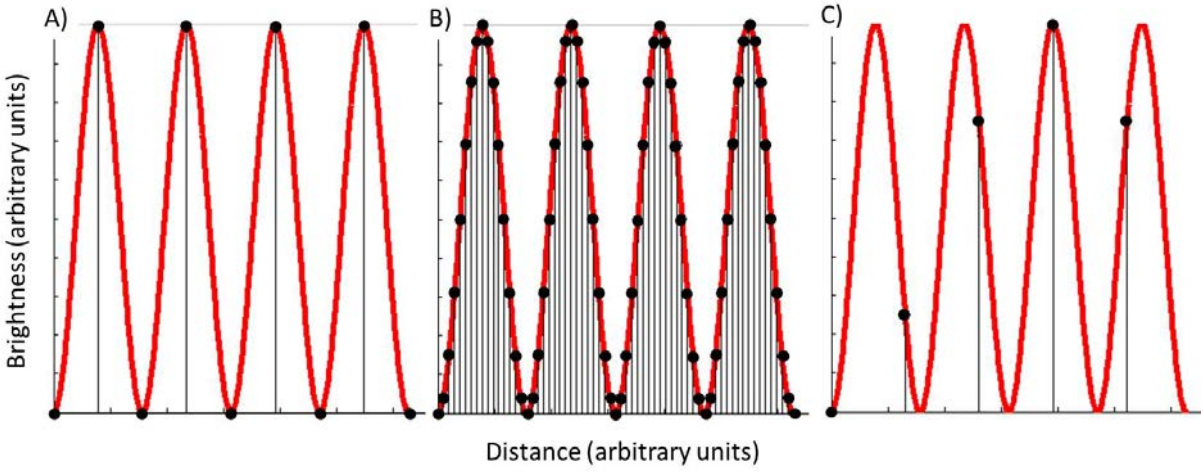

Figure 1.19: *The Nyquist criterion. The red line represents an analogue signal to be recorded and digitised. Black dots indicate pixel spacing and the relative intensities recorded by them. A) shows sampling at the Nyquist frequency, half the frequency of the signal. The general essence of the information is captured. B) shows an example of 'oversampling', where information is acquired at a higher frequency than is necessary. Depending on the method of acquisition this may take longer and will create a larger image file. However it can pick up potentially useful nuances in the data. C) shows an example of undersampled data. The acquisition rate is lower than half the minimum frequency, and the image produced will be misleading. This is known as 'aliasing'.*

Resolution

Resolution is a term that when applied to microscopy can have multiple meanings. These include pixel, spatial, temporal and radiometric resolution.

Pixel resolution A pixel is one unit of a digital image. In general, for any given lens setting, the smaller the size of the pixel, the higher the resolution of the image and the clearer the object will be[141]. Physically, pixels can be formed in a number of different ways depending on the type of sensor.

In a widefield image, where all of the image is acquired at once, a pixel corresponds to a capacitor on a charge-coupled device (CCD) or complementary metal-oxide-semiconductor (CMOS) chip inside the camera[142]. These convert the energy from a photon hitting it to an electrical charge which is then recorded. The number of pixels a camera has depends on the physical size of the detector on the chip, and the size of the chip itself.

In a confocal microscope, an image is generated on a pixel-by-pixel basis[143]. The laser is focussed into a point and scanned across the area of interest. Pixels in the x-direction correspond to the time over which the signal is acquired, and pixels in the y-direction correspond to the distance between scans in the x-direction. Photons emitted by the sample enter a detector, typically a photomultiplier tube, where a photocathode generates an electron, and a series of dynodes (electrodes of increasingly positive charge) generate a detectable electric current. Integration of this current over time corresponds to the recorded pixel intensity. Pixel size in this case depends on the accuracy of the mechanism employed to raster the beam across the sample, and the time spent acquiring the image.

When studying nanoparticles a high pixel resolution is desired. A low pixel resolution would not allow distinction between individual or small groups of particles[144], and make analysis of images impossible.

Temporal resolution Temporal resolution is the precision of a measurement with respect to time. High speed cameras can achieve frame rates of up to 1000 frames per second, though these speeds can often mean a reduction in signal to noise ratio, or in an attempt to combat that, a reduced pixel resolution[145]. The temporal resolution depends on the sensitivity of the camera, with electron-multiplying CCD cameras able to achieve greater framerates as they require fewer photons incident on the chip to form an image. This can also be helped by brighter samples, though in cell biology this can often only be obtained by increasing the light intensity illuminating the sample, which can result in photodamage. Obtaining a useful temporal resolution is necessary when studying the uptake of nanoparticles into cells, a process which takes place over the order of seconds. It is even more necessary for tracking nanoparticles moving inside cells where they can move significant distances in fractions of a second[146].

Radiometric resolution Radiometric resolution is a measure of how finely a system can register differences in intensity. This is expressed as the number of bits in a system, typically 8-bit ($2^8 = 256$ levels) or 16-bit ($2^{16} = 65536$ levels). The detected intensity value is scaled and quantised to fit within this range. This will be especially important in Chapter 5, where a change in intensity when undergoing TIRF microscopy (see Section 1.4.5) can be interpreted in either a distance from the coverslip or a number of fluorophores in the vicinity.

1.4.3 Widefield microscopy

Widefield microscopy involves illumination of the entire sample, and the whole image can be acquired at once on a CCD chip. The light source can consist of an intense xenon or mercury lamp, employing filters to select the desired wavelength to excite specific fluorophores. Alternatively, lasers or LEDs can be used for greater light intensity and a narrower bandwidth of light. Widefield microscopy can use either transmitted light, where the collection optics are on the opposite side of the sample to the light source, or epifluorescent illumination, where the collection optics are located on the same side as the light source[147].

Fluorescence microscopy provides an invaluable way of investigating a myriad of cellular processes. Live cell dyes, protein tags and fluorescent cargo allow information about structure, signalling pathways and kinetic behaviour of cells[148]. They are used as a non-destructive method of tracking or analysing biological molecules. The majority of the light detected by the CCD chip in an epifluorescent microscope is that which has been absorbed by a fluorophore and emitted back towards the objective lens, as shown in Figure 1.20. Care has to be taken to avoid other light entering the camera, either from outside sources or reflections off of the coverslip or cell compartments to ensure the highest possible signal-to-noise ratio.

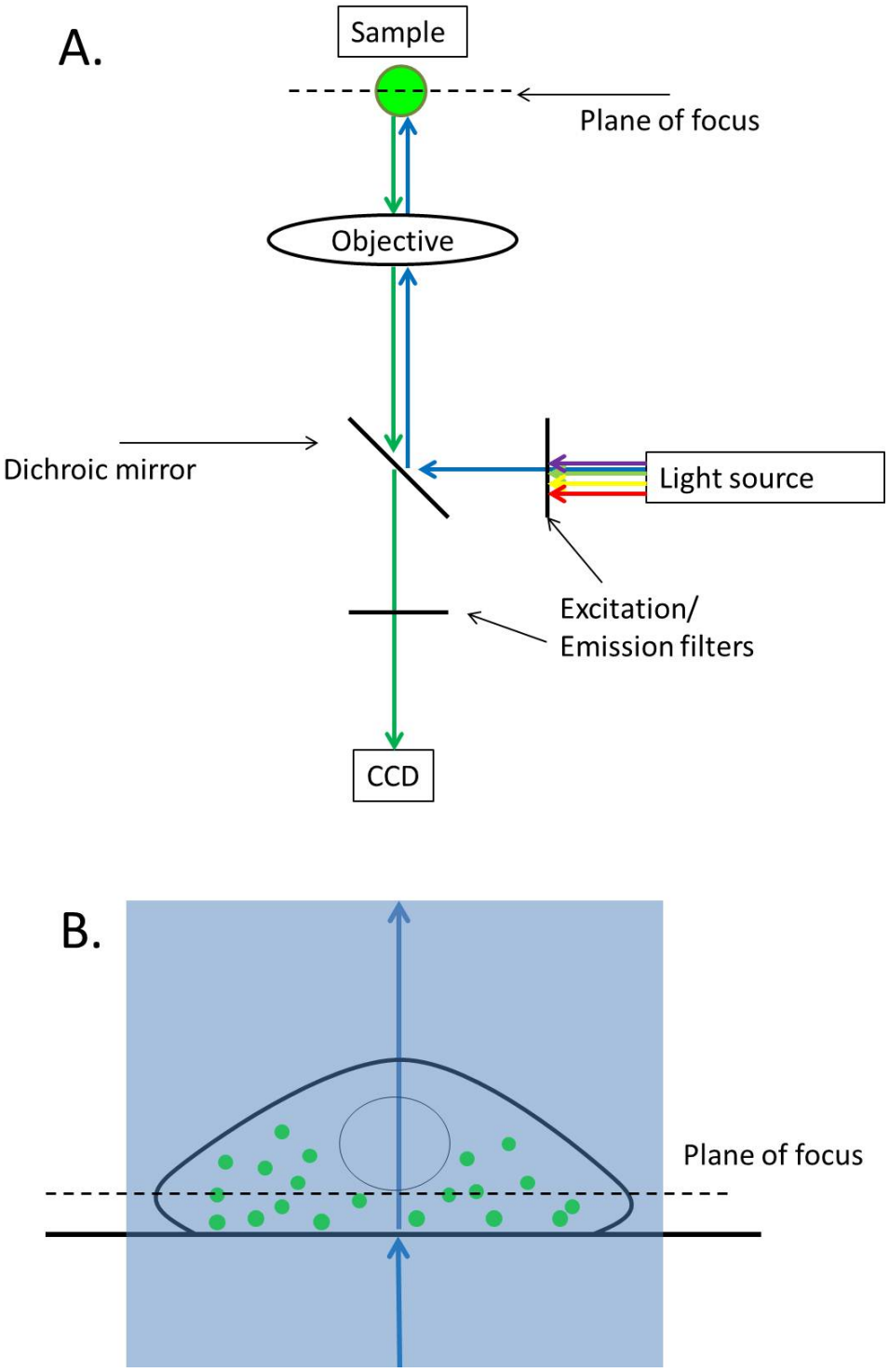

Figure 1.20: *A) A schematic of a widefield epifluorescence microscope. Light goes from a source to a sample via a dichroic mirror. The whole sample is illuminated, with all of the fluorophores excited, as displayed in (B). Light emitted from these fluorophores is collected by the objective lens, passes through the dichroic mirror as it is of a longer wavelength, and hits the detector. As it is a widefield technique the whole image is acquired at once.*

The main limitation of this technique is that when the whole sample is illuminated, the CCD also detects light from out of focus fluorophores. This gives rise to a blurriness in the image[149]. Confocal microscopy offers a method to counteract this.

1.4.4 Confocal microscopy

Confocal microscopy offers many advantages over widefield fluorescence microscopy, including a much shallower depth of field, a significant reduction of out of focus light, and the ability to generate 3D images through optical sectioning of a sample[150]. The way an image is formed in confocal microscopy differs from that of a widefield microscope in several ways. See Figure 1.21 for reference. A laser is typically used to generate the images due to their narrow bandwidth and high intensity. However, LEDs are becoming much more common, and bright lamps in conjunction with notch filters to select specific wavelengths can also be used. The light source is used to create a 'cone' of light that is rapidly scanned across a sample. This restricts the number of fluorophores excited at any one time to those within this diffraction-limited spot, increasing the signal-to-noise ratio when compared to other methods. Emitted light then passes back through the objective lens, through the dichroic mirror, and then through a pinhole aperture. This only lets light that was emitted from the intended plane of focus through, and blocks light from any other planes[151]. Emitted light then reaches a photomultiplier tube and forms the image on a voxel-by-voxel basis.

A photomultiplier tube is much more sensitive than a pixel on a CCD chip as each photon is multiplied many times before it reached the sensor. This requires many fewer initial incident photons from the sample to generate an accurate intensity reading from the sample. The trade off for this increased sensitivity is a much longer image acquisition time. As a two-dimensional confocal image is formed on a pixel-by-pixel basis, a whole image can take approximately two orders of magnitude longer to acquire than that of a widefield image.

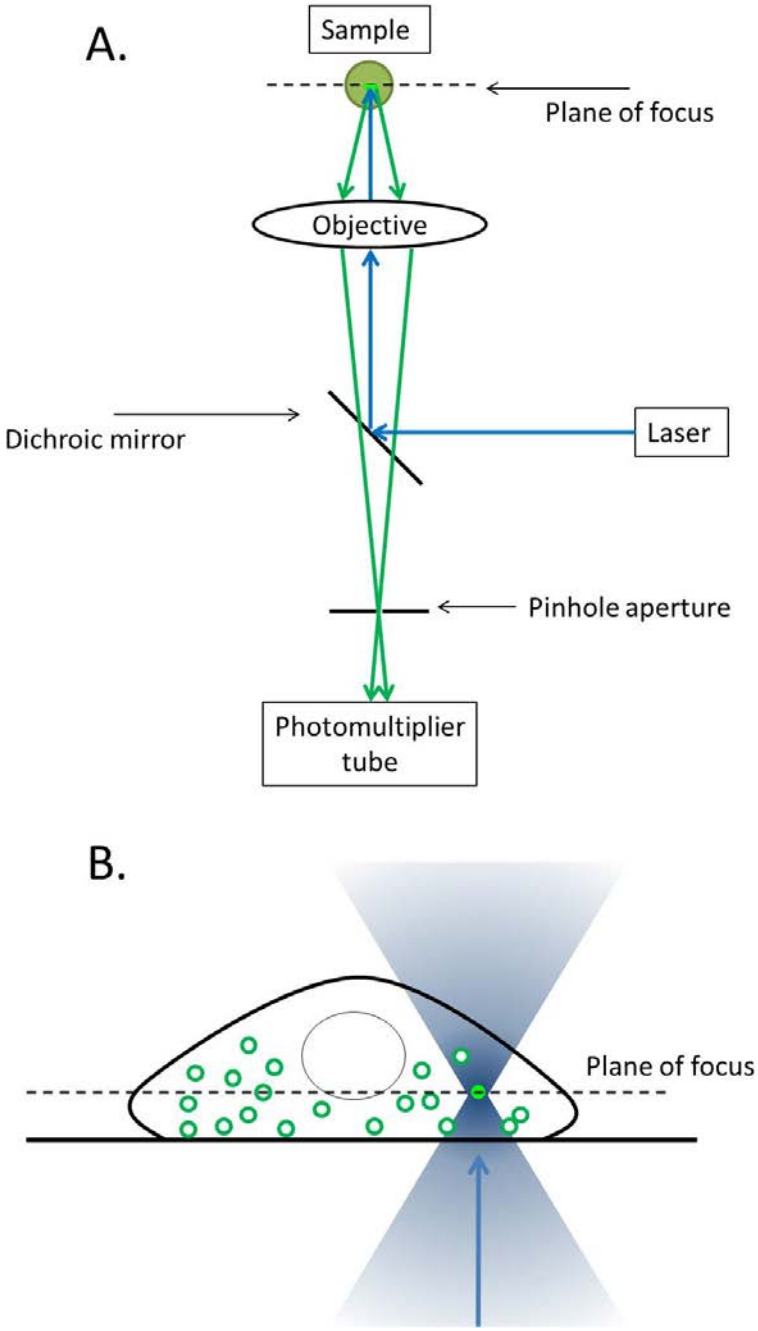

Figure 1.21: *A) A schematic of a confocal microscope. The laser light source is passed through a pinhole aperture which then is focussed by the objective lens into a 'cone' of light. This preferentially excites fluorophores within the centre of this cone, which is scanned across the whole sample, as displayed in (B). The emitted light then passes back through the objective and dichroic mirror and through another pinhole aperture to a photomultiplier tube (PMT). This is to block any out of focus light from reaching the detector. The PMT records values on a pixel-by-pixel basis, meaning that the acquisition time for a confocal laser scanning microscope is much greater than that of an epifluorescence microscope.*

1.4.5 Total internal reflection fluorescence microscopy

Total internal reflection fluorescence (TIRF) microscopy offers an alternative way to eliminate out of focus fluorescence, generating images with a very high signal to noise ratio, by exciting fluorophores within a ∼200 nm band directly above the coverslip. This allows high contrast images of the adherent plasma membrane and part of the cytoplasm[152]. This makes it an invaluable tool for studying the interaction of cargo with the plasma membrane[153], cellular cortical dynamics[154], receptor-ligand interactions[155], initiation of signal transduction at the plasma membrane[156], and cell adhesion[157]. The process is illustrated in Figure 1.22.

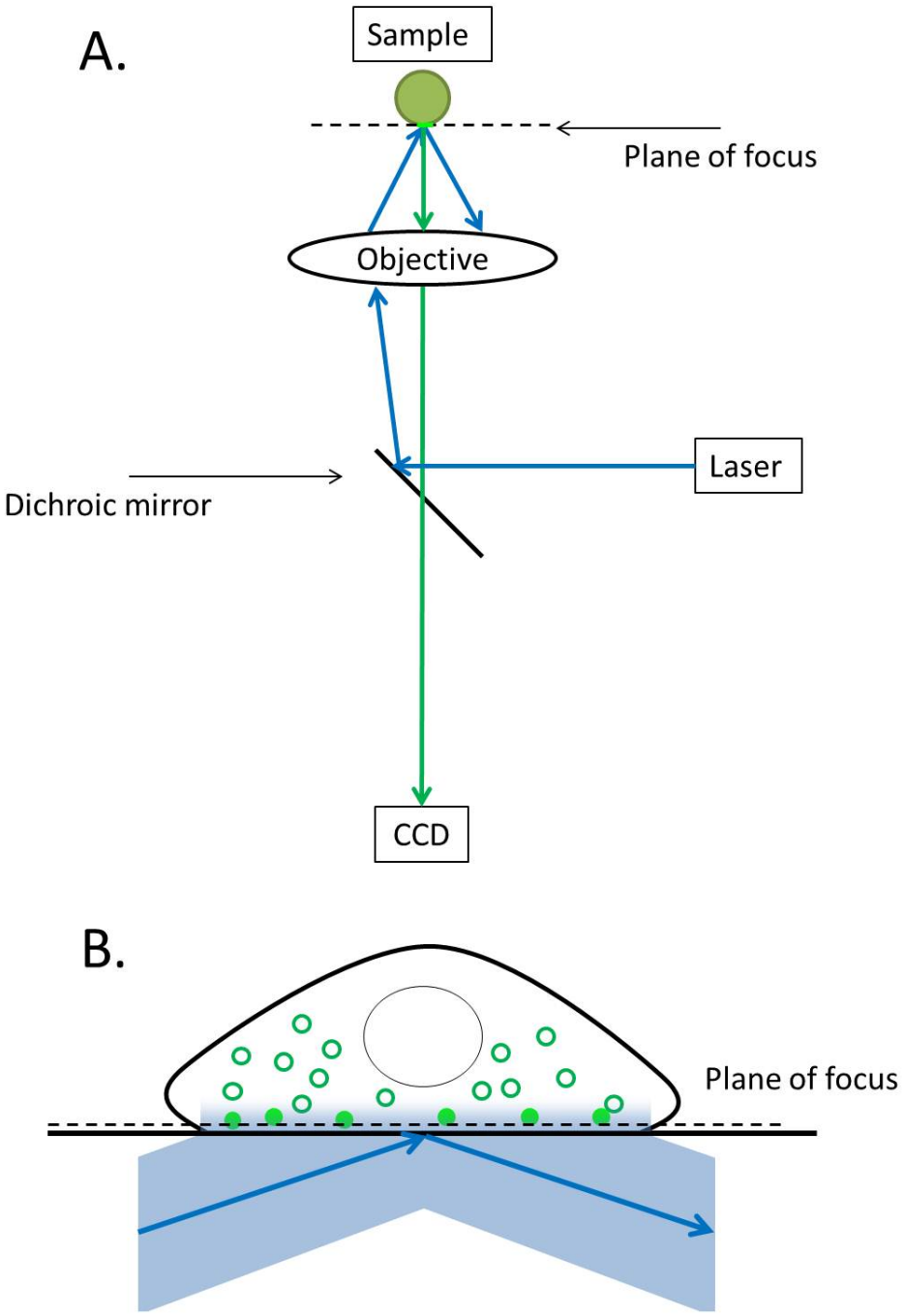

Figure 1.22: *A) A schematic of a TIRF microscope. Laser light goes from the source to a sample via a dichroic mirror. The laser is angled through the objective in such a way as to totally internally reflect off of the cover slip. This creates an evanescent wave, exciting the fluorophores closest to the cover slip as shown in (B). Light emitted from these fluorophores is collected by the objective lens, passes through the dichroic mirror as it is of a longer wavelength, and hits the detector. As it is a widefield technique the whole image is acquired at once.*

TIRF microscopy works by shining an incident laser at an angle at the coverslip, at an angle greater than the critical angle, which totally internally reflects, as described in Section 1.3.4. This interaction induces what is known as an evanescent wave, a standing wave where the intensity exponentially decays as it propagates into the sample. How this intensity changes with respect to distance from the coverslip is described in Equation 1.7, and is represented visually in Figure 1.23.

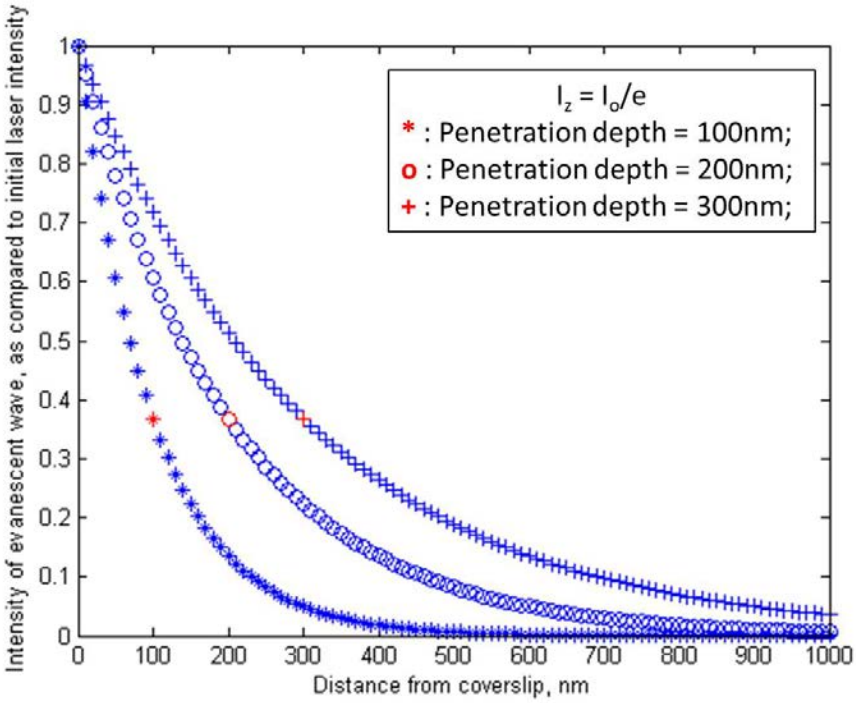

Figure 1.23: *Intensity decay of the evanescent wave. This graph displays the values for a laser of wavelength 488 nm, at incident angles of 68.4°, 64.4° and 63.7° to give penetration depths of 100, 200 and 300 nm. These values are given by the intensity value at I_0/e, obtained from rearranging Equation 1.7 where $z = d$.*

Use of this illumination technique offers a five-fold enhancement of axial optical sectioning compared to confocal microscopy[158]. As this technique employs widefield illumination, pixel values are acquired in parallel, offering several hundreds of frames per second. This is essential when considering the study of the active uptake of nanoparticles, a process which occurs over the order of seconds[159]. Further advancements in the development of TIRF techniques are examined in Chapter 5.

1.5 Aims and objectives of the thesis

The organisation of the thesis is as follows.

1.5.1 Chapter 2: Cellular entry of nanoparticles

It is known that nanoparticles have the potential to enter cells. Variations in cell type, nanoparticle size, shape and composition, and biological environment all have an effect on how, and the extent to which, this happens. This study highlights the amount of work that currently needs to be done in order to characterise the difference seen by changing one of these variables, namely the presence or absence of serum proteins in media. This study was performed using confocal microscopy on fixed HeLa cells with 20 nm carboxylate-modified fluorescent microspheres. Nanoparticles were characterised in different biological media in terms of size, surface charge and intensity under fluorescence microscopy. Affinity for, and subsequent entry into cells was characterised and quantified in different concentrations of serum proteins.

1.5.2 Chapter 3: Development of new computational methods for the analysis of nanoparticle uptake

Colocalisation studies using fluorescence microscopy are a powerful way of determining cellular functions through the study of interactions between proteins and other molecules. Current methods for determining colocalisation are examined and critiqued, and an improved method is proposed. This utilises a recently published novel de-noising software to enhance the signal-to-noise ratio of images prior to analysis. This is compared to existing methods on computationally created data, and further verified against real data that had been analysed by hand.

1.5.3 Chapter 4: Effects of the protein corona on nanoparticle uptake/ Development of new biological methods for analysis of NP internalisation

Chapter 2 looks into how the presence of serum proteins affects the cellular affinity for, and subsequent uptake of, nanoparticles. This study examines the difference in behaviour post-uptake in live cells, and how the absence of serum proteins affects this. Colocalisation studies using the tool proposed in Chapter 3 were performed between nanoparticles, endocytic marker proteins, and stained membranes. A novel protocol for using TIRF to study interactions between nanoparticles and the cell membrane was also developed, and real-time internalisation of nanoparticles was shown by the co-disappearance of nanoparticle and membrane marker from the evanescent TIRF field.

1.5.4 Chapter 5: Development of a novel imaging system to study the cellular uptake of nanoparticles

TIRF microscopy offers an unparalleled view of the basal cell membrane, and the work in Chapter 4 provided a way of visualising nanoparticle entry using this method. This study examines two established modifications to TIRF microscopy, namely variable angle and polarised TIRF. The advantages these methods give in studying membrane dynamics and subsequent motion in the z-direction are highlighted. Currently these two methods are not able to be performed on the same system, and significant steps are made in this direction. Variable angle TIRF is performed using the protocol developed in Chapter 4, and advantages over standard TIRF are highlighted. An instrument that takes an existing laser, splits it into two orthogonally polarised components, and outputs them into separate polarisation maintaining fibres was constructed and tested. Necessary changes to the Olympus IX81 before it can be used are outlined.

1.5.5 Chapter 6: Conclusions

The main conclusions of the thesis are summarised, and a novel alternative implementation for enabling polarised TIRF on any system without needing to modify the excitation optics is discussed.

CHAPTER 2

CELLULAR ENTRY OF NANOPARTICLES

2.1 Overview

As outlined in Chapter 1, the recent boom in nanoparticle production has led to the inevitability of increased exposure to humans. A greater knowledge of how they interact on a cellular level is necessary. Combined with the fact that different routes of exposure lead to formation of protein coronas which result in varying biological outcomes, a more robust and reliable method of characterising particle-cell interactions in a variety of conditions is desired. The aim of this preliminary study was to determine the route of entry of 20 nm carboxy-modified polystyrene nanoparticles into HeLa cells. This included characterising these nanoparticles in media both containing and free from serum proteins used in cell culture, in an effort to ascertain the effect a protein corona can have on a single cell system. It was shown that the primary route of entry for these particles was clathrin-mediated endocytosis, with a proportion of particles entering via direct plasma membrane permeabilisation. Having established the current methods required for characterising nanoparticle-cell interactions, thought is given to how new techniques can be designed to speed up this process.

2.2 Introduction

Increasing production and application of nanomaterials raises serious questions regarding the potential for human exposure and subsequent cellular entry. Structures with at least one dimension below 100 nm naturally occur, but are also being manufactured in ever-increasing quantities and varieties due to their novel and potentially beneficial qualities. This is across a wide range of fields, including medicine, research and industry, and increases the potential for both incidental and deliberate exposure.

As outlined in Chapter 1, even small differences in the nature of a nanoparticle can have large effects on the nature of protein corona formation, and hence any subsequent biological activity[74, 76, 80]. Due to these complexities, it is necessary for each system to be individually analysed in order to be completely understood. To this end, model nanoparticles with well defined characteristics are essential for understanding mechanisms for intracellular exposure and subsequent response.

Polystyrene nanoparticles can be manufactured (*e.g.* FluoSpheres® from Invitrogen Life Technologies, Carlsbad, CA) which are uniform in size and shape, and provided with a variety of fluorescent labels and surface modifications for use in biological applications. The ease and consistency at which they can be synthesised makes them useful for studying interactions between nanoparticles and cells[160]. Numerous studies have been undertaken looking into the methods of entry of polystyrene nanoparticles into different types of cells, but these have been largely inconsistent[93, 161, 162, 163, 164].

2.3 Aims and Objectives

The aim of this study is to look at one type of nanoparticle and one cell line, to characterise their interaction at a very specific level, and to determine the scale of work required to rigorously identify these processes. 20 nm carboxylate-modified polystyrene nanoparticles were chosen as they have been shown to induce less cytotoxicity than cationic

particles[160]. HeLa cells were chosen as they are human cells known for their hardiness and rate of growth[165]. They are a very popular choice for all types of biomedical studies, and are very amenable to microscopy, including TIRF. This study will look at the effect of both the presence and absence of serum proteins and quantify the effect of a protein corona. This is an important issue when considering *in vitro* cell biology, where cells are cultured in media containing 10% foetal calf serum, but traditional assays studying receptor-mediated endocytosis are performed in the absence of serum[166, 167, 168]. The presence of serum proteins will form a corona around the nanoparticles. This should lower their surface charge, and reduce their affinity for the cell membrane. However, the presence of serum proteins in the corona should result in some specific uptake of the nanoparticles. It is hypothesised therefore that in serum free conditions there will be a higher relative proportion of nonspecific particle uptake by cells.

It requires many experiments to characterise these interactions. There are hundreds of different cell types in the human body alone[169], and no conceivable upward limit on the types of nanoparticle theoretically possible to produce. It has been shown that stem cells, cancer cells and immune cells all respond uniquely to variations in nanoparticle type, concentration, and incubation time[170, 171, 172]. With this in mind, thought is given to how to make this process of understanding quicker and more replicable in future, in order to speed up the characterisation process.

2.4 Materials and Methods

2.4.1 Cell culture

HeLa and MDCK cell lines (Health Protection Agency Culture Collections, Salisbury, United Kingdom) were grown within T75 flasks (Corning Life Sciences, Amsterdam, The Netherlands) in Gibco® Dulbeccos modified Eagle medium (DMEM) (Invitrogen) supplemented with 10% foetal bovine serum (FBS) (Invitrogen), and 1% penicillin/streptomycin

(Invitrogen). This will henceforth be referred to as serum containing medium (SCM). Cells were incubated in a CO_2 incubator (MCO-17AIC; SANYO, Osaka, Japan) at 37°C in the presence of 5% carbon dioxide. In preparation for experimentation or passaging, cells were washed with 5 mL Gibco phosphate buffered saline (PBS) (Invitrogen), rinsed briefly with 2 mL trypsin (Invitrogen), and incubated at 37°C for 5 minutes in 1 mL trypsin. Cells were diluted appropriately in SCM and either transferred into new flasks or used for experimentation. For assays, cells were plated onto glass coverslips 24 hours prior, and were 60 - 80% confluent at time of use.

2.4.2 Plate reader assay

Detached cells were transferred to μClear® black 96-well glass bottom plates (Greiner Bio-One GmbH, Frickenhausen, Germany) and incubated for 24 hours to 60 - 70 % confluence. Yellow/green 20 nm carboxylate-modified polystyrene FluoSpheres (Invitrogen) (stock 0.02 g/mL $\equiv 4.54 \times 10^{15}$ nanoparticles/mL) were diluted to 1% in either SCM or Gibco® DMEM (henceforth referred to as serum free medium (SFM)). Preliminary experiments were performed with nanoparticle concentrations of 0.1 and 10%, however 1% was deemed the most appropriate in terms of fluorescence intensity. Cells were rinsed with PBS, and incubated with diluted nanoparticles for 0, 5, 15, 30, 60, or 120 minutes. Cells were then immediately rinsed twice with 100 μL PBS and fixed through incubation in 100 L of PBS containing 4% paraformaldehyde (Electron Microscopy Sciences, Hatfield, PA)for 5 minutes. They were then rinsed twice more with 100 μL PBS. The fluorescence was observed with PBS solution inside the wells with a FLUOStar Omega fluorescence plate reader (BMG LABTECH GmbH, Ortenberg, Germany).

2.4.3 Dynamic and electrophoretic light scattering assay

For zeta potential and hydrodynamic diameter measurements of dispersed nanoparticles, stock was diluted to 0.5% in SCM, SFM and PBS. This was sonicated in ultrasonic

bath (XUB18; Grant Instruments, Shepreth, UK) for 20 minutes immediately before measurement using a Zetasizer® Nano ZS ZEN3600 (Malvern Instruments Ltd, Malvern, United Kingdom). Zeta potential is measured by applying a uniform electric field over the sample, and measuring the particles' movement relative to the fluid. Hydrodynamic diameter is determined by characterising the scattering of laser light by the sample; the faster the scattered intensity varies, the smaller the particles.

2.4.4 Cytotoxicity assay

Detached cells were incubated in 6-well plates for 24 hours. The media was exchanged for one of the following: SCM; SFM; SCM with 1% nanoparticles from stock solution; or SFM with 1% nanoparticles from stock solution for 15 minutes at 37°C. These were then replaced with SCM and returned to the incubator for a further 24 or 72 hours. For counting, the cells were rinsed twice briefly with 2 mL PBS, and incubated at 37°C in 1 mL trypsin for 1 minute to remove dead cells. They were rinsed twice more with 2 mL PBS, and incubated at 37°C in 1 mL trypsin for a further 4 minutes. Cells were put into a Hawksley counting chamber (AS1000 Improved Neubauer Double Cell Standard; Hawksley, Sussex, United Kingdom) and counted.

2.4.5 Nanoparticle uptake assay at 37°C

24 mm glass coverslips were sterilised in 100% ethanol, dried and placed in 6-well plates. Detached cells were introduced and incubated at 37°C for 24 hours. Cells were pre-incubated at 37°C for 15 minutes in 2 mL of either SCM or SFM. They were then incubated at 37°C for a total of 30 minutes. This consisted of 15 minutes in 2 mL of either SCM or SFM containing 1% nanoparticles from stock solution, and 15 minutes in either SCM or SFM. They were then rinsed with 2 mL PBS before fixing. Studies performed with cancer cells found that a total incubation time of 30 minutes was optimal in terms of viability and functionality[170]. For fixation, cells were rinsed twice in 2 mL PBS at the

relevant temperature and fixed with 1 mL PBS containing 4% paraformaldehyde for 5 minutes. They were then rinsed twice more with 2 mL PBS. The 24 mm glass coverslips were then removed and mounted on a larger coverslip with a small drop of Vectashield® containing 4,6-diamidino-2-phenylindole (DAPI) (Vector Laboratories Ltd, Peterborough, United Kingdom) between the cells and coverslip. They were secured using a small coat of nail varnish around the edge and stored in a refrigerator for imaging.

2.4.6 Nanoparticle uptake assay at 4°C

For the experiments that required cells to be at 4°C, the protocol for the 37°C was followed, with some changes. The six-well plates containing cells were put on ice for 5 minutes prior to the start of the experiment, and remained there for the duration. All media introduced to the cells was chilled beforehand. Only once the 4% paraformaldehyde for fixing was added to the cells were they taken off the ice and brought back to room temperature.

2.4.7 Dynasore assay

24 mm glass coverslips were sterilised in 100% ethanol, dried and placed in 6-well plates. Detached cells were introduced and incubated for 24 hours. Cells were rinsed twice with warm SFM and incubated with 2 mL of either SFM containing 0.1% Dynasore (Sigma-Aldrich Corporation, St. Louis, MO) from 80 mM stock or SFM containing 0.1% dimethyl sulfoxide (DMSO) (Sigma-Aldrich) from 5 μg/mL stock. After 15 minutes the media was removed and replaced with 1 mL of either SCM or SFM containing a 0.1% dilution of Dynasore or DMSO and 1% red FluoSpheres, and incubated for 15 minutes. Cells were then rinsed with 2 mL PBS and fixed as described previously.

2.4.8 Dominant negative AP-2 and Caveolin 1 transfection

24 mm glass coverslips were sterilised in 100% ethanol, dried and placed in 6-well plates. Detached cells were introduced and incubated for 24 hours. Cells were transfected with 4

μg of either green fluorescent protein (GFP; Clontech Laboratories Inc, Mountain View, CA), EH29-GFP (provided by Alexandre Benmerah, Institut Cochin, Paris, France), or Caveolin1(Y14F)-GFP (provided by Mark McNiven, Mayo Clinic, Rochester, MN) using Lipofectamine^{TM} 2000 (Invitrogen) according to the manufacturers protocol. Nanoparticle uptake assays were conducted 24 hours later as described previously.

2.4.9 Transferrin uptake experiments at 37°C

24 mm glass coverslips were sterilised in 100% ethanol, dried and placed in 6-well plates. Detached cells were introduced and incubated at 37°C for 24 hours. Cells were pre-incubated at 37°C for 10 minutes in either SCM or SFM. Cells were then incubated at 37°C for 15 minutes in SFM containing 0.2% Alexa Fluor 488-labelled transferrin (Invitrogen). Cells were fixed as described in Section 2.4.5.

2.4.10 Transferrin uptake experiments at 4°C

For the experiments that required cells to be at 4°C, the protocol for the 37°C was followed, with some changes. The six-well plates containing cells were put on ice for 5 minutes prior to the start of the experiment, and remained there for the duration. All media introduced to the cells was chilled beforehand. Only once the 4% paraformaldehyde for fixing was added to the cells were they taken off the ice and brought back to room temperature.

2.4.11 Sytox® Green (Invitrogen)

For the general procedure, see the Nanoparticle Uptake Assay. Sytox Green (Invitrogen, Grand Island, NY) is a membrane-impermeant stain that only fluoresces when bound to nucleic acids. It was introduced to determine the extent of, if any, membrane permeabilisation that could be directly attributed to the presence of nanoparticles. A negative control was performed where Sytox Green was present when there were no nanoparticles. For both the negative control and where nanoparticles were present, Sytox Green was

introduced during incubation at a concentration of 0.02%. For the positive control condition, fixed cells were incubated for 5 minutes at room temperature in PBS containing 0.1% Triton X100 solution (SigmaAldrich Corporation, St Louis, MO), rinsed in PBS, and then incubated for 5 minutes in PBS containing 0.02% Sytox Green before mounting.

2.4.12 Imaging and image analysis

Coverslips from the Nanoparticle Uptake and Sytox Green experiments were imaged on a Nikon A1R inverted confocal microscope (Nikon Corporation, Tokyo, Japan) using a 60×/ 1.49 NA oil immersed objective. Coverslips from the Dynasore, Dominant Negative and Transferrin experiments were imaged on a Zeiss LSM 710 confocal microscope (Carl Zeiss Microscopy GmbH, Oberkochen, Germany) using 488 nm and 543 nm lasers with a 40×/ 1.3 NA or 60×/ 1.4 NA oil objective lens. As images from conditions free from serum were brighter, for each experiment these were performed first and identical laser settings were used in the less intense conditions where serum was present. A healthy looking cell that wasn't in contact with any others and displaying efficient transfection (where necessary) was selected for imaging. All analyses were conducted using NIS-Elements 3.2 (Nikon) or Zeiss Efficient Navigation System (Zeiss) imaging software, where an image from the centre of the confocal Z-stack was chosen for analysis. Nanoparticle 'spot' (defined as the visible accumulation of nanoparticles within a cell) intensity was calculated by manually drawing around every spot and recording individual intensity values. The intracellular background fluorescence from an area of equal size as, and adjacent to, the spot was subtracted. The number of visible nanoparticle spots in the chosen slice were counted and divided by the area of the cell in that slice to obtain the number of nanoparticle spots per cell area. Any spots that lay on the cell membrane were not counted. Each experiment was performed three times, and from each experiment ten cells were analysed.

2.4.13 Statistical analysis

Error bars in each Figure show the standard error in the data. For analysis of two data sets, p-vales were gained using Student's t-test which determines the probability that two populations are the same. The convention throughout this thesis is to indicate a 5% significance level unless otherwise reported. For analysis of experiments where three or more independent data sets were obtained, a one-way (or single factor) analysis of variance (ANOVA) test was performed. This tests the null hypothesis that the means of all populations are the same. Results were reported in the general form displayed in Equation 2.1.

$$F(df_{between}, df_{within}) = F_{ratio}, p \tag{2.1}$$

Where F indicates the mean squared ratio, df indicates the degrees of freedom between and within the data sets, and p is the p-value obtained. A statistically significant result, where p is less than 0.05, leads to accepting the alternative hypothesis, *i.e.* at least one of the means tested is significantly different from the others. Where this is the case, Bonferroni-corrected post hoc Student's t-tests were performed, where the 5% significance level is divided by the number of comparisons made[173] to reduce the chance of making a Type I error. Any post hoc t-tests that met this reduced significance level were considered statistically significant. Data was tested for normality and homogeneity of variances as is necessary for performing a one-way ANOVA.

2.5 Results and Discussion

2.5.1 The effects of serum on nanoparticles

In order to fully understand how nanoparticles interact with cells, it is necessary to learn how their behaviour is affected in different experimental conditions. In an environmental setting, a nanoparticle will come into contact with many naturally occurring proteins. However when utilising traditional assays used for studying receptor-mediated endocytosis, serum free conditions are standard[166, 167, 168]. Therefore preliminary studies have been performed to ascertain the effects, if any, the presence or absence of proteins have on nanoparticle interactions with cells.

It has been determined in fluorescence plate reader experiments that the magnitude of fluorescence from cells incubated with nanoparticles in the presence of serum proteins was 20-fold smaller than that from cells incubated with nanoparticles in media free from serum (Fig 2.1). This suggests that any experiments done in the absence of serum, as traditional receptor-mediated endocytosis assays are traditionally performed, may result in different outcomes. Before any reliable conclusions could be drawn from the effects of introducing nanoparticles to cells, the nanoparticles had to be fully characterised in the presence and absence of serum proteins. If the presence of serum proteins caused the nanoparticles to aggregate, or quenched fluoresence for example, then definitive results could not be drawn from the acquired data.

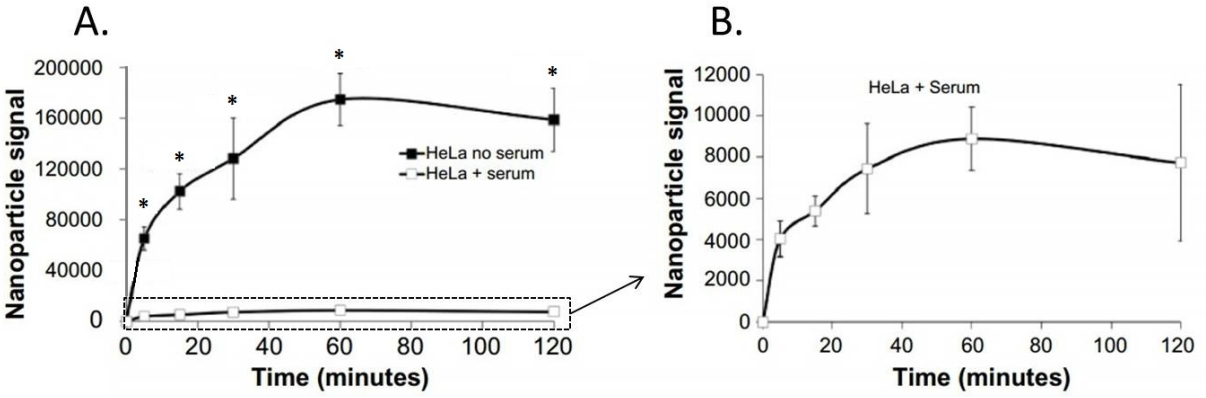

Figure 2.1: *Fluorescence plate reader measurements of HeLa associated nanoparticle intensity over two hours in either serum-free or serum-containing media. A) Data from both serum-free (black) and serum-containing (white) conditions. B) Magnified data of cells incubated in serum containing medium. There was a statistically significant difference between groups as determined by one-way ANOVA* ($F(11, 576) = 5.21, p = 7.35x10^{-5}$). *Significant* p*-values indicated refer to different conditions at the same time measurement and were calculated using a Bonferroni corrected post hoc t-test. The experiment was repeated three times, with 16 wells in each 96-well plate used for each condition. Error bars show the standard error in the data. Experimental data is attributed to Jennifer Thorley[104].*

Serum does not cause aggregation of nanoparticles

For measuring the hydrodynamic diameter of nanoparticles in suspension, a technique called dynamic light scattering (DLS) is employed. A laser is shone at the sample and the light scattered by the particles is measured. The speckle pattern created is used to determine whether the particles are small and fast moving, or larger and slow moving. Previously published dynamic light scattering data has demonstrated that the presence of serum proteins does not cause aggregation of polystyrene nanoparticles[174]. This was verified in the current study, as seen in Figure 2.2. The observed hydrodynamic diameter of the nanoparticles did not change when measured in serum-containing media compared to serum-free media. This shows that it was not aggregation of the nanoparticles in the presence of serum proteins that was causing the reduction in fluorescence seen in the plate reader experiments. A hydrodynamic diameter of around 50 nm is observed as DLS measures the size of a hypothetical hard sphere that diffuses in the same fashion as that of the particle being measured[175].

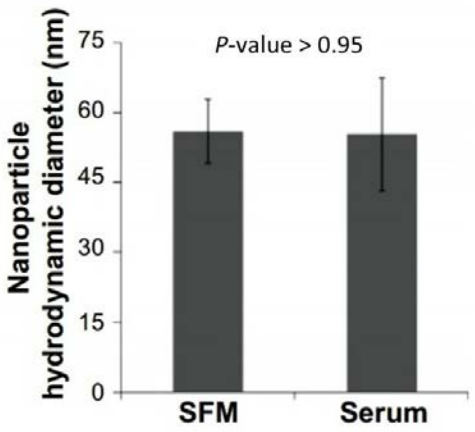

Figure 2.2: *Nanoparticle hydrodynamic diameter as calculated by dynamic light scattering. This was measured in both serum-free and serum-containing media. Three experiments were performed, with three samples for each condition and each sample was repeated three times. Error bars show the standard error in data.* P*-value was obtained using a Student's t-test, and shows no significant difference between the two data sets. Experimental data is attributed to Bjorn Stolpe[104].*

Serum does not affect nanoparticle fluoresence

Time-lapse confocal microscopy of the nanoparticles before and after the addition of working concentrations of serum proteins have shown no effect on the ability of the particles to fluoresce, as shown in Figure 2.3. The particles in a single field of view were individually quantified over time, and no overall change in fluoresence was observed. This shows that the serum proteins were not causing the reduction in fluorescence seen in the plate reader experiments.

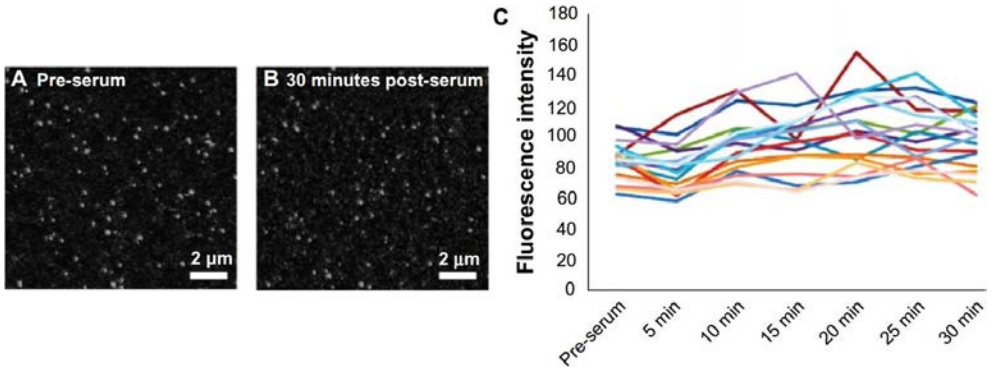

Figure 2.3: *Fluorescence intensity measurements of nanoparticles taken with a confocal microscope upon addition of serum. A) Nanoparticles in serum free media. B) Nanoparticles 30 minutes after introduction of working concentrations of serum. C) Fluorescence intensity of spots in a single frame over 30 minutes.* n *= 1.*

Serum does affect the measured zeta potential of nanoparticles

It can be concluded from these two experiments that the serum proteins present in the media must in some way be inhibiting the nanoparticles from associating with cells. One possible explanation for this is the effect serum proteins have on the zeta potential of the nanoparticles. The zeta potential of a particle is the potential difference between the suspending medium and the layer of stationary fluid encasing the particle[176]. This is measured by applying an electric potential across the liquid and using the scattering of laser light to determine the resultant velocity of particles. This knowledge allows calculation of the zeta potential of the nanoparticles via application of the Henry equation, shown in Equation 2.2.

$$U_E = \frac{2\epsilon z f(ka)}{3\eta} \tag{2.2}$$

Where z is the zeta potential, U_E is the electrophoretic mobility of the medium, ϵ is the dielectric constant, and η is the viscosity of the medium. $f(ka)$ is Henry's function, which approximates to 1.5 for aqueous media. When the nanoparticles are in serum containing medium, the proteins present in the media are attracted to the electronegative surface of the bare particle, and encase it in a protein corona as defined in Section 1.1.4. This results in the reduced magnitude of the zeta potential of these particles when compared to those incubated in serum free medium. The result of this is that the less charged particles have a reduced affinity for cell membranes, and so result in lower adherence, and hence uptake. It can be seen in Figure 2.4 that the introduction of serum to the nanoparticles results in a three-fold decrease in electronegativity of the particles.

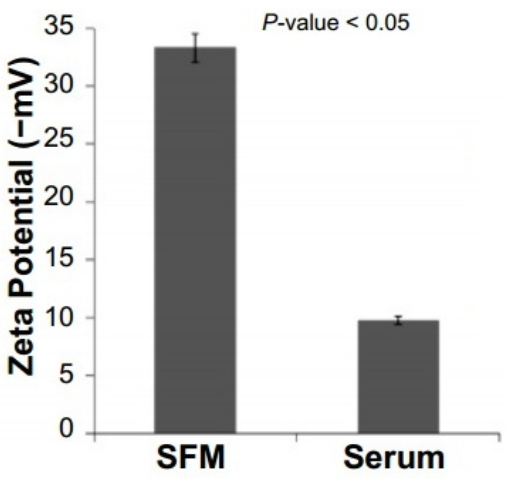

Figure 2.4: *Zeta potential measurements of nanoparticles within serum-containing or serum-free media. Three experiments were performed, with three samples for each condition and each sample was repeated three times. Error bars show the standard error in data.* P*-value was obtained using a Student's t-test, and shows there is a significant difference between the two data sets. Experimental data is attributed to Bjorn Stolpe[104].*

Further study into the protein corona

Further insight into the nature of the protein corona and its effects on the membrane affinity of 20 nm polystyrene beads can be gained from considering the results of a concurrent study. Continuing on from the work visualised in Figure 2.1, nanoparticles were incubated in different amounts of either foetal bovine serum (FBS) or the corresponding amount of bovine serum albumin (BSA). This is the most abundant protein in FBS, and was chosen so there was the same amount of BSA in both cases. This was calculated from the information provided by BioSera regarding the relative concentrations of ingredients within their FBS. This incubation was only for 15 minutes, and so a soft corona can be assumed to be present[78]. For the cell membrane associated nanoparticle fluorescence studies, cells were incubated for 15 minutes with these nanoparticles in media containing 0%, 0.05%, 0.25%, 1%, 2.5%, 5% and 10% FBS by volume, or the equivalent amount of BSA. For the zeta potential studies, FBS concentrations were at 0%, 0.025%, 0.05%, 1%, and 10% by volume in DMEM, while again the BSA concentrations were equivalent to the amount of BSA contained in FBS. Each concentration was tested in triplicate three times ($n = 3$). Full methodology can be found in [177].

Comparison of serum to BSA on nanoparticle associated cellular fluorescence A 5-fold reduction in membrane associated fluorescence can be seen when comparing media free from serum and media at a concentration of 10% serum (the first and last red points of Figure 2.5). This study used the same plate reader protocol as used for the results in Figure 2.1. What was interesting about this study is the reduction seen in the affinity of nanoparticles to a cell membrane, seen dramatically even at very low (0.05%) concentrations of serum. This decay begins to reach a plateau at working concentrations of serum (10%), but suggests that even at these relatively high concentrations the corona is still unsaturated and more interactions could occur even at higher concentrations of serum.

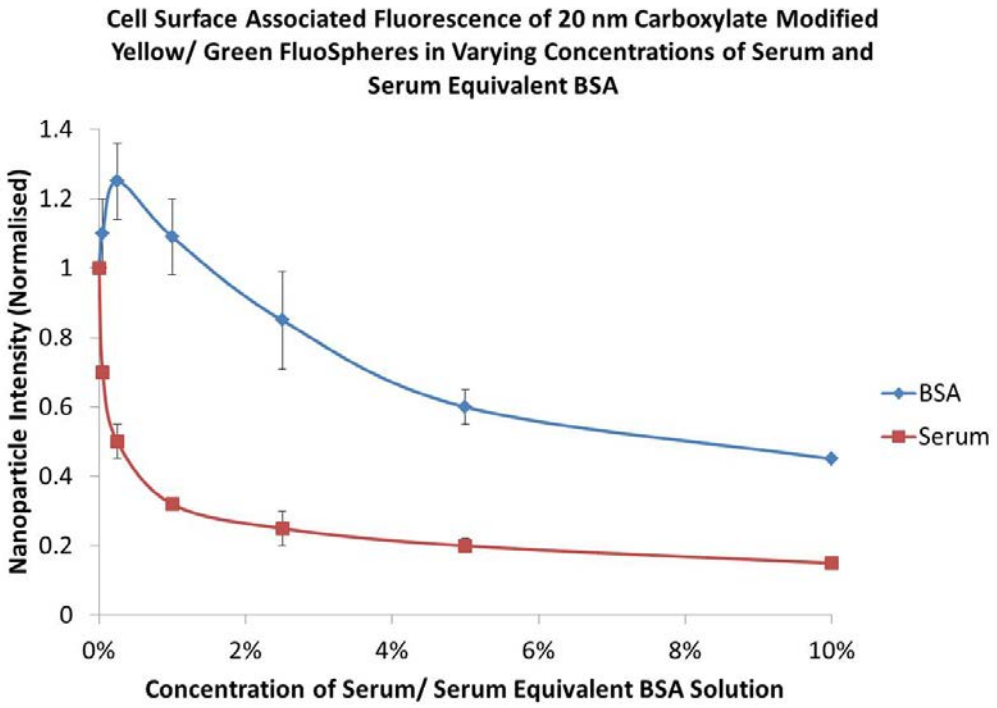

Figure 2.5: *A graph showing the reduction of plasma membrane associated cellular fluorescence as measured with a fluorescence plate reader. This is from 20 nm polystyrene nanoparticles incubated for 15 minutes with varying concentrations of FBS and BSA at 15.4 g/l, an amount of albumin equivalent to that found in FBS. It can be seen that although BSA causes a reduction in the plasma membrane associated cellular fluorescence, it is not to the same extent as FBS. Three experiments were performed, with three samples for each condition and each sample was repeated three times. Error bars show standard error of the mean. Experimental data is attributed to Abdullah Khan[177].*

When looking at the BSA data in tandem, although it is clear that there is a similar concentration dependent reduction in the associated cellular fluorescence overall, it is not to the same extent as in the FBS case. This is significant as it shows clearly the effect less abundant proteins have on the corona and hence interactions on a cellular level. This is relevant to experimental design as some published studies have used albumin in isolation to study corona formation and subsequent cellular uptake, with the assumption that because it is the most abundant protein, it must be the most relevant[178].

While the overall trend in Figure 2.5 is a decrease in the membrane associated cellular fluorescence, there can be seen an increase in fluorescence for the lower concentrations of BSA. While this was reproducible, it was not statistically significant compared to the 0% value with an n of 3 using a Student's t-test. It is interesting when looked at in parallel with the zeta potential data in Figure 2.6 however.

Comparison of serum to BSA on zeta potential of nanoparticles As displayed earlier, Figure 2.6 replicates the finding that there is a three-fold reduction in the magnitude of the zeta potential displayed by nanoparticles incubated in media with 0% and 10% serum. Again, the additional data points reveal a sharp decrease and then a plateau in the relationship between the amount of serum proteins present and the resulting zeta potential of the nanoparticles similar to that seen in Figure 2.5. In this case however, it is clear a plateau is reached. The zeta potential doesn't decrease with additional amounts of serum.

This could be explained by the Vroman effect; that at 1% serum the quantity of protein forming the corona is stable, and hence the zeta potential observed does not change. With an increase in the volume of serum, and hence the number of less abundant proteins, the proteins with a lower binding energy are displaced by those with a higher binding energy. This could have an effect on the ability of nanoparticles to bind to cell membranes without altering the zeta potential.

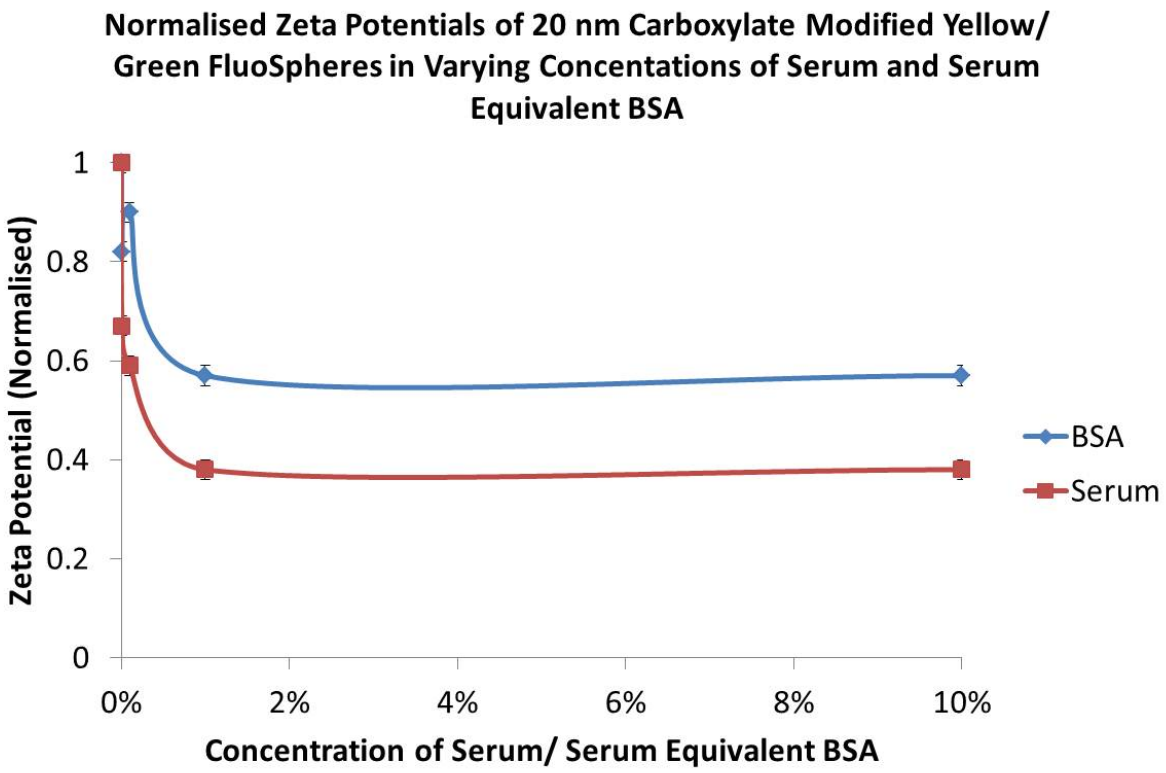

Figure 2.6: *A graph comparing the normalised zeta potentials of nanoparticles incubated in FBS and the equivalent amount of BSA. Three experiments were performed, with three samples for each condition and each sample was repeated three times. Error bars show standard error of the mean. Experimental data is attributed to Abdullah Khan[177].*

When looking at the BSA data, it is clear that a similar decay in zeta potential can be seen when compared to the FBS data. This supports the hypothesis that an increase in protein concentration reduces the zeta potential of the nanoparticle, which in turn leads to reduced cell surface interactions and decreased uptake of nanoparticles by the cell. This isn't quite to the same extent however, showing definitively that the protein corona formation around this specific type of nanoparticle depends not only on the most abundant protein in the medium in which it resides, but also that less common proteins have more of a binding affinity. It also shows that using BSA alone for an assay studying cellular uptake of nanoparticles could lead to misleading results for experiments, as the most abundant protein isn't necessarily the most biologically relevant[178].

It is interesting to note in the BSA zeta potential data that there is a slight increase at a concentration of 0.05%. This corresponds to the increase in signal in the fluorescence plate reader data in Figure 2.5. This could be due to a phenomenon seen in some studies which have shown that certain concentrations of proteins in media have stabilised nanoparticles and prevented aggregation that would otherwise occur. This would allow more binding sites to become available for cell interactions. This has been shown for magnetic iron oxide nanoparticles, where a suitably high concentration of FBS caused their disaggregation, yielding particles with a significantly smaller hydrodynamic diameter than controls[179]. This seems to be material dependent, with no effect observed in polystyrene nanoparticles with suphonated surface modifications that had been incubated in many different concentrations of FBS[180].

Findings like these are significant when considering biomedical applications. If it is known what conditions can cause nanoparticles to aggregate or disaggregate, the most effective way of administering nanoparticulate drugs or imaging agents can be utilised. It is also necessary to know exactly how a nanoparticle will behave in relation to a cell when it reaches its target.

Preliminary microscopy studies

It has been established that incubating nanoparticles with cells in the presence of serum greatly reduces associated cellular fluorescence. It is hypothesised that the increased concentration of proteins reduces the ability of nanoparticles to enter cells. This is because more proteins reduce the zeta potential of nanoparticles, affecting their ability to associate with plasma membranes, resulting in reduced uptake. As a fluorescence plate reader cannot distinguish between intracellular and cell surface signal, confocal microscopy studies have to be performed to determine this.

It can be seen in Figure 2.7 that when identical laser power and gain settings are used on the microscope, both the intracellular accumulations and cell surface binding are significantly higher in serum-free conditions than when the cells are incubated with nanoparticles in serum-containing media. It is clear that the five- to twenty-fold increase in overall fluorescence intensity observed in the plate reader experiments is primarily due to cell surface binding, as there is only a two-fold increase in fluorescence intensity when looking at intracellular accumulations alone. It is interesting to note that although the spot fluorescence is higher in the serum-free condition (Figure 2.7 C), the number of intracellular accumulations per unit area does not differ between the two cases. This suggests that it is possible that the nanoparticles may be entering the cells through similar pathways, the affinity for the cell surface being the limiting factor in internalisation. It was also observed from these preliminary studies that these particles did not accumulate in the cell nucleus. This is in contrast to studies with similar nanoparticles (same size and surface modifications) in HEp-2 cells, where fluorescence was detected in the nucleus[181].

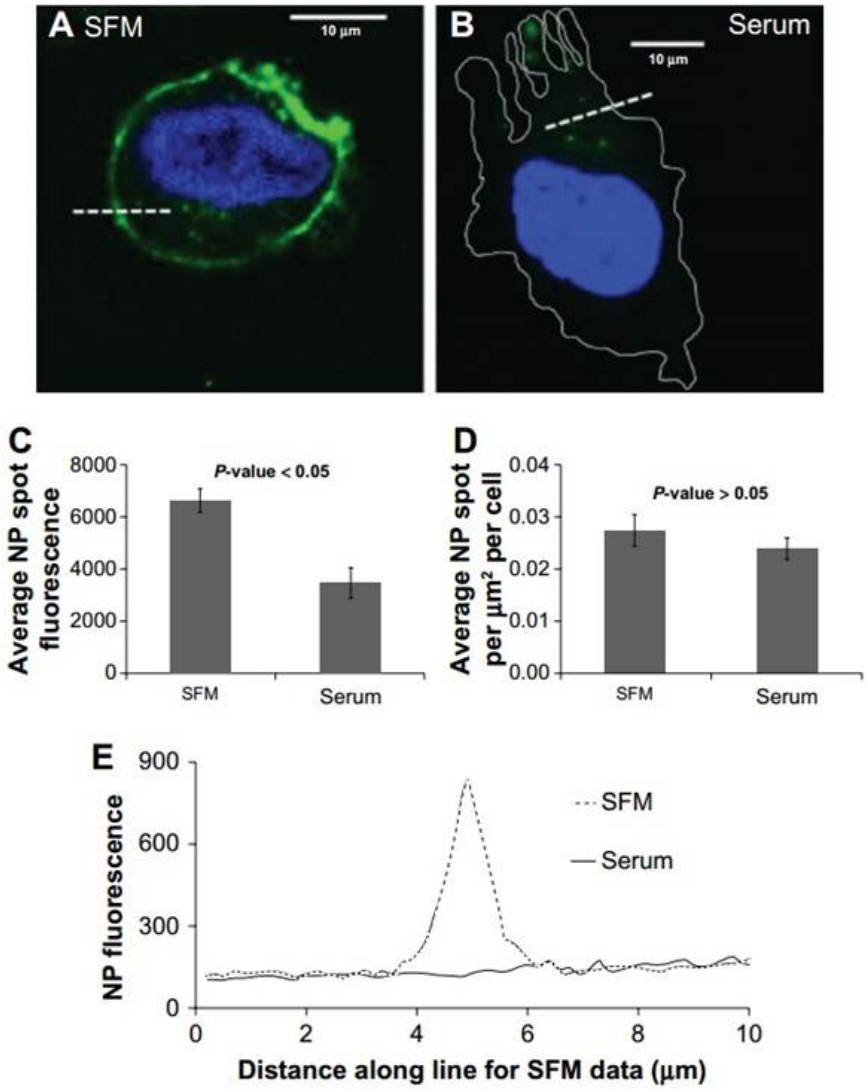

Figure 2.7: *Representative confocal microscope images of a HeLa cell incubated for 15 minutes with 20 nm carboxylate-modified polystyrene nanoparticles in (A) serum-free media and (B) serum-containing media. (C) Average nanoparticle spot fluorescence in both conditions. There is a significant decrease in observed nanoparticle fluorescence for cells incubated in serum using a Student's t-test. (D) Average nanoparticle spot density inside cells in both conditions. There is no significant difference between the two using a Student's t-test. Each experiment was performed three times, and from each experiment ten cells were analysed. Error bars in (C) and (D) show the standard error in the data. (E) Representative line scan profiles across the cell membrane display greatly increased cell surface nanoparticle binding in serum-free media relative to serum-containing media.*

Cytotoxicity assay

Figure 2.7E shows that for cells incubated with nanoparticles in SFM, there is significant accumulation on the plasma membrane. This is in contrast to cells incubated with nanoparticles in SCM, where a line profile of the intensity readings shows no observable change from background fluorescence. The significant increase in fluorescence intensity as observed by the plate reader experiments can be attributed to this increased affinity for the plasma membrane in serum free conditions. A cytotoxicity assay was performed to determine whether this increased cell surface binding observed had a negative effect on cells. Figure 2.8 shows a insignificant level of cytotoxicity in both SFM and SCM. A decrease of between 25 - 38% in cell count can be seen in both cases, 24 and 72 hours after exposure. It can also be seen that viable cell number increases with time after exposure. This would seem to indicate that although cells are initially affected negatively by the presence of nanoparticles, this is reversible to a certain extent.

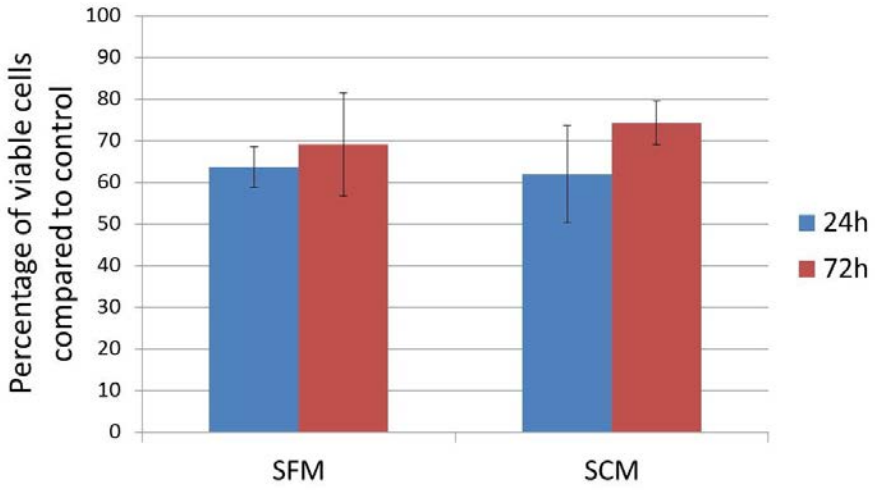

Figure 2.8: *Nanoparticles do not affect cell viability in the presence or absence of serum. Plated cells were incubated for 15 minutes in either SCM, SFM, SCM and NPs, or SFM and NPs. They were rinsed and incubated for either 24 or 72 hours in SCM before counting. The graph shows the percentage of live cells that were incubated with NPs compared to the control group that were incubated without NPs, for equivalent times. The experiments were performed on separate groups of cells. Results are obtained from an experiment count of* n = *4, with three dishes of cells analysed per experiment. Bars show standard error in data. Single factor ANOVA revealed no significant difference between the means of the control experiments and the nanoparticle experiments (F(3,12) = 0.36, p = 0.78).*

2.5.2 Endocytosis studies

Cellular entry of nanoparticles is extremely dependent on the cell line being studied, the physiochemical properties of the particles themselves (size, composition, or surface characteristics), and the environment they are in[73, 93, 164, 163, 162]. When designing and testing targeted nanoparticle-based drugs for example, all of these factors will affect whether and how they are internalised by a specific cell type. This is important, as it will affect whether the intended target is reached, and if side effects to other organs are reduced[182]. Modes of uptake are also important, as some internalisation routes will be more effective at successful drug delivery than others[183]. As a result, it is useful to be able to determine how changes in environment for example affect how nanoparticles interact with cells. Consequently, the aim of this project was to determine whether the route of nanoparticle entry was affected by the presence of serum proteins. This is an important issue when considering *in vitro* cell biology, where cells are cultured in media containing 10% foetal calf serum, but traditional assays studying receptor-mediated endocytosis are performed in the absence of serum[166, 167, 168].

Based on the findings from Figure 2.7, it is hypothesised that nonspecific uptake of these 20 nm carboxylate-modified polystyrene beads into HeLa cells is greater in conditions free from serum than in conditions where serum is present. This is due to increased nonspecific binding brought on by the reduction in zeta potential as a result of protein corona formation. Proteins incubated in serum free conditions are assumed to display a greater degree of specific uptake as they will be internalised as a consequence of being attached to certain proteins.

Dynamin dependency

As described in Section 1.2.1, Dynamin is a large GTPase which regulates several endocytosis pathways. Dynasore is a small membrane- permeable molecule which specifically inhibits dynamin function[99, 184], during both coated-pit formation and vesicle scission. With the introduction of Dynasore prior to nanoparticle incubation, it would be possible to determine whether nanoparticles are entering cells via a dynamin- dependent route. As seen in Figure 2.9, in serum-free conditions the introduction of Dynasore results in a clear, significant inhibition of nanoparticle entry. It can be concluded that the majority of these particles are entering through dynamin-dependent routes. It is important to note that the results from studies containing serum have been omitted, as Dynasore binds to serum proteins and loses activity[185].

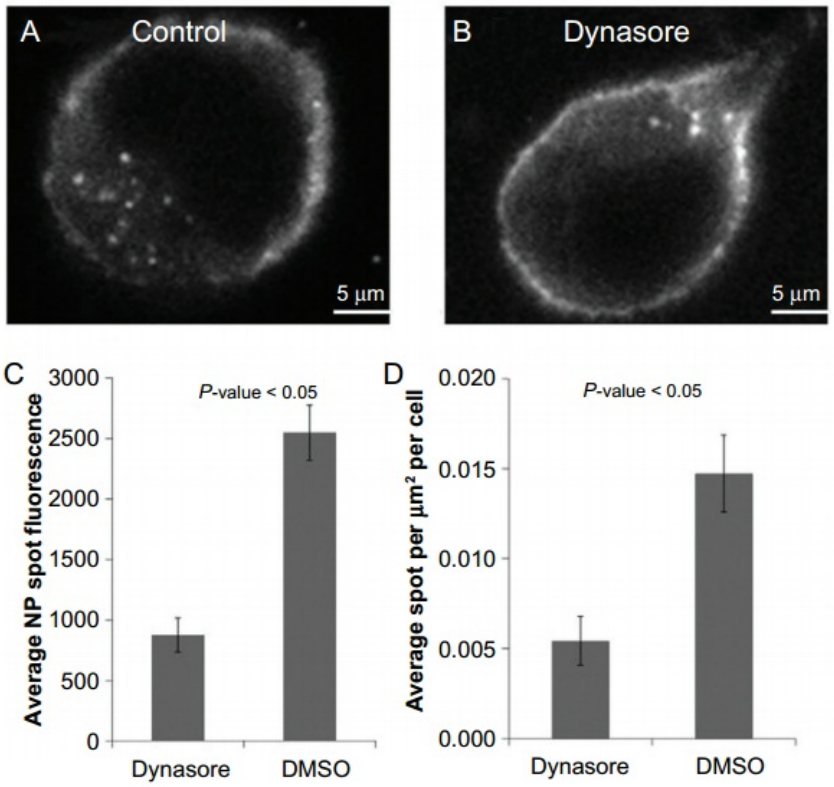

Figure 2.9: *Dynasore inhibits nanoparticle entry into cells incubated in serum-free media. A) HeLa cell incubated with nanoparticles in serum-free media and dimethyl sulfoxide (DMSO) as a control. B) HeLa cell incubated with nanoparticles treated with Dynasore in serum-free media. C) Average nanoparticle spot fluorescence and D) average spot density for HeLa cells in these conditions. Bars show standard error in data,* n *= 10 cells × 3 experiments.* p *value gained from Student's t-test.*

Clathrin-mediated versus caveolar endocytosis

Two of the main endocytosis pathways regulated by dynamin are clathrin-mediated and caveolar endocytosis[99]. To determine whether either of these are involved in the entry of 20 nm carboxylate-modified polystyrene beads, it was necessary to specifically inhibit both of these routes and quantify the effects. Positive controls for the inhibitors used have previously been confirmed [166, 167, 168, 186, 187, 188].

Inhibition of CME As described in Section 1.2.1, the recruitment of clathrin to the membrane is controlled specifically by the adapter protein complex AP-2. Associated with this complex is Eps15, which contains domains that are essential for correct coated-pit formation. It is possible to make cells express genes coding a mutated version of Eps15, without these specific domains (referred to hence as the EH29 mutant). Upon expressing Eps15(EH29), AP-2 is distributed evenly across the membrane, preventing clathin from forming punctate spots, and hence inhibiting CME[189].

Inhibition of caveolar endocytosis Caveolar endocytosis can also be inhibited by transfection of a dominant negative gene encoding region. Caveolar assembly is stimulated via Src-phosphorylation on tyrosine-14, which causes a conformational change allowing it to bind to the membrane. The mutant form, Cav1(Y14F), is not able to undergo Src-phosphorylation, which prevents caveolae from being formed[190].

Effects in serum free media It can be seen in Figure 2.10 that expression of dominant negative Eps15(EH29) significantly reduces both nanoparticle uptake and spot fluorescence when incubated in serum free media. This is in contrast to cells expressing dominant negative Cav1(Y14F) to block caveolar endocytosis, which had no statistically significant effect on spot density or fluorescence. This would indicate that nanoparticles are gaining entry to the cell interior in part by clathrin-mediated endocytosis. To ensure that the transfection process wasn't affecting how the cells react to the presence of nanoparticles, cells were transfected with GFP as a control. This shouldn't have had any effect on cellular function in terms of nanoparticle internalisation.

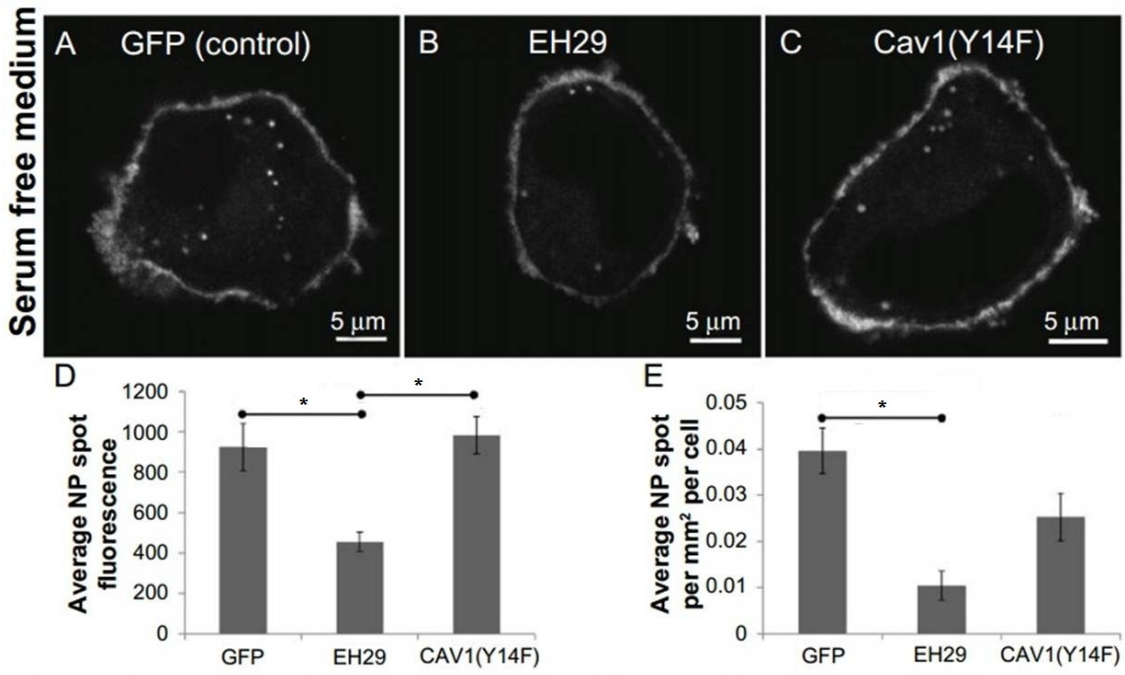

Figure 2.10: *Effects of endocytosis inhibitors on nanoparticle entry in serum-free media. Representative images of HeLa cells incubated with nanoparticles in serum-free media expressing A) green fluorescent protein, B) EH29, and C) Y14F. D) Average nanoparticle spot fluorescence intensity in each condition. There was a statistically significant difference between groups as determined by one-way ANOVA* ($F(2, 186) = 4.46, p = 0.013$). *E) average spot density in each condition. There was a statistically significant difference between groups as determined by one-way ANOVA* ($F(2, 24) = 10.50, p = 0.00053$). n = *3, and 3 cells were analysed per experiment. Significant* p*-values indicated were calculated using a Bonferroni corrected post hoc t-test. Bars show standard error in data. Images were obtained by Helen Wiggins.*

Effects in serum containing media Similar effects were observed in cells expressing these constructs incubated with nanoparticles in serum containing media. This can be seen in Figure 2.11. The expression of EH29 significantly decreased the number of nanoparticle accumulations in the cell relative to the control, however this time the reduction in spot fluorescence intensity was not statistically significant. Interestingly, the increase in average spot fluorescence intensity induced by expression of Cav1(Y14F) compared to the control was significant, and suggests that nanoparticle entry could be increased by inhibiting caveolar endocytosis. A similar effect was seen with the uptake of fluorescent dextran[191], where inhibiting caveolar endocytosis resulted in almost a 200% increase in its uptake compared to a control.

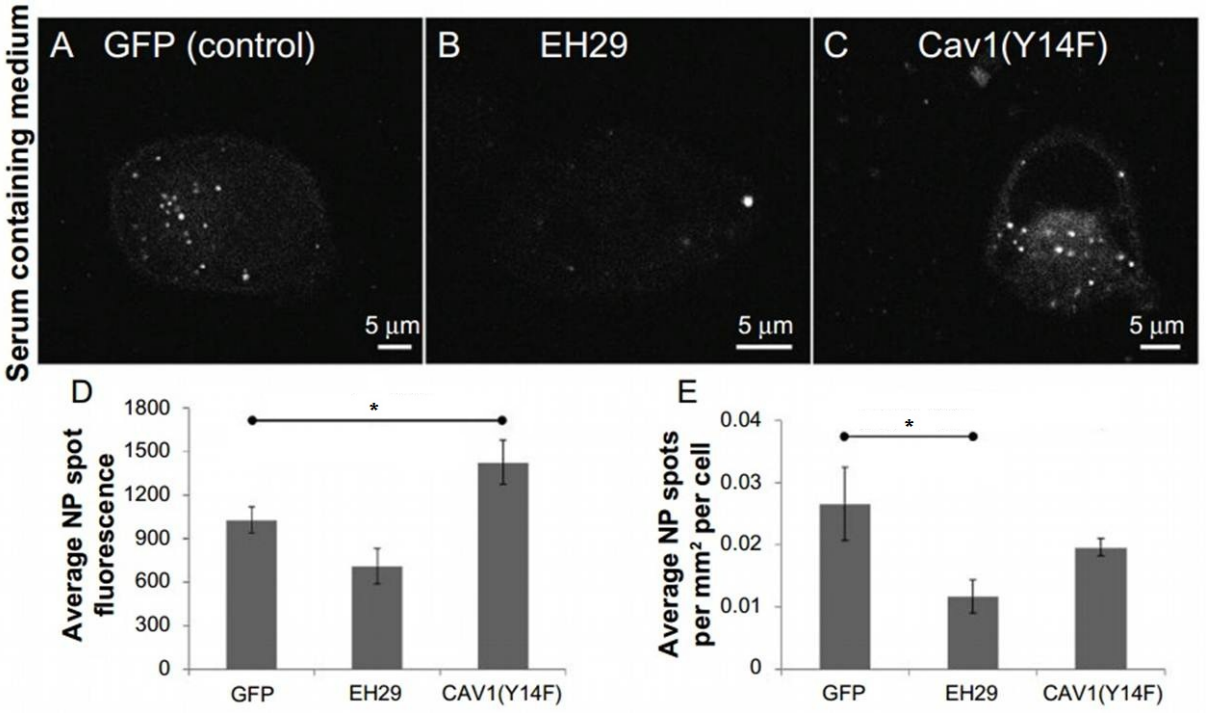

Figure 2.11: *Effects of endocytosis inhibitors on nanoparticle entry in serum-containing media. Representative images of HeLa cells incubated with nanoparticles in serum-containing media expressing A) green fluorescent protein, B) EH29, and C) Y14F. D) Average nanoparticle spot fluorescence intensity in each condition. There was a statistically significant difference between groups as determined by one-way ANOVA* ($F(2, 185) = 6.02, p = 0.0029$). *E) average spot density in each condition. There was a statistically significant difference between groups as determined by one-way ANOVA* ($F(2, 24) = 3.65, p = 0.041$). n = *3, and 3 cells were analysed per experiment. Significant Bonferroni corrected* p*-values indicated were calculated via post hoc t-test. Images obtained by Helen Wiggins.*

Taken together, these results provide evidence for a dynamin-dependent, clathrin-mediated route of entry for 20 nm carboxylate modified polystrene beads. This is true for cases where serum is present or absent at the time of incubation. These results also suggest that caveolar endocytosis does not play a direct part in this process. However, both cases show that nanoparticles are still getting into cells even when clathrin-mediated and caveolar endocytosis are inhibited. Even though it is likely that these endocytic routes were not completely inhibited, internalisation of these nanoparticles by another route is still possible.

2.5.3 Nanoparticle-mediated cellular permeabilisation

To rule out other routes of endocytosis that nanoparticles may be utilising to enter cells (see Section 1.2.1), cells were cooled to 4°C before and during incubation, and immediately fixed afterwards. Cooling to this temperature is known to inhibit endocytosis[192], and so if nanoparticles were still seen inside cells after this process then it could be concluded that some internalisation of nanoparticles was endocytosis-independent. To confirm this, cells were incubated with fluorescently tagged transferrin, a cargo molecule known to be internalised via clathrin-mediated endcytosis. When comparing data at 4°C and 37°C, endoctytosis was nearly completely inhibited (Figure 2.12).

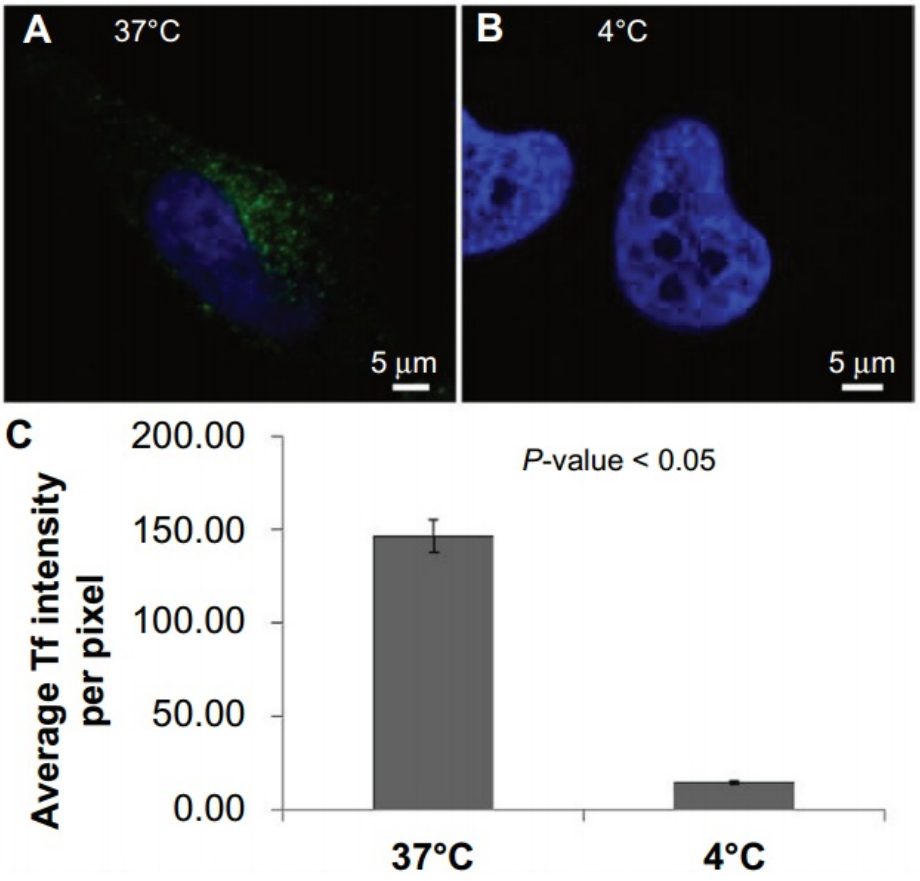

Figure 2.12: *Control for endocytosis inhibition at 4°C. Representative images of HeLa cells incubated at A) 37°C and B) 4°C with transferrin. Identical imaging conditions and display values show the almost total inhibition of transferrin entry at 4°C. Number of experiments,* n = *3, with 10 cells analysed in each experiment. Bars show standard error in data.* p*-value obtained using Student's t-test. Image acquisition and analysis attributed to Helen Wiggins.*

This experiment was performed with nanoparticles in both SFM and SCM, with the results displayed in Figure 2.13. Although the magnitude of entry is significantly reduced in both conditions, nanoparticles are still observed within the cytosol. This would imply that nanoparticles can enter cells via an endocytosis-independent route.

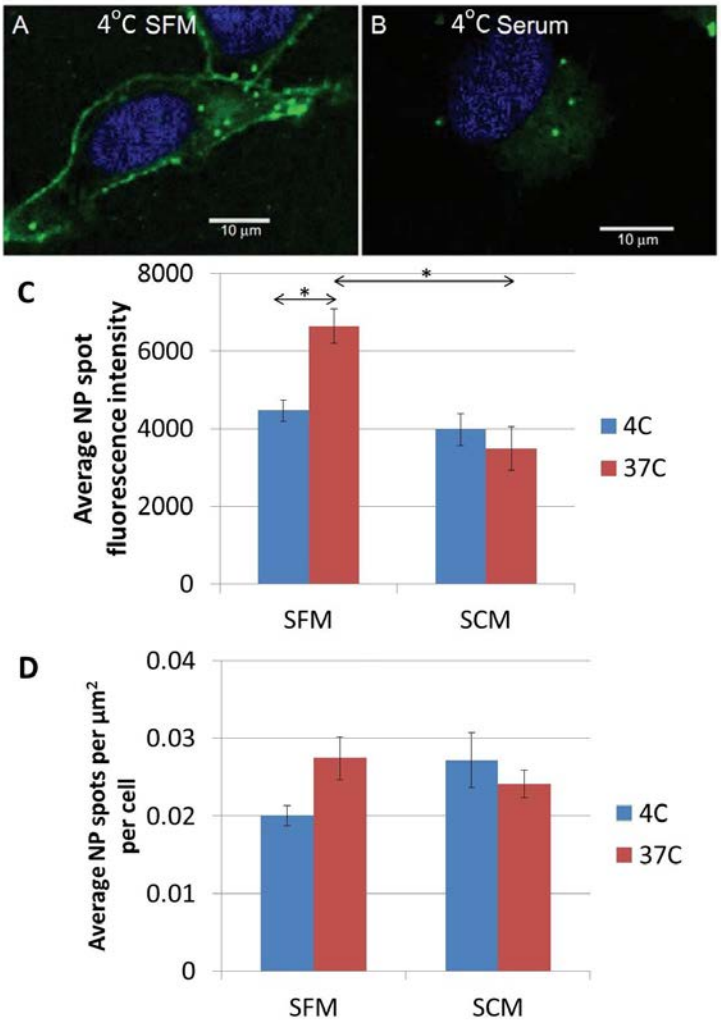

Figure 2.13: *Nanoparticles gain entry to the cytosol even when endocytosis is inhibited. Representative images of a HeLa cell incubated with nanoparticles in A) serum-free media at 4°C and B) serum-containing media at 4°C. C) Average nanoparticle spot fluorescence intensity in each condition, as compared to 37°C data from Figure 2.7. There was a statistically significant difference between groups as determined by one-way ANOVA* ($F(3, 1066) = 10.82, p = 5.28x10^{-7}$). *D) Average nanoparticle spot density in each condition, as compared to 37°C data from Figure 2.7. There were no statistically significant differences between group means as determined by one-way ANOVA* ($F(3, 98) = 2.15, p = 0.099$). *Number of experiments,* n = *3, with 10 cells analysed in each experiment. Bars show standard error in data.* p*-values obtained using Student's t-test.*

As the nanoparticles are negatively charged, it is highly unlikely that they are able to freely diffuse across the plasma membrane. It has also been shown that while rod-shaped polystyrene nanoparticles are able to induce macropinocytosis, spherical nanopartices have not exhibited this same property[193]. It would be possible for the nanoparticles to enter through discontinuities in the plasma membrane however, either pre-existing or induced. It becomes necessary to confirm that cooling cells to 4°C for the length of time of the experiment does not compromise the cell's integrity in any way.

Sytox® Green is a membrane impermeant molecule that only fluoresces when bound to nucleic acids. It is traditionally used to distinguish dead from live cells in flow cytometry assays[194, 195] by detecting those with compromised membranes. By introducing this and quantifying the resultant fluorescence intensity, it can be determined if, and to what extent, the membrane has been compromised in different conditions. According to the manufacturer's protocol, cells should be fixed prior to Sytox Green exposure. However, Figure 2.8 showed even if the nanoparticles are permeabilising the cell membrane during an experiment, they are not causing significant levels of cytotoxicity. This would suggest the cells had the ability to recover from any stress caused by the nanoparticles. For this reason, it was decided to incubate live cells with Sytox Green in the negative control and nanoparticle conditions at 4°C.

Cells were incubated at 4°C in either SFM or SCM with Sytox Green in three different conditions: with nanoparticles present, with a detergent present, and a negative control with nothing extra added. It can be seen in Figure 2.14 that the resultant fluorescence intensity in the negative control condition is significantly less than in other conditions, confirming that cooling the cells was not disrupting the cell membrane. As a positive control, cells were incubated with Sytox Green and 0.1% Triton X-100, a detergent known to permeabilise cell membranes[196, 197]. This would ensure entry of the Sytox Green to the cell interior, and the resultant increase in fluorescence can be seen in Figure 2.14. When Sytox Green is introduced to the condition where nanoparticles are present, a statisti-

cally significant amount of fluorescence is observed when using a t-test compared to the negative control condition. This would indicate that the nanoparticles are indeed having a disruptive effect on the plasma membrane, and are able to gain entry to the cytosol without being actively taken up by the cell. This effect cannot be explained by surfactants or detergents present in the nanoparticle manufacturing process[198]. The sodium azide used as a preservative in the stock nanoparticle solution also has no discernible effects on mammalian cells at the concentration or times used in this experiment[199].

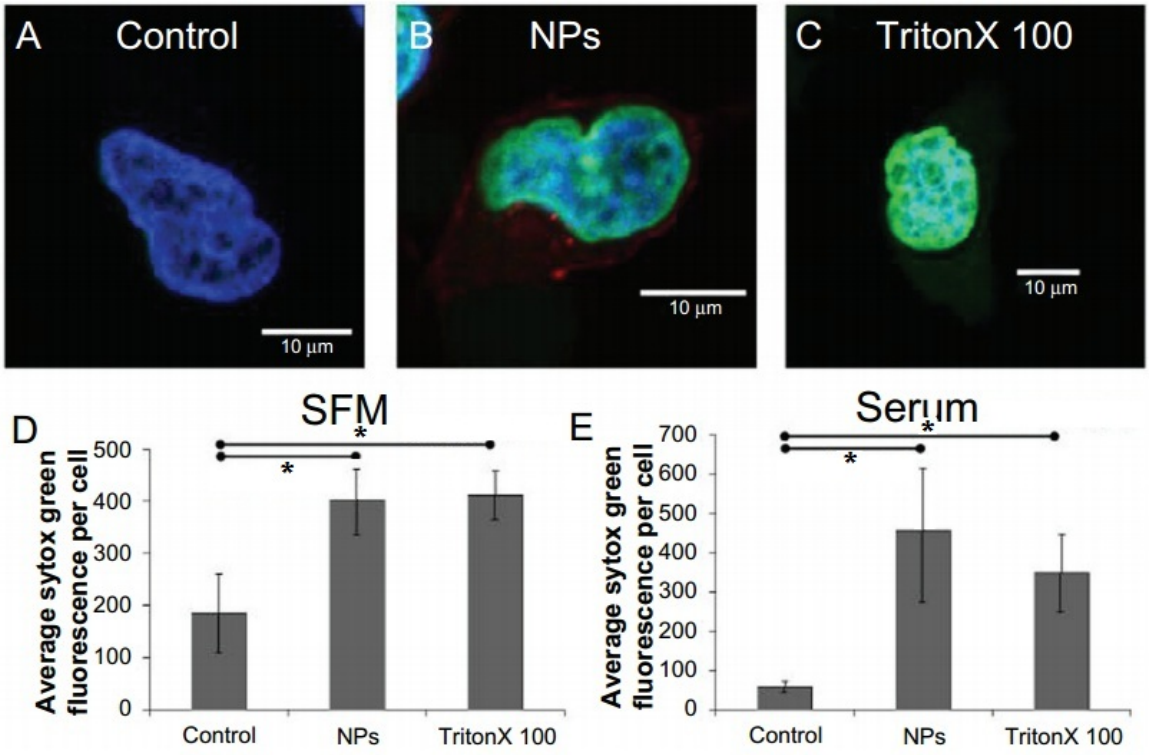

Figure 2.14: *Nanoparticles and detergent permeabililse cell membranes to a similar extent. Representative images of a HeLa cell incubated with A) Sytox Green only, B) Sytox Green and nanoparticles, and C) Sytox Green and Triton X-100 in serum-free media at 4°C. D) displays levels of Sytox Green fluorescence within serum-free media. There was a statistically significant difference between groups as determined by one-way ANOVA* ($F(2, 25) = 4.40, p = 0.023$). *E) displays levels of Sytox Green fluorescence within serum-containing media. There was a statistically significant difference between groups as determined by one-way ANOVA* ($F(2, 23) = 7.15, p = 0.0038$). *In images, blue channel shows DAPI nuclear stain, green channel shows Sytox Green nuclear stain, and red channel shows nanoparticles. Significant Bonferroni corrected* p*-values indicated were calculated via post hoc t-test. Number of experiments* n *= 3, number of cells analysed per experiment = 10.*

These experiments were repeated at 37°C to see whether cooling the cells had an effect on the nanoparticles' ability to permeabilise the cell membrane. Cells were incubated with Sytox Green as before alongside either nanoparticles, detergent, or nothing else added as a control. It was hypothesised that the detergent would permeabilise the membrane as before, and high levels of fluorescence in the nucleus would be seen. However, due to the changes made to the recommended manufacturer's protocol, results concerning the negative control and nanoparticle experiments may be higher than previously observed. Results from these experiments can be seen alongside the 4°C data in Figure 2.15.

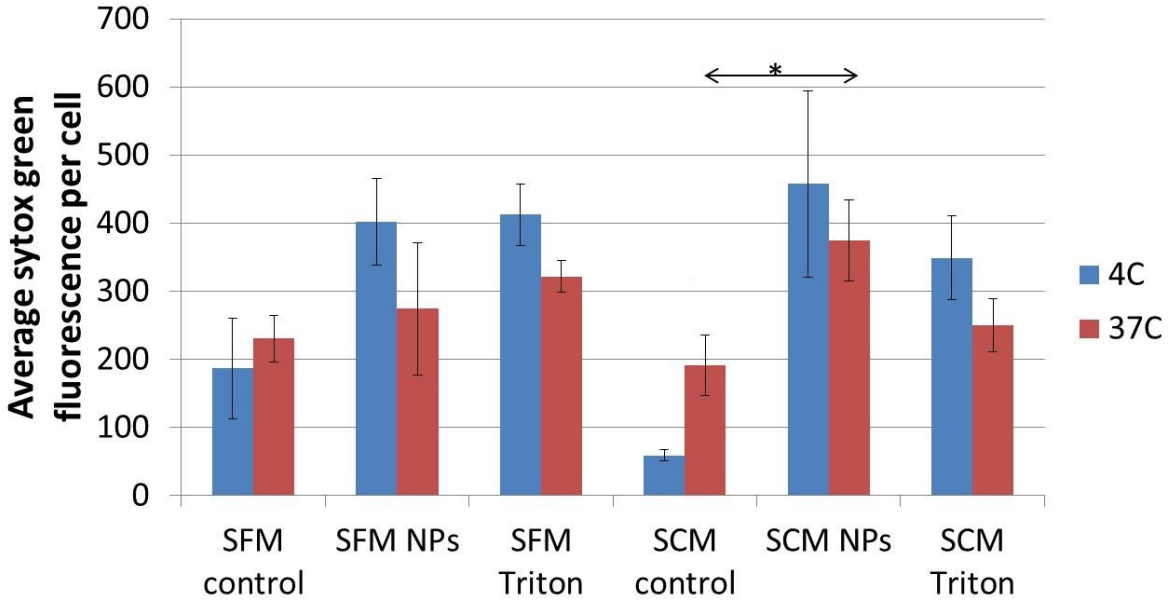

Figure 2.15: *Membrane permeabilisation by nanoparticles at 37°C. Data is shown next to the 4°C data shown in Figure 2.14. Similar trends can be seen as in the previous data; control values for Sytox Green fluorescence were lowest, and once more Sytox fluorescence from conditions where nanoparticles were present were equal to, or greater than those seen when a detergent was present. Levels of Sytox Green fluorescence within serum-free media at 37°C indicated no statistically significant difference between group means as determined by one-way ANOVA* ($F(2, 27) = 0.55, p = 0.58$). *Levels of Sytox Green fluorescence within serum-containing media indicated a statistically significant difference between groups as determined by one-way ANOVA* ($F(2, 27) = 3.74, p = 0.37$). *The only significant result not previously indicated was between the control and nanoparticle containing conditions in serum containing media at 37°C. Significant Bonferroni corrected* p*-values indicated were calculated via post hoc t-test. Number of experiments* n *= 3, number of cells analysed per experiment = 10.*

Figure 2.15 shows direct comparison between Sytox green fluorescence from cells incubated with nanoparticles, Triton X-100, and plain controls at 4°C and 37°C. Similar trends are seen in both cases, with both nanoparticles and the detergent permeating the cell membrane to the extent where Sytox Green fluorescence can be seen in the nucleus. Results were only significant when comparing nanoparticles and the negative control in serum containing conditions. It was also seen that there are higher levels of Sytox Green entry at 37°C than at 4°C in serum containing medium in the negative control. This can be explained by our necessary changes to the protocol. At 37°C, the cell is undergoing normal processes, including endocytosis. If the Sytox Green is entering the cell via this route, then that would explain why there is not a significant difference in fluorescence when compared to the scenario where detergent is present. This would explain why the experiment at 4°C worked, and results are meaningful.

It is important to be aware that serum starvation and stimulation is often used to trigger cell signalling, for example of Rho family GTPases[200]. This is due in part to negative feedback mechanisms within the cell which downregulate signalling from constant stimulation from the medium in which cells are incubated[201]. Serum starving ablates this negative feedback and allows observation of robust signalling responses [202]. The process of serum starvation could therefore affect the observed results in Figures 2.7, 2.8, 2.10, 2.11, 2.13, 2.14, 2.15. However, cells traditionally need between 8 and 24 hours to metabolise constituents in serum containing media[203], and so the 15 minutes employed in these experiments should not affect cells to any significant degree[204].

The presence or absence of serum can also result in different levels of cell stimulation, which could affect nanoparticle uptake. Serum contains growth factors which are known to cause increases in dorsal ruffles in cells[205], which leads to increased macropinocytosis[92]. Cell stimulation caused by the presence of serum has also been shown to increase levels of clathrin mediated endocytosis [206]. This could lead to an increase in the amount of internalised nanoparticles. However, the opposite was observed in this study; a greater

number of nanoparticles were seen to be internalised in conditions free from serum. In future studies the effect of serum stimulated endocytosis will need to be evaluated in greater detail, for example conjugating growth factors onto the nanoparticles before introducing them to cells. This would allow greater understanding as to what factors both promote and inhibit uptake.

2.6 Conclusion

It has been demonstrated that the entry of 20 nm carboxylate-modified polystyrene nanoparticles into HeLa cells is primarily via clathrin mediated endocytosis, with an element of direct membrane permeabilisation. This was determined through the use of dominant negative gene transfections and cooling to 4°C, which prevented clathrin-mediated and caveolar, or all routes of endocytic entry respectively. Membrane permeabilisation was inferred via the use of Sytox Green, a membrane impermeant fluorophore, which was able to gain entry to the cell interior when nanoparticles were present.

The extent to which nanoparticles are able to gain entry to the interior of the cell is reduced by the presence of serum proteins. These form a corona around the nanoparticle, which does not affect their size, aggregation or florescence intensity, but does reduce the magnitude of the particle's zeta potential. This reduces their affinity for the plasma membrane, as observed in fluorescence plate reader experiments. These showed between a 5- and 20-fold decrease in the cellular associated fluorescence when serum proteins were present, depending on incubation times, as opposed to serum-free conditions. Confocal microscopy studies showed that this resulted in a two-fold reduced uptake when looking at internal cellular fluorescence. When comparing the total number of nanoparticle accumulations however, there was no difference in the two conditions. This indicates that this increased nonspecific binding in serum-free conditions allows for significantly more particles to enter the cell.

With the increased production of nanoparticles comes a greater potential for human exposure, whether deliberate or accidental. While in a majority of cases extensive studies are done on these particles before they enter our daily lives, it is clear that it is currently not possible to characterise fully a nanoparticle's behaviour in all situations and environments. The sheer volume of variations in nanoparticle composition, size and surface chemistry, nature of cells- both human and environmental- and the vast array of suspending media and corresponding proteins associated for nanoparticles to come into contact with renders full nanoparticle characterisation in all scenarios non-trivial.

While we have examined the route of entry for 20 nm carboxylate-modified polystyrene beads into HeLa cells with and without traditional serum proteins, this process needs to be accelerated in order to cover the vast and ever-changing conditions of this rapidly expanding field. A standardised and streamlined method for nanoparticle characterisation would enable faster, direct comparison between changes in the many variables associated with this area of study.

To this end, there are three areas that can be improved upon to generate more suitable methods of nanoparticle characterisation. Firstly, the image processing and data analysis. This is all currently done completely by hand, which is not only very time consuming, but the results also inevitably vary from person to person. Automating the nanoparticle spot detection process computationally would not only provide much more accurate, reproducible analysis of images, but also decrease the time it takes to complete. Secondly, biological assays can be improved. There are currently no protocols that allow study of nanoparticle uptake via TIRF microscopy. This technique would allow a more detailed view of what was occurring at the plasma membrane than confocal microscopy. Finally, if TIRF microscopy was possible, then modifications to this technique to observe nanoparticle-induced membrane deformation or permeabilisation would enable quantifiable information to be gained, and in fewer experiments than is currently possible. These issues will be addressed, with solutions offered, in the following chapters.

CHAPTER 3

DEVELOPMENT OF NEW COMPUTATIONAL METHODS FOR THE ANALYSIS OF NANOPARTICLE UPTAKE

3.1 Overview

In Chapter 2 it was established that 20 nm carboxylate- modified polystyrene beads enter HeLa cells through a combination of clathrin mediated endocytosis and direct plasma membrane permeabilisation. This work involved extensive time-consuming manual image analysis. This Chapter looks at existing methods for computational analysis of spot detection and colocalisation within images, and the benefits of adopting such a procedure. Furthermore the development and authentication of a purpose written semi-automated program, resulting in a much reduced analysis time, is outlined in detail.

3.2 Introduction

In cell biology, the location of a protein within a certain subcellular region generally determines its function. Likewise, the destination of a particular cargo determines what effect it has on the cell. Colocalisation studies use information gained from fluorescence microscopy images to understand certain biological processes by looking at the proximity of molecules of interest and well characterised labelled markers within the cell[207].

To understand what effect a nanoparticle will have on a cell once it is internalised, knowing its final location and how it gets there is paramount. To this end, colocalisation experiments are ideal. Many studies have been performed using colocalisation as a tool for determining how and where particles are trafficked within a cell, however these often use very different analysis methods[208, 209, 210, 211]. This highlights the uncertainty concerning the ideal method to use, and renders direct comparison of results from different research groups impossible.

Colocalisation studies and analysis are made especially difficult when considering that for different applications, different techniques may be required (in terms of both biological assay and image acquisition). There is not one program that is able to successfully analyse all possible colocalisation experiments considering the various morphologies in the cell- from linear components of the cytoskeleton, to more complex structures such as the Golgi network, to simple punctate vesicles- any better than specialised programs designed to work for each of those conditions alone. In simplistic circumstances, simply looking at the overlapping pixels may be sufficient, whereas in other conditions more complex solutions are required, looking at the global statistical analysis of pixel intensity distributions[212]. There is also a high dependence on the resolution of the microscope one has access to, and whether partial overlap is sufficient to warrant counting an event as 'colocalised', or whether complete overlap is required.

3.2.1 Requirements

There are several requirements for successful colocalisation studies, which if aren't followed can lead to incorrect conclusions being drawn.

Fluorophores

The choice of fluorophore is especially important when undergoing colocalisation studies. As mentioned in Section 1.3.5, a fluorophore is preferentially excited at a certain wavelength, and emits at a longer wavelength[127]. These values can be visualised in the form of an excitation/ emission spectrum. It is important that the fluorophore combinations chosen for colocalisation studies have distinctively different excitation or emission spectra- or at least that they are known well enough that the necessary precautions can be put in place. Failure to take this into account can lead to both fluorophores being excited by the same light source, or light from both fluorophores detected through the same emission filter[213]. An example of co-excitation can be seen in Figure 3.1.

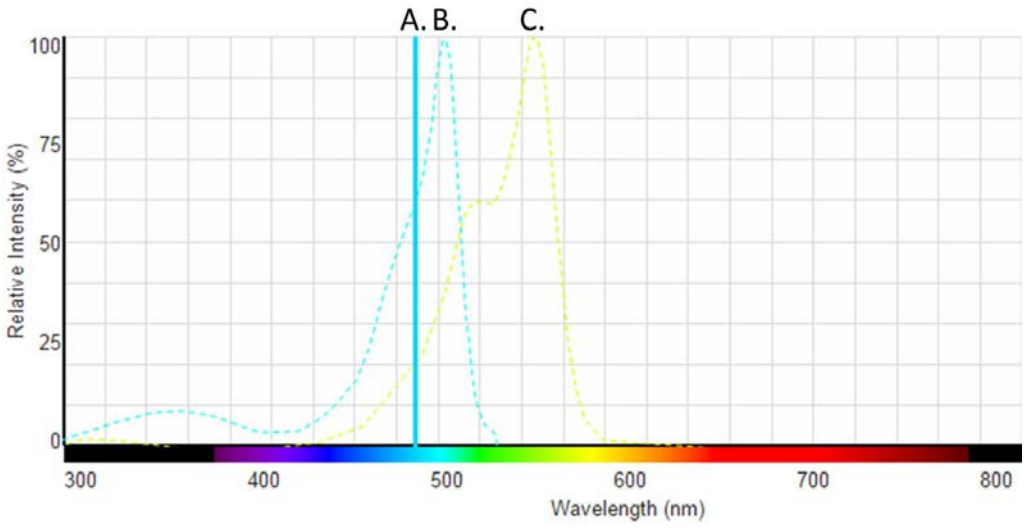

Figure 3.1: *An example of fluorophore co-excitation; two different fluorophores being excited by a single laser. A) Laser excitation at 488 nm. B) Excitation spectrum of the FluoSpheres used in the previous Chapter. C) Excitation spectrum of DiI, a membrane stain used later in this thesis. Although the excitation efficiencies are not the same for each fluorophore, if the correct precautions are not put in place, erroneous data may be obtained.*

Co-excitation occurs when excitation spectra of two different fluorophores overlap, and so can be excited by the same light source. This will cause the belief that a certain tagged component is present when in fact it is not. One way around it is to use laser excitation, where the narrow bandwidth minimises its extent.

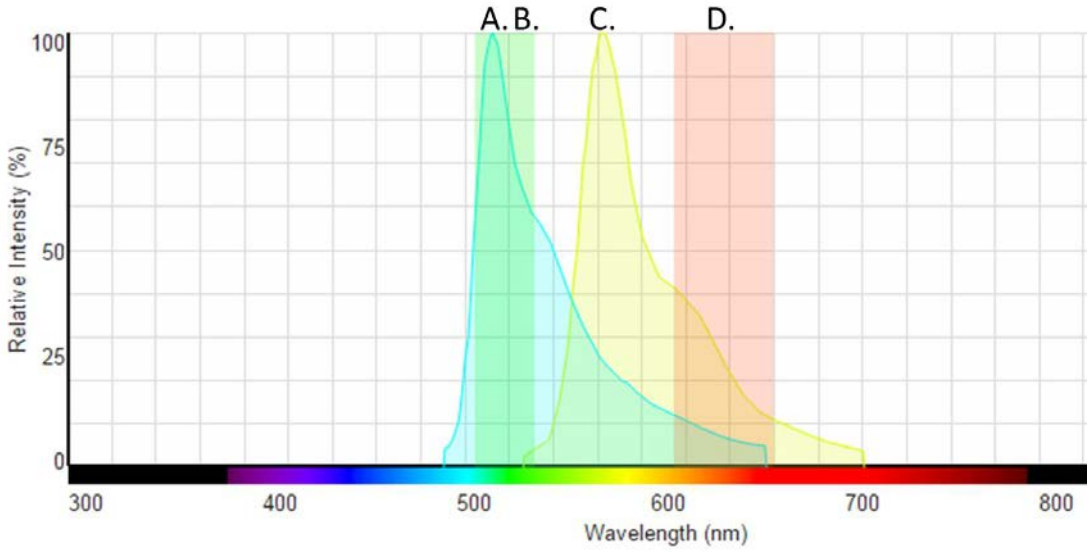

Figure 3.2: *An example of bleedthrough; when the emission spectra of two fluorophores overlap. A) The emission spectrum of the FluoSpheres used in the previous Chapter. B) One of the filters in place in the DualView, an emission splitter used later in this thesis, 520/30. C) The emission spectrum of DiI, a membrane stain used later in this thesis. D) The second of the two filters in place in the DualView, 630/50.*

Bleedthrough is when emission spectra overlap, so in an image it is not possible to know the exact proportion of light from each individual fluorophore. This can again lead to the belief that a certain molecule of interest is present when it in fact is not. Therefore emission filters are used between the sample and the camera to reduce background from unwanted sources[214]. This will mean that even if two different fluorophores are excited by the same laser, only the light from one of them will reach the detector and be recorded. An example of this can be seen in Figure 3.2, where both fluorophores can be excited by a laser operating at 491 nm, and even with emission filters in place signal from both fluorophores can be detected. In this instance it is necessary to prepare single colour controls of samples.

In some cases co-excitation of fluorophores can prove to be beneficial. For example with an emission splitter system in place (see Section 4.4.7), images of two different fluorophores can be obtained at once, halving the amount of laser exposure time and reducing the risk of photodamage[215]. Bleedthrough, as visualised in Figure 3.2, requires more preparation to work around. In an ideal scenario, a different fluorophore would be used instead. However this is not always possible. Single colour controls have to be made, samples that are identical in every way to the experiment containing both fluorophores, but with only one or the other present. In this way, the sample can be illuminated with settings for fluorophore A, for example, but with only fluorophore B present. If no signal can be seen then it is possible to be confident that when both fluorophores are present, when illuminating with setting for fluorophore A, none of the resultant signal is emanating from fluorophore B. It is also necessary to have completely unstained samples, to ensure there is no background autofluorescence that may interfere with the interpretation of results[216].

Microscopes

Along with confirming the fluorophores chosen have sufficiently separate spectral properties and there is no discernible autofluorescence, co-excitation or bleedthrough with the unstained or single colour controls, there are properties of the microscope that have to be optimised for reliable and accurate data suitable for colocalisation analysis.

As discussed in Section 1.3.3, due to dispersion, a standard objective lens can lead to errors in analysis of images. This is because coloured light from a single source will be in focus in different z-planes. The use of plan apochromatic objective lenses reduces this chromatic shift and prevents dispersion of photons of different wavelengths[217].

For fixed samples, sequential acquisition of colours helps to minimise any potential inaccuracies arising from co-excitation of fluorophores. This may not be suitable for live samples however, as these could move between acquisitions. For live samples or scenarios which require rapid acquisition of images it is necessary for the use of a dual colour imaging system which features a beamsplitter in the emission optics to separate the two wavelengths from the fluorescent probes. This allows much more rapid imaging and incorporates emission filters which reduces bleedthrough of light[218].

Although avoiding saturation of pixels is paramount to obtaining good images, extra care must be taken when performing colocalisation studies as this will affect any analysis done on the images.

The format in which the image is saved will also have an impact on colocalisation analysis. Saving the file as a JPEG, BMP or PICT for example will result in loss of potentially relevant data. A non-lossy format such as a TIFF file must be chosen instead[207].

Image registration is another area which needs to be taken into account when performing colocalisation analysis. The correct aligning of multiple colour channels or modes of image acquisition in terms of scale, translation and rotation has to be accurate to acquire precise values for levels of colocalisation. A slight misalignment in image channels can result in a value for colocalisation being obtained that is low, or nonexistent. One way of ensuring accurate registration is to use diffraction limited fiducial markers, for example fluorescent nanoparticles that can be detected in more than one imaging channel. By taking images over the whole field of view, control points can be determined and a mapping calculated. This can then be used on future data sets to map points acquired in one imaging channel directly onto another. This technique can be implemented using MatLab's image processing toolbox[219].

3.2.2 Existing Techniques

There exist many ways of determining whether colocalisation occurs within an image, and to what extent. These range from subjective to calculated, and vary in their relevance to each individual case. This section evaluates the most common, and suggests why a new technique is needed when considering nanoparticles in particular.

Subjective analysis

Subjective identification of colocalisation between two probes can be determined by the appearance of a colour change when two existing images of probes are superimposed. This is traditionally shown by the appearance of yellow pixels upon the merge of red and green images. This poses a problem for those that are colourblind of course, but is dependent on both of the probes exhibiting similar intensities. This renders this method useful only in instances where the fluorescence of the two probes occurs in nearly equal proportions.

A more reliable method is to show the two images side-by-side with arrows pointing to the probe of interest in the first, and duplicating these in the second. While this eliminates the problems associated with overlaying the images, it still offers no quantifiable solution to the problem of defining colocalisation.

Manual analysis

The most common form of quantitatively calculating the extent of colocalisation between two fluorophores is by manually analysing the data in question. Typically the probes of interest are identified and highlighted in one of the colour channels, and these co-ordinates are examined in the other channel to determine the amount of overlap. Factors such as size, fluorescence intensity, and number of these areas are used to give quantifiable information about probes present. The advantage manual analysis of data has over computational methods is the ability of people to distinguish between actual fluorescent

signal and noise within an image. This could be salt-and-pepper, gaussian or shot noise. Dealing with noise has always been an issue for computational methods of determining colocalisation, with techniques ranging from filters to wavelet transforms and probabilistic neural networks having varying degrees of success[220, 221]. However, when considering the speed at which a computer program can analyse image data, computational methods are necessary for large data, high throughput experiments. With multiple cells analysed per experiment, and repeats needed for validation, it can take days to manually analyse the results of a single experiment. This can result in either fatigue related errors, or 'user bias' where points that support the hypothesis in question are preferentially selected[222]. An automated way of determining colocalisation values is necessary, for both replication of results and feasibility in regards to time when considering the volume of raw data.

There exist a number of existing computational techniques designed for evaluating the level of colocalisation between two fluorescent probes. These differ significantly in approach and relevance to certain applications, and will be considered here.

Scatterplots

A scatterplot offers a relatively simple graphical way of representing results of fluorescence colocalisation studies. The intensity of one colour is plotted against the intensity of the second colour on a pixel-by-pixel basis. This results in the points clustering around a line for positive colocalisation between the two fluorescent markers. Examples of both this and when there is no correlation can be seen in Figure 3.3.

While scatterplots offer an indication of the degree of colocalisation, they are not useful for comparing the extent of colocalisation in different experimental conditions, or distinguishing actual colocalisation from random coincidence[224]. Other methods to quantify the extent of colocalisation are much more useful.

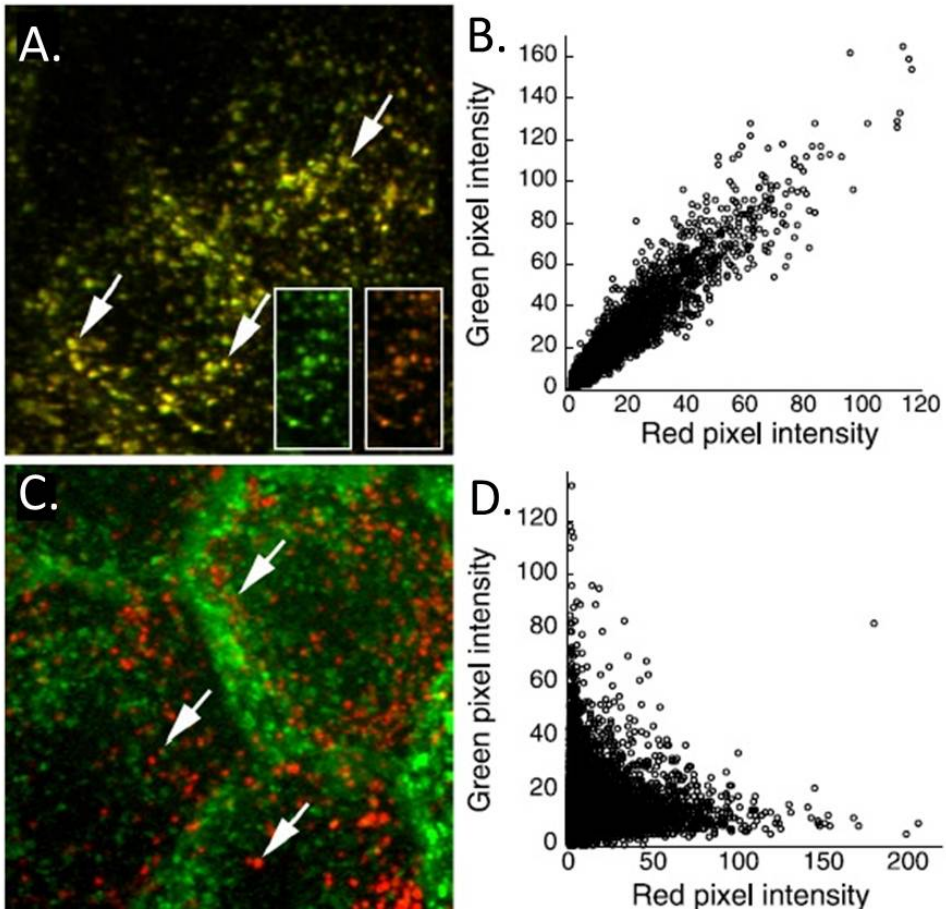

Figure 3.3: *Colocalisation analysis of endocytic probes. A) Madin Derby Canine Kidney (MDCK) cells incubated with transferrin conjugated to both Alexa 488 and Texas Red. B) A scatterplot of the red and green intensities from the image in A. The points cluster around a line characteristic of colocalised pixel intensites. C) MDCK cells incubated in both Alexa 488-transferrin and Texas Red-dextran. D) A scatterplot of the red and green intensities from the image in C. High values in one channel corresponding with low values in the other indicate a lack of colocalisation. Adapted from [223].*

Pearson's correlation coefficient

The use of scatterplots suggests Pearson's correlation coefficient (PCC) would be a useful measure of quantifying colocalisation between different colours in an image[225]. PCC measures the amount of linear dependence between two variables, in this case the intensities of pixels in two colour channels. The value varies between -1 for complete negative dependence, 0 for no correlation, and +1 for total positive dependence. The method for calculating the PCC between two variables can be seen in Equation 3.1.

$$PCC = \frac{\Sigma_i(R_i - \bar{R}) \times (G_i - \bar{G})}{\sqrt{\Sigma_i(R_i - \bar{R})^2 \times \Sigma_i(G_i - \bar{G})^2}} \tag{3.1}$$

where R_i and G_i are the i^{th} pixel intensity values in the red and green channels respectively, and $\bar{R}$ and $\bar{G}$ are the mean intensity values of the entire red and green images. For example, the PCC values in Figure 3.3 B and 3.3 D are 0.944 and -0.045 respectively.

PCC as a tool for quantification is simple, fast, and is free from user bias. As the mean intensity is subtracted from each individual pixel value, this technique is independent of signal levels and background noise. However, while extreme values are easy to interpret, intermediate values are more ambiguous, except when used in comparative studies. This is because the magnitude of the PCC is generally taken to be r^2, giving a magnitude of between 0 and 1. The result of this is that half of the possible values for the PCC are contained within 25% of the range of values for r^2 ($-0.5 < r < 0.5 \mapsto 0 < r^2 < 0.25$).

Additionally, when using freely available analysis software, the whole image is generally used for measurement. However, a region of interest (ROI) should be drawn around the cell so as not to depress the degree of correlation, either from the background or from multiple cells expressing different overall intensity values. It should also be noted that this method does not work if a simple linear relationship is not expected. If one fluorophore is present in multiple areas while the other is confined to fewer, a much lower value for PCC is obtained. While this can be overcome by only looking at pixels which contain both fluorophores, this eliminates all analysis of negative correlation, which is just as useful as positive correlation[207]. This also raises the issue of distinguishing signal from background noise. This is not a trivial process, but will be addressed later.

Manders overlap coefficient

The Manders overlap coefficient (MOC) is related to the PCC, but doesn't subtract the mean signal at all, eliminating negative values. The calculation can be seen in Equation 3.2:

$$MOC = \frac{\Sigma_i(R_i \times G_i)}{\sqrt{\Sigma_i R_i^2 \times \Sigma_i G_i^2}} \tag{3.2}$$

While eliminating negative values makes the result less confusing, it does have consequences which make the MOC undesirable as a method of quantifying colocalisation[226]. This is due to the fact that the MOC does not take into account signal proportionality, only co-occurrence of pixels with positive values in both channels. This is completely independent of signal values. An example where the MOC fails as a useful indicator of colocalisation can be seen in the scatterplots in Figure 3.4. While 3.4 A and B have high magnitude values for both the PCC and MOC, 3.4 C has a very low value for the PCC, but a very high value for the MOC.

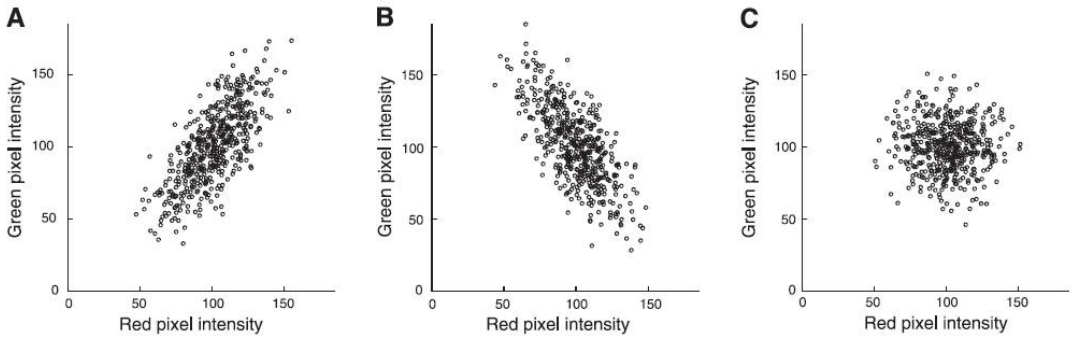

Figure 3.4: *Three scatterplots useful for comparing Pearsons correlation coefficient (PCC) to Manders overlap coefficient (MOC). A) Overall positive correlation: PCC = 0.73, MOC = 0.99. B) Overall negative correlation. PCC = -0.71, MOC = 0.92. C) No correlation. PCC = -0.03, MOC = 0.97. Adapted from [223].*

Rather than study the co-occurence of two probes it is typically much more biologically relevant to look at the fraction of one probe that is coincident with the second.

Fractional overlap

Typically in cell biology one wishes to know the extent of how much one probe interacts with another, not the amount of co-occurrence of both. To this end, Manders' correlation coefficients (MCC) can be calculated[227]. These give values for the fraction of fluorophore 1 (R) present in compartments containing fluorophore 2 (G) and *vice versa*. These are calculated as:

$$M_1 = \frac{\Sigma_i R_{i,colocal}}{\Sigma_i R_i} \tag{3.3}$$

where $R_{i,colocal} = R_i$ if $G_i > 0$ and $R_{i,colocal} = 0$ if $G_i = 0$. M_2, which calculates the fraction of G in compartments containing R is calculated in the same way with the pixel values reversed.

While this gives an intuitive and biologically relevant value for the colocalisation of probes, this method relies on having no background fluorescence at all, as seen in the numerator of Equation 3.3. This raises problems, as the combination of out of focus light, autofluorescence, light leakage into the system and non specific labelling render the vast majority of pixels in an image non-zero. This requires post-processing to be performed on an image before MCC can be calculated. In most cases, simple thresholding of an image is very sensitive to the value chosen, and introduces user bias into the calculation. An automated method for selecting threshold values is therefore much more robust and relevant.

Thresholding

Costes One way of automatically thresholding an image is using the Costes method[212]. This works by calculating the PCC for all pixels, and works down the intensity values for each colour down the regression line while the value is greater than or equal to zero. Once zero is reached, any pixels still remaining are counted as background, *i.e.* the red and green values at this point are used as the threshold values. MCC is then calculated for these remaining 'colocal' pixels. This process can be visualised in Figure 3.5.

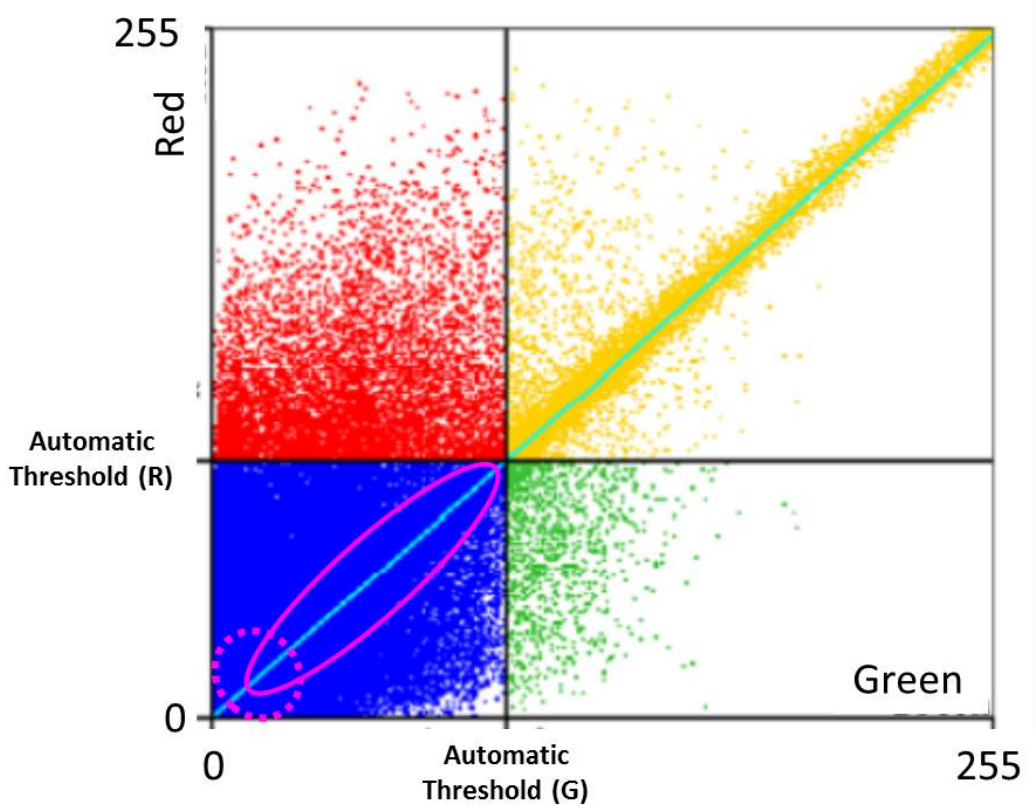

Figure 3.5: *An illustration of Coste's method of thresholding. The line of best fit (cyan) is calculated using linear least-square fit of the two intensities. Following this, intensity values starting at the maximum are used to calculate the PCC. These intensity values are then reduced incrementally until the PCC equals zero. These values are used for the automatic threshold values. Points shown in yellow are considered colocalised. Some pixels are still colocalised, as shown in the pink oval. However as they get dimmer it becomes harder to distinguish them from background noise, as shown in the dotted pink circle. Adapted from [212].*

This method is reproducible, simple to implement, and eliminates user bias. It has been shown to work successfully, and has been widely applied to studies in cell biology[228, 229]. However, there are limitations to this technique for automatic thresholding. It has been shown that in cases of very high labelling density or large differences in the quantity of cellular compartments labelled it can fail to find a suitable threshold[230]. It is also not optimal for images with low signal-to-noise ratios, where it identifies a value for the threshold that is far too low as to be useful for quantifying the data. It is possible in these cases to manually select regions of the regression used to identify thresholds, however this once again introduces the possibility for user bias. This method is also unsuitable for images in which there is spatial variation in the levels of background fluorescence, a problem to be addressed later.

Otsu's method Another way of thresholding an image so it is suitable for colocalisation analysis is Otsu's method. This is a clustering-based image thresholding technique used to binarize a greyscale image. It does this by assuming the image contains two classes of pixels, the signal fluorescence and background noise, *i.e.* that the histogram is bi-modal. It then maximises the variance between these two presupposed clusters. Using this technique makes it possible to discount the background pixels and use only those considered signal in the analysis. An example can be seen in Figure 3.6C.

Otsu's method has successfully been used for thresholding images prior to colocalisation analysis. It has been demonstrated in a wide range of conditions including studying healthy and compromised bacteria[231], mitochondria between frames in time lapse images[232], and Rab5 colocalisation with Pten within endosomes[233].

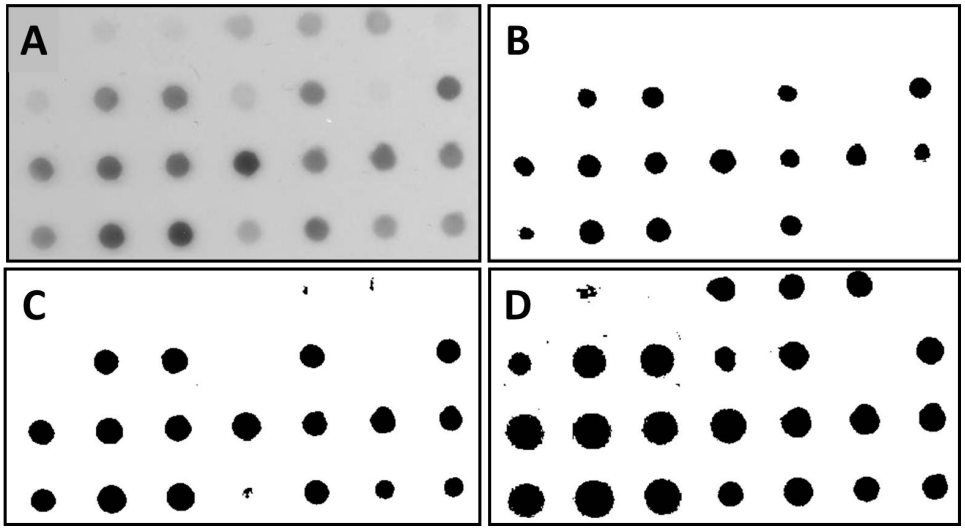

Figure 3.6: *The effect choice of threshold value can have on an image. A shows the original image ("Dot_Blot.jpg", taken from the sample folder in ImageJ). C shows the image after being thresholded using the value gained from Otsu's method. Images B and D show the image using threshold values 10% above and below the value gained from Otsu's method. There is a compromise between selecting as many points as possible without including erroneous data points. If manually selecting a threshold value, all of these positions have merit for being chosen, and would depend on the individual.*

While Otsu's method is fast and easy to implement, it does not, for example, take into account potential variations in background intensities. Another shortcoming, as with the other methods examined thus far, is that it neglects accounting for the spatial distribution of pixels in the image. A more reliable technique when considering biological applications would incorporate some sort of object based thresholding process.

Object-based analysis

All the methods reviewed so far calculate colocalisation or suitable threshold levels on a pixel-by-pixel basis. This does not take into account at all the fact that what is being analysed is part of a unique structure, and thus is highly susceptible to noise in both colour channels. A more biologically relevant way of analysing images when looking at colocalisation within fluorescence images is by considering structures in three dimensions, and taking into account the optical distortion introduced by the microscope. This is known as object-based analysis.

One way of doing this involves manually identifying the structures. Plotting fluorescence intensity curves of the structures makes it possible to discern biologically relevant details in the image from background noise[234]. This technique has been successfully used to quantify the colocalisation of pre-vacuolar compartments with Golgi stacks. While this method is generally more reliable than merely considering fluorescence intensity in images on a pixel-by-pixel basis, it requires manual input which can introduce user error, and can also be very time consuming.

A much better way to perform object-based analysis is by performing morphological operations to segment the structures of interest within an image. Many ways of doing this have been tried, usually through delineation of each structure through edge-detection software, for example Sobel or Laplacian filters[235, 236], followed by basic morphological operations. A slightly different approach commonly used where the structures being studied are of a similar shape and size is the top hat filter[237]. This uses a pre-determined 'structuring element' to identify the required cellular compartments. The effect of applying this on the image seen earlier shows both its usefulness and limitations, as demonstrated in Figure 3.7. If structures are still not completely separated, a watershed filter is commonly used to identify common boundaries between objects[238]. This is where edges are determined by identifying local minima in an image, analogous to catchment basins within height maps.

Once the structures in an image have been singled out and separated, a three dimensional centroid detection algorithm can position each of the elements. Either this, or the centre of intensity for each of the volumes can be used. These coordinates will be the same if the structures are below the resolution limit, or are homogeneously fluorescent. This will depend on the subcellular compartment of interest, and will need to be determined in individual cases. Structures can be considered colocalised if the distance between centroids in each colour channel are below the resolution limit, as has been displayed with the golgi association of AtPIN1[239]; or if the centres of intensities display this property, observed

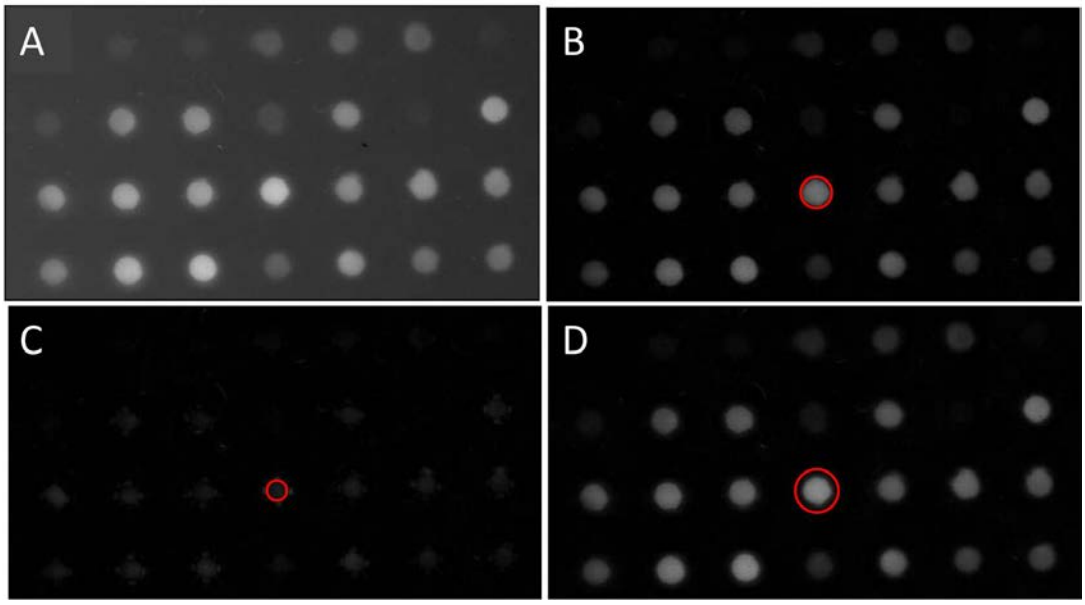

Figure 3.7: *An illustration of the top hat method of thresholding. A shows the same image used in Figure 3.6A, with the values inverted so as to better highlight the effects of the filter. B shows the result of applying a disc shaped structuring element of radius 15 pixels (in red). C and D have used disc shaped structuring elements of radii 10 and 20 pixels respectively. This shows that an appropriate choice of structuring element can do a very good job of highlighting desired elements within an image, and eliminating background noise. However, if the wrong choice is made, or if the required structures in an image have different sizes or shapes, this method would not be suitable.*

when studying formation of membrane proteins in mammalian cells[240]. It is common to specify a fraction of overlap, over which the two objects are considered colocalised[241]. This is to determine whether the two objects of interest are close enough to each other so as to be able to interact[242].

While object-based colocalisation methods are generally much more robust than pixel-based approaches, there are still shortcomings of the approach. Images with high amounts of noise are still susceptible to incorrect quantification, such as those in high speed time-lapse studies of vesicle tracking. The top hat filter tends to underestimate the amount of colocalisation in an image due to its rigid adherence to detection of predefined structures only. The watershed transform is particularly susceptible to noise and highlights inconsistencies in illumination, and attempts to counteract this tend to result in over-segmentation. It should also be noted that use of centres of intensity or centroids of

segmented objects results in a massive underestimation of colocalisation if the structures in question are larger than the optical resolution limit[207]. This can be overcome by looking at overlap of the centroid of one of the fluorophores in question with the entire volume of the other[240], however this still only gives information on one class of structure rather than giving an overall estimate of colocalisation.

More recent advances in the strive for an ideal automated colocalisation program have included probabilistic models for the likelihood of whether a pixel belongs to an object[243] and quantification of random noise and estimations of colocalisation uncertainty[244]. Despite these attempts, a reliable automated colocalisation analysis method for computationally thresholding and segmenting an image is not yet available. This makes comparing results from different research groups impossible. In an attempt to remedy this, a method to standardise colocalisation analysis for biological applications has been developed.

Colocalisation Benchmark Source

The Colocalisation Benchmark Source (CBS) is a collection of free downloadable images designed to help researchers validate the degree of colocalisation of probes in fluorescence microscopy images[245]. They are provided as sets of ten computationally simulated images, ranging from 0% to 90% colocalisation, and the values for PCC, MOC and MCC are provided. The method for generating these images uses a known protein-protein proximity index, described in detail in reference [246]. This allows researchers to compare the values from their images, and provides a way to standardise colocalisation levels over different scenarios[247, 248]. It employs a fuzzy linguistic system model, allowing researchers to state confidently whether the degree of colocalisation is Very Weak, Weak, Moderate, Strong, or Very Strong. This is both easy to understand and makes comparing images from different experiments simple. While quantifiable results are not the outcome of using these images, they do make it easier for researchers to understand and communicate their results.

Of particular interest for this research is the computationally generated data that is provided by this service. Images supplied are independently made and freely provided, with exact colocalisation values known. Use of this to test the development of a new colocalisation method will allow production of reliable and reproducible data.

3.2.3 Noise reduction methods

One way to improve the accuracy of automated methods for determining the extent of colocalisation is via the removal of noise. This allows more accurate analysis by enhancing the features of interest with respect to their surroundings. This is widely performed by convolution of the noisy image with a Gaussian kernel, which has the effect of 'smoothing' the image[249]. While not computationally demanding and easy to implement, this process tends to blur images and as such should not be used in isolation for accurate image analysis.

A more robust method that reliably preserves structure in an image is based on non-local means. The value of a pixel is determined via comparison to all the pixels in the image, weighted by how similar they are to the target pixel. The digital image is then compared to its denoised version, and the difference between the two is modelled on white noise[250]. While effective, this method has a high computational complexity which renders it impractical for processing large image sets.

Some of the most promising methods of noise reduction are based on wavelet transforms[251]. An image is split into different bands based on the frequency of the data it contains. Relevant image information is contained within a few of these, with noise evenly spread throughout[252]. The challenge with this method is determining which planes contain accurate image information, and which can be discarded. Models based on Bayesian statistics which accurately describe the signal and noise components have shown to be successful in this regard[252].

Noise reduction methods were traditionally used in separating signal from noise in astronomy images[253]. These methods were then successfully applied as a preliminary step in spot detection approaches in cell biology[254], prior to signal thresholding and spot classification. A novel approach to spot detection and classification has been published recently[255], the initial step involving an improved method for noise reduction. This has demonstrated both an increase in accuracy and speed. It combines optimal Gaussian filtering, with the standard deviation of the Gaussian kernel matched to the width of the point spread function of the microscope. This enhances the spot-like features in the image while simultaneously suppressing noise. It combines this with an isotropic undecimated wavelet transform, which is well suited to biological images[254]. This effectively removes noise without blurring the image, and eliminates uneven background features. By utilising this novel approach to noise reduction and applying it to established methods of colocalisation calculation it will be possible to acquire much more accurate values.

3.3 Aims and Objectives

The aim of this Chapter is to develop a reliable and fast method for determining the relative colocalisation of two structures of interest within a cell. For the purpose of this thesis, particular attention will be given to fluorescently tagged cargo within vesicles, or proteins associated with vesicles. The process will be automated so as to eliminate user bias or human error from any results. Select parts of a novel algorithm designed for spot detection and classification will be used to denoise images. This process will be combined with current methods for measuring colocalisation. This new method will be applied to both computer generated and manually acquired data, and the results compared to traditional methods.

3.4 Materials and Methods

3.4.1 Determining a suitable threshold value: validation of denoising algorithm

The images used to compare the ability of different methods to find threshold values were of HeLa cells expressing fluorescent Rab5 proteins. Rab5 is responsible for much of the immediate responses to vesicle internalisation[256], and is described along with the method for obtaining the images in Chapter 4. The images exhibit a high level of noise as they are single frames from high-speed timelapse series. This was deliberately chosen to test the limits of the methods studied. All calculations of Otsu's method of thresholding, Sobel filter application, and top hat segmentation were implemented in MatLab version R2014a (8.3.0.532), 64-bit. The novel denoising software[255] was run through ImageJ version 1.49g running Java 1.6.0.24 (Fiji), accessed from MatLab via the Miji command.

3.4.2 Colocalisation program development

The colocalisation program was implemented in MatLab version R2014a (8.3.0.532), 64-bit. Images were required to have either two colour channels, or two colour channels and a brightfield channel, and be of a .tif or .nd2 format (saved as standard by Olympus and Nikon respectively). All images in a specified folder were loaded, and cropped to the outline of the cell area using the brightfield image if it was available. The colour channels were run through the denoising software[255], through ImageJ version 1.49g running Java 1.6.0.24 (Fiji), accessed from MatLab via the Miji command. These were then turned into binary masks via Otsu's method of thresholding and subjected to 'opening', a morphological operation to erode single pixels from the analysis followed by a dilation so larger spots returned to their original size. The two colour channels were then overlaid, and one was chosen to be the focus of the analysis. Intensity centroids of the spots in this channel were determined, and the proportion of these that overlapped with the mask in the second channel was calculated. This value was used as the colocalisation value. Original versions

of this program rotated the second image 180° to calculate a value for random overlap. This was used to calculate the amount of overestimation given by the program, and a correction was built in for this. Full documentation of the final program can be found in Appendix B.

3.4.3 Computationally simulated data for validation

Computationally simulated images and data for validation of the program were obtained from the Colocalisation Benchmark Source, and are freely available at *http://www.colocalization-benchmark.com/*. These images were used to test the new colocalisation program alongside the PCC, MOC and MCC, the values of which were all calculated using the 'Coloc2' plugin from ImageJ version 1.49g running Java 1.6.0.24 (Fiji). Data was plotted in Microsoft Excel, which was used to calculate the trendline for the data given by the program. This was then used (along with the 'random overlap' of 15% gained from the program) to calculate the equation to counter the level of overestimation given by the program.

3.4.4 Experimental data for validation

Experimentally acquired images and data for validation of the program were obtained with permission from Sylwia Jones. All documentation regarding this research can be found in reference [257]. Image sets of both high and low colocalisation were run through the newly recalibrated program and compared to the results gained by hand.

3.5 Results and Discussion

3.5.1 Validation of new noise reduction algorithm

The main problem in trying to quantify colocalisation is a lack of a consistent standard of analysis. While there are many ways of quantifying the colocalisation of two fluorescent probes, there are always scenarios in which they are not relevant, or simply do not work. In a majority of cases, this is due to the signal to noise ratio being too low for computational techniques to automatically threshold. In these cases someone has to intervene, introducing user bias into the process.

To account for the difficulty of automatic computational calculation of a suitable threshold value, or the shortcomings associated with existing segmentation algorithms, this program utilises a new novel de-noising algorithm developed by William Pitkeathly[255] to vastly improve the signal-to-noise ratio before thresholding. This consists of a spot detection framework based on variance stabilisation, optimal matched Gaussian smoothing, and wavelet analysis. This rapidly and consistently separates spot-like features from noisy pixel values and varying background intensity. The effect of this new algorithm can be seen alongside those of Otsu's thresholding, application of a Sobel filter, and top hat segmentation in Figure 3.8. An image displaying a HeLa cell expressing fluorescent Rab5 proteins was selected for this side-by-side comparison. It is a single frame from a high speed time lapse experiment, hence the relatively low signal-to-noise ratio. This was deliberately chosen as a representative image for future experiments looking at tracking of nanoparticles in fast moving vesicles.

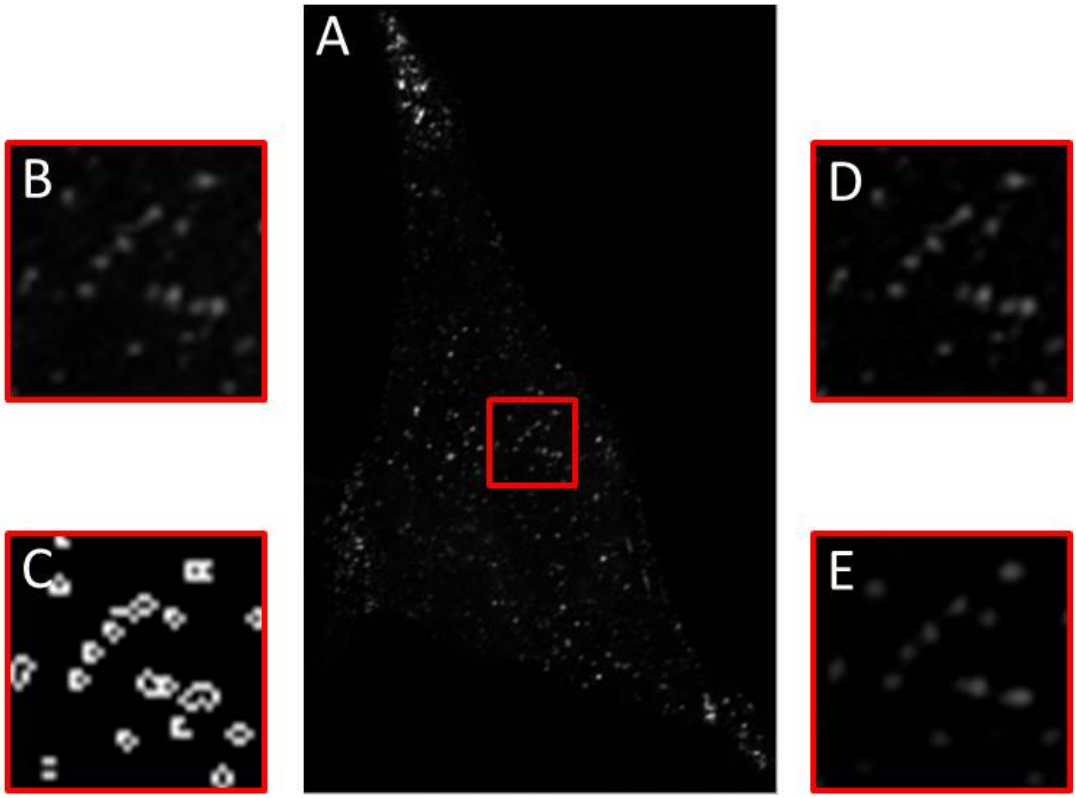

Figure 3.8: *A comparison of de-noising and segmentation algorithms. A) Original noisy image of fluorescent Rab5 proteins in a HeLa cell. B) A magnified copy of the highlighted region in Figure A. C) The result of applying a Sobel filter to the image. The edge detection is effective for spots with clear boundaries, but less so for faint, or multiple close spots. D) The result of applying a top hat filter to the image. It produces a good result in this case, however the structuring element chosen was specific to this image and would have to be optimised for each experimental condition. E) The result of the new novel de-noising algorithm. It can be seen subjectively that the new method is much more effective at noise reduction than the other established methods, and required no additional input.*

When applied to the image in Figure 3.8A, Otsu's thresholding method simply does not work. The whole image is interpreted as background noise, and no signal can be seen. The combination of low intensity levels in the image and poor signal to noise ratio renders this technique inadequate. The levels given by Coste's algorithm gave an identical result, with no features being detected at all. With these being the main methods of image processing for pixel-based colocalisation analysis techniques, it is clear that object based segmentation is necessary for nanoparticle colocalisation analysis in this case.

Edge detection filters such as the Sobel filter in Figure 3.8C were also shown to be inadequate for determining the boundaries of these vesicles. The lack of a distinct edge results from a combination of the small size of these vesicles, and the low exposure time required for imaging at such high speeds.

The top hat filter employed (Figure 3.8D) used a disc shaped structuring element with a radius of 3 pixels. This gave a satisfactory outcome, however the choice of structuring element required for each case has to be manually selected, resulting in a program that is not fully automated. A closer look at the result of applying this filter compared to the new de-noising algorithm can be seen in Figure 3.9.

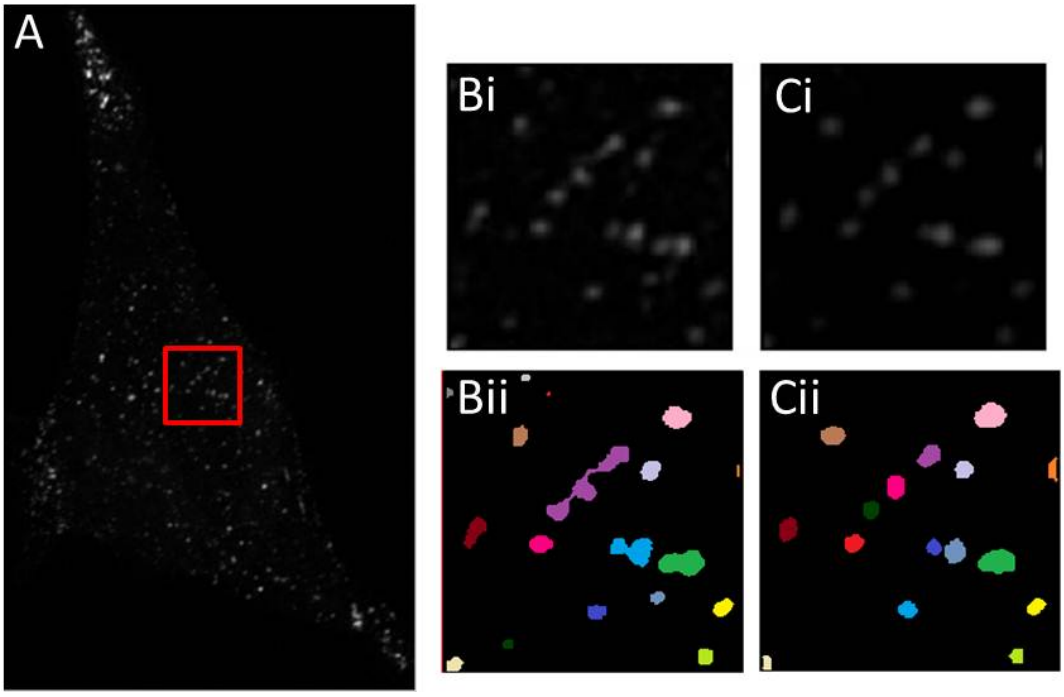

Figure 3.9: *A more in depth comparison of the top hat filter to the new de-noising algorithm on a noisy image of fluorescent Rab5 proteins in a HeLa cell (A). Bi) The highlighted area in A, after application of the top hat filter using a disc shaped structuring element of radius 3. Ci) The highlighted area in A, after application of the new de-noising algorithm. Bii, Cii) The corresponding images after Otsu's method of thresholding. Individual spots have been coloured to indicate separation. It can be seen that the top hat method is inferior to the new de-noising algorithm at separating individual spots.*

Figure 3.9 shows an enhanced comparison between the top hat filter and the new de-noising algorithm. It can be seen that while there is noise reduction associated with the top hat filter, it does not compare to the complete background elimination of the new technique. Colouring of the binary image highlights an inability of the top hat filter to separate distinct spots. The top hat filter regularly provides images that after Otsu thresholding claim 74% fewer vesicles than the new de-noising algorithm ($n = 3$, 10 cells analysed per experiment). This is with a dedicated circular structuring element in place, with a radius of three pixels. This size was selected as most of the observed spots were of this size. A smaller structuring element was tried, which gave a vesicle count of 48% more than the de-noising algorithm. However, inspection of this revealed a high level of noisy pixels being detected, and larger spots being split due to the algorithm fitting smaller spot sizes to what were originally larger vesicles. The new algorithm cleanly and consistently separates stained vesicles. This is seen regardless of size of the structure being analysed. This renders it more consistent and easier to implement than the top hat filter, which requires user input, or any of the other methods traditionally used for processing of images used in colocalisation analysis.

Now that this technique has been validated, it is possible to implement it in a program dedicated to the detection and analysis of colocalisation.

3.5.2 Workflow

Now that a method of improving the signal to noise ratio of fluorescent images has been developed, the process of using this to develop a better colocalisation program can continue. Methods already shown to be effective can be used reliably, but with improved spot detection we can be confident that more reliable results can be obtained.

The general process is described in Figure 3.10. Images of most file types have been shown to work, including those saved as standard by Nikon and Olympus microscopes (.nd2 and .tif respectively). Firstly, the image is cropped to the size of the selected

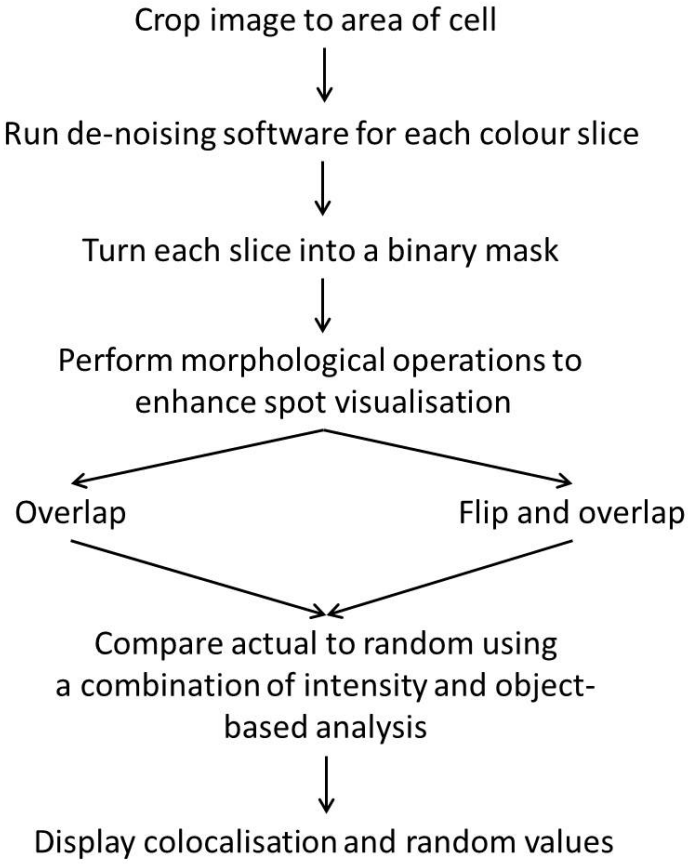

Figure 3.10: *A flow chart showing the sequence of steps undergone by the proposed colocalisation program.*

cell boundary. This is to reduce processing time. Images then undergo the de-noising program. This reliably and effectively reduces noise from images and separates individual spots. Morphological processes such as Otsu thresholding and opening of the subsequent binary mask, which have been shown to be effective in previous methods of colocalisation analysis, are then performed. These masks are then overlaid, and the intensity centroids of the spots in the nanoparticle frame checked to see if they are located within the spots containing the other fluorescent marker. The percentage of those that do is then displayed, alongside a value for random colocalisation. This is calculated by rotating the nanoparticle channel and performing the same calculation. Images showing the step-by-step process are displayed in Figure 3.11.

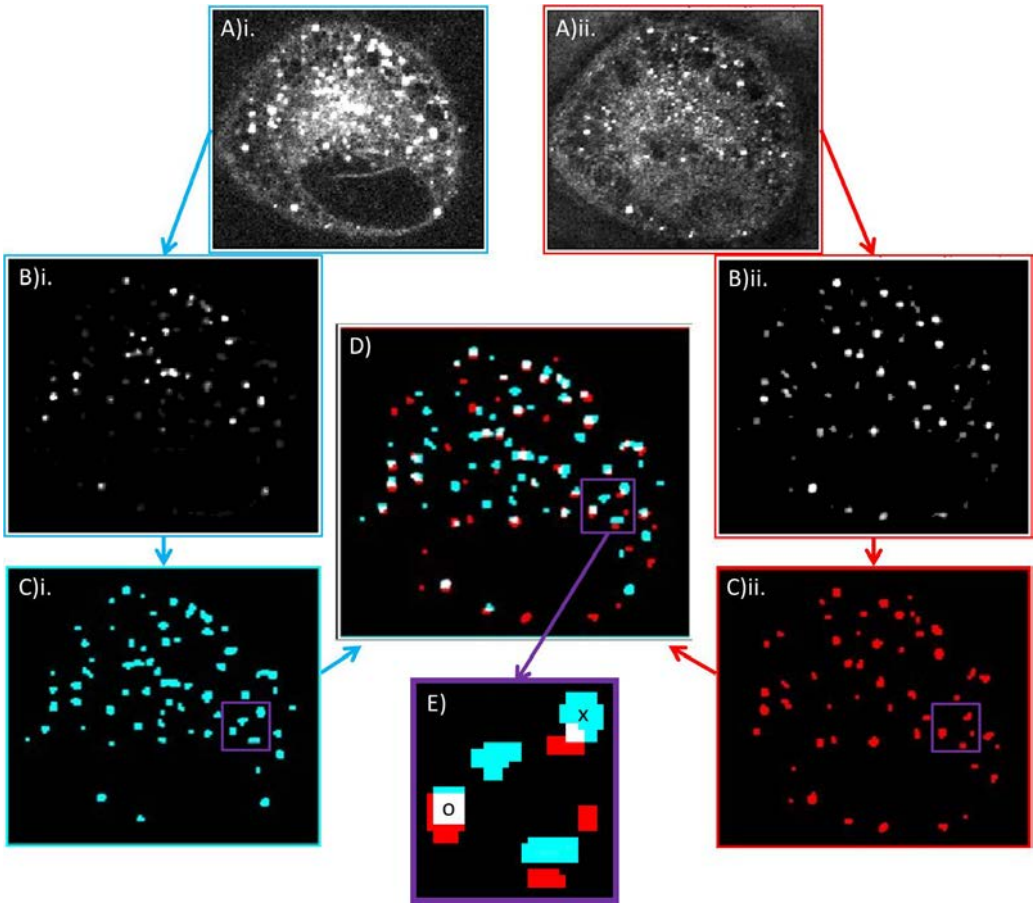

Figure 3.11: *Images showing the steps performed in the colocalisation program. i: nanoparticle channel (cyan borders); ii: DiI channel (red borders). A) The original individual colour channels. B) Cells are identified and images undergo de-noising. C) Binary masks are created from the images. D) Masks are overlaid and the percentage of spots in the nanoparticle frame that significantly overlap with those in the marker channel is calculated. E) extracted section from the image (purple). The left shows two spots that significantly overlap ('o', white). This is counted as a colocalisation event. The centre of the image shows nanoparticle (cyan) and DiI (red) spots that do not colocalise with one another. Top right of the image shows slight overlap (white). However, because the centroid of the nanoparticle spot ('x') is not contained within the DiI spot, this is not counted as a colocalisation event.*

3.5.3 Validation of new colocalisation program

To ensure that the program is working correctly, it has to be tested in situations where the outcome is already known. To this end, tests were done on both the computationally simulated data from the Colocalization Benchmark Source (CBS)[258], and real data that has already been analysed by hand. This is to make sure that when analysis is done on new data, the results obtained by the program can be trusted.

Comparison to simulated data

The ten simulated images provided by the CBS[258] range from 0% to 90% colocalisation. These are provided in several image sets, for comparison to red/ green images, green/ blue images and blue/ red images. They are designed to be compared to experimentally obtained images so that reliable and consistent quantitative data can be acquired. However, for the purpose of validating the program on a series of images of different colours and accurately known qualities, they are invaluable. If the program gives the same values as these images are known to have, this builds confidence that it can give the correct results for images where the values are not known. The program was run on all image sets to ensure maximum validity, and the results are displayed in Figure 3.12.

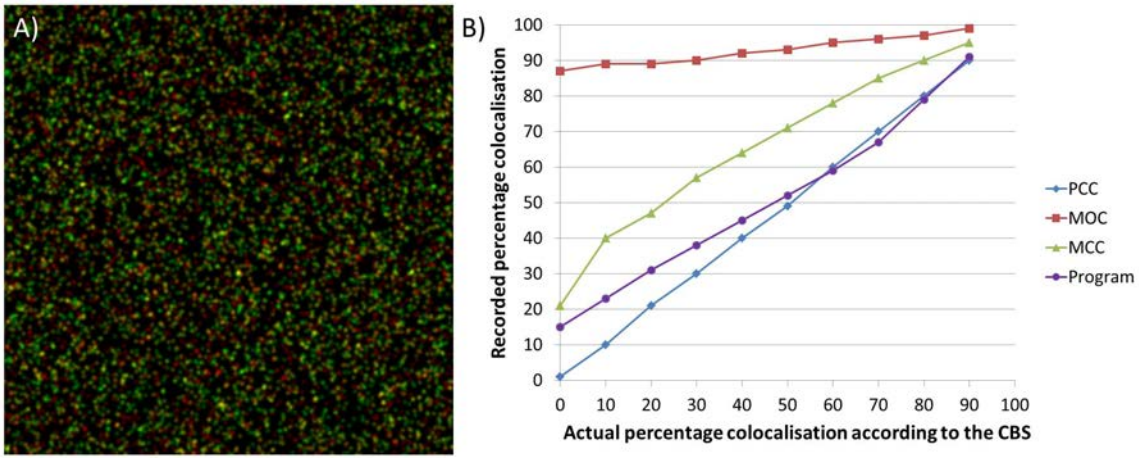

Figure 3.12: *Results from several measures of colocalisation when applied to the simulated images from the Colocalisation Benchmark Source. A) shows an example image from the CBS, of 50% colocalisation between red and green images. B) graphically shows the results of performing Pearson's Correlation Coefficient (blue), Manders Overlap Coefficient (red), Manders Correlation Coefficient (green), and the new program (purple) based on the improved de-noising algorithm described earlier. Each point was calculated from the average of the values obtained from the red/green image, red/blue image, and green/blue image provided by the CBS[258].*

It can be seen in Figure 3.12 that the most accurate method for analysing the colocalisation in the case of these computer generated images is the Pearson's Correlation Coefficient. This is unsurprising, as the method used to generate the images initially was based on this[258]. It does not match precisely to the stated values because of the

synthetic noise added to the images. The Manders Overlap Coefficient and Correlation Coefficients give much higher values than those stated. This is because of the tendency of these methods to overestimate the amount of colocalisation between two variables due to randomly overlapped pixels[246]. It can also be seen that while the new program designed to measure colocalisation gives very accurate results for values above 50%, there is a variable amount of overestimation for lower values. This ranges from 15% at zero, to 5% at 40. One possible explanation for this is the program overestimates at lower values due to noise in the images, which has less of an impact at higher values of colocalisation.

It becomes necessary to counteract this overestimation seen by the program at lower values of colocalisation. A formula can be constructed to map the observed values to what is expected according to the values given by the CBS images. Using the 'plot trendline' function in Microsoft Excel, and fitting the observed trend to a quadratic polynomial gives the equation of the line of best fit as:

$$y = 0.0024x^2 + 0.5889x + 16.7 \tag{3.4}$$

or

$$y = \frac{3}{1250}x^2 + \frac{5889}{10000}x + \frac{167}{10} \tag{3.5}$$

Because we are only interested in values between 0 and 100% colocalisation, Equation 3.5 is a one-to-one function and as a result can be inverted. The coefficient of x^2 must first be taken as a factor and can be moved to the other side of the equation:

$$y = \frac{3}{1250}(x^2 + \frac{1963}{8}x + \frac{20875}{3}) \tag{3.6}$$

so

$$\frac{1250}{3}y = x^2 + \frac{1963}{8}x + \frac{20875}{3} \tag{3.7}$$

It is now possible to complete the square:

$$\frac{1250}{3}y = (x + \frac{1963}{16})^2 - (\frac{1963}{16})^2 + \frac{20875}{3} \tag{3.8}$$

so

$$\frac{1250}{3}y = (x + \frac{1963}{16})^2 - \frac{8093889327}{1000000} \tag{3.9}$$

This can now be rearranged to find x in terms of y, and the mapping from the equation given by the new program to the desired outcome is complete:

$$\sqrt{\frac{1250}{3}y + \frac{8093889327}{1000000}} - \frac{1963}{16} = x \tag{3.10}$$

As the original equation was an approximation of a trendline, and for simplicity and visual clarity, numbers have been rounded to the nearest integer in Equation 3.11. Figure 3.13 shows the effect of applying this mapping to the data obtained in Figure 3.12.

$$\sqrt{417y + 8094} - 123 = x \tag{3.11}$$

The results seen in Figure 3.13 show that the program gives values that are almost identical to those that the images represent according to the CBS. By transforming the data by the function in Equation 3.11, values obtained with colocalisation values above 50% remain largely unchanged, while lower values of colocalisation are compensated for previously observed overestimation. The shortcoming associated with this mapping is that if values under 16.87% (obtained by equating Equation 3.11 to zero and calculating the value of y for which this occurs) are obtained by the program, they will be transformed to a negative number. This shouldn't be seen as a problem however, as this is only the case in images where the true value for colocalisation (according to the CBS data) is very close to zero, as seen in Figure 3.12.

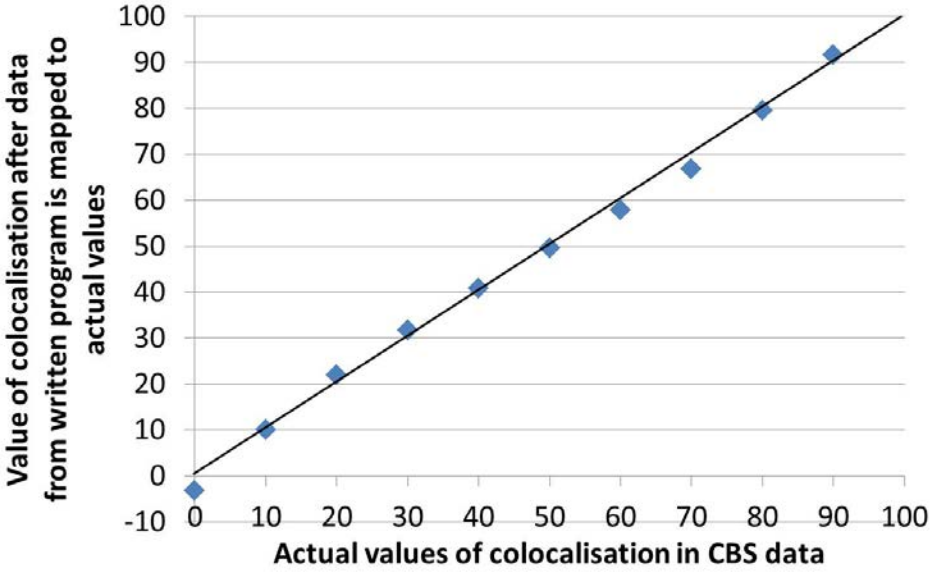

Figure 3.13: *Values obtained from CBS images after transformation by Equation 3.11 (blue). Black line indicates* y = x, i.e. *the line the points should lie on if the precise values are obtained.*

Comparison to human analysis

It can be argued that human interpretation of colocalisation can be open to "experimenter's bias". Results can be skewed by deciding fluorophore proximity is 'close enough' in cases where it suits the hypothesis, and *vice versa*. By computationally analysing data this bias is minimised, with every scenario treated equally. However, in order to further test the program, comparing it to human analysis as a 'ground truth' is another way to ensure accurate results are being obtained. To give added credibility to the following, comparisons with the program were obtained using data not previously quantified by the author. The results shown in Figure 3.14 were gained from images and data kindly provided by Sylwia Jones[257]. Results from six different colocalisation studies were used, covering a range of levels of colocalisation and spot morphology. This included many small points as seen in 3.14B, or fewer larger spots as seen in A and C. T-tests on the data are not significant enough to reject the null hypothesis, *i.e.* it is not possible to distinguish between data acquired by hand and results obtained by the program. This is very promising as it cuts analysis time from days down to minutes, and is consistently

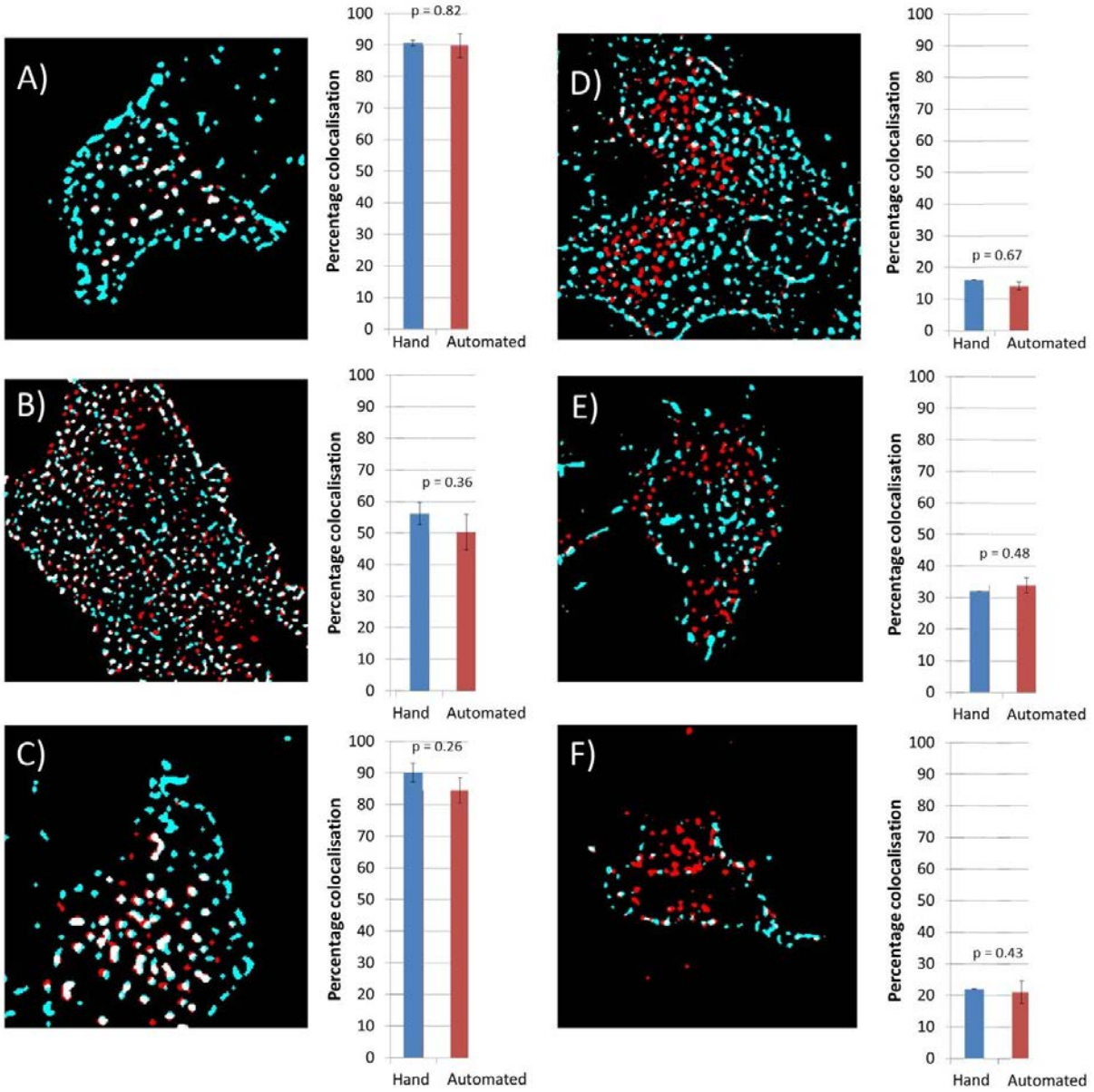

Figure 3.14: *Validation of the proposed colocalisation program when compared to human analysis. In the centre, the graph shows significant similarity between human and automated analysis of six separate biological colocalisation studies, indicating robustness for cases exhibiting both high and low colocalisation. A) mCherry-Ack1 with EGFR-GFP; B) mCherry-Ack1 with p62/SQSTM1; C) mCherry-ΔUBA with EGFR-GFP; D) mCherry-tAck1 with EGFR-GFP; E) mCherry-ΔSrc with EGFR-GFP; F) Clathrin ds-red with EGFR-GFP. Surrounding are representative images of results from the running of the program (Red: mCherry tagged fluorophores in A-E and ds-red in F; Cyan: GFP tagged fluorophores in A and C-F and p62/SQSTM1 in B; White: points of red and cyan colocalisation). Data used for this Figure was obtained with permission from Sylwia Jones [257]. p-values gained via Student's t-test indicate no statistically significant differences so the null hypothesis, that the means of the acquired data sets in each case are similar, stands. 9 cells were analysed in each experiment. Bars show standard error in data.*

replicable. One way to improve the validity of these results would be to perform many more equivalent calculations on a wider range of data from multiple sources. This would reduce further the probability of having made a type II statistical error, and increase confidence that the data provided by the program is reliable.

3.6 Conclusion

It has already been established that with the rapidly increasing field of nanotechnology, more research is needed to ascertain the effects of new nanoparticles at the cellular level. One method to attain this information involves experiments to determine the progression of nanoparticles throughout the live cell cycle. These typically include colocalisation studies, using fluorescently tagged nanoparticles and cell compartments to determine what parts of the cell nanoparticles come into contact with.

With the many different methods for determining colocalisation, direct comparison of results has typically been a challenge. Either computational methods have been used, where the choice of method can depend on the individual experiment or the image acquisition technique. These methods have typically also been heavily susceptible to noise, which can give misleading results. Alternatively, analysis has been done by hand, introducing user error and bias into the process, as well as proving to be time consuming. To this end, a new colocalisation program designed for the detection and colocalisation of nanoparticles with cellular substructures has been realised. It employs a novel noise reduction algorithm which has been shown to be more robust and reliable than existing automated methods. It also gives comparable results to human analysis, but is much faster and free from user bias.

Now that a reliable method for the analysis of nanoparticle colocalisation studies has been realised, research into more effective biological assays in studying nanoparticle uptake into cells can be performed.

CHAPTER 4

EFFECTS OF THE PROTEIN CORONA ON NANOPARTICLE UPTAKE/ DEVELOPMENT OF NEW BIOLOGICAL METHODS FOR ANALYSIS OF NP INTERNALISATION

4.1 Overview

In Chapter 2, it was established that the presence of serum proteins within cell culture media reduced the cellular association of 20 nm carboxylate-modified fluorescent modified beads by up to 20 times relative to those cells incubated in serum-free media. Confocal microscopy analysis revealed that not only the cell surface association of the beads, but also the potential for internalisation is greatly reduced by the presence of serum proteins. However, in both serum-containing and serum-free conditions, internalisation of these nanoparticles was highly dependent on clathrin-mediated endocytosis. Studies on cells at 4°C also revealed a likelihood of plasma membrane permeabilisation being a contributing factor to the presence of intracellular nanoparticle accumulations.

In Chapter 3, a program for performing colocalisation analysis on multichannel images was outlined and validated. This will be utilised in the following Chapter to allow a more thorough range of experiments to be accomplished in a much shorter time frame, and enable a deeper understanding of not only what factors affect the internalisation

of nanoparticles through studies of the protein corona, but also what happens to the nanoparticles once they have been internalised.

All of the studies in Chapter 2 were performed on fixed cells so as to get consistent timings for the image acquisition process. However, when looking at live cells on the microscope other discrepancies arise between those cells incubated in serum-containing and serum-free media. These will be examined in this Chapter. Using the program developed in the previous Chapter it will also be possible to examine the extent of colocalisation with fluorescent markers for various proteins, enabling rapid quantification of the location of nanoparticles under different experimental conditions.

In tandem to this, it would be valuable to know how nanoparticles are interacting with the membrane in terms of the internalisation process. Rather than merely detecting the permeabilisation of the membrane in terms of the presence of Sytox Green fluorescence as performed in Chapter 2, if real time identification of the internalisation of nanoparticles at the cell membrane could be detected, and endocytosis distinguished from direct permeabilisation, then immediate quantification is a possibility. To this end, a novel protocol for using TIRF as a means of studying nanoparticle uptake is established.

4.2 Introduction

4.2.1 Live cell imaging

While there are advantages to imaging of fixed cells, such as the time to maximise resolution and contrast, minimise noise, and the ability to image at room temperature, live cell imaging brings many benefits that justify the added complexity. There are no fixation artefacts when imaging live cells, and it is the only way of recording real time sequential events such as cell migration. Dynamic processes, for example microtubule turnover can be recorded, and sensitive processes such as monitoring of ion gradients and membrane potential is possible. When considering nanoparticle uptake and trafficking, live cell imaging provides an opportunity to identify differences in dynamics that wouldn't have been noticed in studies involving fixed cells, such as motility discrepancies.

Live cell imaging has been used extensively in the study of nanoparticle uptake[259, 260, 261, 262]. These include both studying the uptake of nanoparticles themselves, or using fluorescent nanoparticles as tags to track other molecules of interest. One thing that is clear from all studies is that there is no way of knowing how a cell will react to a nanoparticle before they are introduced, and even then the results can be disputed[181]. The need for a more rapid and robust method of characterisation of new and existing nanoparticles in different conditions remains[263]. Rapid live cell imaging is arguably the most relevant way to approach this. The capability for real-time visualisation enables a unique insight into dynamic interactions in the cellular environment, and would permit new information to be gained regarding nanoparticle affinity to, and uptake by, cells. Colocalisation studies with fluorescent proteins or stained membranes, such as those designed to take into account both spatial and temporal data[264], are uniquely able to attain this data in real time.

4.2.2 Endocytic trafficking

One way of determining the behaviour of nanoparticles after internalisation is via colocalisation studies with fluorescent probes. As discovered in Chapter 2, clathrin mediated endocytosis is a primary route of entry for 20 nm carboxy-modified polystyrene nanoparticles. With this in mind, colocalisation experiments with fluorescent markers of endocytic pathways are an ideal method of discerning what happens to nanoparticles once they are inside the cell. Most current studies have shown that nanoparticles, regardless of shape, size and composition, end up in lysosomes (with exceptions, [112, 163, 265, 266]), where degradation traditionally occurs. However these studies have tended to examine only the nanoparticles' final destination. Knowledge of the route they take to end up there could prove valuable in terms of nanomedicine, where specific subcellular compartments are targeted. However this process is a complicated one, as the interactions between different cellular compartments are complex, and much remains unknown.

Arguably the most studied regulators of intracellular trafficking are the Rab family of GTPases. Rab5 for example is responsible for much of the immediate responses to vesicle internalisation[256], for example regulation of early endosomal membrane fusion[267], facilitation of vesicle uncoating following clathrin mediated endocytosis[268], and regulation of the microtubule motility of early endosomes[269]. Studies highlighting how the size of particles affects the route and rate of entry have shown a faster uptake of 40 nm nanoparticles through Rab5-containing vesicles compared to 100 nm particles. A transfer to vesicles containing Rab9, a marker of organisation of late endosomes was shown, and subsequent colocalisation with Rab7 and lysosomal-associated membrane protein 1, a late endosomal-to-lysosome marker and lysosomal marker respectively[270]. Also nanoparticles modified to cross the blood-brain barrier have been shown to colocalise with vesicles positive for Rab5 in hippocampal neurons[211]. Live cell imaging studies looking at the interaction between nanoparticles and Rab5 would give quantifiable information on the extent to which nanoparticles are endocytosed compared to uptake via other means.

4.2.3 Membrane stains

Another, more general way of determining how a nanoparticle behaves within a biological system is to see how it interacts with the cell membrane itself. If the membrane is fluorescently labelled, a confocal image should display whether any nanoparticle accumulations within a cell, such as those studied in Chapter 2, are contained inside vesicles. The choice of membrane stain for live cell imaging is important, as cell viability must not be affected and long-term staining for extended studies is preferable. Carbocyanine dyes, such as DiI, are ideal for this use[271].

With the advancement of nanotechnology, nanomaterial based biosensors and drug delivering nanocarriers are being developed[272, 273]. These are designed to pass through the plasma membrane and out of any endosomal entrapment in order to detect for the presence of certain chemical markers, or deliver drugs to specific locations. Because of the high rate of cellular mortality related to microinjection, electroporation and gene gun, biochemical methods of entry are a much more desirable route for nanomedicine[274]. Membrane dyes or fluorescent organelle markers are key for determining the intracellular destination of nanoparticles in real-time live cell imaging.

4.3 Aims and Objectives

In Chapter 2, it was observed that the presence of serum proteins resulted in a much lower cellular association and uptake than when serum proteins were absent. It was also seen that changing the type of proteins also had an effect on the affinity of nanoparticles for cells[177]. However, these studies gave no indication of the active processes that were affecting these discrepancies. It has been shown that increased protein concentration in the media reduces the zeta potential of the nanoparticles, and it is likely to be this that negatively affects the affinity for the cell membrane. It is hypothesised that due to this, cells in serum free conditions will internalise a higher proportion via non-specific endocytosis. In contrast, conditions where serum is present will result in a protein corona enveloping the nanoparticles. These are more likely to internalised by cells via receptor-mediated endocytosis. It has already been shown in Chapter 2 that in both conditions, a proportion of nanoparticles enter by directly permeabilising the plasma membrane. By performing live cell imaging with fluorescent protein markers and membrane stains, it will be possible to see to what extent these differences manifest themselves.

It would also be desirable to be able to visualise membrane dynamics in real time at the moment of nanoparticle internalisation. This would permit acquisition of information about how the cell directly reacts to changes in nanoparticle size, shape and properties. It should be possible to develop a protocol enabling the use of TIRF microscopy for this purpose.

4.4 Materials and Methods

4.4.1 Nikon A1R imaging and analysis

Confocal microscopy images were taken on a Nikon A1R inverted confocal microscope (Nikon Corporation, Tokyo, Japan) using a 60× 1.49 NA oil immersed objective. 488 nm and 560 nm lasers were used, and images taken using the NIS-Elements 3.2 imaging software (Nikon). Temperature was regulated at 37°C for live cell experiments.

4.4.2 Cell imaging media

For live cell microscopy, the samples have to be in a solution that contains a pH buffer and is free from autofluorescent compounds. To make this cell imaging media (CIM), 9.7 g Hanks Balanced Salt (Sigma) and 2.38 g HEPES (Fisher Scientific) were dissolved in a litre of distilled water. 1 M hydrochloric acid (Fisher Scientific) was added until pH 7.4 was measured on a Basic pH meter (Denver Instruments). This was sterile filtered using a 0.1 m pore Vacuum Filter System (Corning) and stored at 4°C prior to use.

4.4.3 High speed imaging of nanoparticles

In order to successfully track nanoparticles once they have already been internalised into cells, high speed imaging techniques had to be employed. HeLa cells were plated onto MatTek dishes for 24 hours so they were 60 - 70 % confluent at time of imaging. Cells were prepared as described in Section 2.4.5, up to the point of the PBS rinse. Following this, CIM containing 5% FCS was added and cells were imaged immediately. The scanning area was set marginally larger than the size of the cell being imaged so no time was wasted imaging the background. The Nikon A1R microscope was set to bi-directional resonant scanning and the pinhole was opened to 5 airy units, allowing more light in a shorter space of time to increase the speed of acquisition. The motion in Z was powered by a piezo z-drive (Mad City Labs; Madison, WI) with no delay between acquisition. All

of the setup was designed with speed of acquisition in mind, in the knowledge that the poor signal-to-noise ratio obtained in the images could be corrected by the de-noising algorithm described in the previous Chapter. This method permitted up to 25 frames per second, but with a better z-resolution than that obtainable using a widefield microscope. Each cell was imaged for two minutes, long enough to get a good time sequence of vesicle movement, but not long enough to cause visible cell damage.

4.4.4 Transfection with fluorescently labelled Rab5

For studying the colocalisation of nanoparticles to vesicles containing Rab5, cells were transfected with a gene that encoded a fluorescent variant of the protein. Cells were transfected with 4 μg of Rab5-GFP plasmid construct (kindly provided by Dr. Alexandre Benmerah, Necker Hospital, Paris, France) using Lipofectamine^{TM} 2000 (Invitrogen) according to the manufacturers protocol. They were then incubated with nanoparticles, fixed and imaged as described in Section 2.4.5.

4.4.5 Membrane staining with DiI for confocal microscopy

CellTracker^{TM} CM-DiI (Invitrogen) was made up to 1 mg/ml in dimethyl sulfoxide (DMSO) (Thermo Fisher Scientific Inc., Massachusetts) and stored at -20°C. This was defrosted and diluted to 5 μg/ml in PBS as required. Cells were incubated at room temperature for 10 minutes. This allowed the dye to label the plasma membrane but slowed endocytosis, reducing dye localization in cytoplasmic vesicles. Cells were then rinsed twice with 2 ml PBS and were immediately incubated with nanoparticles, fixed and imaged as described in Section 2.4.5.

4.4.6 Olympus IX81 imaging and analysis

TIRF images were obtained using an Olympus IX81 inverted microscope (Olympus Medical, Essex, UK) using Olympus ApoN 60×/ 1.49 NA and UApoN 100×/ 1.49 NA oil immersed objective lenses and 488, 561 and 640 nm lasers. The Olympus *exCellence RT* software was used to acquire the images.

4.4.7 Dual wavelength imaging system

As mentioned in Section 3.2.1, one way of avoiding the result of bleedthrough when looking at fluorophore emissions is by employing emission filters to discern between two fluorophores. While this is trivial when looking at fixed samples as images can be acquired separately, rapid live cell imaging requires additional hardware. For concurrent acquisition of two colour channels, a DualView (Photometrics, Tucson, AZ) system was integrated into the emission optics of the Olympus IX81 TIRF system. The effect of this was to split the CCD into two equal halves, showing the same view in each case but made up of light of different wavelengths. The schematic can be seen in Figure 4.1. The "DV2 filter cube" contains dichroic and emission filters, ensuring one half of the CCD receives wavelengths between 505 and 535 nm, and the other half between 605 and 655 nm. These correspond to the filters shown also in Figure 3.2.

4.4.8 Auto-Align

The two colour channels present in the single image acquired through use of the DualView imaging system were computationally co-registered using Auto-Align. This is freely available as an ImageJ plugin from *www.sourceforge.net/projects/imageautoalign/*. Full documentation can be found in reference [275].

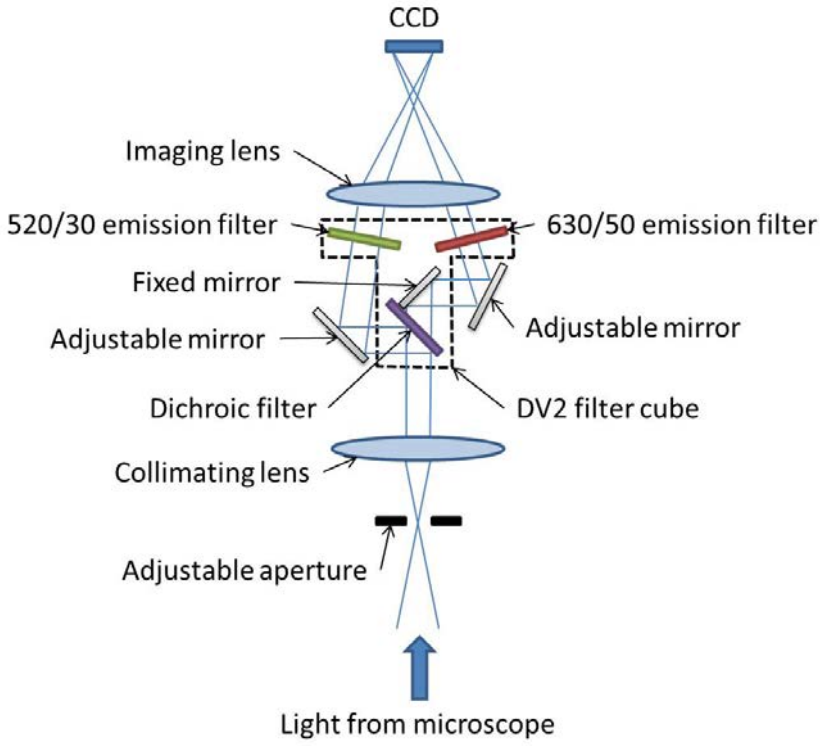

Figure 4.1: *Schematic of the inside of the DualView hardware. Light passes from the microscope into the system, where it is collimated. It passes into a filter cube, containing a dichroic filter which splits the beam into corresponding wavelengths, and aligns the two beams with mirrors before sending them through wavelength filters. The beams are then focussed and sent to different halves of the CCD.*

4.4.9 Matrigel

Prior to cell adherence, MatTek dishes (MatTek Corp, Massachusetts, USA) were coated with a thin layer of phenol-red free Matrigel (BD Biosciences, Oxford, UK). Matrigel was thawed on ice and diluted 1:1000 in Gibco® DMEM straight from the fridge, as Matrigel gels rapidly at 22°C. 100 μl and 400 μl were pipetted on MatTek dishes of diameter 10 mm and 20 mm respectively and left for one hour. These were then rinsed twice with 2 ml room temperature DMEM. Yellow/green 20 nm carboxylate-modified polystyrene FluoSpheres (Invitrogen) (stock 0.02 g/mL $\equiv 4.54 \times 10^{15}$ nanoparticles/mL) were diluted in PBS at a ratio of 1:100000, sonicated, and 2 ml was pipetted on to the Matrigel and left for 20 minutes. It was then rinsed twice with 2 ml PBS and left for no longer than 24 hours at room temperature before cells were plated.

4.4.10 Transfection with fluorescent clathrin

For quantifying the colocalisation of nanoparticles with clathrin coated vesicles, cells were transfected with cDNA encodeding a fluorescent variant of the protein. Cells were transfected with 4 μg of Clathrin-dsRed plasmid construct (provided by Prof. Thomas Kirchausen, Harvard Medical School, Boston) using Lipofectamine^{TM} 2000 (Invitrogen) using the manufacturers protocol. After 24 hours of expression, media was aspirated, and cells were rinsed with 2 ml PBS and incubated in 250 μl of trypsin at 37°C for 5 minutes. This was added to 8 ml SCM and divided into 4 MatTek dishes that had been prepared with Matrigel and nanoparticles. They were incubated for 4 hours before imaging.

4.4.11 Membrane staining with DiI for TIRF microscopy

The plasma membrane of HeLa cells had to be stained prior to plating onto the Matrigel. To ensure the least amount of time between staining and experiment, this had to occur while the cells were in suspension. CellTracker^{TM} CM-DiI (Invitrogen) was made up to 1 mg/ml in dimethyl sulfoxide (DMSO) (Thermo Fisher Scientific Inc., Massachusetts) and stored at -20°C. This was defrosted and diluted to 5 μg/ml in PBS as required. Detached cells in serum containing media were centrifuged at 1200 rpm for 5 minutes and the supernatant removed. The pellet was resuspended in 2 ml PBS and centrifuged again at 1200 rpm for 5 minutes. The pellet was then resuspended in 2 ml 5 μg/ml CM-DiI in PBS and gently vortexed for 10 minutes at room temperature, before centrifuging as before. Two PBS rinse/ centrifuge cycles followed, and the pellet was resuspended in serum containing media and plated onto the preprepared Matrigel and nanoparticle coated MatTek dishes. These were then incubated at 37°C for between 2 and 48 hours before imaging.

4.5 Results and Discussion

4.5.1 Live cell imaging in serum and serum-free conditions

Prior to fluorescent labelling of different cellular components, experiments were performed with live HeLa cells and nanoparticles with and without serum. This was to ascertain whether there was any immediate observable difference between the two conditions. Figure 4.2 shows some of these images. It was observed that in cases where serum was present, nanoparticles inside the cell exhibited a high degree of mobility. This movement was not seen to any significant extent with nanoparticles that had been incubated with cells in serum-free medium. It is therefore hypothesised that particles that are internalised in conditions where serum is present are actively transported within vesicles, driven by active motors potentially along microtubules, whereas the extent to which this happens in serum free conditions is greatly reduced. Quantification of the observed rates of transport in each condition will be performed and compared to published rates of vesicle motion.

4.5.2 Identifying and quantifying nanoparticle movement

In Chapter 2, uptake of 20 nm carboylate-modified polystyrene nanoparticles was observed in HeLa cells. This was confirmed with confocal microscopy, where a layer of nanoparticles could be seen coating the coverslip and the cell membrane that was exposed to the medium. A 'footprint' where nanoparticles couldn't get between the cell and coverslip can be seen in Figure 4.2 Ai and Bi. Individual nanoparticle spots seen in this area were considered to be inside the cell. As seen in Figure 4.2, the presence of serum proteins during the incubation with, and subsequent uptake of, nanoparticles results in their directed movement within the cell. This is seen in contrast to those nanoparticles internalised in serum free conditions, which display much reduced movements. This was quantified by applying the de-noising algorithm described in Chapter 3 to time frames one second apart over the course of a 20 second imaging run, and comparing the centroids of the resulting

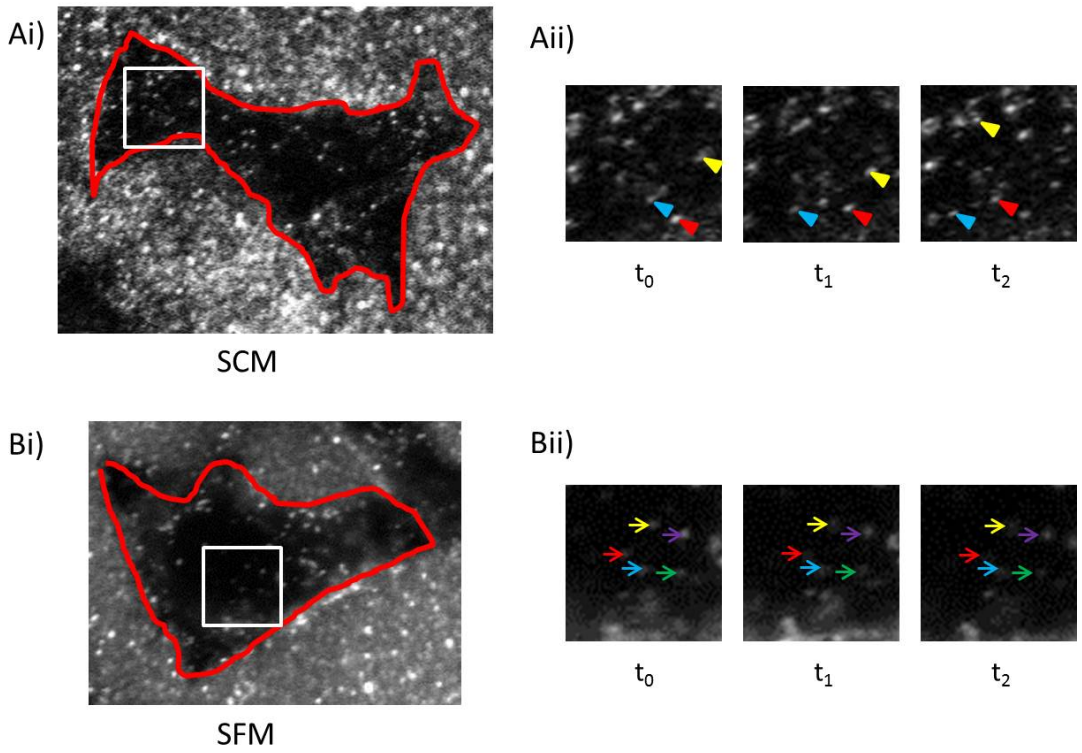

Figure 4.2: *Imaging live cells after the internalisation of nanoparticles shows a discrepancy between those incubated in the presence of serum proteins and those where serum proteins are absent. Ai) Representative image of a HeLa cell incubated with 20 nm carboxylate nanoparticles imaged over 20 seconds. Aii) A majority of the nanoparticle spots are displaying a high level of movement within the cell. Bi) Representative image of a HeLa cell incubated with nanoparticles in the absence of serum proteins. Bii) The movement of the nanoparticles is greatly reduced, and in most cases non-existent. t1 = 10 seconds, t2 = 20 seconds. The size of the enlarged section is 8 μm × 8 μm. The out of focus background seen in the images is from nanoparticles adsorbed to the glass coverslip. Cell outlines (red) were obtained from brightfield images.*

detected spots over the course of the experiment. The spots whose centroids in one frame are still within the area of the spot in the next frame over the 20 second interval are counted as being static. As the average diameter of nanoparticle spot size was 530 nm (calculated from measuring the spots from five cells from each of the three experiments), this means that the nanoparticles in the serum free condition were moving at a speed of less than 0.265 μm/s. Average velocity of directed movement of complexes and cargo within cells has been reported between 0.3 and 0.85 μm/s[218, 276, 277, 278], with average speeds of 0.3 μm/s for myosin V[279], 0.8 μm/s for kinesin motor proteins[280], and up to 8 μm/s reported for early endosome movement along microtubles via the motor protein

dynein[281]. This is in contrast to Brownian motion, which within cells for objects of this size is reported to be around 0.21 μm/s[282]. The results of this analysis is quantified in Figure 4.3.

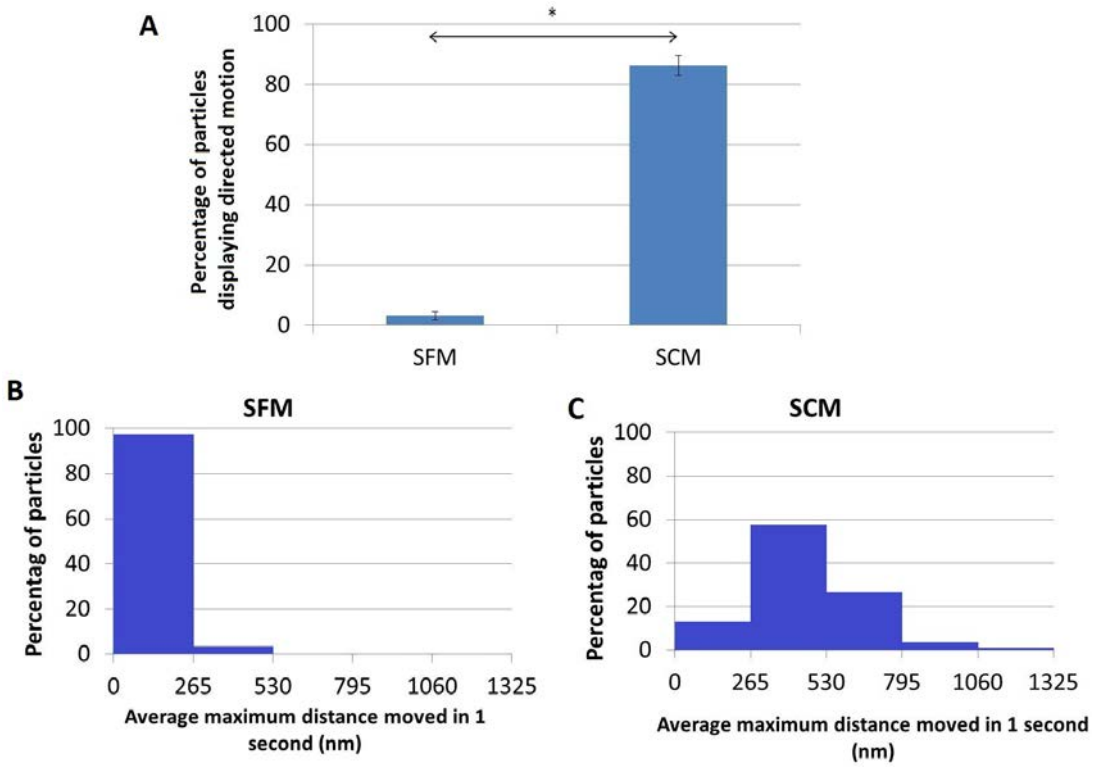

Figure 4.3: *Quantification of intracellular nanoparticle movement in conditions containing, and free from, serum proteins. A) shows percentage of nanoparticle accumulations in each condition that displayed directed motion of more than 265 nm in one second over the time frame recorded. B) and C) display maximum recorded distances moved by particles in one second as normalised histograms. Distance measures relate to the average radius of nanoparticle accumulations. It can be seen that a majority of the nanoparticles internalised in serum free medium displayed movement consistent with Brownian motion. A majority of those incubated in the presence of serum proteins moved further than this. Average maximum distance travelled was calculated by taking the average of the three highest distances recorded between frames 1 second apart. Number of experiments,* n, *= 3 with 8 cells analysed per experiment. Bars show standard error in data,* p *value < 0.005 in A) obtained from a Student's t-test.*

It can be seen that 96.6% of the nanoparticles internalised in SFM displayed movement consistent with Brownian motion. The 3.4% of particles that showed directed movement did so at speeds comparable with those seen by myosin V. In SCM, 13.5% of particles displayed movement consistent with Brownian motion, 58.9% moved at speeds observed by

myosin V, and 27.6% moved at speeds of over 530 nm per second, consistent with velocities observed by vesicles transported along microtubules. The distance moved by a nanoparticle spot between each frame was calculated using the ImageJ plugin MTrackJ[283], with the average maximum distance calculated by taking the mean of the three highest distances moved by each spot. This was chosen as it was rare for spots to move the same distance between each frame. Indeed, it was common for nanoparticles to be stationary for a majority of the time, and display movement in short bursts. The average of the highest three was chosen to mitigate any outlying results stemming from potential inaccuracies in the MTrackJ program.

The presence of serum proteins forming a corona around the nanoparticles seems to have a significant effect on their subsequent behaviour upon internalisation. This could be explained by the nanoparticles being internalised primarily via receptor mediated endocytosis, and so the nanoparticles display greater movement within the cell as they are passengers in normal protein trafficking pathways. If nanoparticles internalised in serum-free conditions are being taken up via non-specific routes of entry such as pinocytosis then this could explain the observed differences. Colocalisation studies with different intracellular markers could confirm this hypothesis.

4.5.3 Colocalisation of nanoparticles to intracellular markers

It is hypothesised that nanoparticles internalised in the presence of serum proteins follow different intracellular pathways to those that are internalised lacking a protein corona. In order to verify this, confocal microscopy was used to perform colocalisation studies with different cellular markers.

Pathways: Rab5 Rab5 is a small GTPase which is responsible for much of the immediate responses to vesicle internalisation. Imaging of cells that have been transfected with fluorescent Rab5 and incubated with nanoparticles in either serum-free or serum-containing media could reveal whether or not this uptake pathway is being used.

30 minutes after being incubated with nanoparticles, cells were imaged. A representative image can be seen in Figure 4.4B, along with the results of the colocalisation analysis described in the previous Chapter. It can be seen that 41% of the nanoparticle accumulations were colocalised with vesicles present for Rab5.

Membrane: DiI As an alternative to looking at markers within the cell, studies of the cell membrane are another potential way of determining how nanoparticles enter cells. If nanoparticles are entering via endocytic routes, they are transported through vesicles composed of phospholipids that previously made up the outer cell membrane. If this was stained then it would make it possible to identify those intracellular spots that entered via endocytosis rather than direct membrane permeabilisation, which would not display any colocalisation with the membrane.

As before, cells were imaged 30 minutes after incubation with nanoparticles (Figure 4.4C). As displayed in Figure 4.4A, 42% of nanoparticle accumulations are within vesicles stained with DiI. Unfortunately there was no fluorophore combination available with the lasers on the Nikon A1R confocal system that allowed simultaneous imaging of nanoparticles, Rab5 and DiI so there was no way of confirming that these vesicles were the same ones, as the numbers would suggest.

Identical studies were performed alongside these, using media free from serum during incubation to try and determine what effect the protein corona might have on the behaviour of nanoparticles during and after cellular uptake.

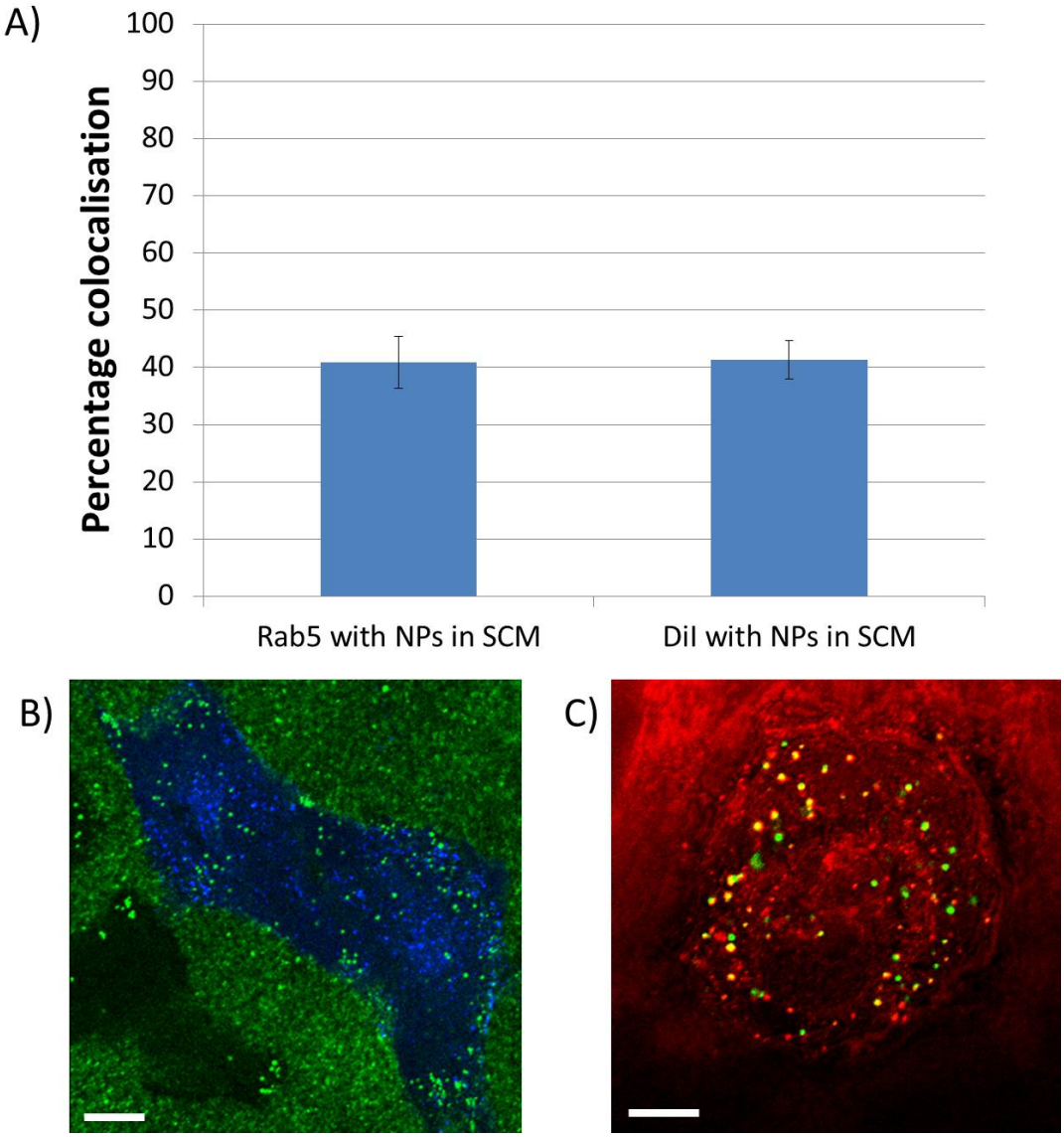

Figure 4.4: *Quantifying colocalisation of nanoparticle accumulations with vesicles stained with Rab5 or the membrane stain DiI. A) When imaged with confocal microscopy, after 30 minutes 41% of the nanoparticle accumulations seen inside a cell that had been incubated in serum-containing media showed colocalisation with fluorescent Rab5, a protein present in early endosomes. In separate experiments where the cell membranes had been stained with DiI, after 30 minutes 42% of the nanoparticle accumulations seen inside a cell that had been incubated in serum-containing media showed colocalisation with DiI-stained vesicles within the cell. Bars show standard error in data. B) Representative confocal microscope image of a HeLa cell transfected with fluorescent Rab5 (blue) and incubated in serum-containing media with 20 nm carboxylate-modified polystyrene nanoparticles (green). C) Representative confocal microscope image of a HeLa cell stained with DiI (red) and incubated in serum-containing media with 20 nm carboxylate-modified polystyrene nanoparticles (green). Number of experiments,* n, *= 3 with 10 cells analysed per experiment. Scale bars = 10 μm.*

4.5.4 SFM data

All of the experiments performed in this Chapter were run concurrently in serum free conditions. This was to continue the work studying the effects of the protein corona on nanoparticle uptake begun in Chapter 2, and continued further with noticing the lack of motility of nanoparticles inside cells that had been incubated in serum-free media. Unfortunately there were problems associated with these experiments which meant quantifiable data could not be obtained from the images. These are visualised in Figure 4.5.

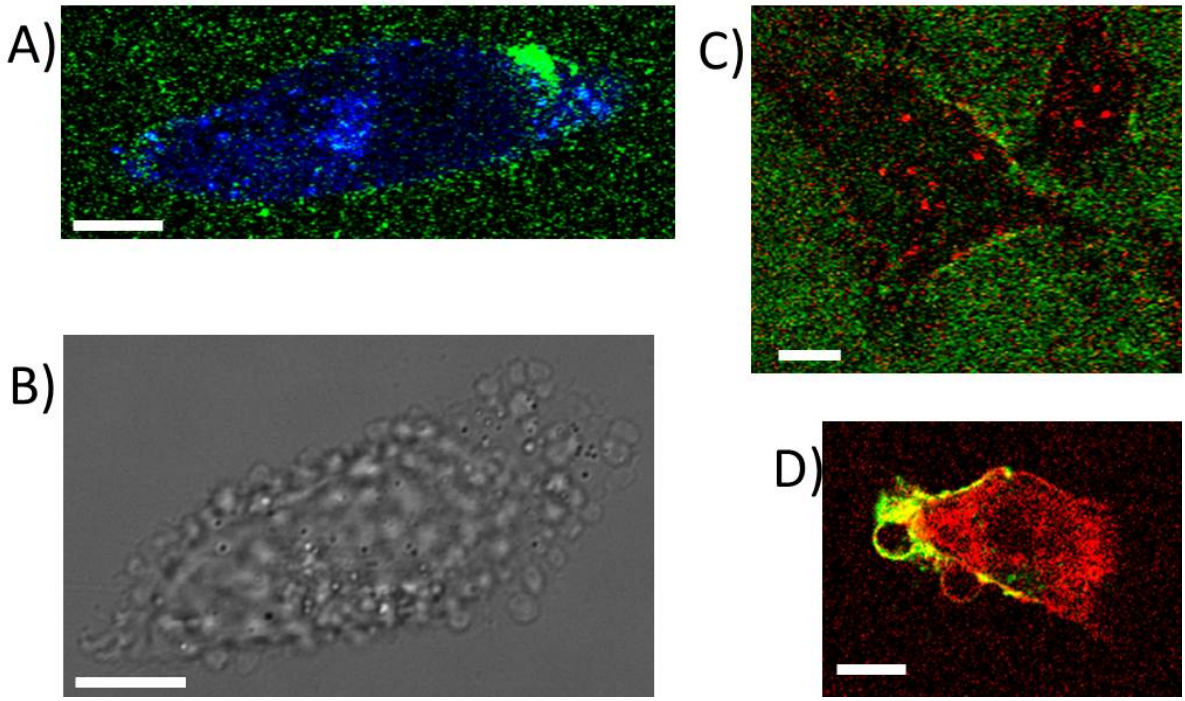

Figure 4.5: *Images of nanoparticles incubated with HeLa cells either transfected with fluorescent Rab5, or stained with the membrane stain DiI in serum-free media. A) The best example of a confocal microscope image of a HeLa cell transfected with fluorescent Rab5 (blue) and incubated in serum-free media with 20 nm carboxylate-modified polystyrene nanoparticles (green). B) a typical brightfield image of a HeLa cell after transfection with Rab5 and incubation in serum-free media with nanoparticles. C) The best example, and D) a typical example of a confocal microscope image of a HeLa cell stained with DiI (red) and incubated in serum-free media with 20 nm carboxylate-modified polystyrene nanoparticles (green). In both cases cells either died before or soon after beginning imaging, or the staining was irregular. Number of separate experiments for each condition,* n, *= 5 with similar results observed each time. Scale bars = 10 μm.*

In the Rab5 experiments displayed in Figure 4.5A and B, cells were transfected with Rab5-GFP as described in Section 4.4.4, and prepared for imaging as outlined in Section 4.4.3. The few that were alive on imaging displayed irregular Rab5 fluorescence staining (4.5A), and laser power and gain settings had to be much higher than usual, hence the low signal-to-noise ratio in the images. However, most of the cells died once they were serum starved for the requisite amount of time and nanoparticles were introduced. Blebbing or detachment was seen in all repeats of the experiment (4.5B).

In the DiI experiments displayed in Figure 4.5C and D, the staining of DiI was irregular. Most cells were either not stained at all, or the DiI fluorescence was far higher than had been seen in any other experiment. For the cells that had an appropriate amount of even staining, apoptosis occurred in the very early stages of imaging.

In conditions where a protein corona had formed around the nanoparticles, just over 40% of internalised nanoparticle spots had colocalised with either Rab5, a marker of early endosomes, or DiI, a membrane stain. In conditions where serum was not present, no useable data could be obtained. This made it impossible to determine what process is occurring to allow the majority of nanoparticles to enter the cell. It is possible that in conditions where serum is present nearly 60% of nanoparticles are entering through inconsistencies in the cell membrane, which would agree with what was observed in Chapter 2. This would also suggest that in serum free conditions with the lack of a corona, the transfection or staining process made the cells more susceptible to membrane permeabilisation, and it is this that led to the high levels of cell death observed, something reported previously[284]. An alternative explanation could be that in conditions where serum proteins are forming a corona around the nanoparticles, entry is also possible via other methods of receptor mediated endocytosis. It is also possible that nanoparticles are entering via endocytosis and subsequently released into the cytoplasm after entry, as has been observed with colloidal gold nanoparticles[285].

Due to the availability of necessary fluorophores, cells couldn't be simultaneously imaged with fluorescent nanoparticles, DiI, and Rab5. This required alternative methods to determine and accurately quantify routes of nanoparticle entry. With this knowledge in mind, and a desire to obtain quantifiable data in serum free conditions, other live cell imaging modalities were considered. TIRF microscopy allows the acquisition of detailed images of the cell membrane, and would permit views of the precise moments where a nanoparticle was internalised.

4.5.5 Making TIRF suitable for studying nanoparticle uptake: Protocol development

TIRF microscopy offers superior resolution and sensitivity over widefield and confocal microscopy for studying the basal membrane of adherent cells. This could prove advantageous in the study of nanoparticle uptake. If it was possible to obtain more detailed knowledge about their interactions with the plasma membrane, the speed and extent of uptake of specialised targeted nanoparticulate drugs for example could be examined in great detail, and affinity for different cell types could be accurately quantified. This would be significant in the search for an accurate and quantifiable method of nanoparticle characterisation in biological conditions. Another advantage TIRF microscopy has over confocal is widefield image acquisition. This means the whole field of view can be obtained at once, and real time rates of uptake can be studied.

Before TIRF could be used to study nanoparticle uptake, a new assay had to be developed. Due to the way the TIRF microscope illuminates the specimen, it was necessary to have a layer of nanoparticles on the coverslip before cells were introduced on top. This way, nanoparticles would be clearly vivsible in the evanescent TIRF field, and would disappear from view upon internalisation. Initial tests relied on electrostatic interactions between nanoparticles and the glass coverslip before the introduction of cells. This didn't work however, as the cells either wouldn't adhere (Figure 4.6A), or would detach after a few seconds exposure to incident laser light (Figure 4.6B and C).

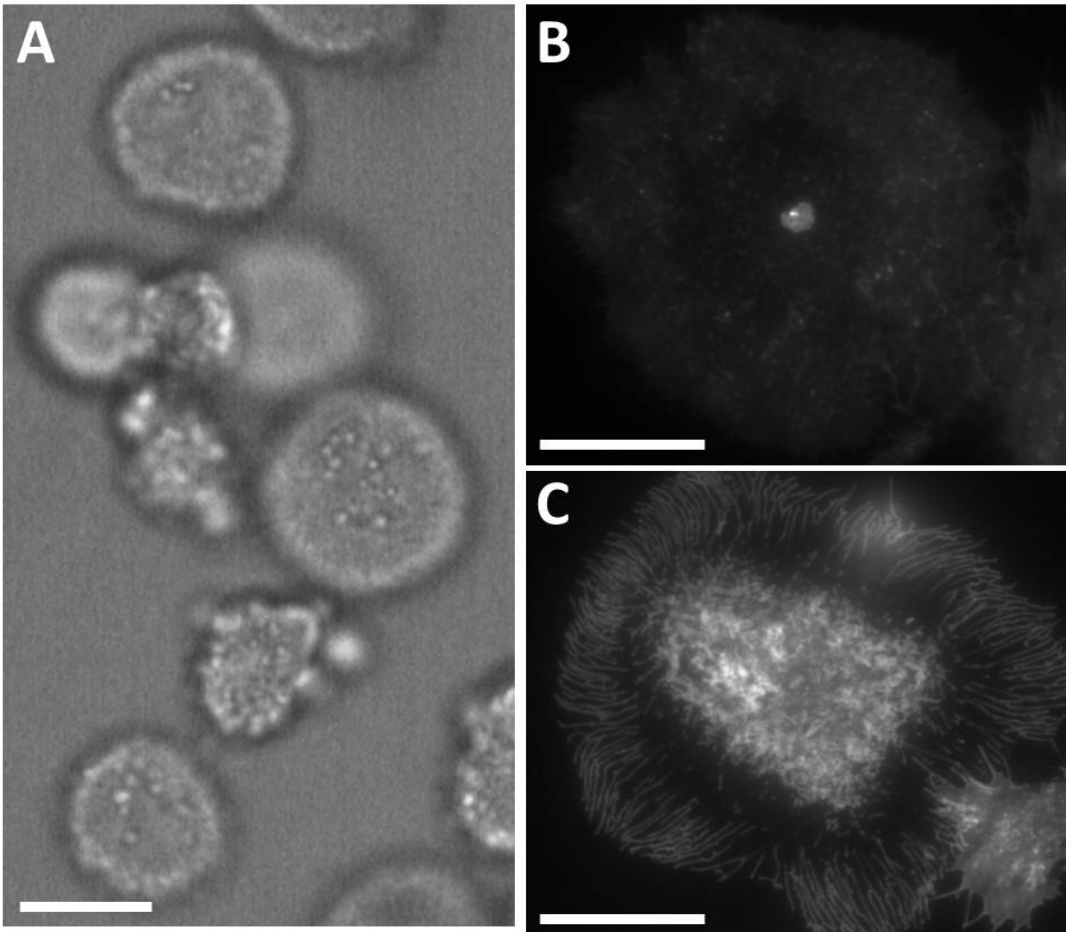

Figure 4.6: *Cells are unable to settle and spread on top of nanoparticles. A) shows a representative brightfield image of Hela cells four hours after plating in a MatTek dish with nanoparticles on. B) and C) show representative TIRF images of a HeLa cell stained with DiI six hours after plating in a MatTek dish with nanoparticles on. B) shows the cell immediately after locating on the Olympus IX81 microscope, and C) shows the same cell approximately 10 seconds after the image in B) was taken. The cell is seen to lift away from the coverslip and eventually out of the TIRF evanescent wave. Scale bar is 20 μm.*

To get around this, a thin layer of Matrigel was formed on the coverslip prior to nanoparticle introduction. Matrigel is a basement membrane preparation rich in extra cellular matrix proteins, derived from mouse sarcoma cells. It is chiefly comprised of laminin, collagen IV, entactin and heparan sulfate proteoglycan, which provide a substrate for the nanoparticles to embed in, and aid the subsequent adherence of cells[286]. The Matrigel was dissolved at a concentration of 1:1000 in serum free media, and 100 μL were pipetted onto a MatTek dish containing an optical glass coverslip of 10 mm diameter. This volume would have resulted in a maximum gel depth of around 100 nm on the coverslip,

calculated by assuming an even layer of Matrigel (0.1 μL) over the whole coverslip (0.79 cm^2). Nanoparticles were then introduced to this thin layer of Matrigel, where they stayed readily for up to a week as long as the Matrigel was kept hydrated under PBS. The schematic of this can be seen in Figure 4.7.

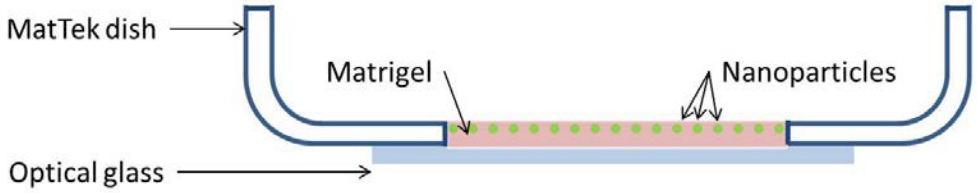

Figure 4.7: *Schematic of how Matrigel acts as a cell adherence aid in the presence of nanoparticles. Matrigel is added to the MatTek dish before nanoparticles are added, ensuring the presence of nanoparticles before cells are introduced, and encouraging the adherence of cells to the glass surface.*

The amount of Matrigel used differs greatly from the manufacturers instructions. A much smaller amount was used than recommended, as even though the refractive index of gelled Matrigel is very similar to that of water (1.3406 compared to 1.3333[287]), it was necessary to introduce as few aberrations to the TIRF field as possible. Relevant studies were done to ensure that Matrigel did not affect the illumination of the TIRF field. The results of these can be seen in Chapter 5.

4.5.6 Making TIRF suitable for studying nanoparticle uptake: DiI staining

To test the Matrigel protocol, cells were placed on top of nanoparticles and imaged with TIRF microscopy over time. The disappearance of nanoparticles from the evanescent field was observed (Figure 4.8), indicating they have been internalised by the cell. This indicates that the ability of cells to internalise nanoparticles has not been restricted by

introducing them to the basal membrane. A large decrease in the number of nanoparticles early in the experiment indicates that uptake is immediate, and levels off when fewer nanoparticles are available for internalisation.

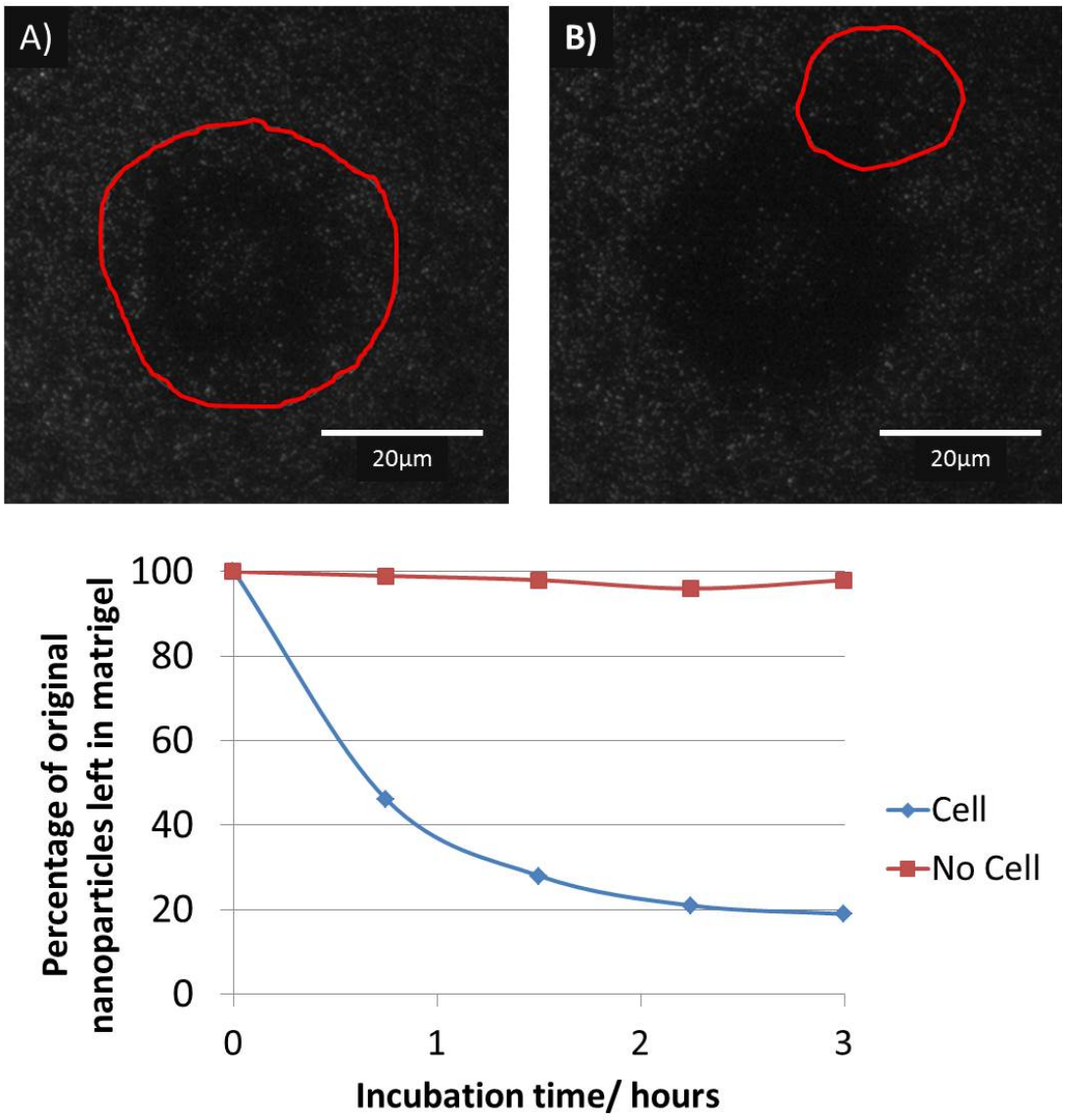

Figure 4.8: *TIRF microscopy reveals nanoparticle uptake over a three hour period. A) and B) show TIRF images focussed on the matrigel surface where nanoparticles are embedded at times of 45 minutes and 3 hours respectively after cells were introduced. Graph shows how the relative number of nanoparticles in the matrigel decreases over this time period, comparing the original area where the cell was and an equivalent area where there were no cells throughout the experiment. This was to show decrease was not due to photobleaching or other external factors. Sample was imaged immediately after cells were plated. Images were taken every 45 minutes during the timelapse. Depth of evanescent field was 100 nm.* n = *1. Scale bar is 20 µm.*

Cells were stained with the membrane stain DiI to see whether it was possible to determine if the nanoparticles that were disappearing from the evanescent field were internalised via endocytosis, or whether they were entering cells outside of formed vesicles. Figure 4.9 shows a case where a nanoparticle spot has colocalised with a DiI containing vesicle. The intensity of both spots subsequently decreases, indicating that the nanoparticle has been internalised within this vesicle. Control intensities have been shown, confirming this observation is not due to photobleaching.

Further experiments were carried out to see how the rate of uptake changed over time. Figure 4.10 shows how the association of DiI spots with nanoparticles at the basal membrane peaks at earlier stages of cell adhesion and seems to level off. This is likely due to there being fewer nanoparticles in the Matrigel after that amount of time. It should not be due to the membrane stain dissipating, as the manufacturer claims fluorescent signal is retained for "at least 72 hours"[288].

To compare to the previous results seen in Figures 4.4 and 4.10, widefield images were taken to observe the amount of colocalisation between nanoparticles and vesicles stained with DiI inside the cell. It can be seen in Figure 4.11 that the colocalisation of nanoparticles and DiI increases over time. This follows from the data in Figure 4.10. There is a higher percentage colocalisation when looking at this data than compared to the confocal microscopy data in Figure 4.4. This however can be explained in reference to the previous Chapter, where it was outlined that less accurate z-resolution can affect obtained colocalisation values. It would not surprising if the values gained by the program in widefield studies gave a higher colocalisation value than from using confocal microscopy images due to a higher proportion of light emanating from out of focus nanoparticles or vesicles.

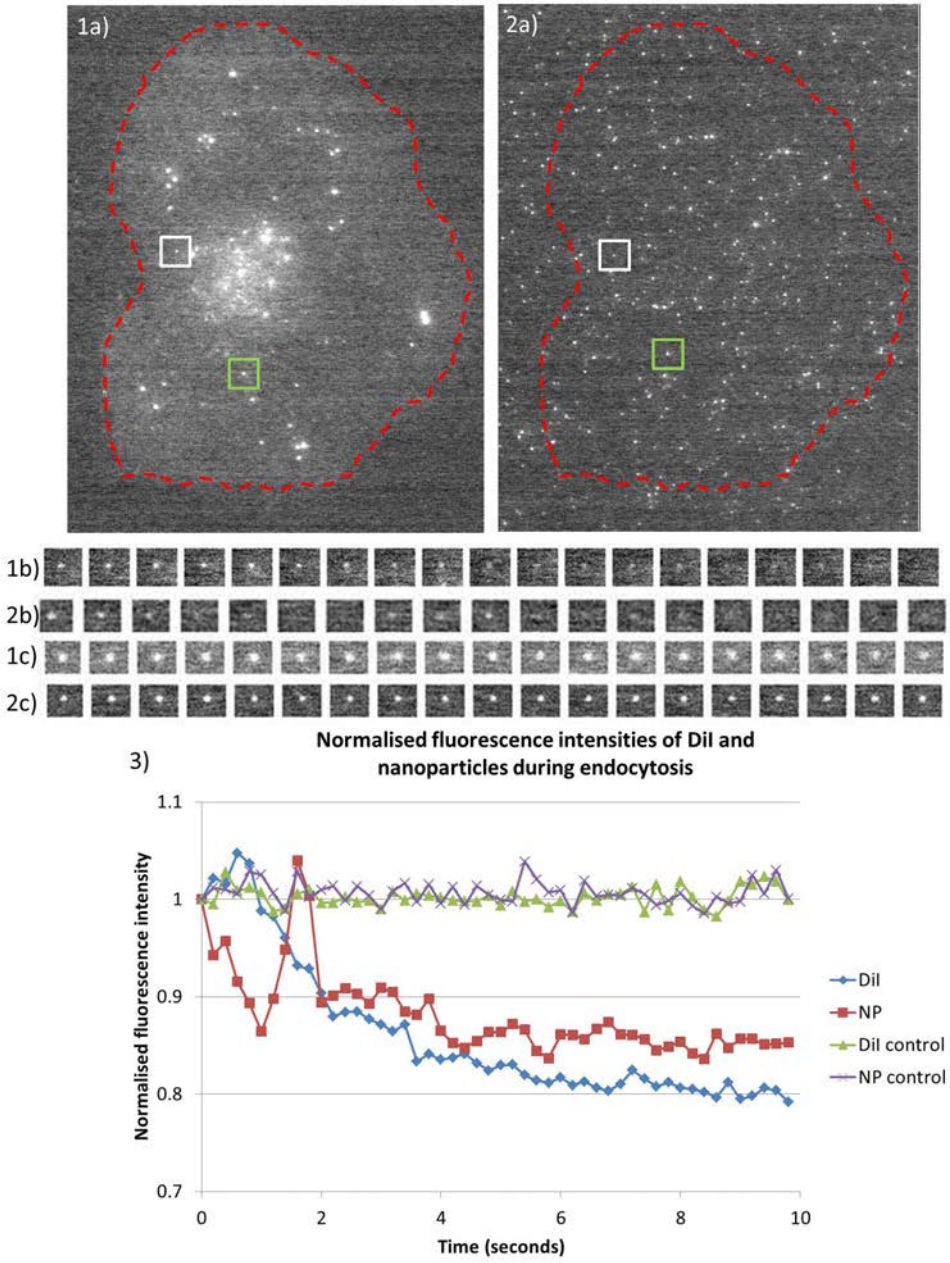

Figure 4.9: *TIRF microscopy with DiI staining shows nanoparticle uptake. 1) TIRF image of a cell stained with DiI 2 hours after plating on top of nanoparticles embedded in Matrigel. 1a) DiI channel. 2a) Nanoparticle channel. Red dotted line marks the cell boundary. Squares show the analysed timelapses. 1b) Disappearing DiI spot over the first four seconds of the timelapse (white). 2b) Disappearing Nanoparticle spot over the first four seconds of the timelapse (white). 1c) Control DiI spot over the first four seconds of the timelapse (green). 2c) Control nanoparticle spot over the first four seconds of the timelapse (green). 3) Graph showing the average intensity of the 3x3 pixel area at the centre of each spot (the same pixels in each image). It can be seen that the intensity of both decreases with respect to the control, indicating the disappearing nanoparticle was internalised within a vesicle.*

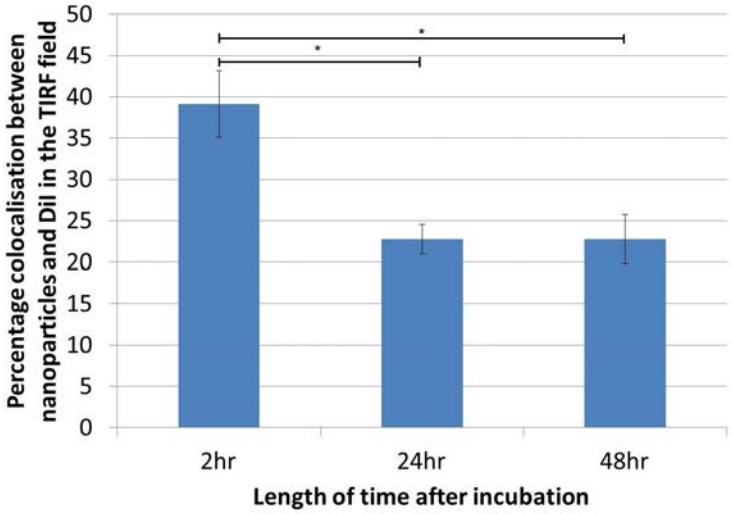

Figure 4.10: *Quantifying nanoparticle uptake via TIRF microscopy. HeLa cells were stained with the membrane stain DiI before introduction to nanoparticles on a Matrigel coated surface. They were incubated at 37°C for different times before being imaged with TIRF microscopy. It can be seen that the colocalisation of nanoparticles with DiI stained vesicles decreases over time. There was a statistically significant difference between groups as determined by one-way ANOVA* ($F(2, 21) = 5.94, p = 0.0090$). *Significant* p*-values indicated were calculated using a Bonferroni corrected post hoc t-test. Number of experiments,* n, *= 3 with 10 cells analysed per experiment. Bars show standard error in data.*

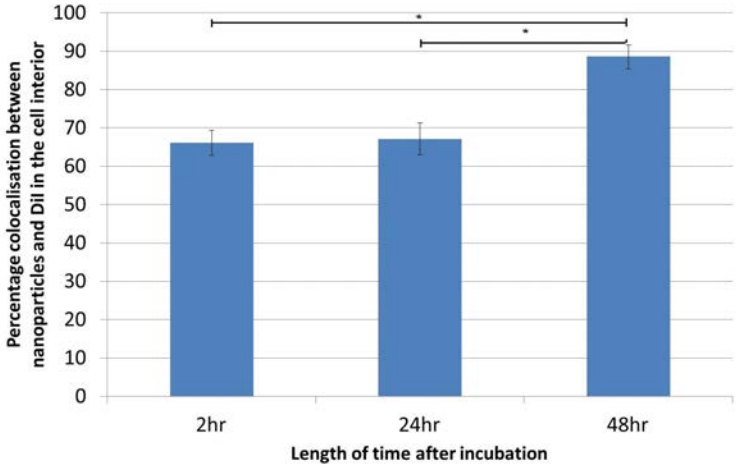

Figure 4.11: *Widefield microscopy for studying nanoparticle uptake. HeLa cells were stained with DiI before introduction to nanoparticles on a Matrigel coated surface. They were incubated at 37°C for different times before imaging with widefield microscopy. It can be seen that the colocalisation of nanoparticle accumulations with DiI stained vesicles within the cell increased over time. There was a statistically significant difference between groups as determined by one-way ANOVA* ($F(2, 21) = 7.55, p = 0.0034$). *Significant* p*-values indicated were calculated using a Bonferroni corrected post hoc t-test.* n, *= 3 with 10 cells analysed per experiment. Bars show standard error in data.*

4.5.7 SFM data

Experiments using TIRF microscopy were also attempted in serum free conditions. However, due to the nature of the developed Matrigel experiments, it was not possible for cells that had already adhered to the Matrigel to have the media swapped for serum free media, as internalisation would have already begun. This meant cells had to be plated in serum free conditions. Unfortunately consistent adherence was not seen in these cases, even with the presence of Matrigel. What minimal adherence did occur happened several hours after serum containing conditions, and attempts at imaging resulted in the cell lifting away from the coverslip and out of the illuminating evanescent field.

4.6 Conclusions

It has been established that there is a significant difference in internalisation of nanoparticles in serum-containing and serum-free conditions. Results in Chapter 2 have been expanded further, with live cell experiments showing that the nature of nanoparticles upon internalisation are different in the two conditions. Internalisation in the presence of serum proteins results in directed movement, which is not seen in their absence. Internalisation methods were examined in more detail, looking at both intracellular markers in Rab5 and membrane stains in DiI using confocal microscopy. While preliminary results were promising in cases where serum-containing media was used, no data was able to be gained in conditions free from serum. This resulted in the establishment of a novel protocol whereby nanoparticles are imaged from the basal membrane of the cell, allowing the use of TIRF microscopy to image the exact moment of uptake of nanoparticles. While, once more, the conditions free from serum proteins failed to yield any data, this protocol nevertheless yielded encouraging results whereby real-time imaging of nanoparticle uptake was observed and quantified.

Faster and more reliable analysis of uptake of different nanoparticle types across multiple cell lines is highly desirable. When considering novel targeted drug delivery methods for example, a technique that permitted direct, detailed visualisation of nanoparticle interactions with the cell membrane would be invaluable. With this new Matrigel protocol, potential for identifying and analysing nanoparticle uptake in real time is closer to being realised. This can be improved further by the development of novel TIRF microscopy hardware which would be able to identify points of membrane curvature and have the potential to track internalisation of nanoparticles within the first few hundred nanometers from the coverslip.

CHAPTER 5

DEVELOPMENT OF A NOVEL IMAGING SYSTEM TO STUDY THE CELLULAR UPTAKE OF NANOPARTICLES

5.1 Overview

With the increased use of nanoparticles in the manufacturing, cosmetics, pharmaceuticals and bio-medical sectors, the potential for nanoparticle entry into cells needs to be examined in greater detail. In terms of targeted nanoparticulate drug delivery, cellular specificity, internalisation and subsequent behaviour is paramount to increasing the theraputic index of a drug. Visualising interactions at a detailed level would provide greater insight into how variation of nanoparticles in size, shape and surface chemistry result in vastly different interactions. Through research culminating in a published paper, it has been determined that the primary route of entry of 20nm carboxylate-modified polystyrene nanospheres into HeLa cells is via clathrin-mediated endocytosis. It was also established that there is a proportion that are entering through direct permeabilisation of the plasma membrane[104]. It was then seen that the protein corona that forms when a nanoparticle is present in biological milieu results in a fundamental difference in the way a cell not only reacts to a nanoparticle associated with the outer membrane, but if and how it internalises it, and what occurs next. Real-time visualisation and quantification of these events at the cell membrane would be desirable for studying medical issues in terms

of targeted drug or contrast agent delivery. This can be realised via modification of both hardware and software of the Birmingham Advanced Light Microscopy's Olympus TIRF microscope, which is the focus of this Chapter.

5.2 Introduction

As has been referred to throughout this thesis, there are many factors contributing to if and how nanoparticles enter cells. These include, but are not limited to, the size and shape of the nanoparticle, the proteins present in the surrounding medium, the amount of time the nanoparticle has spent in that particular milieu, and the cell type. This makes detailed analysis necessary, but extremely time consuming for each and every condition.

As described in Chapter 1, TIRF microscopy is a technique that generates an excitation field of the order of hundreds of nanometres above a coverslip. This means that only a select portion of the fluorophores in a sample are excited, and consequently emit detectable light. This results in an image of a basal cell surface with a high signal to noise ratio and high contrast. It is proposed that adapting this microscopy technique to allow observation of both nanoparticle dynamics and the cell membrane in relation to them would make quantifiable analysis of each condition much more straightforward. This could be possible by combining two existing but currently separate techniques: variable angle TIRF and polarised TIRF.

5.2.1 Variable Angle TIRF

One of the limitations of TIRF miroscopy is that it is impossible to tell from a single image whether a difference in fluorescence intensity is due to the brightness of a fluorophore or its distance from the coverslip. This can be seen in Figure 5.1, where two different models give the same resultant image. A change has to be made to the image acquisition process in order to be able to differentiate between these scenarios.

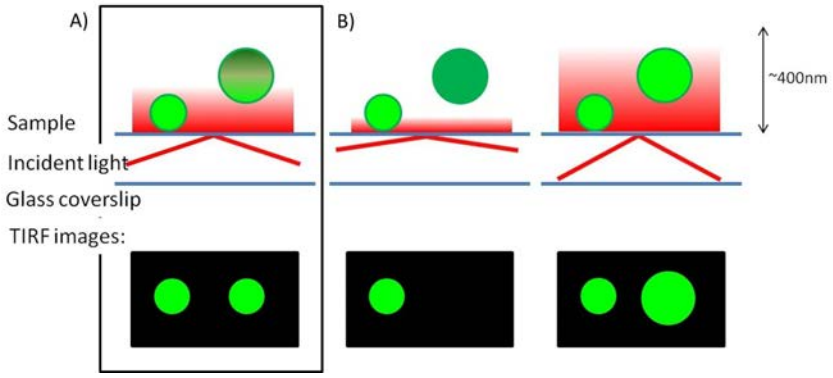

Figure 5.1: *Standard TIRF versus variable angle TIRF. A) a typical TIRF image, with a fixed depth of evanescent wave. It is impossible to tell the difference between a smaller (or dimmer) fluorophore on the coverslip and a larger (or brighter) fluorophore further away. This is due to the exponentially decaying intensity nature of the evanescent wave. B) With variable angle TIRF, it is possible to differentiate between the two scenarios.*

One way to be able to differentiate between these two different scenarios would be to vary the penetration depth of the evanescent field during an experiment. This would obviously have to be very rapid for live cell imaging to accurately determine cell dynamics in real time. As described in Equation 1.7, the penetration depth of the evanescent wave is dependent on four variables: the wavelength of the light; the refractive indicies of the objective lens and sample; and the angle of incidence of the light source. The only thing it is possible to have direct control over during an experiment is the angle of the incoming laser beam, resulting in the aptly-named technique of variable-angle TIRF (VA-TIRF). Figure 5.2 shows the intensity profiles of a 561 nm laser at the incident angles required to give corresponding penetration depths of 100, 200 and 300 nm.

As mentioned in Chapter 1, the refractive index of everything from water to diamond has a slightly different value for each wavelength of light. This known as dispersion and is how a rainbow can be formed from white light and a prism. For TIRF, this means that lasers of different wavelengths incident on a coverslip at the same angle will experience a different change in refractive index, and hence generate evanescent waves of varying penetration depths. This is visualised in Figure 5.3, and means that for comparable penetration depths of evanescent wave, each laser input would ideally be able to be adjusted individually. This is much easier for some systems rather than others.

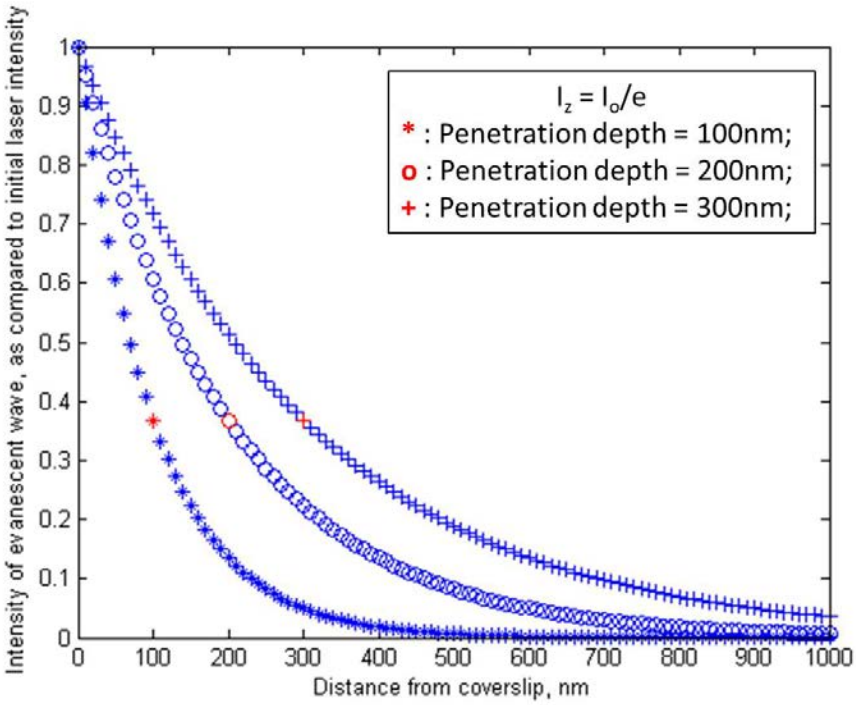

Figure 5.2: The intensity of an evanescent wave varies with distance from the coverslip. Intensities are shown for three different penetration depths for a 561 nm laser.

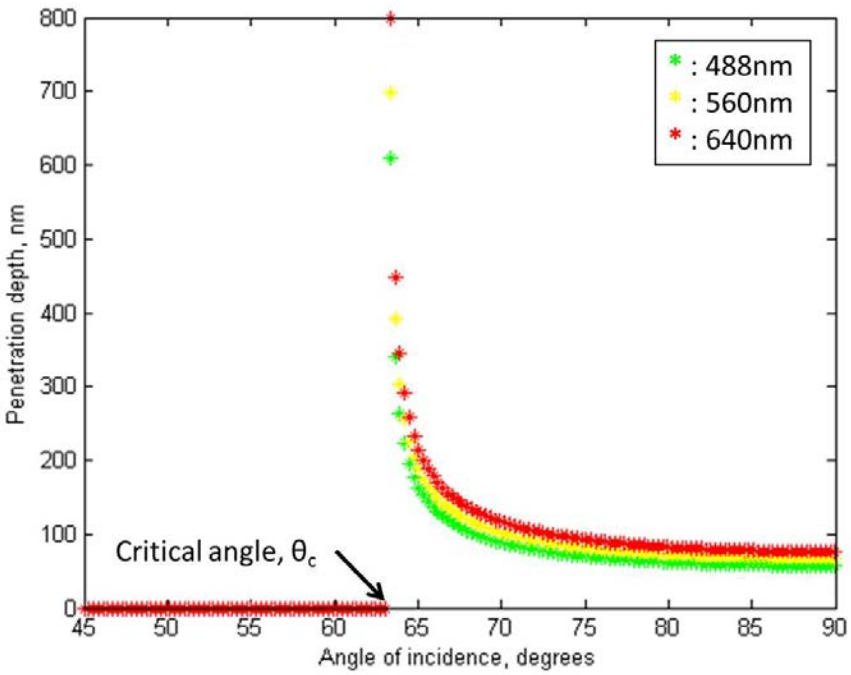

Figure 5.3: Variation of evanescent wave penetration depth with incident angle. It is also shown how this differs for lasers of different wavelengths.

There are several possible methods to implement VA-TIRF, and this depends on whether the TIRF system is prism- based or objective- based (see Figure 5.4). For a prism- based TIRF system, the most common set-up involves one or a series of rotating parabolic mirrors[289, 290], although it is possible to incorporate acousto-optic modulator and telecentric lens optics to enable wavelength-dependant deflection angles and varying image planes[158, 291]. That there is a correction factored into the optics for the lateral movement of the laser spot in the x-y plane is the only requirement for the potential for VA-TIRF on any system. For objective- based TIRF systems such as the one based at the BALM facility, lateral movement of the laser within the objective lens changes the angle at which the laser reflect off of the coverslip, without affecting the position of the TIRF field in the x-y plane.

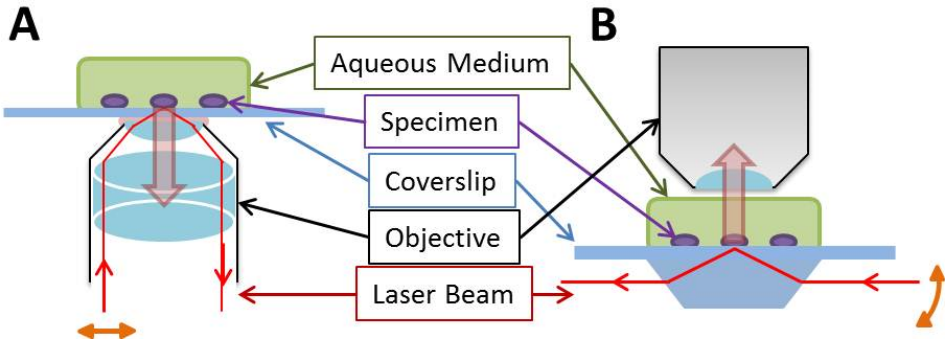

Figure 5.4: Comparison of objective- and prism- based TIRF. A) an objective-based TIRF system. The means of sample illumination and capture of fluorescence both happen through the objective lens. To enable variable angle TIRF, the laser beam must be moved laterally within the objective lens (orange arrow), so that the angle of incidence is altered and a different penetration depth can be acquired. B) a prism-based TIRF system. The laser is under the sample, and prisms are used to attain the correct angle of incidence. The objective lens is above the sample to collect the fluorescence emission. To enable variable angle TIRF in this instance it is necessary to have a system in place that allows the angle of the laser to be altered (orange arrow), without any lateral movement at the sample.

Depending on the physical restraints of the system, and the wavelength of the laser being used, a penetration depth from 60 nm to 600 nm is theoretically possible, although 100 nm to 400 nm is more realistic. Depending on the accuracy of tuning, the measurement of sub-microscopic z-distances is possible, with slices up to five times thinner than

achievable with a confocal scanning microscope[158]. This not only allows the determination of the intensity and distance from the coverslip of a fluorophore, but also has many more applications in *in vitro* studies. Not only qualitatively, where membrane-bound fluorophores can be differentiated from those located in the cytosol, but also quantitative observations have been made based on relative levels of fluorophore excitation[292]. This fine level of detail has made it possible to accurately determine distances between membranes and fluorescent probes[289, 293], and provided the ability to confidently determine cell-substrate topology[290].

VA-TIRF has also made valuable contributions in the field of plant biology. Previously, TIRF microscopy in plant cells was impossible as the plant cell wall can be up to several μm thick, which is much greater than the depth of the evanescent field. Subcritical incident angles had been used to excite only a few select fluorophores in a technique known as variable angle epifluorescence microscopy[294]. This worked to avoid illuminating the whole sample and so inducing much less out of focus light in the resultant images. However, this uneven illumination made quantitative interpretation of the images difficult. With VA-TIRF however, it was shown to be possible to refract the laser light through the outer cell wall membrane at such an angle that it totally internally reflected off of the inner cell wall membrane, setting up a TIRF field in the cytosol of the plant cell[295].

Crucially for this project, the penetration depth of the evanescent field is independent of the polarisation of the incident laser[296].

5.2.2 Polarised TIRF

A standard laser emerges from the fibre unpolarised. This means that the electric field vectors vibrate in all planes lying perpendicular to the direction of transmission. This is the case in standard TIRF microscopy, which results in an evanescent field which is also unpolarised and thus able to excite fluorophores of any given orientation. When light is linearly polarised, all of the electric field vectors vibrate in a single orientation. When

this state of plane polarisation is used in TIRF microscopy, it results in an evanescent field which is also polarised. This is shown in Figure 5.5. *S*-polarised light, which has its electric field vectors parallel to the coverslip, generates an evanescent field which is completely polarised in the y plane, also parallel to the coverslip. *P*-polarised light, which has its electric field vectors perpendicular to the coverslip, generates an evanescent wave which is polarised in the x-z plane.

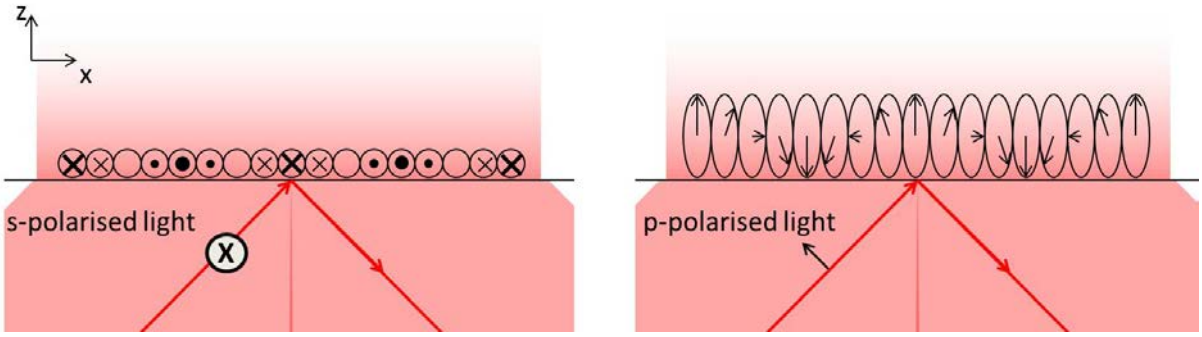

Figure 5.5: An illustration of the evanescent wave when it is generated with a polarised incident laser. S-polarised light generates an evanescent field which is completely polarised in the y plane. P-polarised light generates an evanescent wave which is polarised in the x-z plane.

Photons with electric field vectors parallel to the transition moment of a fluorophore are far more likely to be absorbed. The excitation probability is dependent on the relationship between the orientations of both the fluorophore and the electric field vector of the photon. This relationship is proportional to $\cos^2\theta$, and can be visualised in Figure 5.6.

The polarisation of the emitted photon depends on the orientation of the transition moment. This is the theory behind fluorescence anisotropy studies[297, 298]. Using this property of fluorophores and polarised evanescent waves, incorporating a specialised fluorescent probe that lies in the plane of the membrane will allow detailed knowledge about the orientation of biological membranes. When this is used to study what happens when nanoparticles are introduced, real time responses can be determined, such as affinity and uptake of novel types of particulate drugs.

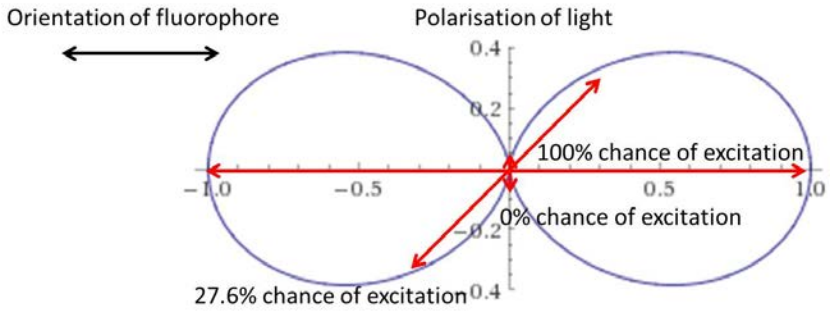

Figure 5.6: An graphical representation of Malus' Law. If a fluorophore is oriented horizontally (black arrow), then the probability of excitation depends on the relative orientation of the electric field vector of the incident photon. Imagine a theoretically perfect system, with a photon travelling directly into (or out of) the page at (0,0), and electric field vector completely aligned to the fluorophore. There is a 100% chance of excitation. This drops to 27.6% for a photon at a 45° angle, and 0% for a photon orthogonally polarised to the fluorophore.This holds true in three dimensions where the fluorophore is free to rotate in the (x,z) plane.

It has been shown that the amphipathic, long acyl chain fluorescent carbocyanine dye, diI-C_{18}-(3) (DiI) lies in the plane of the membrane, not only in artificial bilayers consisting of phospholipids[299] or oxidised cholesterol[300], but also biological plasma membranes[301]. The conjugated bridge chromophore is parallel to the surface of the cell, with the acyl chains embedded in the bilayer parallel to the phospholipid acyl chains, as visualised in Figure 5.7.

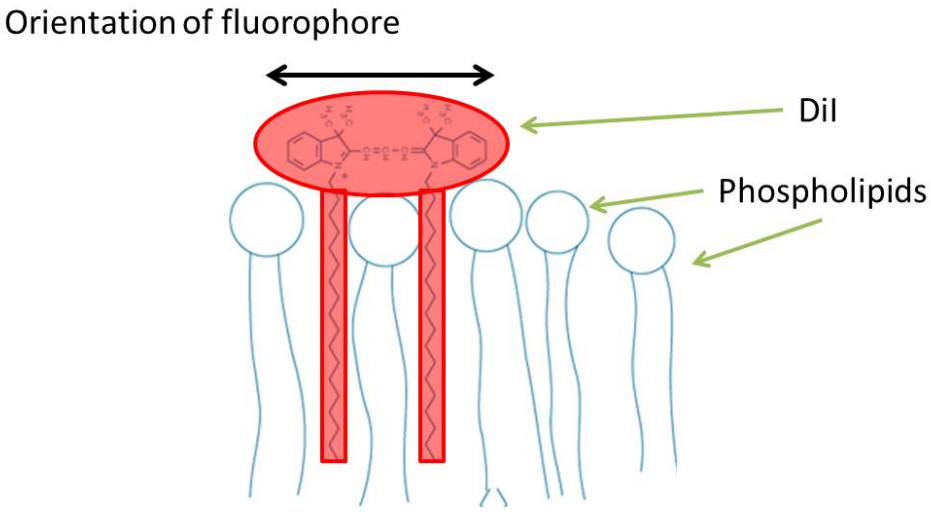

Figure 5.7: A DiI molecule inserts into the phospholipid bilayer of the plasma membrane, with the conjugated bridge chromophore parallel to the membrane surface and the acyl chains parallel to those of the phospholipids.

With polarised evanescent waves, and the chromophore of the DiI molecule lying flat in the cell membrane, it will be possible to preferentially excite those orthogonal to the coverslip, *i.e.* those that are undergoing vesicle formation. It should also be possible to differentiate between those that are entering via endocytosis and those that are directly permeating the membrane (see Figures 5.8 and 5.9). This would make it possible to quantify the results seen in Chapter 2. It would also allow studies of many permutations of nanoparticle and cell types, making it possible to see a cell's response to different particles. For example, it could be shown that targeted anticancer drugs are only endocytosed by certain cell types.

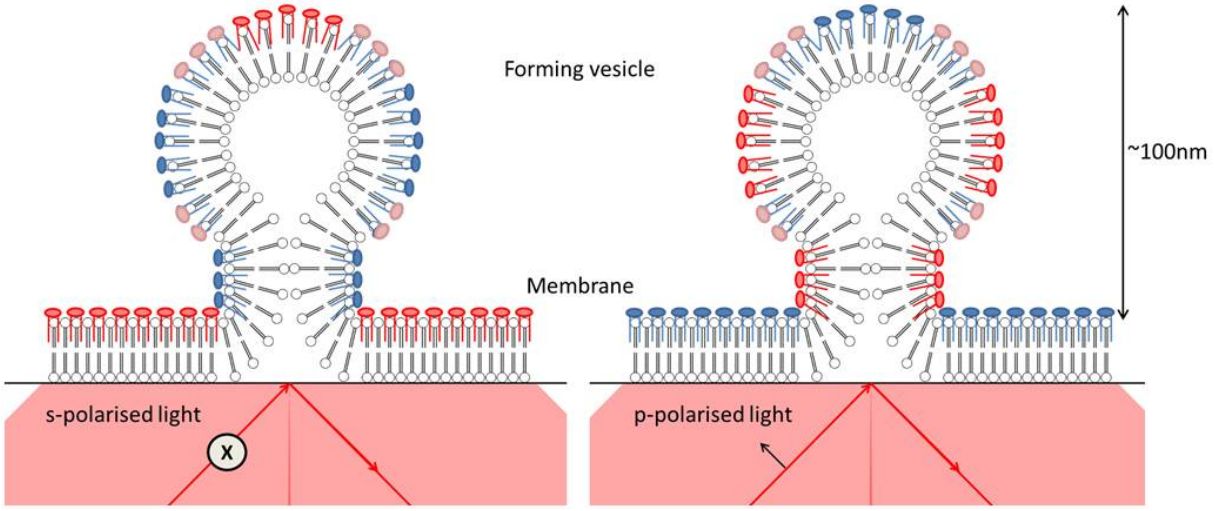

Figure 5.8: *A schematic of how DiI embedded in a forming vesicle would look when illuminated by light of* s- *and* p-*polarisations.*

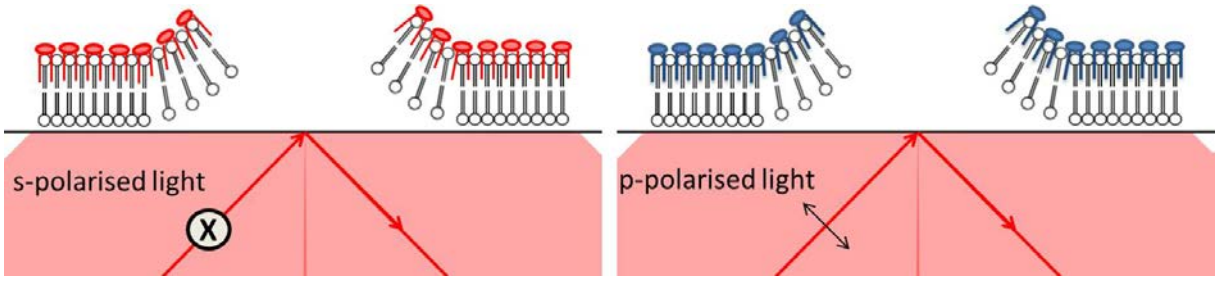

Figure 5.9: *A schematic of how DiI embedded in a permeabilised membrane would look when illuminated by light of* s- *and* p-*polarisations.*

With cell membranes stained with DiI, and using the biological techniques developed in Chapter 4, it will be possible to use TIRF microscopy to study the effects that different nanoparticles have on cell membranes in real time.

Early uses of polarised light in microscopy studied DiI in synthetic vesicles with epi-fluorescence microscopy. These techniques progressed to the use of TIRF with synthetic bilayers to measure how the total fluorescence changed with polarisation angle[302]. As the technique got more sophisticated the types of cell lines used increased through to macrophages and enthrocytes[303]. The mathematical modelling of such events was also able to become more accurate, and benefited greatly from the new data that this technique was able to provide[304]. More recently, individual events of endo- and exocytosis have been identified, with the fusion of chromaffin granules seen to induce changes in plasma membrane topology even before the fusion has occurred[305]. The same group has also analysed exocytosing secretory granules in chromaffin cells, and distinguished these from endocytic events[306].

Other uses have also been found for polarised TIRF. One group used this technique to study the three dimensional strucural dynamics, orientation and rotations of single molecules[307, 308, 309, 310]. They also improved their technique to add in two extra polarisations at 45° to the standard *s*- and *p*- polarisations to be able to successfully measure the rotation of an actin filament about its axis using rhodamine labelled actin monomers[311]. Orientation has also been able to be resolved in plastic films [312]. One technique involved in resolving the orientation of molecules in membranes used polarised fluorescence and acquired images over several angles[313]. This works on the principle of fluorescence anisotropy, so if many fluorophores are lined up in the same orientation then some acquisition angles will detect more emitted light than others[298], thus the orientation of the molecules can be calculated.

Polarised TIRF has also been successfully combined with other imaging modalities to great effect. One group has combined P-TIRF with an Atomic Force Microscope to examine both peptide-induced membrane disorder[314] and the phase separation properties of ternary model membranes[315]. P-TIRF has also been combined with Fluorescence Resonant Energy Transfer measurements, allowing only one camera exposure as opposed to the several usually needed for this type of experiment[316]. This has allowed better time resolution of dynamic associations among subcellular components.

There are several methods suitable for implementation of P-TIRF. The most common way involves using a $\frac{\lambda}{2}$ waveplate to polarise the laser and rotating it to produce the desired evanescent field[314]. This is a relatively slow method, however and would be unsuitable for witnessing real-time endocytic events. Other ways involve using a Pockels cell, a device that changes the polarisation of incident light based on the voltage applied to it[311]. A third way to achieve polarised TIRF would be to have a fast filter wheel in the beamline with orthogonal polarising filters in two of the slots. This would allow rapid changing of the beam polarisation, enabling fast image acquisition times. This gives the option to select a blank filter in the wheel so the unpolarised beam can be used when required. The final way is to have a series of beamsplitting prisms and shutters, so either polarisation can be achieved, or the two beams can pass through if both shutters are open and the original beam can be reformed[303].

5.3 Aims and Objectives

The two techniques of VA-TIRF and P-TIRF are established and well documented. However, there aren't yet any systems that can perform them simultaneously. The aim of this Chapter is to make significant progress towards this goal. The Olympus cell^{tirf} MITICO combiner allows precise and rapid changes to the incident angle of the laser, providing the capability for accurate evanescent wave depth control. This will be preceded by a system of beamsplitting prisms and high speed shutters, built to take the 561 nm laser line, split the beam into orthogonal components, and output the two via polarising fibres. This will have the capability to independently fire either polarisation individually, or having both shutters open will cause the original beam to recombine.

Once complete, this novel imaging system will allow the high spatial and temporal resolution images of membrane dynamics mentioned in the aforementioned publications, with the ability to track these events in three dimensions. It is intended that this system will then be used to study interactions and uptake of nanoparticles with multiple cell types. This will prove useful for visualising the potential for new drugs to enter specific cells, as well as expose any possible health concerns posed by nanoparticles used in edible or cosmetic products.

5.4 Materials and Methods

5.4.1 Olympus IX81 TIRF microscope

The Olympus IX81 microscope comes equipped with 488, 561 and 640 nm Olympus cell* laser lines, which enter the system through the Olympus cell^{tirf} MITICO combiner. This unit allows independent tuning of the laser angle for each individual laser, allowing the controlled adjustment of evanescent wave penetration depths. This process is fully automated and controlled through the Olympus cellSens software. Controlled depths of evanescent wave are achievable from 65 nm to around 800 nm depending on the wavelength of the laser.

5.4.2 Fluorescent bead intensity profiling in Matrigel

10 mm diameter MatTek dishes were prepared with a thin layer of Matrigel as described in Section 4.5.5. 200 nm yellow-green carboxylate-modified fluospheres (Invitrogen) were sonicated for one minute and diluted from stock at a ratio of 1:1000 in PBS. 2 ml were pipetted into the MatTek dish and left at room temperature for one hour. The fluid was aspirated and replaced with 2 ml of PBS before imaging. Images were taken using the 561 nm cell* laser at a power of 5%. Image sets were acquired using the full range of available penetration depths for fluorescence intensity profiling. A fluorescence profile was established by drawing a line across the centre of each of the beads and using ImageJ's 'Plot Profile' function.

5.4.3 Variable angle TIRF with HeLa cells

10 mm diameter MatTek dishes were prepared with a thin layer of Matrigel and 20 nm yellow-green carboxylate-modified fluospheres as described in Section 4.5.5. HeLa cells were plated to achieve 20% confluence and left to settle for two hours. Media was aspirated and replaced with 2 ml of cell imaging media as described in Section 4.4.2. Images were obtained at a range of evanescent wave penetration depths, and the increase in number of fluorescent spots at each step was calculated by counting all within the cell boundary (established from a brightfield image) and subtracting the number seen in the previous frame.

5.4.4 List of components composing the laser polarisation unit

All of the components were sourced from ThorLabs (Ely, UK).

Solid aluminium breadboard (part number MB3045\M) x 1

Single mode fibre patch cable (P1-460A-FC-1) x 1

Aspheric fibreport (PAF-X-11-PC-A) x 3

Post mounting bracket (HCP) x 3

10 mm polarising beamsplitter cube (PBS101) x 1

Small adjustable clamping arm (PM3\M) x 1

Kinematic platform mount (KM100B\M) x 1

Optical beam shutter (SH05) x 2

Optical beam shutter controller (SH10) x 2

Broadband dielectric mirror 400 - 750 nm (BB1-E02) x 4

Precision kinematic mirror mount (KS1) x 4

488 nm, polarising maintaining, FC\PC patch cable, panda style (P1-488PM-FC2) x 2

Optical post (TR75\M) x 10

Post holder (PH50E\M) x 10

Clamping fork (CF175) x 10

5.4.5 Construction of the laser polarisation unit

Design of the laser polarisation unit was based on designs that have been shown to work in other cases[303, 311, 315]. A majority of previous designs were built around prism-based TIRF, so after polarisation, the laser had to be angled and oriented correctly. However, some adaptations had to be made to these due to the objective-based nature of the Olympus IX81 TIRF microscope. For simultaneous variable angle TIRF, it was necessary that after polarisation, the lasers had to enter via the MITICO combiner. Therefore coupling to polarisation maintaining fibres was essential. A diagram showing the planned configuration is shown in Figure 5.10.

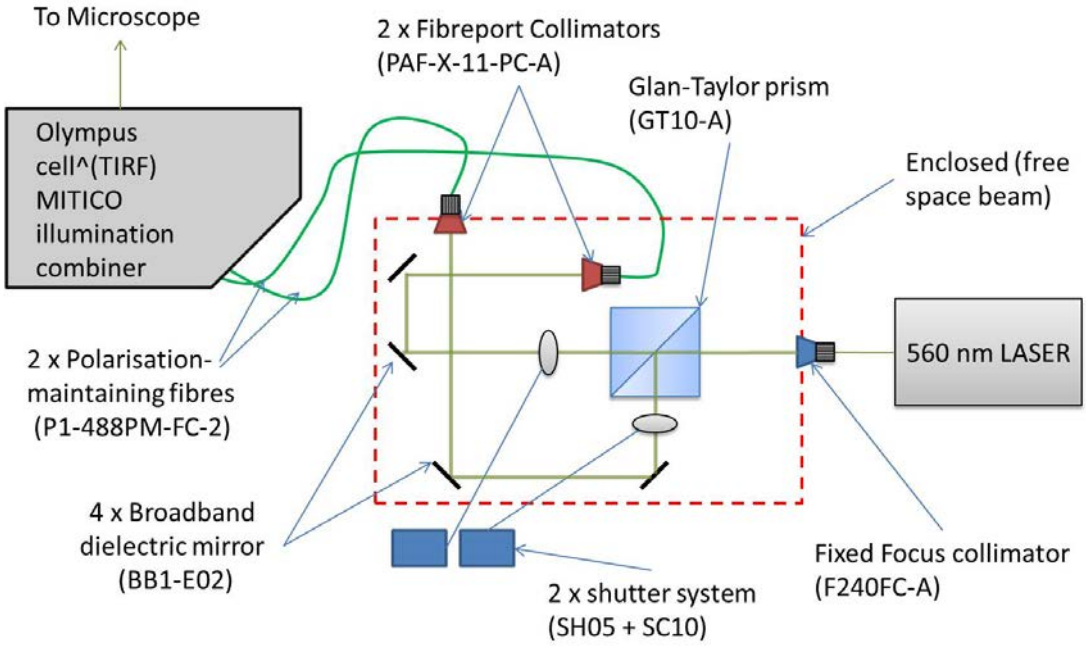

Figure 5.10: *A diagram showing the plan for laser polarisation unit. The input laser is collimated into free space by the F240FC-A. The beam is then split into orthogonal components by the GT10-A Glan Taylor prism. The beams are either blocked or let through by the SH05 shutters. The beams are then reflected off of BB1-E02 broadband mirrors to align them into the PAF-X-11-PC-A fibre couplers. They then pass through the P1-488PM-FC-2 polarisation maintaining fibres and enter the microscope through the MITICO combiner. Components sourced from ThorLabs.*

5.4.6 Testing and optimisation of the laser polarisation unit

Preliminary testing of the laser polarisation unit was carried out using a 0.9 mW, 532 nm laser diode module (ThorLabs, Ely). Initial tests were performed using this light source and a linear polarising filter. Once satisfactory results were seen, accurate measurements were performed using a polarisation extinction ratio meter (OZ Optics, Ontario). This works by calculating the ratio between the optical power of the signal on the intended state of polarisation and the power on the orthogonal axis. The intention was to tune the instrument as accurately as possible using this less intense laser before fine tuning using the 561 nm Olympus cell* laser, prior to aligning to the cell^{tirf} MITICO combiner.

5.5 Results and Discussion

5.5.1 VA TIRF proof of principle

Based on the results from Section 4.5.6, it is hypothesised that through use of variable angle TIRF, it should be possible to distinguish between nanoparticles embedded in Matrigel, and those that have been internalised by the cell.

Matrigel testing and nanoparticle intensity profiling

Firstly, it had to be established that having a layer of Matrigel on the coverslip did not affect the nature of the TIRF field. It was also necessary to confirm that the fluorescence of the nanoparticles was not affected by the presence of the Matrigel proteins. The coverslips were prepared in the same way as described in Chapter 4, using 200 nm particles. The reason for this was because 20 nm particles are much smaller than the resolution of the system, so 200 nm particles would give a clearer view of the results. It was also due to the constraints of the variable angle TIRF; the smallest possible penetration depth of the evanescent field for the 561 nm laser was 65 nm, and could be increased in steps of roughly 30 nm (originating from the stepwise changes in laser angle). These increases are larger than the diameter of the 20 nm particles. The results from this can be seen in Figure 5.11.

It can be seen in both cases that increasing the penetration depth of the evanescent field results in a decrease in fluorescence intensity of the nanoparticle, without affecting the full width at half maximum (FWHM) of the bead profile. This is 260 nm ($\pm 5\%$, $n = 3$, 10 spots in each image) for all penetration depths in both conditions. Where Matrigel proteins are present, intensity levels are on average 2.45 times less intense than those observed where the nanoparticle is on the bare glass coverslip. This was calculated by examining the ratio between the intensity levels at each individual depth and x-position in the graphs in Figure 5.11. The reason for this could be due to either the particles in

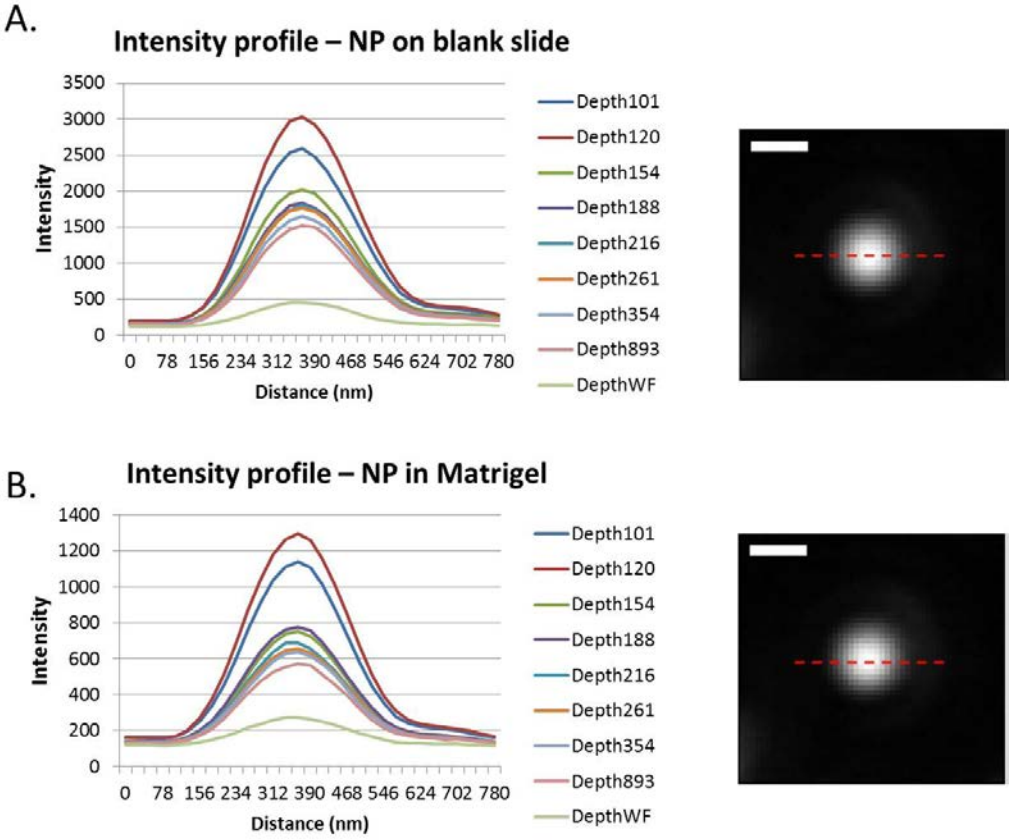

Figure 5.11: *Intensity line scans and corresponding pictures of 200 nm particles illuminated with evanescent waves of varying depths. Intensity profiles are taken from values along the dotted red lines. A) shows the intensity profiles/ image of a nanoparticle on a plain glass coverslip. B) shows the intensity profiles/ image of a nanoparticle embedded in Matrigel, as prepared for an experiment. The image is taken with a 60× objective lens in the focal plane of the coverslip. This, and the highly fluorescent nature of these particles, helps to explain why the particles appear so large. This shows that the Matrigel isn't having any adverse effects on the images, aside from overall intensity, and so won't cause a problem in image processing. Average full width at half maximum of both of the intensity profiles is 260 nm (±5%). Scale bar is 500 nm.*

the Matrigel being further away from the coverslip, or if the Matrigel itself was causing recorded intensity levels to be lower. If the particles on the Matrigel were a greater distance from the coverslip than the particles on bare glass, a small penetration depth of evanescent wave would result in a lower relative intensity than deeper penetration depths. However, when these levels are normalised as displayed in Figure 5.12, a strikingly similar trend is observed.

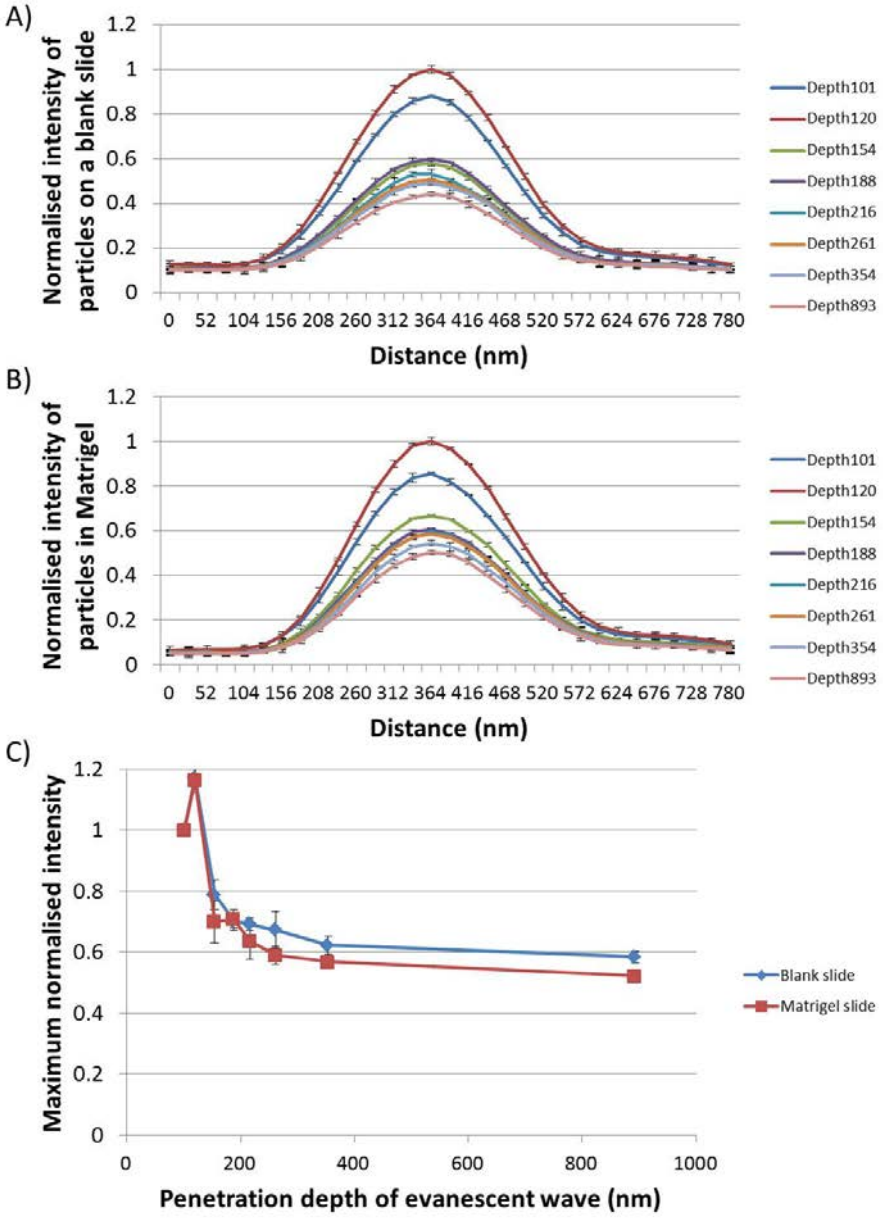

Figure 5.12: *Normalised nanoparticle spot intensity at the coverslip for different penetration depths of evanescent wave. A and B) normalised spot instensity for particles on a blank slide and embedded in Matrigel respectively. C)The normalised maximum intensities of the particles on a blank slide (blue) or embedded in Matrigel (red), plotted against the penetration depth of the evanescent wave at the point of imaging. It can be seen that there is no significant difference between the normalised intensities of a nanoparticle on blank slide or embedded in a thin layer of Matrigel. It can also be seen that the deeper the penetration depth of the evanescent wave, the less intense the fluorescence of the particle when it is on the coverslip. This excludes the peak at 120 nm. Number of experiments,* n *= 3, 20 nanoparticle spots analysed per experiment. Bars show standard error in data.*

The general trend is an exponential decrease in the fluorescence intensity of a particle on the coverslip when the penetration depth of the evanescent wave is increased. This leads to the conclusion that the particles are similar distances from the coverslip in both cases, and so the matrigel itself must be causing the observed decrease in fluorescence intensity.

An increase in normalised fluorescence intensity when the penetration depth is 120 nm can be seen in both cases in Figure 5.12. If the conclusion that particles in both instances are the same distance from the coverslip, this can be explained. For any particle, the point of maximum cross sectional area with respect to the direction of the evanescent wave will be at a depth equal to its radius, plus the distance from the coverslip. Studies have shown that due to electrostatic forces, polystyrene nanoparticles of this size remain around 20 nm from a glass coverslip[317], making the distance of the centre of the nanoparticle 120 nm from the coverslip. It has also been established that the Stokes radius of laminin, the most abundant protein in Matrigel, is 18.6 nm[318]. If the nanoparticle was resting on a layer a single protein thick, which isn't unlikely based on the calculations outlined in Section 4.5.5, then this would explain the observed increase in fluorescence intensity at a depth of 120 nm.

It has been shown that the presence of Matrigel does not affect the fluorescence profile of nanoparticles, although observed intensity is decreased, which may have a negative impact on weaker fluorescent signals. However, the data in Figures 5.11 and 5.12 were obtained with identical laser power settings (5% power). Therefore if a signal is too weak, laser intensity can be increased to combat this. Variable angle TIRF was then performed on live cells.

Live cell imaging

To further the study began in Section 4.5.6, cells were introduced and variable angle TIRF was performed. Figure 5.13 shows the effect of varying the depth of evanescent wave after a two hour incubation on top of the prepared Matrigel/ nanoparticle base.

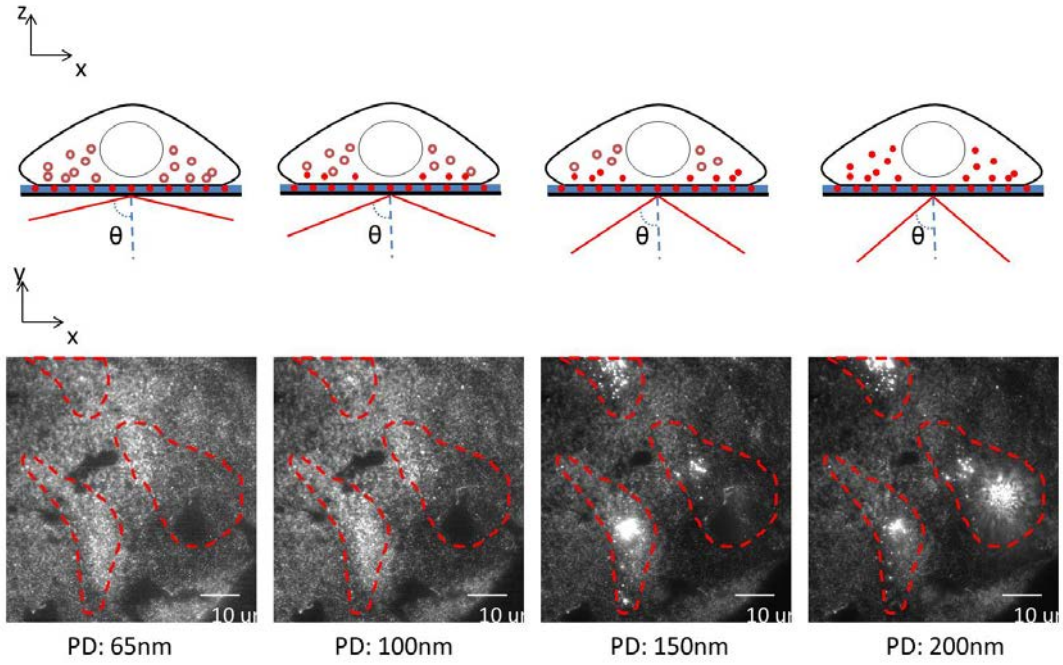

Figure 5.13: *Images show the outline of HeLa cells (red) after a two hour incubation on top of matrigel containing 20 nm nanoparticles. Figures above show a representation of the experimental setup. It can be seem that decreasing the angle of incidence on the coverslip increases the penetration depth of the evanescent wave and so nanoparticles within the cell become illuminated. These nanoparticles are still only a few hundred nanometres inside the cell.*

It can be seen that as the penetration depth of the evanescent field increases, the nanoparticles that have already been taken up by the cells become more visible. It can also be seen that the nanoparticles still embedded in the Matrigel layer get progressively dimmer with increasing penetration depth. This correlates with the findings in Figures 5.11 and 5.12. In this case, the nanoparticles are only 20 nm (as opposed to 200 nm), and so the depth that corresponds to the brightest intensity of these nanoparticles would be around 30 nm (obtained from the assumption that the nanoparticles are 20 nm above the glass and the brightest point would be halfway up the height of the nanoparticle).

Due to the constraints of the system, the smallest possible penetration depth is 65 nm which is why the particles get dimmer throughout the series of images. Figures 5.14 and 5.15 show how both the number and intensity of internalised nanoparticles change with penetration depth.

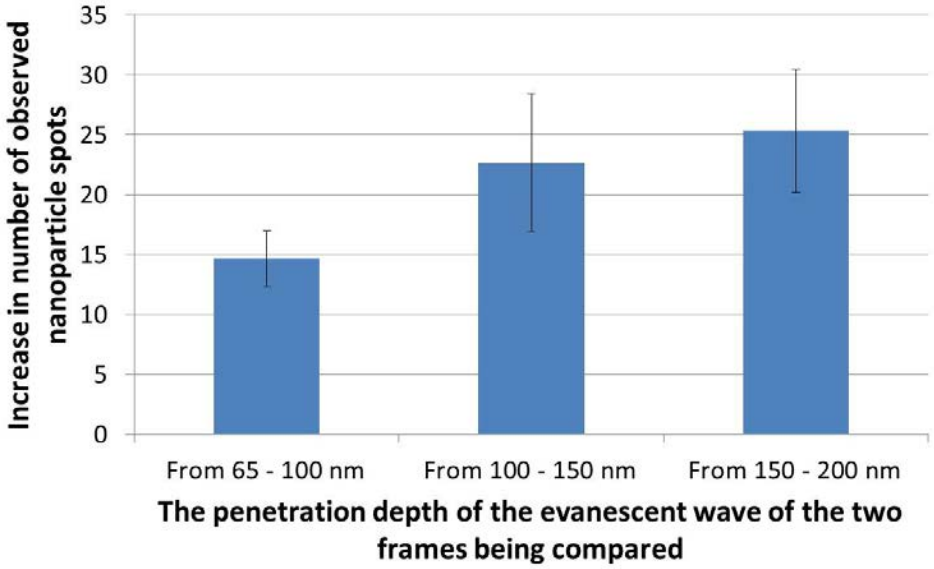

Figure 5.14: *Increasing the penetration depth of the evanescent wave increases the number of nanoparticles that can be visualised after internalisation by a cell. 20 nm particles were on top of Matrigel as described previously. HeLa cells were plated and incubated at 37°C for two hours. TIRF imaging with evanescent waves of different penetration depths was then performed. Increase in number of spots was calculated by counting all spots within the boundary of the cell, and subtracting the number seen from the previous, shallower, depth. Boundary of cell was known from brightfield imaging,* n = *3, bars show standard error in data.*

It can be seen in Figure 5.14 that as the penetration depth of the evanescent wave increases, so do the number of internalised nanoparticles that are excited by it. This is significant as it means that when imaging the cell at a high temporal frequency, by scanning the laser through multiple incidence angles it will be possible to identify those that are moving further away from the coverslip.

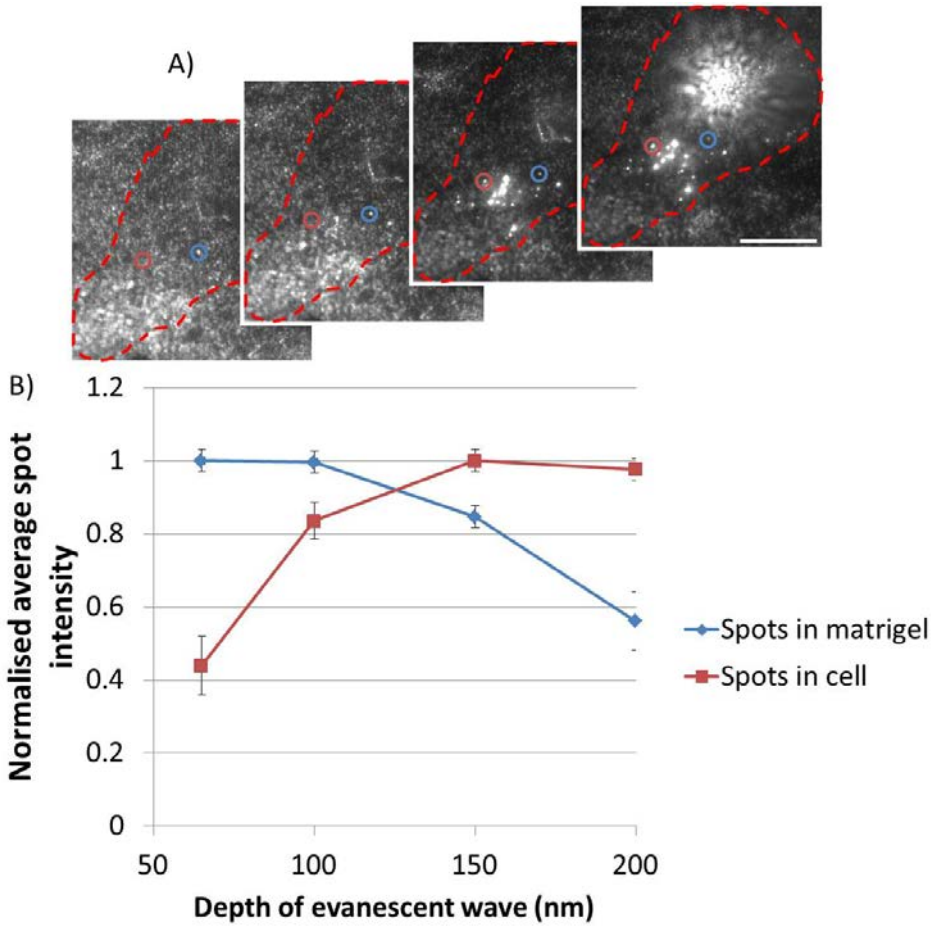

Figure 5.15: *Nanoparticle spot intensity changes under different evanescent wave penetration depths. A) shows an example of a HeLa cell under the same conditions as described in Figure 5.13. Highlighted are examples of two spots, one in Matrigel close to the coverslip (blue), and one that has been internalised by the cell (red). B) shows the normalised average intensity of these spots. The intensity value changes depending on how far the nanoparticle is away from the coverslip. The intensity profiles show that nanoparticles in the Matrigel get dimmer with increasing penetration depth, whereas nanoparticles in the cell get brighter.* n = *3. 5 spots for each condition were deliberately selected for displaying the relevant properties. Bars show standard error in data.*

The graph in Figure 5.15 shows the advantage variable angle TIRF has over standard TIRF microscopy. If the incident angle of the laser is fixed, there would be no way of knowing where a nanoparticle was in relation to the cell, as a point of high fluorescence intensity could indicate multiple distant fluorophores in close proximity to each other; or fewer, closer to the coverslip. In the graph, at a penetration depth of around 125 nm the spots have the same intensity, and so their position in z would be impossible to determine without performing a timelapse imaging run and analysing as shown in Figure 4.9. By

looking at intensity profiles over a range of penetration depths, this difference is resolved instantaneously. It can be seen that the blue line represents nanoparticles close to the coverslip, and the red line highlights those that have been internalised by the cell. The reduction in intensity seen for nanoparticles still embedded in Matrigel in this case is equivalent to that seen in Figure 5.12. This is to do with the excitation light inhabiting larger volumes with increased penetration depth, and so associated intensity for a given area near the coverslip is reduced.

These studies have shown the benefits that variable angle TIRF has over standard TIRF, and that the technique is possible to implement on our instrument. It has been shown that it is possible to distinguish between nanoparticles below the cell and those that have been already internalised from a set of images at a single timepoint, rather than have to take a timelapse as demonstrated in the previous Chapter. If these could then be further enhanced by enabling concurrent polarised TIRF, the methods put forward in the previous Chapter could be used to study in great detail the membrane dynamics associated with uptake of nanoparticles and the effects these will have on cells. For example, modifications to the surface of particles in attempts to either optimise or negate the specificity of drugs to different cell types could be easily and rapidly visualised.

5.5.2 Preparations for polarised TIRF

In order to enable the technique of polarised TIRF on the Olympus IX81 microscope, modifications to the input laser lines and MITICO TIRF combiner unit had to be performed. The Olympus cell* 488, 561 and 640 nm laser lines enter the microscope through the MITICO combiner as displayed in Figure 5.19A. This is the unit that contains the controls that allow variable angle TIRF on the system. Currently there is an empty entry port on the combiner which would be made use of.

Construction of the laser modification unit

To allow polarised TIRF on this instrument, the 561 nm laser would have to be modified before it entered the microscope. Light produced by the Olympus cell* laser emerges unpolarised. By first collimating this beam in free space via coupling the laser fibre to a fixed focus collimator, it could be made to enter a Glan-Taylor polarising prism and split into two orthogonally polarised beams of light. Re-entry into separate fibres that maintained polarisation would then allow coupling to the MITICO combiner. Incorporated into this design are two high speed shutters, to selectively block light of one polarisation. Alternatively, if both shutters are left open, light of both polarisations would enter the microscope at the same time, and would recombine to recover the qualities of the initial unpolarised laser. A photograph of the final configuration can be seen in Figure 5.16.

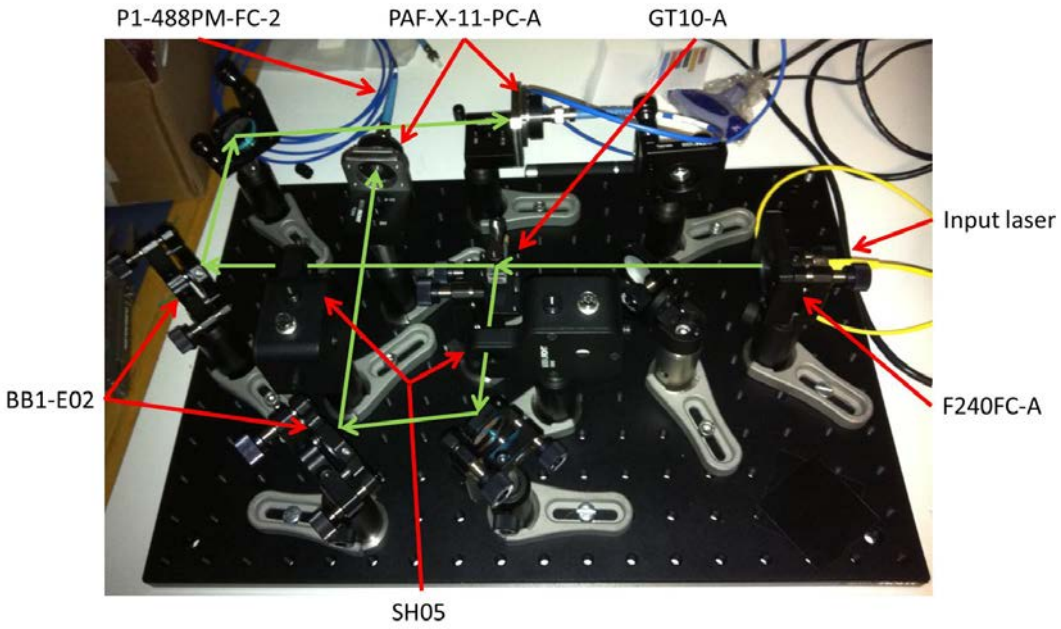

Figure 5.16: *A photograph of the constructed polarising laser system to enable pol-TIRF on the Olympus IX81 microscope. The input laser is collimated into free space by the F240FC-A. The beam is then split into orthogonal components by the GT10-A Glan Taylor prism. The beams are either blocked or let through by the SH05 shutters. The beams are then reflected off of BB1-E02 broadband mirrors to align them into the PAF-X-11-PC-A fibre couplers. They then pass through the P1-488PM-FC-2 polarisation maintaining fibres and enter the microscope through the MITICO combiner.*

The high speed shutters selected for this project have the capability to run at 25 Hz if required. This would allow five separate image stacks of five penetration depths with variable angle TIRF every second. This is equivalent to the frame rate used to acquire the data in Figure 4.9. The adjustable broadband dielectric mirrors were necessary in order to align the lasers to the fibreport collimators. The light must pass through perfectly straight in order to provide the maximum coupling efficiency to the polarisation maintaining fibres. These fibres have cores as illustrated in Figure 5.17, where one axis is known as the slow axis. The stress rods illustrated introduce a linear birefringence which maintains the polarisation of linearly polarised light providing it is aligned correctly upon entry.

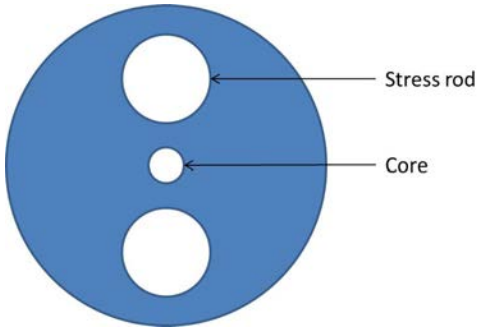

Figure 5.17: *A cross-section of a 'Panda' style polarisation maintaining fibre. The stress rods running either side of the core of the fibre introduce birefringence, slowing the speed of light along this axis and maintaining linear polarisation of the beam.*

Optimising polarisation efficiencies

Once the necessary components were roughly in place, alignment could be established and optimised. The initial configuration was tested using a 0.9 mW, 532 nm laser diode module. This is much smaller and less powerful than the Olympus cell^{TIRF} laser that will be used eventually.

Initial construction It was first established by eye that this source was unpolarised by rotating a basic polarising filter by hand in the path of the light source and noting that the perceived intensity did not change. It was then confirmed that after passing through the Glan-Taylor prism, each component of the laser was polarised to an extent, as seen by maximum and minimum intensities every 90° rotation of the polarising filter. Slight changes to height and angle of the laser beam in relation to the polarising cube were performed as was necessary to ensure the beam was perpendicular to the face of the cube. This was required to maximise the polarisation efficiencies and minimise the extinction ratio[319].

Each of the polarised beams then reflect off two adjustable mirrors before entering the couplers to the polarised fibres. Light must enter these fibres perfectly straight to ensure the reliable transmission of signal. Figure 5.18 highlights this non-trivial process of alignment in two dimensions. Once more, initial confirmation could be attained by eye as the opposite end of the fibre was strongly illuminated upon successful light propagation.

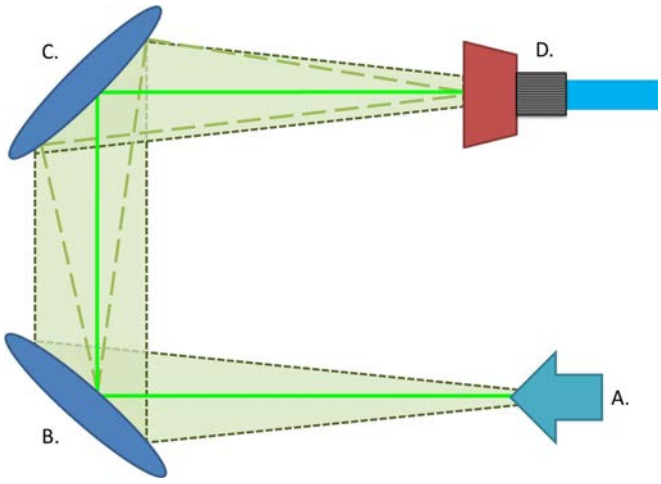

Figure 5.18: *A top-down view of the beam coupling process. A) The direction of light once it has left the Glan-Taylor polarising prism. This could be travelling at one of many angles. B and C) The alignment mirrors. The angle the light hits the mirror determines the angle it leaves the mirror. It is required that the light enters the fibre coupler (D) perfectly straight to allow efficient transmission of polarised light (bright green line). If the mirrors are misaligned, when the light hits the fibre coupler there will be no transmission (light green dashed line). If the laser does not leave the polarising cube straight (due to the angle it enters at) then it makes it very difficult to align the beam successfully (dark green dotted line, transparent green background).*

Intensity measurement Once transmission of light was obtained at the opposite end of both fibres, the power and polarisation extinction ratio for each of the beams can be measured. For this a polarisation extinction ratio meter (PERM) was used. As the laser using to test this system was 0.9 mW, equal splitting of the original laser beam would give 0.45 mW of power to each polarisation. According to the manufacturer's specifications, there is a maximum insertion loss of 1.5 dB in coupling a beam into one of the polarisation maintaining fibres[320]. The insertion loss is calculated using the formula:

$$IL(dB) = 10 \times log_{10}\frac{P_T}{P_R} \tag{5.1}$$

Where 'IL' is the insertion loss in decibels, 'P_T' is the power transmitted to the fibre, and 'P_R' is the power received at the detector. Putting the values IL = 1.5 and $P_T = 0.45$ into this equation gives a maximum output value in each fibre of 0.32 mW, assuming equal distribution of power.

Following alignment, actual measured power outputs in each of the fibres were 0.246 mW for the *p*-polarisation fibre and 0.137 mW for the *s*-polarisation fibre. While this totalled only 60% of the total possible power ($\frac{0.246+0.137}{2\times0.32}$), it was decided that this was suitable to prove the principle, as it would have to be realigned when the Olympus 561 nm laser was attached for use on the microscope.

Polarisation measurement Polarisation extinction ratio is determined by calculating the ratio between the optical power of the signal on the intended state of polarisation and the power of the signal on the orthogonal axis[321]. Intensities are calculated by transmitting the beam through a rotating polariser and onto a detector. As the polarising filter is rotated, intensity values are recorded. Polarisation extinction ratio is then calculated by:

$$ER = 10 \times log\frac{P_{max}}{P_{min}} \tag{5.2}$$

Where 'ER' is the extinction ratio, 'P_{max}' is the maximum recorded power, and 'P_{min}' is the minimum recorded power. If the light is not polarised, then $P_{max} = P_{min}$, and the extinction ratio is 0. According to the manufacturer's specifications, the transmitted (p-polarised) beam should have an extinction ratio T_P:T_S > 1000:1. The reflected (s-polarised) beam will have an extinction ratio of roughly 100:1. Most polarised laser sources claim extinction ratios of around 100:1[322, 323], so the beam profiles from the polarising cube should be adequate for these experiments. Extinction ratios observed once light has travelled through a fibre are much less than these initial values. Measurements from different studies claim between 13:1 and 25:1 to be a 'good' extinction ratio for light of this wavelength[324, 325].

Following alignment, polarisation extinction ratios were determined for each of the fibres[321]. For the p-polarised fibre, a ratio of between 10 and 11:1 was observed, and for the s-polarised fibre, an extinction ratio of between 7 and 8:1. While this is a lower ratio than what other groups have managed to obtain[324, 325], it does show that the instrument is successfully turning an unpolarised laser into two lasers that display polarised behaviour. Once again, more rigorous optimisation of polarisation would have been performed once the microscope was ready. It should also be noted that 'rotating polariser' type PERMs such as the one used tend to give an underestimate for the polarisation extinction ratio[326], as other methods typically subtract signal from random polarisations, and so this value is likely to be pessimistic.

MITICO TIRF combiner modifications

The current set-up of the Olympus cell^{tirf} MITICO system can be seen in Figure 5.19A. This is the unit that aligns the lasers going into the microscope, and contains the necessary components for VA-TIRF. The intention is to move the 640 nm laser line to the bottom input, and couple the polarisation-maintaining fibres to the two central inputs. The dichroic mirrors for the 561 and 640 nm lasers will be moved down, and a specially designed dichroic that allows p-polarised light through but reflects s will be fitted in the second slot. Talks have been held with Cairn Research (Kent, UK) who have agreed to produce a suitable custom piece. The final modification will be to replace the polarising beamsplitter in the top of the MITICO with a standard mirror to prevent disruption of the polarised beams. This is in place to direct and 'clean up' the beam, *i.e.* even out any distortions in intensity and phase profile that may be present. However, the unit built has been tested for efficiency of polarisation and intensity profile, and has been found sufficiently uniform so that the lack of this filter will not prove disadvantageous. The orthogonally polarised fibres will be able to be independently fired using the high-speed shutter system incorporated into the laser unit. Alternatively, if both shutters are open, the 540 nm beam will recombine within the microscope before exposure to the sample.

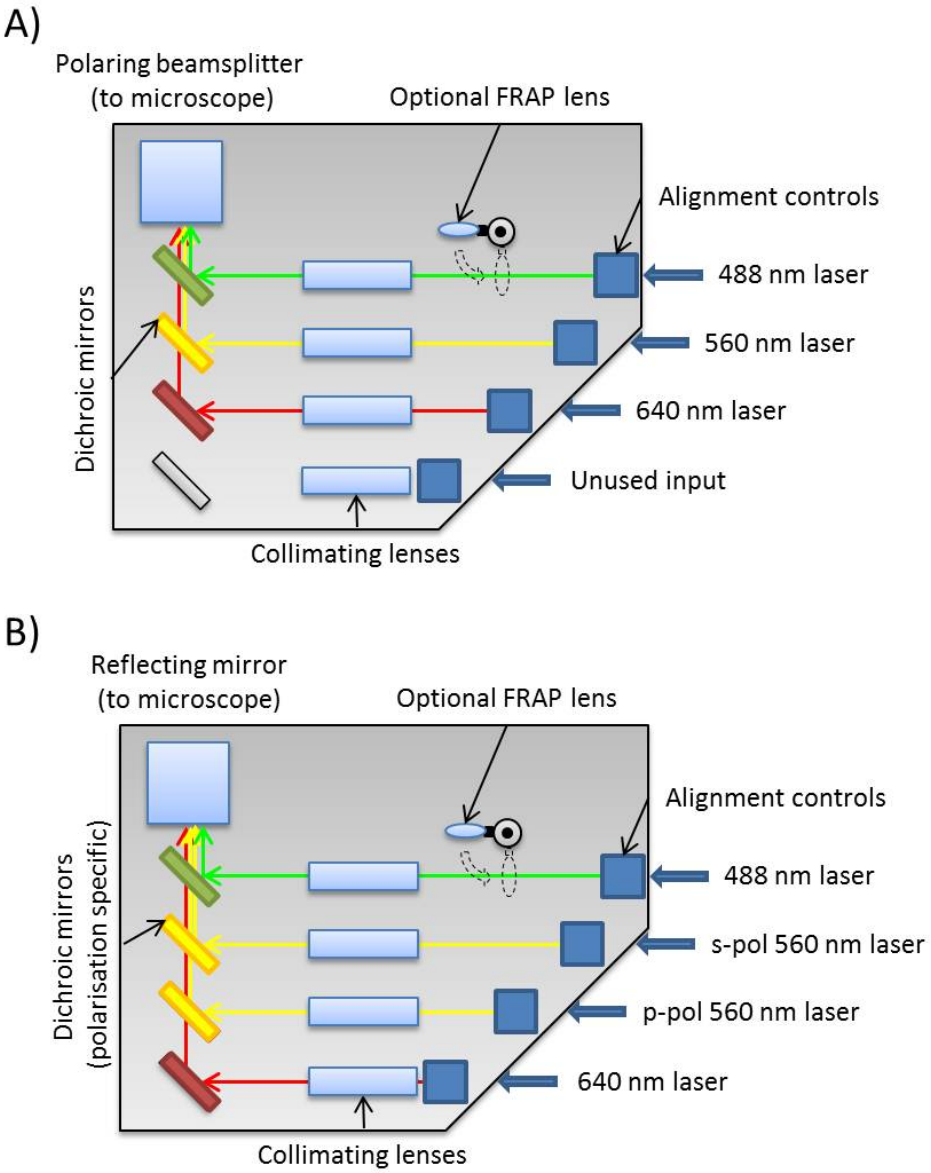

Figure 5.19: *A) The inside of the TIRF combiner as it currently stands. Three laser lines, 488, 561 and 640 nm currently enter the microscope through the combiner. The fibres are connected to the alignment controls, which allow movement in the* (x,y) *plane. The beams pass through individual collimating lenses, reflect off dichroic mirrors, and pass through a polarising beamsplitter to enter the microscope body. The polarising beamsplitter leading to the microscope acts as a "clean-up filter", blocking the unwanted output range from the laser. This would have to be replaced to enable polarised TIRF, with additional checks performed to ensure any noise transmitted is minimised[327]. B) Planned modifications to enable polarised TIRF.*

Unfortunately Olympus were unable to make the requested internal alterations within the time constraints of this thesis, and so the completed and functional laser polarisation unit was not able to be coupled to the microscope.

5.6 Conclusion

There is a need in research for a method of rapid analysis and quantification of the way in which nanoparticles interact on a cellular level. Specifically, if the effect a nanoparticle had on cell membrane dynamics could be determined in real time, rates of active or passive uptake could be calculated. This could be used to provide an immediate insight into whether a newly modified drug was more effective in entering the desired cells, or whether nanomaterials developed for a product proved destructive to the plasma membrane. To this end, modifications of a TIRF microscope have been outlined, allowing detailed and accurate visualisation of z-dimensional profiling with VA-TIRF, in tandem to membrane curvature profiling using P-TIRF. Once final preparations have been made, visualisation of many different nanoparticles and cell types will be possible. This would represent a huge improvement in both speed and detail over current methods.

CHAPTER 6

SUMMARY, CONCLUSIONS AND SUGGESTIONS FOR FUTURE WORK

6.1 Overview of work undertaken in this study

Nanoparticles are being produced faster than ever thanks to their interesting and often unexpected properties when compared to bulk material of the same composition. This has meant they have found uses in many different sectors, from food and beauty products, to medical and bioengineering fields. However the legislation governing their use is not always clear, and the potential for human exposure, intentional or otherwise, is increasing. The range of nanoparticles it is possible to manufacture, in different sizes, shapes and compositions, all with varying characteristics, leads to the need for a more thorough characterisation process in biological environments.

6.1.1 A study into the current methods of studying NP internalisation

A study resulting in a published paper[104] was conducted examining the entry route of one type of nanoparticle into a single cell type. This was not only to characterise this interaction, but also as an insight into the work necessary to complete such a task. It was concluded that 20 nm carboxy-modified spherical polystyrene nanoparticles enter HeLa cells primarily via clathrin-mediated endocytosis, and that they also have the ability to

directly permeate the cell membrane. The amount of time invested in this project, both experimentally and analytically, led to the conclusion that if multiple types of nanoparticle were to be tested with many different cell types, a more efficient technique was required.

In order to improve methods of nanoparticle characterisation, three areas to focus on were identified. These were: the computational analysis of the images obtained through light microscopy; developing new biological protocols enabling more relevant studies to be performed; and upgrades to existing hardware.

6.1.2 Computational methods of improvement

Previous analysis of images involving colocalisation of nanoparticles to fluorescent markers within the cell either relied on manual quantification, which is both time consuming and inconsistent, or computational methods which were often inaccurate when looking at images with high amounts of noise. An object-based approach was developed making use of a new noise-reduction algorithm which was more reliable than existing computational methods, and much faster than manual analysis. Comparisons to both manually and computationally generated data verified the program.

6.1.3 Biological methods of improvement

When studying uptake of nanoparticles into cells, visualisation at the plasma membrane is ideal. Development of a protocol whereby nanoparticles are embedded into a thin layer of matrix proteins before exposure to cells allowed the use of TIRF microscopy in this analysis, enabling colocalisation experiments with fluorescently tagged endocytic markers. The high signal to noise ratio in images obtainable with TIRF microscopy combined with the speed of live cell imaging not possible with confocal microscopy permitted a novel perspective when studying nanoparticle uptake.

6.1.4 Towards physical methods of improvement

By altering the incident angle of the laser in TIRF microscopy, the depth of evanescent illumination can be changed during an experiment. This can be used to provide z-dimensional information on the order of hundreds of nanometres. By incorporating polarised lasers it is also possible to determine an element of membrane curvature on the basal surface of cells. Significant steps have been made to incorporate these two exciting techniques in the same physical system, allowing analysis of nanoparticle uptake never seen before. If the membrane dynamics of a cell internalising a nanoparticle could be determined completely in real time, it would offer a unique view of a cell's initial response to nanoparticle exposure. This would enable rapid quantification over a range of nanoparticle and cell types, and results of human exposure would be better understood. This would not only aid in understanding potential new nanomedicines better, but would also offer a unique method of studying in real time how modifications affect membrane dynamics and cellular uptake.

6.2 Future work

It is proposed that any TIRF microscope can be used for polarised TIRF experiments for determining membrane curvature. All current forms of implementing polarised TIRF involve interfering with the excitation optics, via waveplates, Pockels cells, beamsplitters or filters as outlined in Section 5.2.2. However, no current system at the time of writing attempts to determine orientation of the plasma membrane by looking at the polarisation of emitted fluorescence. The following proposed setup would enable the benefits of polarised TIRF with a modified DualView, without necessary changes to the excitation optics or microscope internal.

Regular TIRF microscopy uses an unpolarised laser and so excites molecules of all orientations. As illustrated in Figure 5.6, a molecule is much more likely to be excited by an incident photon with its electric field vector in the same orientation as its chromophore. When the molecule then fluoresces, the electric field vector of the emitted photon is the same as when it was absorbed. With this knowledge, it is theorised that points of membrane curvature should emit a much higher proportion of p-polarised light than plasma membrane parallel to the coverslip. Therefore if it was possible to differentiate between s- and p- polarisations of emitted light, the same information could be gained as with traditional polarised TIRF, without having to manipulate the incident laser at all. This could be possible using a modified DualView system as outlined in Figure 6.1.

The modifications proposed involve changing the dichroic mirror and coloured filters as seen in Figure 4.1 for a Glan-Taylor prism and orthogonally oriented polarising filters. This would allow all molecules of DiI in the membrane to be excited by the unmodified 561 nm laser, and the light emitted by flat membrane would be sent to one half of the CCD while the light emitted by points undergoing endocytosis or other cases of membrane curvature would go to the other side. These could then be aligned as before. This can be coupled with the variable angle TIRF to obtain z-profile data, and with images of nanoparticles from the 488 nm channel to study internalisation rates and methods.

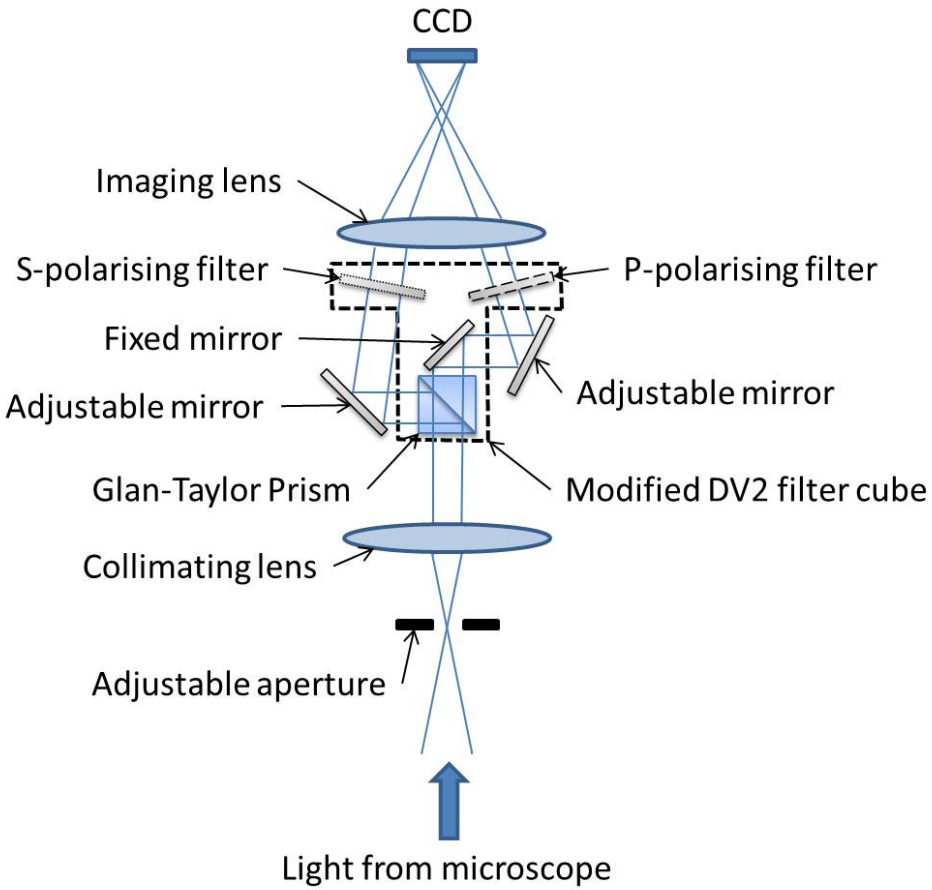

Figure 6.1: A schematic showing a potential for an alternative way of implementing polarised TIRF. Instead of a coloured filter cube in the Dualview system, it is proposed that a Glan-Taylor prism (or equivalent) would be suitable to split the resultant emission from DiI in the membrane and see results of curvature in one rather than two image acquisitions.

Appendices

APPENDIX A

PUBLISHED WORK

Poulter, Natalie S., William TE Pitkeathly, **Philip J. Smith**, and Joshua Z. Rappoport. The Physical Basis of Total Internal Reflection Fluorescence (TIRF) Microscopy and Its Cellular Applications. *Advanced Fluorescence Microscopy*, pp. 1-23. Springer New York, 2015.

Smith, Philip J., and Joshua Z. Rappoport. Development and application of novel imaging methodologies to the study of the cellular uptake of manufactured nanoparticles. *2012 European Microscopy Congress Proceedings*, 2012.

Smith, Philip J., Maude Giroud, Helen L. Wiggins, Florence Gower, Jennifer A. Thorley, Bjorn Stolpe, Julie Mazzolini, Rosemary J. Dyson, and Joshua Z. Rappoport. Cellular entry of nanoparticles via serum sensitive clathrin-mediated endocytosis, and plasma membrane permeabilization. *International journal of nanomedicine* 7: 2045, 2012.

APPENDIX B

COLOCALISATION PROGRAM

%This MatLab code searches folders specified by the user for image files. These image files ideally contain three frames; the brightfield frame for determining the cell boundary, and the two fluorescence image frames for determining colocalisation. If the brightfield image is not available the program will calculate colocalisation using the whole field of view. Denoising is performed on the fluorescence channels, followed by Otsu thresholding and 'opening' of the resulting binary mask. Mask metadata is obtained, and the centroids of the spots in the user-specified channel checked for overlap with the spots in the other channel. This result is given as a percentage of the overall number of spots in the user-specified channel. Commented out at the bottom is the code used originally to determine random colocalisation, and replaced with the formula determined in Section 3.5.3 to correct for this.

```
close all; clear all; clc;

%This is the drawing bit
imtool close all;
                                % Close all previously open figure windows created by imtool
workspace;
                                % Make sure the workspace panel is showing
```

```
fontSize = 16;

    parentFolder = ['(enter name of parent folder)'];

                                %this is the name of the folder that contains the images

    folderList = dir(parentFolder);
lfo = length(folderList);

                                %counting the number of files in the folder

counter = 1;

    for fileCounter = 1:lfo

                                %looping through the whole folder

    if(folderList(fileCounter).isdir)

    fileList2 = dir([parentFolder folderList(fileCounter).name '\*.nd2']);

                        %finding the image files. .nd2 for Nikon images, .tif for Olympus

    lfi = length(fileList2);

                                %ensuring only the images in the folder are considered

    for fileCounter2 = 1:lfi
    filename2 = [parentFolder folderList(fileCounter).name '\' fileList2(fileCounter2).name];

    spotCount = [0,0];

                                %empty matrix for holding spot count values

centroidPoints = [0,0];

                                %empty matrix for holding spot centroid values
```

```
masks = {0,0};
                                        %empty array for containing the cell outline mask
figure;

    BFmeta = imreadBFmeta(filename2);
                                        %loading metadata concerning the image
    z = ceil((BFmeta.zsize)/3);
    t = ceil((BFmeta.nframes)/2);
    origBF = imreadBF(filename2,z,t,3);
                                        %these select the first colour frame and middle timeframe
    for denoiseLoop = 1:2
    %Trying to draw round the cell
    if denoiseLoop == 1
                                        %Only want to do it once
imshow(origBF, []);
axis on;
title('Original Brightfield Image', 'FontSize', fontSize);
set(gcf, 'Position', get(0,'Screensize'));
                                        % Maximize figure.
message = sprintf('Left click and hold to begin drawing.\n Simply lift the mouse button to
finish');
uiwait(msgbox(message));
hFH = imfreehand();
```

% Create a binary image ("mask") from the ROI object. These next 11 lines take the values from the brightfield cell outline and define parameters for the rectangle that surrounds it. The "binaryImage" sets all the pixel values outside this outline to 0.

```
binaryImage = hFH.createMask();
xy = hFH.getPosition;
    xyMin = min(xy);
xyMax = max(xy);
xmin = xyMin(1);
ymin = xyMin(2);
width = xyMax(1) - xmin;
height = xyMax(2) - ymin;
rekt = [xmin ymin width height];
binaryImage = imcrop(binaryImage,rekt);
end
```

```
    orig = imreadBF(filename2,z,t,denoiseLoop);
```

%reads the fluorescence image

```
    blackMaskedOrig = orig; blackMaskedOrig = imcrop(blackMaskedOrig,rekt);
```

%crops the fluorescence image according to the brightfield outline

```
imageDenoised = ericDenoise(blackMaskedOrig);
```

%performs denoising on the fluorescence image

```
    level = graythresh(imageDenoised);
```

%calculates the threshold level using Otsu's method

```
BW = im2bw(imageDenoised,level);
```

%turns the denoised image into a binary mask using the threshold level

BW(binaryImage) = 0; subplot(3,2,denoiseLoop); imshow(BW);

%displays the mask for reference

if denoiseLoop == 1
title([fileList2(fileCounter2).name '(*enter name of first fluorescence channel*)']);
end

if denoiseLoop == 2
title([fileList2(fileCounter2).name '(*enter name of second fluorescence channel*)']);
end

%This performs opening of the image to get rid of all the spots that are only one pixel big after thresholding, using a disc of radius 1.
se1 = strel('disk',1);
openBW = imopen(BW,se1);

subplot(3,2,denoiseLoop+2);
imshow(openBW);

%displays the opened mask for reference

if denoiseLoop == 1
title([fileList2(fileCounter2).name '(*enter name of first fluorescence channel*)']);
end

if denoiseLoop == 2
title([fileList2(fileCounter2).name '(*enter name of second fluorescence channel*)']);
end

```
%These next 6 lines calculate and save the metadata of the spots for the opened masks to
                                                                    calculate colocalisation

openCC = bwconncomp(openBW,4);
openSpotData = regionprops(openCC,'basic');
centroidSpotData = regionprops(openCC,'centroid');
masks{denoiseLoop} = openBW;
spotCount(denoiseLoop) = openCC.NumObjects;
centroidPoints(denoiseLoop) = cat(1,centroidSpotData.Centroid);


    end


    maskBlend = logical(masks{2}.* centroidPoints{1});

   %choose between '1' and '2' for which fluorophore channel you want the centroid data

maskBlendCC = bwconncomp(maskBlend,4);


    coloc = round( 100 * (maskBlendCC.NumObjects) / spotCount(1) )
%maskRandom = logical(masks{2}.* imrotate(centroidPoints{1},180,'nearest','crop'));
%maskRandomCC = bwconncomp(maskRandom,4);
%uncoloc = round( 100 * ( maskRandomCC.NumObjects / spotCount(1) ) )

    %choose between '1' and '2' for which fluorophore channel you want the random data

    T = ones(size(openBW,1),size(openBW,2),3) .* 255;
T(:,:,1) = T(:,:,1) .* masks{1};
T(:,:,2) = T(:,:,2) .* masks{2};
T(:,:,3) = T(:,:,3) .* masks{2};
```

```
    subplot(3,2, denoiseLoop+3);
imshow(T);


                                        %Showing the two coloured masks overlaid

    coloc = sqrt(417 * coloc + 8094) - 123;
title([num2str(coloc) '% of NP spots are colocalised with DiI.']);

        %Putting the corrected value for the colocalisation in the title. Change the words
                                                    depending on what you are imaging.

    set(gcf, 'Position', get(0, 'ScreenSize'));
    counter = counter + 1;


    end


    end


    end
```

LIST OF REFERENCES

[1] M. Auffan, J. Rose, J.Y. Bottero, G.V. Lowry, J.P. Jolivet, and M.R. Wiesner. Towards a definition of inorganic nanoparticles from an environmental, health and safety perspective. *Nature nanotechnology*, 4(10):634–641, 2009.

[2] Stephanie D Steichen, Mary Caldorera-Moore, and Nicholas A Peppas. A review of current nanoparticle and targeting moieties for the delivery of cancer therapeutics. *European Journal of Pharmaceutical Sciences*, 48(3):416–427, 2013.

[3] Ph Buffat and Jean Pierre Borel. Size effect on the melting temperature of gold particles. *Physical Review A*, 13(6):2287, 1976.

[4] Yasitha L Hewakuruppu, Leonid A Dombrovsky, Chuyang Chen, Victoria Timchenko, Xuchuan Jiang, Sung Baek, and Robert A Taylor. Plasmonic pump–probe method to study semi-transparent nanofluids. *Applied optics*, 52(24):6041–6050, 2013.

[5] Marie-Christine Daniel and Didier Astruc. Gold nanoparticles: assembly, supramolecular chemistry, quantum-size-related properties, and applications toward biology, catalysis, and nanotechnology. *Chemical reviews*, 104(1):293–346, 2004.

[6] Gyorgy Csaba, Alexandra Imre, Gary H Bernstein, Wolfgang Porod, and Vitali Metlushko. Nanocomputing by field-coupled nanomagnets. *Nanotechnology, IEEE Transactions on*, 1(4):209–213, 2002.

[7] Philip Ball. Chemistry meets computing. *Nature*, 406(6792):118–120, 2000.

[8] Cuichen Wu, Shuo Wan, Weijia Hou, Liqin Zhang, Jiehua Xu, Cheng Cui, Yanyue Wang, Jun Hu, and Weihong Tan. A survey of advancements in nucleic acid-based logic gates and computing for applications in biotechnology and biomedicine. *Chemical Communications*, 2015.

[9] Mingxu You, Guizhi Zhu, Tao Chen, Michael J Donovan, and Weihong Tan. Programmable and multiparameter dna-based logic platform for cancer recognition and targeted therapy. *Journal of the American Chemical Society*, 2014.

[10] Jan Zimmermann, Felix A Reifler, Giuseppino Fortunato, Lutz-Christian Gerhardt, and Stefan Seeger. A simple, one-step approach to durable and robust superhydrophobic textiles. *Advanced Functional Materials*, 18(22):3662–3669, 2008.

[11] Amit Singh, Vijay Krishna, Alexander Angerhofer, Bao Do, Gavin MacDonald, and Brij Moudgil. Copper coated silica nanoparticles for odor removal. *Langmuir*, 26(20):15837–15844, 2010.

[12] M Joshi and A Bhattacharyya. Nanotechnology–a new route to high-performance functional textiles. *Textile Progress*, 43(3):155–233, 2011.

[13] Meng Chao Ma and Zhong Hua Jiang. Application of nanometer materials in the design of clothing. *Applied Mechanics and Materials*, 416:1698–1701, 2013.

[14] Jun Sung Kim, Eunye Kuk, Kyeong Nam Yu, Jong-Ho Kim, Sung Jin Park, Hu Jang Lee, So Hyun Kim, Young Kyung Park, Yong Ho Park, Cheol-Yong Hwang, et al. Antimicrobial effects of silver nanoparticles. *Nanomedicine: Nanotechnology, Biology and Medicine*, 3(1):95–101, 2007.

[15] Christopher Walsh. Where will new antibiotics come from? *Nature Reviews Microbiology*, 1(1):65–70, 2003.

[16] Mohammad J Hajipour, Katharina M Fromm, Ali Akbar Ashkarran, Dorleta Jimenez de Aberasturi, Idoia Ruiz de Larramendi, Teofilo Rojo, Vahid Serpooshan, Wolfgang J Parak, and Morteza Mahmoudi. Antibacterial properties of nanoparticles. *Trends in biotechnology*, 30(10):499–511, 2012.

[17] Agha Zeeshan Mirza and Farhan Ahmed Siddiqui. Nanomedicine and drug delivery: a mini review. *International Nano Letters*, 4(1):1–7, 2014.

[18] Svetlana Gelperina, Kevin Kisich, Michael D Iseman, and Leonid Heifets. The potential advantages of nanoparticle drug delivery systems in chemotherapy of tuberculosis. *American journal of respiratory and critical care medicine*, 172(12):1487–1490, 2005.

[19] D Patrick O'Neal, Leon R Hirsch, Naomi J Halas, J Donald Payne, and Jennifer L West. Photo-thermal tumor ablation in mice using near infrared-absorbing nanoparticles. *Cancer letters*, 209(2):171–176, 2004.

[20] S Moein Moghimi, A Christy Hunter, and J Clifford Murray. Nanomedicine: current status and future prospects. *The FASEB journal*, 19(3):311–330, 2005.

[21] Maureen R Gwinn and Val Vallyathan. Nanoparticles: health effects: pros and cons. *Environmental health perspectives*, pages 1818–1825, 2006.

[22] Irène Brigger, Catherine Dubernet, and Patrick Couvreur. Nanoparticles in cancer therapy and diagnosis. *Advanced drug delivery reviews*, 64:24–36, 2012.

[23] Lin Wang, Wenjun Zhao, and Weihong Tan. Bioconjugated silica nanoparticles: development and applications. *Nano Research*, 1(2):99–115, 2008.

[24] Alberto Gabizon, Hilary Shmeeda, and Yechezkel Barenholz. Pharmacokinetics of pegylated liposomal doxorubicin. *Clinical pharmacokinetics*, 42(5):419–436, 2003.

[25] Theresa M Allen and Pieter R Cullis. Drug delivery systems: entering the mainstream. *Science*, 303(5665):1818–1822, 2004.

[26] Kwangjae Cho, XU Wang, Shuming Nie, Dong M Shin, et al. Therapeutic nanoparticles for drug delivery in cancer. *Clinical cancer research*, 14(5):1310–1316, 2008.

[27] Jayanth Panyam and Vinod Labhasetwar. Biodegradable nanoparticles for drug and gene delivery to cells and tissue. *Advanced drug delivery reviews*, 55(3):329–347, 2003.

[28] Dong-Eun Lee, Heebeom Koo, In-Cheol Sun, Ju Hee Ryu, Kwangmeyung Kim, and Ick Chan Kwon. Multifunctional nanoparticles for multimodal imaging and theragnosis. *Chemical Society Reviews*, 41(7):2656–2672, 2012.

[29] MNV Kumar, M Sameti, SS Mohapatra, X Kong, RF Lockey, U Bakowsky, G Lindenblatt, C H Schmidt, and C-M Lehr. Cationic silica nanoparticles as gene carriers: synthesis, characterization and transfection efficiency in vitro and in vivo. *Journal of nanoscience and nanotechnology*, 4(7):876–881, 2004.

[30] Maxine J McCall. Environmental, health and safety issues: nanoparticles in the real world. *Nature nanotechnology*, 6(10):613–614, 2011.

[31] Ayush Verma and Francesco Stellacci. Effect of surface properties on nanoparticle–cell interactions. *Small*, 6(1):12–21, 2010.

[32] Michael Chorny, Ilia Fishbein, Ivan S Alferiev, Origene Nyanguile, Richard Gaster, and Robert J Levy. Adenoviral gene vector tethering to nanoparticle surfaces results in receptor-independent cell entry and increased transgene expression. *Molecular Therapy*, 14(3):382–391, 2006.

[33] Charlotte M Beddoes, C Patrick Case, and Wuge H Briscoe. Understanding nanoparticle cellular entry: a physicochemical perspective. *Advances in colloid and interface science*, 218:48–68, 2015.

[34] Chenggang Li, Haolin Liu, Yang Sun, Hongliang Wang, Feng Guo, Shuan Rao, Jiejie Deng, Yanli Zhang, Yufa Miao, Chenying Guo, et al. Pamam nanoparticles promote acute lung injury by inducing autophagic cell death through the akt-tsc2-mtor signaling pathway. *Journal of molecular cell biology*, 1(1):37–45, 2009.

[35] The Project on Emerging Nanotechnologies. PEN Consumer Products Inventory. *http://www.nanotechproject.org/cpi/*, 2015. Accessed: 27-08-2015.

[36] Marissa D Newman, Mira Stotland, and Jeffrey I Ellis. The safety of nanosized particles in titanium dioxide–and zinc oxide–based sunscreens. *Journal of the American Academy of Dermatology*, 61(4):685–692, 2009.

[37] Lei Shi, Jingning Shan, Yiguang Ju, Patricia Aikens, and Robert K Prudhomme. Nanoparticles as delivery vehicles for sunscreen agents. *Colloids and Surfaces A: Physicochemical and Engineering Aspects*, 396:122–129, 2012.

[38] Robert Landsiedel, Lan Ma-Hock, Ben Van Ravenzwaay, Markus Schulz, Karin Wiench, Samantha Champ, Stefan Schulte, Wendel Wohlleben, and Franz Oesch. Gene toxicity studies on titanium dioxide and zinc oxide nanomaterials used for uv-protection in cosmetic formulations. *Nanotoxicology*, 4(4):364–381, 2010.

[39] Nancy A Monteiro-Riviere, Karin Wiench, Robert Landsiedel, Stefan Schulte, Alfred O Inman, and Jim E Riviere. Safety evaluation of sunscreen formulations containing titanium dioxide and zinc oxide nanoparticles in uvb sunburned skin: an in vitro and in vivo study. *Toxicological Sciences*, page kfr148, 2011.

[40] Alex Weir, Paul Westerhoff, Lars Fabricius, Kiril Hristovski, and Natalie von Goetz. Titanium dioxide nanoparticles in food and personal care products. *Environmental science & technology*, 46(4):2242–2250, 2012.

[41] Qasim Chaudhry, Michael Scotter, James Blackburn, Bryony Ross, Alistair Boxall, Laurence Castle, Robert Aitken, and Richard Watkins. Applications and implications of nanotechnologies for the food sector. *Food additives and contaminants*, 25(3):241–258, 2008.

[42] Rebecca Bullard-Dillard, Kim E Creek, Walter A Scrivens, and James M Tour. Tissue sites of uptake of 14 c-labeled c 60. *Bioorganic Chemistry*, 24(4):376–385, 1996.

[43] Tobias J Brunner, Peter Wick, Pius Manser, Philipp Spohn, Robert N Grass, Ludwig K Limbach, Arie Bruinink, and Wendelin J Stark. In vitro cytotoxicity of oxide nanoparticles: comparison to asbestos, silica, and the effect of particle solubility. *Environmental science & technology*, 40(14):4374–4381, 2006.

[44] Eva Oberdörster. Manufactured nanomaterials (fullerenes, c60) induce oxidative stress in the brain of juvenile largemouth bass. *Environmental health perspectives*, pages 1058–1062, 2004.

[45] Karen Tiede, Alistair BA Boxall, Steven P Tear, John Lewis, Helen David, and Martin Hassellöv. Detection and characterization of engineered nanoparticles in food and the environment. *Food Additives and Contaminants*, 25(7):795–821, 2008.

[46] Tian Xia, Michael Kovochich, Monty Liong, Lutz Madler, Benjamin Gilbert, Haibin Shi, Joanne I Yeh, Jeffrey I Zink, and Andre E Nel. Comparison of the mechanism of toxicity of zinc oxide and cerium oxide nanoparticles based on dissolution and oxidative stress properties. *ACS nano*, 2(10):2121–2134, 2008.

[47] Wei Bai, Zhiyong Zhang, Wenjing Tian, Xiao He, Yuhui Ma, Yuliang Zhao, and Zhifang Chai. Toxicity of zinc oxide nanoparticles to zebrafish embryo: a physicochemical study of toxicity mechanism. *Journal of Nanoparticle Research*, 12(5):1645–1654, 2010.

[48] Bing Wang, Weiyue Feng, Meng Wang, Tiancheng Wang, Yiqun Gu, Motao Zhu, Hong Ouyang, Junwen Shi, Fang Zhang, Yuliang Zhao, et al. Acute toxicological impact of nano-and submicro-scaled zinc oxide powder on healthy adult mice. *Journal of Nanoparticle Research*, 10(2):263–276, 2008.

[49] Qi Fang, Xiongjie Shi, Liping Zhang, Qiangwei Wang, Xianfeng Wang, Yongyong Guo, and Bingsheng Zhou. Effect of titanium dioxide nanoparticles on the bioavailability, metabolism, and toxicity of pentachlorophenol in zebrafish larvae. *Journal of hazardous materials*, 283:897–904, 2015.

[50] Douglas W Dockery, C Arden Pope, Xiping Xu, John D Spengler, James H Ware, Martha E Fay, Benjamin G Ferris Jr, and Frank E Speizer. An association between air pollution and mortality in six us cities. *New England journal of medicine*, 329(24):1753–1759, 1993.

[51] William H Smith. Air pollution and forests. *Springer-Verlag*, 1990.

[52] Arka Soewono and Steve Rogak. Morphology and microstructure of engine-emitted particulates. Technical report, SAE Technical Paper, 2009.

[53] Maria Grundström, HW Linderholm, Jenny Klingberg, and Håkan Pleijel. Urban no 2 and no pollution in relation to the north atlantic oscillation nao. *Atmospheric Environment*, 45(4):883–888, 2011.

[54] Philip E Silkoff, Lening Zhang, Steven Dutton, Esther L Langmack, Sverre Vedal, James Murphy, and Barry Make. Winter air pollution and disease parameters in advanced chronic obstructive pulmonary disease panels residing in denver, colorado. *Journal of allergy and clinical immunology*, 115(2):337–344, 2005.

[55] CL Myung and S Park. Exhaust nanoparticle emissions from internal combustion engines: A review. *International Journal of Automotive Technology*, 13(1):9–22, 2012.

[56] C Arden Pope III, Michael J Thun, Mohan M Namboodiri, Douglas W Dockery, John S Evans, Frank E Speizer, and Clark W Heath Jr. Particulate air pollution as a predictor of mortality in a prospective study of us adults. *American journal of respiratory and critical care medicine*, 151(3_pt_1):669–674, 1995.

[57] C ARDEN III POPE, Douglas W Dockery, Richard E Kanner, G Martin Villegas, and Joel Schwartz. Oxygen saturation, pulse rate, and particulate air pollution: a daily time-series panel study. *American Journal of Respiratory and Critical Care Medicine*, 159(2):365–372, 1999.

[58] William A Heitbrink, Douglas E Evans, Thomas M Peters, and Thomas J Slavin. Characterization and mapping of very fine particles in an engine machining and assembly facility. *Journal of occupational and environmental hygiene*, 4(5):341–351, 2007.

[59] Andrew S Ross, Kay Teschke, Michael Brauer, and Susan M Kennedy. Determinants of exposure to metalworking fluid aerosol in small machine shops. *Annals of Occupational Hygiene*, 48(5):383–391, 2004.

[60] Ellen A Eisen, Thomas J Smith, David Kriebel, Susan R Woskie, Douglas J Myers, Susan M Kennedy, Stuart Shalat, and Richard R Monson. Respiratory health of automobile workers and exposures to metal-working fluid aerosols: Lung spirometry. *American journal of industrial medicine*, 39(5):443–453, 2001.

[61] Neely Kazerouni, Terry L Thomas, Sandra A Petralia, and Richard B Hayes. Mortality among workers exposed to cutting oil mist: update of previous reports. *American journal of industrial medicine*, 38(4):410–416, 2000.

[62] Mark Russi, Robert Dubrow, John T Flannery, Mark R Cullen, and Susan Taylor Mayne. Occupational exposure to machining fluids and laryngeal cancer risk: contrasting results using two separate control groups. *American journal of industrial medicine*, 31(2):166–171, 1997.

[63] Ying-Fang Wang, Perng-Jy Tsai, Chun-Wan Chen, Da-Ren Chen, and Yu-Tung Dai. Size distributions and exposure concentrations of nanoparticles associated with the emissions of oil mists from fastener manufacturing processes. *Journal of hazardous materials*, 198:182–187, 2011.

[64] Anthony P Pietropaoli, Mark W Frampton, Richard W Hyde, Paul E Morrow, Günter Oberdörster, Christopher Cox, Donna M Speers, Lauren M Frasier, David C Chalupa, Li-Shan Huang, et al. Pulmonary function, diffusing capacity, and inflammation in healthy and asthmatic subjects exposed to ultrafine particles. *Inhalation toxicology*, 16(sup1):59–72, 2004.

[65] Henry Jr Gong, William S Linn, Kenneth W Clark, Karen R Anderson, Michael D Geller, and Constantinos Sioutas. Respiratory responses to exposures with fine particulates and nitrogen dioxide in the elderly with and without copd. *Inhalation toxicology*, 17(3):123–132, 2005.

[66] Jane Q Koenig, Therese F Mar, Ryan W Allen, Karen Jansen, Thomas Lumley, Jeffrey H Sullivan, Carol A Trenga, Timothy V Larson, and L-Jane S Liu. Pulmonary effects of indoor-and outdoor-generated particles in children with asthma. *Environmental health perspectives*, pages 499–503, 2005.

[67] Craig A Poland, Rodger Duffin, Ian Kinloch, Andrew Maynard, William AH Wallace, Anthony Seaton, Vicki Stone, Simon Brown, William MacNee, and Ken Donaldson. Carbon nanotubes introduced into the abdominal cavity of mice show asbestos-like pathogenicity in a pilot study. *Nature nanotechnology*, 3(7):423–428, 2008.

[68] Jaana Palomaki, Elina Valimaki, Jukka Sund, Minnamari Vippola, Per Axel Clausen, Keld Alstrup Jensen, Kai Savolainen, Sampsa Matikainen, and Harri Alenius. Long, needle-like carbon nanotubes and asbestos activate the nlrp3 inflammasome through a similar mechanism. *Acs Nano*, 5(9):6861–6870, 2011.

[69] Günter Oberdörster, Zachary Sharp, Viorel Atudorei, Alison Elder, Robert Gelein, Alex Lunts, Wolfgang Kreyling, and Christopher Cox. Extrapulmonary translocation of ultrafine carbon particles following whole-body inhalation exposure of rats. *Journal of Toxicology and Environmental Health Part A*, 65(20):1531–1543, 2002.

[70] WG Kreyling, M Semmler, F Erbe, P Mayer, S Takenaka, H Schulz, G Oberdörster, and A Ziesenis. Translocation of ultrafine insoluble iridium particles from lung epithelium to extrapulmonary organs is size dependent but very low. *Journal of toxicology and environmental health Part A*, 65(20):1513–1530, 2002.

[71] Günter Oberdörster, Andrew Maynard, Ken Donaldson, Vincent Castranova, Julie Fitzpatrick, Kevin Ausman, Janet Carter, Barbara Karn, Wolfgang Kreyling, David Lai, et al. Principles for characterizing the potential human health effects from exposure to nanomaterials: elements of a screening strategy. *Particle and fibre toxicology*, 2(1):1, 2005.

[72] Abderrahim Nemmar, Peter HM Hoet, and Benoit Nemery. Translocation of ultrafine particles. *Environmental health perspectives*, 114(4):A211, 2006.

[73] A.E. Nel, L. Mädler, D. Velegol, T. Xia, E.M.V. Hoek, P. Somasundaran, F. Klaessig, V. Castranova, and M. Thompson. Understanding biophysicochemical interactions at the nano–bio interface. *Nature Materials*, 8(7):543–557, 2009.

[74] Carl D Walkey and Warren CW Chan. Understanding and controlling the interaction of nanomaterials with proteins in a physiological environment. *Chemical Society Reviews*, 41(7):2780–2799, 2012.

[75] Iseult Lynch and Kenneth A Dawson. Protein-nanoparticle interactions. *Nano today*, 3(1):40–47, 2008.

[76] Martin Lundqvist, Johannes Stigler, Giuliano Elia, Iseult Lynch, Tommy Cedervall, and Kenneth A Dawson. Nanoparticle size and surface properties determine the protein corona with possible implications for biological impacts. *Proceedings of the National Academy of Sciences*, 105(38):14265–14270, 2008.

[77] Silvia Milani, Francesca Baldelli Bombelli, Andrzej S Pitek, Kenneth A Dawson, and Joachim Radler. Reversible versus irreversible binding of transferrin to polystyrene nanoparticles: soft and hard corona. *ACS nano*, 6(3):2532–2541, 2012.

[78] Eudald Casals, Tobias Pfaller, Albert Duschl, Gertie Janneke Oostingh, and Victor Puntes. Time evolution of the nanoparticle protein corona. *ACS nano*, 4(7):3623–3632, 2010.

[79] Stefan Tenzer, Dominic Docter, Jörg Kuharev, Anna Musyanovych, Verena Fetz, Rouven Hecht, Florian Schlenk, Dagmar Fischer, Klytaimnistra Kiouptsi, Christoph Reinhardt, et al. Rapid formation of plasma protein corona critically affects nanoparticle pathophysiology. *Nature nanotechnology*, 8(10):772–781, 2013.

[80] Zhou J Deng, Gysell Mortimer, Tara Schiller, Anthony Musumeci, Darren Martin, and Rodney F Minchin. Differential plasma protein binding to metal oxide nanoparticles. *Nanotechnology*, 20(45):455101, 2009.

[81] Carl D Walkey, Jonathan B Olsen, Hongbo Guo, Andrew Emili, and Warren CW Chan. Nanoparticle size and surface chemistry determine serum protein adsorption and macrophage uptake. *Journal of the American Chemical Society*, 134(4):2139–2147, 2012.

[82] Babylakshmi Muthusamy, G Hanumanthu, Shubha Suresh, B Rekha, D Srinivas, L Karthick, BM Vrushabendra, Salil Sharma, Goparani Mishra, Pritam Chatterjee, et al. Plasma proteome database as a resource for proteomics research. *Proteomics*, 5(13):3531–3536, 2005.

[83] Ruxandra Gref, Yoshiharu Minamitake, Maria Teresa Peracchia, Vladimir Trubetskoy, Vladimir Torchilin, and Robert Langer. Biodegradable long-circulating polymeric nanospheres. *Science*, 263(5153):1600–1603, 1994.

[84] JR Casley-Smith. Endocytosis: the different energy requirements for the uptake of particles by small and large vesicles into peritoneal macrophages. *Journal of Microscopy*, 90(1):15–30, 1969.

[85] Satyajit Mayor and Richard E Pagano. Pathways of clathrin-independent endocytosis. *Nature reviews Molecular cell biology*, 8(8):603–612, 2007.

[86] Katarzyna Kwiatkowska and Andrzej Sobota. Signaling pathways in phagocytosis. *Bioessays*, 21(5):422–431, 1999.

[87] JOHN M MARSHALL and Vivianne T Nachmias. Cell surface and pinocytosis. *J. Histochem. Cytochem*, 13(92):104, 1965.

[88] Tore-Geir Iversen, Tore Skotland, and Kirsten Sandvig. Endocytosis and intracellular transport of nanoparticles: present knowledge and need for future studies. *Nano Today*, 6(2):176–185, 2011.

[89] Bruno Marks, Michael HB Stowell, Yvonne Vallis, Ian G Mills, Adele Gibson, Colin R Hopkins, and Harvey T McMahon. Gtpase activity of dynamin and resulting conformation change are essential for endocytosis. *Nature*, 410(6825):231–235, 2001.

[90] Michael HB Stowell, Bruno Marks, Patrick Wigge, and Harvey T McMahon. Nucleotide-dependent conformational changes in dynamin: evidence for a mechanochemical molecular spring. *Nature cell biology*, 1(1):27–32, 1999.

[91] Anne-Karine Bouzier-Sore, Emeline Ribot, Véronique Bouchaud, Sylvain Miraux, Etienne Duguet, Stéphane Mornet, Gisèle Clofent-Sanchez, Jean-Michel Franconi, and Pierre Voisin. Nanoparticle phagocytosis and cellular stress: involvement in cellular imaging and in gene therapy against glioma. *NMR in Biomedicine*, 23(1):88–96, 2010.

[92] Markus C Kerr and Rohan D Teasdale. Defining macropinocytosis. *Traffic*, 10(4):364–371, 2009.

[93] J. Dausend, A. Musyanovych, M. Dass, P. Walther, H. Schrezenmeier, K. Landfester, and V. Mailänder. Uptake mechanism of oppositely charged fluorescent nanoparticles in hela cells. *Macromolecular bioscience*, 8(12):1135–1143, 2008.

[94] Harvey T McMahon and Emmanuel Boucrot. Molecular mechanism and physiological functions of clathrin-mediated endocytosis. *Nature reviews Molecular cell biology*, 12(8):517–533, 2011.

[95] Sandra L Schmid. Clathrin-coated vesicle formation and protein sorting: an integrated process. *Annual review of biochemistry*, 66(1):511–548, 1997.

[96] CR Hopkins, K Miller, and JM Beardmore. Receptor-mediated endocytosis of transferrin and epidermal growth factor receptors: a comparison of constitutive and ligand-induced uptake. *Journal of cell science*, 1985(Supplement 3):173–186, 1985.

[97] Royston E Carter and Alexander Sorkin. Endocytosis of functional epidermal growth factor receptor-green fluorescent protein chimera. *Journal of Biological Chemistry*, 273(52):35000–35007, 1998.

[98] Thomas J Raub and Sandra L Kuentzel. Kinetic and morphological evidence for endocytosis of mammalian cell integrin receptors by using an anti-fibronectin receptor β subunit monoclonal antibody. *Experimental cell research*, 184(2):407–426, 1989.

[99] G.J. Doherty and H.T. McMahon. Mechanisms of endocytosis. *Annual review of biochemistry*, 78:857–902, 2009.

[100] Wei Li, Chunying Chen, Chang Ye, Taotao Wei, Yuliang Zhao, Fang Lao, Zhen Chen, Huan Meng, Yuxi Gao, Hui Yuan, et al. The translocation of fullerenic nanoparticles into lysosome via the pathway of clathrin-mediated endocytosis. *Nanotechnology*, 19(14):145102, 2008.

[101] Jae-Min Oh, Soo-Jin Choi, Go-Eun Lee, Jung-Eun Kim, and Jin-Ho Choy. Inorganic metal hydroxide nanoparticles for targeted cellular uptake through clathrin-mediated endocytosis. *Chemistry–An Asian Journal*, 4(1):67–73, 2009.

[102] Dong-Ming Huang, Yann Hung, Bor-Sheng Ko, Szu-Chun Hsu, Wei-Hsuan Chen, Chung-Liang Chien, Chih-Pin Tsai, Chieh-Ti Kuo, Ju-Chiun Kang, Chung-Shi Yang, et al. Highly efficient cellular labeling of mesoporous nanoparticles in human mesenchymal stem cells: implication for stem cell tracking. *The FASEB journal*, 19(14):2014–2016, 2005.

[103] Min Huang, Zengshuan Ma, Eugene Khor, and Lee-Yong Lim. Uptake of fitc-chitosan nanoparticles by a549 cells. *Pharmaceutical Research*, 19(10):1488–1494, 2002.

[104] P.J. Smith, M. Giroud, H.L. Wiggins, F. Gower, J.A. Thorley, B. Stolpe, J. Mazzolini, R.J. Dyson, and J.Z. Rappoport. Cellular entry of nanoparticles via serum sensitive clathrin-mediated endocytosis, and plasma membrane permeabilization. *International Journal of Nanomedicine*, 7:2045, 2012.

[105] Tobias Richter, Matthias Floetenmeyer, Charles Ferguson, Janette Galea, Jaclyn Goh, Margaret R Lindsay, Garry P Morgan, Brad J Marsh, and Robert G Parton. High-resolution 3d quantitative analysis of caveolar ultrastructure and caveola–cytoskeleton interactions. *Traffic*, 9(6):893–909, 2008.

[106] Terence M Williams, Michael P Lisanti, et al. The caveolin proteins. *Genome biology*, 5(3):214–214, 2004.

[107] Solange Monier, Robert G Parton, Frank Vogel, Joachim Behlke, A Henske, and TV Kurzchalia. Vip21-caveolin, a membrane protein constituent of the caveolar coat, oligomerizes in vivo and in vitro. *Molecular biology of the cell*, 6(7):911–927, 1995.

[108] Akiko Tagawa, Anna Mezzacasa, Arnold Hayer, Andrea Longatti, Lucas Pelkmans, and Ari Helenius. Assembly and trafficking of caveolar domains in the cell caveolae as stable, cargo-triggered, vesicular transporters. *The Journal of cell biology*, 170(5):769–779, 2005.

[109] Zhenjia Wang, Chinnaswamy Tiruppathi, Richard D Minshall, and Asrar B Malik. Size and dynamics of caveolae studied using nanoparticles in living endothelial cells. *ACS nano*, 3(12):4110–4116, 2009.

[110] Gaurav Sahay, Daria Y Alakhova, and Alexander V Kabanov. Endocytosis of nanomedicines. *Journal of controlled release*, 145(3):182–195, 2010.

[111] Yingjuan Lu and Philip S Low. Folate-mediated delivery of macromolecular anticancer therapeutic agents. *Advanced drug delivery reviews*, 64:342–352, 2012.

[112] Samuel K Lai, Kaoru Hida, Stan T Man, Clive Chen, Carolyn Machamer, Trina A Schroer, and Justin Hanes. Privileged delivery of polymer nanoparticles to the perinuclear region of live cells via a non-clathrin, non-degradative pathway. *Biomaterials*, 28(18):2876–2884, 2007.

[113] Henri-François Renard, Mijo Simunovic, Joël Lemière, Emmanuel Boucrot, Maria Daniela Garcia-Castillo, Senthil Arumugam, Valérie Chambon, Christophe Lamaze, Christian Wunder, Anne K Kenworthy, et al. Endophilin-a2 functions in membrane scission in clathrin-independent endocytosis. *Nature*, 517(7535):493–496, 2015.

[114] A. Ishimaru. *Electromagnetic wave propagation, radiation, and scattering*. Prentice Hall Englewood Cliffs, NJ:, 1991.

[115] R.D. Knight. *Physics for Scientists and Engineers: a strategic approach*. Pearson/Addison Wesley, 2004.

[116] J. Rietdorf and T.W.J. Gadella. *Microscopy techniques*, volume 95. Springer Verlag, 2005.

[117] I Newton. Optiks book ii. 1704.

[118] Christiaan Huygens. *Traité de la lumière: où sont expliquées les causes de ce qui luy arrive dans la reflexion, & dans la refraction, et particulierement dans l'etrange refraction du cistal d'Islande.* Chez Pierre vander Aa, 1885.

[119] J.G. Speight. *Lange's handbook of chemistry*, volume 1. McGraw-Hill New York, 2005.

[120] Jagadis Chunder Bose. On the determination of the wave-length of electric radiation by diffraction grating. *Proceedings of the Royal Society of London*, 60(359-367):167–178, 1896.

[121] Daniel Axelrod, Thomas P Burghardt, and Nancy L Thompson. Total internal reflection fluorescence. *Annual review of biophysics and bioengineering*, 13(1):247–268, 1984.

[122] James Clerk Maxwell. On physical lines of force, 1861. *A dynamical theory of the electromagnetic field*, pages 1875–89, 1865.

[123] M. Ahmad and L.L. Hench. Effect of taper geometries and launch angle on evanescent wave penetration depth in optical fibers. *Biosensors and Bioelectronics*, 20(7):1312–1319, 2005.

[124] P Eisenberger and PM Platzman. Compton scattering of x rays from bound electrons. *Physical Review A*, 2(2):415, 1970.

[125] Roger N Clark et al. Spectroscopy of rocks and minerals, and principles of spectroscopy. *Manual of remote sensing*, 3:3–58, 1999.

[126] Marston Taylor Bogert and Ralph Garrigue Wright. Some experiments on the nitro derivatives of fluorescein. 1. *Journal of the American Chemical Society*, 27(10):1310–1316, 1905.

[127] George Gabriel Stokes. On the change of refrangibility of light. *Philosophical Transactions of the Royal Society of London*, pages 463–562, 1852.

[128] Douglas E Caldwell, Darren R Korber, and John R Lawrence. Confocal laser microscopy and digital image analysis in microbial ecology. In *Advances in microbial ecology*, pages 1–67. Springer, 1992.

[129] Shi-Wei Chu, I-Hsiu Chen, Tzu-Ming Liu, Ping Chin Chen, Chi-Kuang Sun, and Bai-Ling Lin. Multimodal nonlinear spectral microscopy based on a femtosecond cr: forsterite laser. *Optics Letters*, 26(23):1909–1911, 2001.

[130] Arthur L Schawlow and Charles H Townes. Infrared and optical masers. *Physical Review*, 112(6):1940, 1958.

[131] Fumitomo Hide, Maria A Diaz-Garcia, Benjamin J Schwartz, Mats R Andersson, et al. Semiconducting polymers: a new class of solid-state laser materials. *Science*, 273(5283):1833, 1996.

[132] Emil Wolf. Unified theory of coherence and polarization of random electromagnetic beams. *Physics Letters A*, 312(5):263–267, 2003.

[133] A Fresnel. Mémoire sur linfluence de la polarisation dans laction que les rayons lumineux exercent les uns sur les autres. *FO*, 1:385–409, 1816.

[134] Wikimedia Commons. Airy-pattern. *https://commons.wikimedia.org/wiki/File:Airy-pattern.svg*, 2012. Accessed: 28-06-2016.

[135] HH Hopkins. The airy disc formula for systems of high relative aperture. *Proceedings of the Physical Society*, 55(2):116, 1943.

[136] Ernst Abbe. Beiträge zur theorie des mikroskops und der mikroskopischen wahrnehmung. *Archiv für mikroskopische Anatomie*, 9(1):413–418, 1873.

[137] AJ Den Dekker, A Van den Bos, et al. Resolution: a survey. *JOURNAL-OPTICAL SOCIETY OF AMERICA A*, 14:547–557, 1997.

[138] Stephen Bradley Ippolito, BB Goldberg, and MS Ünlü. High spatial resolution subsurface microscopy. *Applied Physics Letters*, 78(26):4071–4073, 2001.

[139] Wes Wallace, Lutz H Schaefer, and Jason R Swedlow. A workingperson's guide to deconvolution in light microscopy. *Biotechniques*, 31(5):1076–1097, 2001.

[140] HJ Landau. Sampling, data transmission, and the nyquist rate. *Proceedings of the IEEE*, 55(10):1701–1706, 1967.

[141] AK Prasad, RJ Adrian, CC Landreth, and PW Offutt. Effect of resolution on the speed and accuracy of particle image velocimetry interrogation. *Experiments in Fluids*, 13(2-3):105–116, 1992.

[142] Peter J Shaw. Comparison of widefield/deconvolution and confocal microscopy for three-dimensional imaging. In *Handbook of biological confocal microscopy*, pages 453–467. Springer, 2006.

[143] James B Pawley. Fundamental limits in confocal microscopy. In *Handbook of biological confocal microscopy*, pages 20–42. Springer, 2006.

[144] KD Kihm, Arindam Banerjee, CK Choi, and T Takagi. Near-wall hindered brownian diffusion of nanoparticles examined by three-dimensional ratiometric total internal reflection fluorescence microscopy (3-d r-tirfm). *Experiments in Fluids*, 37(6):811–824, 2004.

[145] Derek Toomre and James B Pawley. Disk-scanning confocal microscopy. In *Handbook of biological confocal microscopy*, pages 221–238. Springer, 2006.

[146] Nadia Ruthardt, Don C Lamb, and Christoph Bräuchle. Single-particle tracking as a quantitative microscopy-based approach to unravel cell entry mechanisms of viruses and pharmaceutical nanoparticles. *Molecular therapy*, 19(7):1199–1211, 2011.

[147] David J Stephens and Victoria J Allan. Light microscopy techniques for live cell imaging. *Science*, 300(5616):82–86, 2003.

[148] Andreas Ettinger and Torsten Wittmann. Fluorescence live cell imaging. *Methods in cell biology*, 123:77, 2014.

[149] José-Angel Conchello and Jeff W Lichtman. Optical sectioning microscopy. *Nature methods*, 2(12):920–931, 2005.

[150] T Wilson. Optical sectioning in confocal fluorescent microscopes. *Journal of Microscopy*, 154(2):143–156, 1989.

[151] Robert H Webb. Confocal optical microscopy. *Reports on Progress in Physics*, 59(3):427, 1996.

[152] D. Axelrod. Total internal reflection fluorescence microscopy in cell biology. *Traffic*, 2(11):764–774, 2001.

[153] Paul Temkin, Ben Lauffer, Stefanie Jäger, Peter Cimermancic, Nevan J Krogan, and Mark von Zastrow. Snx27 mediates retromer tubule entry and endosome-to-plasma membrane trafficking of signalling receptors. *Nature cell biology*, 13(6):715–721, 2011.

[154] Yuko Mimori-Kiyosue, Ilya Grigoriev, Gideon Lansbergen, Hiroyuki Sasaki, Chiyuki Matsui, Fedor Severin, Niels Galjart, Frank Grosveld, Ivan Vorobjev, Shoichiro Tsukita, et al. Clasp1 and clasp2 bind to eb1 and regulate microtubule plus-end dynamics at the cell cortex. *The Journal of cell biology*, 168(1):141–153, 2005.

[155] Olov Wahlsten, Anders Gunnarsson, Lisa Simonsson Nystrom, Hudson Pace, Stefan Geschwindner, and Fredrik Hook. Equilibrium-fluctuation analysis for interaction studies between natural ligands and single g protein-coupled receptors in native lipid vesicles. *Langmuir*, 31(39):10774–10780, 2015.

[156] Kenichi GN Suzuki. Single-molecule imaging of signal transduction via gpi-anchored receptors. *Lipid Signaling Protocols*, pages 229–238, 2016.

[157] J Thomas Parsons, Alan Rick Horwitz, and Martin A Schwartz. Cell adhesion: integrating cytoskeletal dynamics and cellular tension. *Nature reviews Molecular cell biology*, 11(9):633–643, 2010.

[158] D. Loerke, B. Preitz, W. Stühmer, and M. Oheim. Super-resolution measurements with evanescent-wave fluorescence excitation using variable beam incidence. *Journal of biomedical optics*, 5(23), 2000.

[159] F.E. Schweizer and T.A. Ryan. The synaptic vesicle: cycle of exocytosis and endocytosis. *Current opinion in neurobiology*, 16(3):298–304, 2006.

[160] Cornelia Loos, Tatiana Syrovets, Anna Musyanovych, Volker Mailänder, Katharina Landfester, G Ulrich Nienhaus, and Thomas Simmet. Functionalized polystyrene nanoparticles as a platform for studying bio–nano interactions. *Beilstein journal of nanotechnology*, 5(1):2403–2412, 2014.

[161] T. Dos Santos, J. Varela, I. Lynch, A. Salvati, and K.A. Dawson. Effects of transport inhibitors on the cellular uptake of carboxylated polystyrene nanoparticles in different cell lines. *PloS one*, 6(9):e24438, 2011.

[162] H.J. Johnston, M. Semmler-Behnke, D.M. Brown, W. Kreyling, L. Tran, and V. Stone. Evaluating the uptake and intracellular fate of polystyrene nanoparticles by primary and hepatocyte cell lines in vitro. *Toxicology and applied pharmacology*, 242(1):66–78, 2010.

[163] J. Rejman, V. Oberle, I.S. Zuhorn, and D. Hoekstra. Size-dependent internalization of particles via the pathways of clathrin-and caveolae-mediated endocytosis. *Biochemical Journal*, 377(Pt 1):159, 2004.

[164] T. Xia, M. Kovochich, M. Liong, J.I. Zink, and A.E. Nel. Cationic polystyrene nanosphere toxicity depends on cell-specific endocytic and mitochondrial injury pathways. *Acs Nano*, 2(1):85–96, 2007.

[165] William F Scherer, Jerome T Syverton, and George O Gey. Studies on the propagation in vitro of poliomyelitis viruses iv. viral multiplication in a stable strain of human malignant epithelial cells (strain hela) derived from an epidermoid carcinoma of the cervix. *The Journal of experimental medicine*, 97(5):695–710, 1953.

[166] J.Z. Rappoport and S.M. Simon. Endocytic trafficking of activated egfr is ap-2 dependent and occurs through preformed clathrin spots. *Journal of cell science*, 122(9):1301–1305, 2009.

[167] J.Z. Rappoport, B.W. Taha, S. Lemeer, A. Benmerah, and S.M. Simon. The ap-2 complex is excluded from the dynamic population of plasma membrane-associated clathrin. *Journal of Biological Chemistry*, 278(48):47357–47360, 2003.

[168] J.Z. Rappoport and S.M. Simon. A functional gfp fusion for imaging clathrin-mediated endocytosis. *Traffic*, 9(8):1250–1255, 2008.

[169] Keith Roberts Martin Raff Julian Lewis Bruce Alberts, Alexander Johnson and Dennis Bray. *Molecular biology of the cell*. Garland Science, 1983.

[170] Oshra Betzer, Rinat Meir, Tamar Dreifuss, Katerina Shamalov, Menachem Motiei, Amit Shwartz, Koby Baranes, Cyrille J Cohen, Niva Shraga-Heled, Racheli Ofir, et al. In-vitro optimization of nanoparticle-cell labeling protocols for in-vivo cell tracking applications. *Scientific reports*, 5, 2015.

[171] Jelena Kolosnjaj-Tabi, Claire Wilhelm, Olivier Clément, and Florence Gazeau. Cell labeling with magnetic nanoparticles: opportunity for magnetic cell imaging and cell manipulation. *J Nanobiotechnology*, 11(Suppl 1):S7, 2013.

[172] Jasmine Davda and Vinod Labhasetwar. Characterization of nanoparticle uptake by endothelial cells. *International journal of pharmaceutics*, 233(1):51–59, 2002.

[173] Juliet Popper Shaffer. Multiple hypothesis testing. *Annual review of psychology*, 46:561, 1995.

[174] A. Lesniak, A. Campbell, M.P. Monopoli, I. Lynch, A. Salvati, and K.A. Dawson. Serum heat inactivation affects protein corona composition and nanoparticle uptake. *Biomaterials*, 31(36):9511–9518, 2010.

[175] Anna Niedzwiecka, Malgorzata Lekka, Per Nilsson, and Anders Virtanen. Global architecture of human poly (a)-specific ribonuclease by atomic force microscopy in liquid and dynamic light scattering. *Biophysical chemistry*, 158(2):141–149, 2011.

[176] Robert J Hunter. *Zeta potential in colloid science: principles and applications*, volume 8. Academic press London, 1981.

[177] Abdullah Khan. Study of the effects of protein corona on nanoparticle-membrane interactions. Master's thesis, University of Birmingham, August 2012.

[178] Swanand Patil, Amanda Sandberg, Eric Heckert, William Self, and Sudipta Seal. Protein adsorption and cellular uptake of cerium oxide nanoparticles as a function of zeta potential. *Biomaterials*, 28(31):4600–4607, 2007.

[179] Hilda TR Wiogo, May Lim, Volga Bulmus, Jimmy Yun, and Rose Amal. Stabilization of magnetic iron oxide nanoparticles in biological media by fetal bovine serum (fbs). *Langmuir*, 27(2):843–850, 2010.

[180] Marco P Monopoli, Dorota Walczyk, Abigail Campbell, Giuliano Elia, Iseult Lynch, Francesca Baldelli Bombelli, and Kenneth A Dawson. Physical- chemical aspects of protein corona: relevance to in vitro and in vivo biological impacts of nanoparticles. *Journal of the American Chemical Society*, 133(8):2525–2534, 2011.

[181] Peter H Hemmerich and Anna H von Mikecz. Defining the subcellular interface of nanoparticles by live-cell imaging. *PloS one*, 8(4):e62018, 2013.

[182] David Schrama, Ralph A Reisfeld, and Jürgen C Becker. Antibody targeted drugs as cancer therapeutics. *Nature reviews Drug discovery*, 5(2):147–159, 2006.

[183] Gang Lv, Fang He, Xuemei Wang, Feng Gao, Gen Zhang, Tao Wang, Hui Jiang, Chunhui Wu, Dadong Guo, Xiaomao Li, et al. Novel nanocomposite of nano fe3o4 and polylactide nanofibers for application in drug uptake and induction of cell death of leukemia cancer cells. *Langmuir*, 24(5):2151–2156, 2008.

[184] E. Macia, M. Ehrlich, R. Massol, E. Boucrot, C. Brunner, and T. Kirchhausen. Dynasore, a cell-permeable inhibitor of dynamin. *Developmental cell*, 10(6):839–850, 2006.

[185] T. Kirchhausen, E. Macia, and H.E. Pelish. Use of dynasore, the small molecule inhibitor of dynamin, in the regulation of endocytosis. *Methods in enzymology*, 438:77–93, 2008.

[186] Michelle J Farquhar, Ke Hu, Helen J Harris, Christopher Davis, Claire L Brimacombe, Sarah J Fletcher, Thomas F Baumert, Joshua Z Rappoport, Peter Balfe, and Jane A McKeating. Hepatitis c virus induces cd81 and claudin-1 endocytosis. *Journal of virology*, 86(8):4305–4316, 2012.

[187] Sarah J Fletcher, Natalie S Poulter, Elizabeth J Haining, and Joshua Z Rappoport. Clathrin-mediated endocytosis regulates occludin, and not focal adhesion, distribution during epithelial wound healing. *Biology of the Cell*, 104(4):238–256, 2012.

[188] Joshua Z Rappoport, Shahrnaz Kemal, Alexandre Benmerah, and Sanford M Simon. Dynamics of clathrin and adaptor proteins during endocytosis. *American Journal of Physiology-Cell Physiology*, 291(5):C1072–C1081, 2006.

[189] A. Benmerah, M. Bayrou, N. Cerf-Bensussan, and A. Dautry-Varsat. Inhibition of clathrin-coated pit assembly by an eps15 mutant. *Journal of cell science*, 112(9):1303–1311, 1999.

[190] L. Orlichenko, B. Huang, E. Krueger, and M.A. McNiven. Epithelial growth factor-induced phosphorylation of caveolin 1 at tyrosine 14 stimulates caveolae formation in epithelial cells. *Journal of Biological Chemistry*, 281(8):4570, 2006.

[191] Dries Vercauteren, Martin Piest, Leonardus J van der Aa, Monerah Al Soraj, Arwyn T Jones, Johan FJ Engbersen, Stefaan C De Smedt, and Kevin Braeckmans. Flotillin-dependent endocytosis and a phagocytosis-like mechanism for cellular internalization of disulfide-based poly (amido amine)/dna polyplexes. *Biomaterials*, 32(11):3072–3084, 2011.

[192] K.L. Goldenthal, I. Pastan, and M.C. Willingham. Initial steps in receptor-mediated endocytosis: The influence of temperature on the shape and distribution of plasma membrane clathrin-coated pits in cultured mammalian cells. *Experimental cell research*, 152(2):558–564, 1984.

[193] Huan Meng, Sui Yang, Zongxi Li, Tian Xia, Justin Chen, Zhaoxia Ji, Haiyuan Zhang, Xiang Wang, Sijie Lin, Connie Huang, et al. Aspect ratio determines the quantity of mesoporous silica nanoparticle uptake by a small gtpase-dependent macropinocytosis mechanism. *ACS nano*, 5(6):4434–4447, 2011.

[194] Catarina Carneiro, Catarina Vaz, Joana Carvalho-Pereira, Célia Pais, and Paula Sampaio. A new method for yeast phagocytosis analysis by flow cytometry. *Journal of microbiological methods*, 101:56–62, 2014.

[195] Bruce L Roth, Martin Poot, Stephen T Yue, and Paul J Millard. Bacterial viability and antibiotic susceptibility testing with sytox green nucleic acid stain. *Applied and environmental microbiology*, 63(6):2421–2431, 1997.

[196] Stephen A Adam, R Sterne Marr, and Larry Gerace. Nuclear protein import in permeabilized mammalian cells requires soluble cytoplasmic factors. *The Journal of Cell Biology*, 111(3):807–816, 1990.

[197] Anna Raffaello, Diego De Stefani, Davide Sabbadin, Enrico Teardo, Giulia Merli, Anne Picard, Vanessa Checchetto, Stefano Moro, Ildikò Szabò, and Rosario Rizzuto. The mitochondrial calcium uniporter is a multimer that can include a dominant-negative pore-forming subunit. *The EMBO journal*, 32(17):2362–2376, 2013.

[198] ThermoFisher Scientific. FluoSpheres Carboxylate-Modified Microspheres. *https://www.thermofisher.com/order/catalog/product/F8787*, 2016. Accessed: 23-April-2016.

[199] D Slameňová and A Gabelova. The effects of sodium azide on mammalian cells cultivated in vitro. *Mutation Research/Fundamental and Molecular Mechanisms of Mutagenesis*, 71(2):253–261, 1980.

[200] Michael F Olson, Hugh F Paterson, and Christopher J Marshall. Signals from ras and rho gtpases interact to regulate expression of p21waf1/cip1. *Nature*, 394(6690):295–299, 1998.

[201] Ido Amit, Ami Citri, Tal Shay, Yiling Lu, Menachem Katz, Fan Zhang, Gabi Tarcic, Doris Siwak, John Lahad, Jasmine Jacob-Hirsch, et al. A module of negative

feedback regulators defines growth factor signaling. *Nature genetics*, 39(4):503–512, 2007.

[202] Eddie Khav. Visualizing an rb-e2f cellular switch that controls cell proliferation. 2013.

[203] Masoomeh Aghababazadeh and Mohammad Amin Kerachian. Cell fasting: Cellular response and application of serum starvation. *Journal of Fasting and Health*, 2(4):147–150, 2014.

[204] Sergej Pirkmajer and Alexander V Chibalin. Serum starvation: caveat emptor. *American Journal of Physiology-Cell Physiology*, 301(2):C272–C279, 2011.

[205] James D Orth and Mark A McNiven. Get off my back! rapid receptor internalization through circular dorsal ruffles. *Cancer research*, 66(23):11094–11096, 2006.

[206] Amandio V Vieira, Christophe Lamaze, and Sandra L Schmid. Control of egf receptor signaling by clathrin-mediated endocytosis. *Science*, 274(5295):2086, 1996.

[207] S Bolte and Fabrice P Cordelières. A guided tour into subcellular colocalization analysis in light microscopy. *Journal of microscopy*, 224(3):213–232, 2006.

[208] Pavel Novak, Andrew Shevchuk, Pakatip Ruenraroengsak, Michele Miragoli, Andrew J Thorley, David Klenerman, Max J Lab, Teresa D Tetley, Julia Gorelik, and Yuri E Korchev. Imaging single nanoparticle interactions with human lung cells using fast ion conductance microscopy. *Nano letters*, 14(3):1202–1207, 2014.

[209] Lennart Treuel, Stefan Brandholt, Pauline Maffre, Sarah Wiegele, Li Shang, and G Ulrich Nienhaus. Impact of protein modification on the protein corona on nanoparticles and nanoparticle–cell interactions. *ACS nano*, 8(1):503–513, 2014.

[210] Zhenjia Wang, Jing Li, Jaehyung Cho, and Asrar B Malik. Prevention of vascular inflammation by nanoparticle targeting of adherent neutrophils. *Nature nanotechnology*, 9(3):204–210, 2014.

[211] Antonietta Vilella, Giovanni Tosi, Andreas M Grabrucker, Barbara Ruozi, Daniela Belletti, Maria Angela Vandelli, Tobias M Boeckers, Flavio Forni, and Michele Zoli. Insight on the fate of cns-targeted nanoparticles. part i: Rab5-dependent cell-specific uptake and distribution. *Journal of Controlled Release*, 174:195–201, 2014.

[212] Sylvain V Costes, Dirk Daelemans, Edward H Cho, Zachary Dobbin, George Pavlakis, and Stephen Lockett. Automatic and quantitative measurement of protein-protein colocalization in live cells. *Biophysical journal*, 86(6):3993–4003, 2004.

[213] Claire M Brown. Fluorescence microscopy-avoiding the pitfalls. *Journal of cell science*, 120(10):1703–1705, 2007.

[214] Turan Erdogan. New optical filters improve high-speed multicolor fluorescence imaging. *Biophotonics International*, 13(3):34, 2006.

[215] Mitchell W Ross, David J Mitchell, John C Cain, Kiev R Blasier, and K Kevin Pfister. Live cell imaging of cytoplasmic dynein movement in transfected embryonic rat neurons. *Methods in Cell Biology*, 2015.

[216] Joshua D Larson, Margaret L Rodgers, and Aaron A Hoskins. Visualizing cellular machines with colocalization single molecule microscopy. *Chemical Society Reviews*, 43(4):1189–1200, 2014.

[217] H Ernst Keller. Objective lenses for confocal microscopy. In *Handbook of biological confocal microscopy*, pages 145–161. Springer, 2006.

[218] Joshua Z Rappoport and Sanford M Simon. Real-time analysis of clathrin-mediated endocytosis during cell migration. *Journal of cell science*, 116(5):847–855, 2003.

[219] L Stirling Churchman and James A Spudich. Colocalization of fluorescent probes: accurate and precise registration with nanometer resolution. *Cold Spring Harb Protoc*, 2012:141–149, 2012.

[220] T Santhanam and S Radhika. Probabilistic neural network–a better solution for noise classification. *Journal of Theoretical and Applied Information Technology*, 27(1):39–42, 2011.

[221] Gurmeet Kaur and Rupinder Kaur. Image de-noising using wavelet transform and various filters. *International Journal of Research in Computer Science*, 2(2):15, 2012.

[222] Béla Kajtár, Gábor Méhes, Thomas Lörch, Linda Deák, Marika Kneifné, Donát Alpár, and László Pajor. Automated fluorescent in situ hybridization (fish) analysis of t (9; 22)(q34; q11) in interphase nuclei. *Cytometry Part A*, 69(6):506–514, 2006.

[223] Kenneth W Dunn, Malgorzata M Kamocka, and John H McDonald. A practical guide to evaluating colocalization in biological microscopy. *American Journal of Physiology-Cell Physiology*, 300(4):C723–C742, 2011.

[224] P Garcia Penarrubia, X Férez Ruiz, and Jesús Gálvez. Quantitative analysis of the factors that affect the determination of colocalization coefficients in dual-color confocal images. *IEEE transactions on image processing*, 14(8):1151–1158, 2005.

[225] Jeremy Adler and Ingela Parmryd. Quantifying colocalization by correlation: the pearson correlation coefficient is superior to the mander's overlap coefficient. *Cytometry Part A*, 77(8):733–742, 2010.

[226] John H Mcdonald and Kenneth W Dunn. Statistical tests for measures of colocalization in biological microscopy. *Journal of microscopy*, 252(3):295–302, 2013.

[227] EMM Manders, FJ Verbeek, and JA Aten. Measurement of co-localization of objects in dual-colour confocal images. *Journal of microscopy*, 169(3):375–382, 1993.

[228] Emmanuelle Berret, Pascal Y Smith, Mélaine Henry, Denis Soulet, Sébastien S Hébert, Katalin Toth, Didier Mouginot, and Guy Drolet. Extracellular na+ levels regulate formation and activity of the nax/alpha1-na+/k+-atpase complex in neuronal cells. *Frontiers in cellular neuroscience*, 8, 2014.

[229] Manjot Singh Bal, Victor Castro, Jörg Piontek, Christine Rueckert, Juliane K Walter, Aliaksei Shymanets, Barbara Kurig, Hannelore Haase, Bernd Nürnberg, and Ingolf E Blasig. The hinge region of the scaffolding protein of cell contacts, zonula occludens protein 1, regulates interacting with various signaling proteins. *Journal of cellular biochemistry*, 113(3):934–945, 2012.

[230] Jonathan WD Comeau, Santiago Costantino, and Paul W Wiseman. A guide to accurate fluorescence microscopy colocalization measurements. *Biophysical journal*, 91(12):4611–4622, 2006.

[231] Stacy Sommerfeld Ross, Joseph M Reinhardt, and Jennifer Fiegel. Enhanced analysis of bacteria susceptibility in connected biofilms. *Journal of microbiological methods*, 90(1):9–14, 2012.

[232] Eero Lihavainen, Jarno Mäkelä, Johannes N Spelbrink, and Andre S Ribeiro. Mytoe: automatic analysis of mitochondrial dynamics. *Bioinformatics*, 28(7):1050–1051, 2012.

[233] Yijia Li, Ley-Hian Low, Ulrich Putz, Choo-Peng Goh, Seong-Seng Tan, and Jason Howitt. Rab5 and ndfip1 are involved in pten ubiquitination and nuclear trafficking. *Traffic*, 15(7):749–761, 2014.

[234] Susanne Bolte, Spencer Brown, and Béatrice Satiat-Jeunemaitre. The n-myristoylated rab-gtpase m-rabmc is involved in post-golgi trafficking events to the lytic vacuole in plant cells. *Journal of Cell Science*, 117(6):943–954, 2004.

[235] Irwin Sobel. Camera models and machine perception. Technical report, DTIC Document, 1970.

[236] Xavier Ronot and Yves Usson. *Imaging of nucleic acids and quantitation in photonic microscopy*. CRC Press, 2014.

[237] Fernand Meyer and Serge Beucher. Morphological segmentation. *Journal of visual communication and image representation*, 1(1):21–46, 1990.

[238] Jos BTM Roerdink and Arnold Meijster. The watershed transform: Definitions, algorithms and parallelization strategies. *Fundamenta informaticae*, 41(1):187–228, 2000.

[239] Yohann Boutté, Marie-Thérèse Crosnier, Nicola Carraro, Jan Traas, and Béatrice Satiat-Jeunemaitre. The plasma membrane recycling pathway and cell polarity in plants: studies on pin proteins. *Journal of cell science*, 119(7):1255–1265, 2006.

[240] E Lachmanovich, DE Shvartsman, Y Malka, C Botvin, YI Henis, and AM Weiss. Co-localization analysis of complex formation among membrane proteins by computerized fluorescence microscopy: application to immunofluorescence co-patching studies. *Journal of microscopy*, 212(2):122–131, 2003.

[241] Ben J Woodcroft, Luke Hammond, Jennifer L Stow, and Nicholas A Hamilton. Automated organelle-based colocalization in whole-cell imaging. *Cytometry Part A*, 75(11):941–950, 2009.

[242] Patrick A Fletcher, David RL Scriven, Meredith N Schulson, and Edwin DW Moore. Multi-image colocalization and its statistical significance. *Biophysical journal*, 99(6):1996–2005, 2010.

[243] Aurélien Rizk, Grégory Paul, Pietro Incardona, Milica Bugarski, Maysam Mansouri, Axel Niemann, Urs Ziegler, Philipp Berger, and Ivo F Sbalzarini. Segmentation

and quantification of subcellular structures in fluorescence microscopy images using squassh. *Nature protocols*, 9(3):586–596, 2014.

[244] Yannis Kalaidzidis, Inna Kalaidzidis, and Marino Zerial. A probabilistic method to quantify the colocalization of markers on intracellular vesicular structures visualized by light microscopy. In *BAYESIAN INFERENCE AND MAXIMUM ENTROPY METHODS IN SCIENCE AND ENGINEERING (MAXENT 2014)*, volume 1641, pages 580–587. AIP Publishing, 2015.

[245] Vadim Zinchuk, Yong Wu, and Olga Grossenbacher-Zinchuk. Bridging the gap between qualitative and quantitative colocalization results in fluorescence microscopy studies. *Scientific reports*, 3, 2013.

[246] Yong Wu, Mansoureh Eghbali, Jimmy Ou, Rong Lu, Ligia Toro, and Enrico Stefani. Quantitative determination of spatial protein-protein correlations in fluorescence confocal microscopy. *Biophysical journal*, 98(3):493–504, 2010.

[247] Vadim Zinchuk and Olga Grossenbacher-Zinchuk. Quantitative colocalization analysis of confocal fluorescence microscopy images. *Current Protocols in Cell Biology*, pages 4–16, 2008.

[248] Vadim Zinchuk, Yong Wu, Olga Grossenbacher-Zinchuk, and Enrico Stefani. Quantifying spatial correlations of fluorescent markers using enhanced background reduction with protein proximity index and correlation coefficient estimations. *nature protocols*, 6(10):1554–1567, 2011.

[249] Hiroyuki Takeda, Sina Farsiu, and Peyman Milanfar. Kernel regression for image processing and reconstruction. *Image Processing, IEEE Transactions on*, 16(2):349–366, 2007.

[250] Antoni Buades, Bartomeu Coll, and Jean-Michel Morel. A review of image denoising algorithms, with a new one. *Multiscale Modeling & Simulation*, 4(2):490–530, 2005.

[251] Bo Zhang, Nicolas Chenouard, J-C Olivo-Marin, and Vannary Meas-Yedid. Statistical colocalization in biological imaging with false discovery control. In *Biomedical Imaging: From Nano to Macro, 2008. ISBI 2008. 5th IEEE International Symposium on*, pages 1327–1330. IEEE, 2008.

[252] Mohamad Forouzanfar, Hamid Abrishami Moghaddam, and Sona Ghadimi. Locally adaptive multiscale bayesian method for image denoising based on bivariate normal

inverse gaussian distributions. *International Journal of Wavelets, Multiresolution and Information Processing*, 6(04):653–664, 2008.

[253] Jean-Luc Starck and Fionn Murtagh. Image restoration with noise suppression using the wavelet transform. *Astronomy and Astrophysics*, 288:342–348, 1994.

[254] Jean-Luc Starck, Fionn D Murtagh, and Albert Bijaoui. *Image processing and data analysis: the multiscale approach*. Cambridge University Press, 1998.

[255] William Thomas Eric Pitkeathly. *Four dimensional analysis of vesicle dynamics during directed cell migration*. PhD thesis, University of Birmingham, 2016.

[256] Cecilia Bucci, Robert G Parton, Ian H Mather, Henk Stunnenberg, Kai Simons, Bernard Hoflack, and Marino Zerial. The small gtpase rab5 functions as a regulatory factor in the early endocytic pathway. *Cell*, 70(5):715–728, 1992.

[257] Sylwia Jones, Debbie L Cunningham, Joshua Z Rappoport, and John K Heath. The non-receptor tyrosine kinase ack1 regulates the fate of activated egfr by inducing trafficking to the p62/nbr1 pre-autophagosome. *Journal of cell science*, 127(5):994–1006, 2014.

[258] Colocalisation Benchmark Source. CBS Colocalization Benchmark Source. *www.colocalization-benchmark.com*, 2015. Accessed: 18-02-2015.

[259] RH Chow, Z Borok, KJ Kim, ED Crandall, and A Sipos. Nanoparticle uptake into rat alveolar epithelial cells by live cell imaging. *Am J Respir Crit Care Med*, 189:A3414, 2014.

[260] Cécile Leduc, Satyabrata Si, Jérémie Gautier, Martinho Soto-Ribeiro, Bernhard Wehrle-Haller, Alexis Gautreau, Grégory Giannone, Laurent Cognet, and Brahim Lounis. A highly specific gold nanoprobe for live-cell single-molecule imaging in confined environments: Intracellular tracking and long-term single integrin tracking in adhesion sites. *Biophysical Journal*, 106(2):193a–194a, 2014.

[261] Cécile Leduc, Satyabrata Si, Jérémie J Gautier, Zhenghong Gao, Edakkattuparambil S Shibu, Alexis Gautreau, Grégory Giannone, Laurent Cognet, and Brahim Lounis. Single-molecule imaging in live cell using gold nanoparticles. *Methods in Cell Biology*, 2015.

[262] Ramsey N Majzoub, Kai K Ewert, Venkata R Kotamraju, Chia-Ling Chan, Keng S Liang, Erkki Ruoslahti, and Cyrus R Safinya. Live cell imaging with rab-gtpases elucidates intracellular pathways of rgd and irgd tagged cationic lipid-dna nanoparticles. *Biophysical Journal*, 106(2):421a, 2014.

[263] Alexandre Albanese, Peter S Tang, and Warren CW Chan. The effect of nanoparticle size, shape, and surface chemistry on biological systems. *Annual review of biomedical engineering*, 14:1–16, 2012.

[264] Dries Vercauteren, Hendrik Deschout, Katrien Remaut, Johan FJ Engbersen, Arwyn T Jones, Jo Demeester, Stefaan C De Smedt, and Kevin Braeckmans. Dynamic colocalization microscopy to characterize intracellular trafficking of nanomedicines. *Acs Nano*, 5(10):7874–7884, 2011.

[265] Christina Tekle, Bo van Deurs, Kirsten Sandvig, and Tore-Geir Iversen. Cellular trafficking of quantum dot-ligand bioconjugates and their induction of changes in normal routing of unconjugated ligands. *Nano letters*, 8(7):1858–1865, 2008.

[266] Zhan-Guo Yue, Wei Wei, Pi-Ping Lv, Hua Yue, Lian-Yan Wang, Zhi-Guo Su, and Guang-Hui Ma. Surface charge affects cellular uptake and intracellular trafficking of chitosan-based nanoparticles. *Biomacromolecules*, 12(7):2440–2446, 2011.

[267] Harald Stenmark, Robert G Parton, Olivia Steele-Mortimer, A Lütcke, Jean Gruenberg, and M Zerial. Inhibition of rab5 gtpase activity stimulates membrane fusion in endocytosis. *The EMBO journal*, 13(6):1287, 1994.

[268] Sophia Semerdjieva, Barry Shortt, Emma Maxwell, Sukhdeep Singh, Paul Fonarev, Jonathan Hansen, Giampietro Schiavo, Barth D Grant, and Elizabeth Smythe. Coordinated regulation of ap2 uncoating from clathrin-coated vesicles by rab5 and hrme-6. *The Journal of cell biology*, 183(3):499–511, 2008.

[269] Erik Nielsen, Fedor Severin, Jonathan M Backer, Anthony A Hyman, and Marino Zerial. Rab5 regulates motility of early endosomes on microtubules. *Nature Cell Biology*, 1(6):376–382, 1999.

[270] Peter Sandin, Laurence W Fitzpatrick, Jeremy C Simpson, and Kenneth A Dawson. High-speed imaging of rab family small gtpases reveals rare events in nanoparticle trafficking in living cells. *ACS nano*, 6(2):1513–1521, 2012.

[271] Scott E Fraser. Iontophoretic dye labeling of embryonic cells. *Methods in cell biology*, 51:147–161, 1996.

[272] Qing Li, Lin Liu, Jin-Wen Liu, Jian-Hui Jiang, Ru-Qin Yu, and Xia Chu. Nanomaterial-based fluorescent probes for live-cell imaging. *TrAC Trends in Analytical Chemistry*, 58:130–144, 2014.

[273] Dan Peer, Jeffrey M Karp, Seungpyo Hong, Omid C Farokhzad, Rimona Margalit, and Robert Langer. Nanocarriers as an emerging platform for cancer therapy. *Nature nanotechnology*, 2(12):751–760, 2007.

[274] Maria J Ruedas-Rama, Jamie D Walters, Angel Orte, and Elizabeth AH Hall. Fluorescent nanoparticles for intracellular sensing: a review. *Analytica chimica acta*, 751:1–23, 2012.

[275] W.T.E. Pitkeathly, N.S. Poulter, E. Claridge, and J.Z. Rappoport. Auto-align–multi-modality fluorescence microscopy image co-registration. *Traffic*, 2011.

[276] Charles S Peskin, Garrett M Odell, and George F Oster. Cellular motions and thermal fluctuations: the brownian ratchet. *Biophysical journal*, 65(1):316, 1993.

[277] R Dean Astumian. Thermodynamics and kinetics of a brownian motor. *science*, 276(5314):917–922, 1997.

[278] Junghae Suh, Denis Wirtz, and Justin Hanes. Efficient active transport of gene nanocarriers to the cell nucleus. *Proceedings of the National Academy of Sciences*, 100(7):3878–3882, 2003.

[279] Jonathon Howard and RL Clark. Mechanics of motor proteins and the cytoskeleton. *Applied Mechanics Reviews*, 55:39, 2002.

[280] Marvin E Tanenbaum, Luke A Gilbert, Lei S Qi, Jonathan S Weissman, and Ronald D Vale. A protein-tagging system for signal amplification in gene expression and fluorescence imaging. *Cell*, 159(3):635–646, 2014.

[281] Neftali Flores-Rodriguez, Salman S Rogers, David A Kenwright, Thomas A Waigh, Philip G Woodman, and Victoria J Allan. Roles of dynein and dynactin in early endosome dynamics revealed using automated tracking and global analysis. *PloS one*, 6(9):e24479, 2011.

[282] Cédric Bouzigues and Maxime Dahan. Transient directed motions of gaba a receptors in growth cones detected by a speed correlation index. *Biophysical journal*, 92(2):654–660, 2007.

[283] E Meijering. Mtrackj (imagej plugin). *Biomedical Imaging Group Rotterdam, Erasmus MCUniversity Medical Center, Rotterdam, Netherlands http://www. imagescience. org/meijering/software/mtrackj*, 2008.

[284] Fengjuan Wang, Lu Yu, Marco P Monopoli, Peter Sandin, Eugene Mahon, Anna Salvati, and Kenneth A Dawson. The biomolecular corona is retained during nanoparticle uptake and protects the cells from the damage induced by cationic nanoparticles until degraded in the lysosomes. *Nanomedicine: Nanotechnology, Biology and Medicine*, 9(8):1159–1168, 2013.

[285] Jerome Gilleron, William Querbes, Anja Zeigerer, Anna Borodovsky, Giovanni Marsico, Undine Schubert, Kevin Manygoats, Sarah Seifert, Cordula Andree, Martin Stöter, et al. Image-based analysis of lipid nanoparticle-mediated sirna delivery, intracellular trafficking and endosomal escape. *Nature biotechnology*, 31(7):638–646, 2013.

[286] Hynda K Kleinman, Mary L McGarvey, John R Hassell, Vicki L Star, Frances B Cannon, Gordon W Laurie, and George R Martin. Basement membrane complexes with biological activity. *Biochemistry*, 25(2):312–318, 1986.

[287] BD Biosciences. BD Matrigel Matrix FAQ. *http://fscimage.fishersci.com/cmsassets/downloads/segment/Scientific/pdf/BD/bd*$_c$*ellculture*$_m$ $30 - 05 - 2016$.

[288] ThermoFisher Scientific. CellTracker CM-DiI Dye. *https://www.thermofisher.com/order/catalog/product/C7001*, 2015. Accessed: 23-August-2015.

[289] B.P. Olveczky, N. Periasamy, and AS Verkman. Mapping fluorophore distributions in three dimensions by quantitative multiple angle-total internal reflection fluorescence microscopy. *Biophysical journal*, 73(5):2836–2847, 1997.

[290] K. Stock, R. Sailer, WSL Strauss, M. Lyttek, R. Steiner, and H. Schneckenburger. Variable-angle total internal reflection fluorescence microscopy (va-tirfm): realization and application of a compact illumination device. *Journal of microscopy*, 211(1):19–29, 2003.

[291] A. Rohrbach. Observing secretory granules with a multiangle evanescent wave microscope. *Biophysical journal*, 78(5):2641–2654, 2000.

[292] D. Loerke, W. Stühmer, and M. Oheim. Quantifying axial secretory-granule motion with variable-angle evanescent-field excitation. *Journal of neuroscience methods*, 119(1):65–73, 2002.

[293] JS Burmeister, GA Truskey, and WM Reichert. Quantitative analysis of variable-angle total internal reflection fluorescence microscopy (va-tirfm) of cell/substrate contacts. *Journal of microscopy*, 173(1):39–51, 1994.

[294] C.A. Konopka and S.Y. Bednarek. Variable-angle epifluorescence microscopy: a new way to look at protein dynamics in the plant cell cortex. *The Plant Journal*, 53(1):186–196, 2008.

[295] W. Yinglang, A. William, F. Lusheng, H. Huaiqin, K. Myung, and L. Jinxing. Variable-angle total internal reflection fluorescence microscopy of intact cells of arabidopsis thaliana. *Plant Methods*, 7, 2011.

[296] P.B. Garland et al. Optical evanescent wave methods for the study of biomolecular interactions. *Quarterly reviews of biophysics*, 29(1):91, 1996.

[297] Gregorio Weber. Rotational brownian motion and polarization of the fluorescence of solutions. *Advances in protein chemistry*, 8:415–459, 1953.

[298] F. Jähnig. Structural order of lipids and proteins in membranes: evaluation of fluorescence anisotropy data. *Proceedings of the National Academy of Sciences*, 76(12):6361, 1979.

[299] RA Badley, WG Martin, and H. Schneider. Dynamic behavior of fluorescent probes in lipid bilayer model membranes. *Biochemistry*, 12(2):268–275, 1973.

[300] Y. Juan and S. Lubert. Fluorescence spectroscopy of an oriented model membrane. *Proc Natl Acad Sci US A*, 68(6):1217–1221, 1971.

[301] D. Axelrod. Carbocyanine dye orientation in red cell membrane studied by microscopic fluorescence polarization. *Biophysical journal*, 26(3):557–573, 1979.

[302] N.L. Thompson, H.M. McConnell, and TP Burhardt. Order in supported phospholipid monolayers detected by the dichroism of fluorescence excited with polarized evanescent illumination. *Biophysical journal*, 46(6):739–747, 1984.

[303] S.E. Sund, J.A. Swanson, and D. Axelrod. Cell membrane orientation visualized by polarized total internal reflection fluorescence. *Biophysical journal*, 77(4):2266–2283, 1999.

[304] A.F. Runge, S.S. Saavedra, and S.B. Mendes. Combination of polarized tirf and atr spectroscopies for determination of the second and fourth order parameters of molecular orientation in thin films and construction of an orientation distribution based on the maximum entropy method. *The Journal of Physical Chemistry B*, 110(13):6721–6731, 2006.

[305] A. Anantharam, D. Axelrod, and R.W. Holz. Polarized tirfm reveals changes in plasma membrane topology before and during granule fusion. *Cellular and molecular neurobiology*, pages 1–7, 2010.

[306] A. Anantharam, B. Onoa, R.H. Edwards, R.W. Holz, and D. Axelrod. Localized topological changes of the plasma membrane upon exocytosis visualized by polarized tirfm. *The Journal of cell biology*, 188(3):415–428, 2010.

[307] J.N. Forkey, M.E. Quinlan, and Y.E. Goldman. Measurement of single macromolecule orientation by total internal reflection fluorescence polarization microscopy. *Biophysical journal*, 89(2):1261–1271, 2005.

[308] J.N. Forkey, M.E. Quinlan, M.A. Shaw, J.E.T. Corrie, Y.E. Goldman, et al. Three-dimensional structural dynamics of myosin v by single-molecule fluorescence polarization. *Nature*, 422(6930):399–404, 2003.

[309] J.F. Beausang, Y. Sun, M.E. Quinlan, J.N. Forkey, and Y.E. Goldman. Orientation and rotational motions of single molecules by polarized total internal reflection fluorescence microscopy. *Single Molecule Techniques. PR Selvin, and T. Ha, editors. Cold Spring Harbor Laboratory Press, Cold Spring Harbor, NY*, pages 121–148, 2008.

[310] M.E. Quinlan, J.N. Forkey, and Y.E. Goldman. Orientation of the myosin light chain region by single molecule total internal reflection fluorescence polarization microscopy. *Biophysical journal*, 89(2):1132–1142, 2005.

[311] J.F. Beausang et al. Twirling of actin by myosins ii and v observed via polarized tirf in a modified gliding assay. *Biophysical journal*, 95(12):5820–5831, 2008.

[312] R.M. Dickson, DJ Norris, and WE Moerner. Simultaneous imaging of individual molecules aligned both parallel and perpendicular to the optic axis. *Physical review letters*, 81(24):5322–5325, 1998.

[313] A. Tronin and JK Blasie. Variable acquisition angle total internal reflection fluorescence: a new technique for orientation distribution studies of ultrathin films. *Langmuir*, 17(12):3696–3703, 2001.

[314] J. Oreopoulos and C.M. Yip. Combinatorial microscopy for the study of protein-membrane interactions in supported lipid bilayers: order parameter measurements by combined polarized tirfm/afm. *Journal of structural biology*, 168(1):21–36, 2009.

[315] J. Oreopoulos and C.M. Yip. Probing membrane order and topography in supported lipid bilayers by combined polarized total internal reflection fluorescence-atomic force microscopy. *Biophysical journal*, 96(5):1970–1984, 2009.

[316] A.L. Mattheyses, A.D. Hoppe, and D. Axelrod. Polarized fluorescence resonance energy transfer microscopy. *Biophysical journal*, 87(4):2787–2797, 2004.

[317] Maurizio Righini, Anna S Zelenina, Christian Girard, and Romain Quidant. Parallel and selective trapping in a patterned plasmonic landscape. *Nature Physics*, 3(7):477–480, 2007.

[318] Jürgen Engel, Erich Odermatt, Andreas Engel, Joseph A Madri, Heinz Furthmayr, Heilwig Rohde, and Rupert Timpl. Shapes, domain organizations and flexibility of laminin and fibronectin, two multifunctional proteins of the extracellular matrix. *Journal of molecular biology*, 150(1):97–120, 1981.

[319] HJ Tang and DENG H Y WU FQ. Transmittance comparison of glan-taylor prism and glan-foucault prism. *Laser Technology*, 30(2):215–217, 2006.

[320] ThorLabs. Polarisation-Maintaining FC/PC Fiber Optic Patch Cables. *https://www.thorlabs.com/newgrouppage9.cfm?objectgroup$_i$d = 3125pn = P1 − 488PM − FC − 2, 2009. Accessed* : 06 − 07 − 2016.

[321] Denis Penninckx and Nicolas Beck. Definition, meaning, and measurement of the polarization extinction ratio of fiber-based devices. *Applied optics*, 44(36):7773–7779, 2005.

[322] CrystaLaser. CrystaLaser Stabilised Lasers. *http://www.crystalaser.com/DL375-488.pdf*, 2016. Accessed: 06-07-2016.

[323] IDEX. How to Select a Laser. *https://marketplace.idexop.com/store/SupportDocuments/*TN_HT $06-07-2016$.

[324] AR El-Damak, Jianhua Chang, Jian Sun, Changqing Xu, and Xijia Gu. Dual-wavelength, linearly polarized all-fiber laser with high extinction ratio. *IEEE Photonics Journal*, 5(4):1501406–1501406, 2013.

[325] Joonhoi Koo, Jaehyun Park, Yong-Won Song, Sangbae Lee, Kwanil Lee, and Ju Han Lee. Fiber optic polarization beam splitter using a reduced graphene oxide-based interlayer. *Optical Materials*, 46:324–328, 2015.

[326] OZOptics. Polarisation Extinction Radio Metre. *http://www.ozoptics.com/*$ALLNEW_PDF/DTS$*0067.pdf*, 2016. *Accessed* : $06-07-2016$.

[327] Chroma. Filters and Mirrors for Laser Applications. *https://www.chroma.com/sites/default/files/*$Laser_App_Note$*.pdf*, 2009. *Accessed* : $30-05-2016$.